



**Politecnico
di Torino**



**UNIVERSITÀ
DEGLI STUDI
DI TORINO**

Doctoral Dissertation
Doctoral Program in Bioengineering and Medical-Surgical Sciences (33rd Cycle)

***Engineered Microphysiological systems of
multicellular-vascular interactions: modeling
nanoparticle transport and drug efficacy using
microfluidic technology***

Marco Campisi

Supervisors:

Prof. Valeria Chiono, Supervisor
Prof. Roger D. Kamm, Co-supervisor
Dr. Clara Mattu, Co-supervisor
Prof. David A. Barbie, Co-supervisor

Doctoral Examination Committee:

Prof. Gianni Ciofani, Istituto Italiano di Tecnologia
Prof. Marco Rasponi, Politecnico di Milano
Prof. Tiziano Serra, AO Research Institute Davos

Politecnico di Torino
May 7th, 2021

This thesis is licensed under a Creative Commons License, Attribution- Noncommercial - NoDerivative Works 4.0 International: see www.creativecommons.org.
The text may be reproduced for non-commercial purposes, provided that credit is given to the original author.

I hereby declare that, the contents and organisation of this dissertation constitute my own original work and does not compromise in any way the rights of third parties, including those relating to the security of personal data.

Marco Campisi

Marco Campisi

Acknowledgements

My Ph.D journey is coming to an end. I am overwhelmed in all humbleness and gratefulness to acknowledge all those who have accompanied me in these years.

Foremost, I would like to express my sincere gratitude to my tutor, Prof. Valeria Chiono, for giving me the opportunity to undertake such a challenging Ph.D, for the continuous support during our study and research, for her patience and immense knowledge. Her guidance helped me in all the time of the research and while writing this thesis.

I would like to express my deep and sincere gratitude to my co-supervisor, Prof. David Barbie, for kindly hosting me in his laboratory at Dana-Farber Cancer Institute and for being a constant source enthusiasm and inspiration. Thanks to his unparalleled mentorship, I have learned so much and grown not only as a scientist but mostly as a human being.

I also would like to express my special gratitude to my co-supervisor Prof. Roger Kamm, who firstly gave me the golden opportunity to start doing research in his laboratory at the Massachusetts Institute of Technology. In this place, during my master thesis in 2016-2017, I fell in love with biomedical research and decided to pursue this long path in collaboration together.

I am grateful to my co-supervisor Dr. Clara Mattu, for the advice and precious contribution in the realization of the project, but also, her guidance, support and motivation in Turin.

I also express my sincere gratitude to Prof. Roberto Chiarle, for kindly hosting me in his laboratory at University of Turin and for his great mentorship in such a short time frame.

Besides my advisors, I also wish to thank the reviewers and the committee members for generously offering their time and their thoughtful feedback.

My sincere thanks go to colleagues and friends of Dana-Farber Cancer Institute, Politecnico di Torino and MIT for their continuous support and motivation over the past few years. They contributed and trained me to be a scientist in every sense of the word. This research work would have not been possible without their constant guidance, science discussion, support and motivation. It has been a privilege to work with such talented and creative people.

I am extremely grateful to the Ermenegildo Zegna Foundation for the generous scholarship I was awarded in 2016-17, that also supported my transition from a Master student in biomedical engineering to Ph.D student.

Finally, I would like to thank my family, for their selfless love, care and sacrifices, and for always making me feel loved in these years away from home and during these challenging times. I would not be the person I am without them. They always believed in me and never stopped encouraging me to pursue my dreams.

Last but not least, I am grateful to my friends and colleagues for always being supportive, especially during this last year in Boston in unprecedented times with a Covid-19 world pandemic. They always encouraged me to do better.

List of publications

M. Campisi, S. H. Lim, V. Chiono, R.D. Kamm, “3D self-organized human Blood-Brain Barrier in a microfluidic chip” Programmed morphogenesis: Methods and Protocols, Methods in Molecular Biology, Springer US, Dec. 2020, Book Chapter. https://doi.org/10.1007/978-1-0716-1174-6_14

M. Campisi, S. K. Sundararaman, S.E. Shelton, Erik H. Knelson, Elena Ivanova, I. Cañadas, R. Yoshida, T. Osaki, S. W. L. Lee, T. Thai, S. Han, B. P. Piel, S. Gilhooley, C. P. Paweletz, V. Chiono, R. D. Kamm, S. Kitajima, and D. A. Barbie, “Tumor-derived cGAMP regulates activation of the vasculature”. *Frontiers in Immunology*. Sept 2020. <https://doi.org/10.3389/fimmu.2020.02090>

W.L. Lee S. (50%), **Campisi M. (50%)**, Osaki T., Possenti L., Mattu C., Adriani G., Kamm R.D., Chiono V. “Modeling Nanocarrier Transport Across a 3D In Vitro Human Blood-Brain-Barrier Microvasculature”. Feb. 2020, *Advanced Healthcare Materials*. <https://doi.org/10.1002/adhm.201901486>

M. Campisi, S. W. L. Lee, T. Osaki, L. Possenti, C. Mattu, G. Adriani, V. Chiono, R.D. Kamm “In vitro microfluidic modelling of the human blood-brain-barrier microvasculature and testing of nanocarrier transport”. *Biomedical Science and Engineering* 2020; <https://pagepress.org/technology/index.php/bse/article/view/105>

M. Campisi, S. Sundararaman, S. Kitajima, I. Canadas, V. Chiono, R. D. Kamm, D. A. Barbie “Tumor-Stroma Interactions Promote cGAS-STING Driven Inflammation in Lung Tumor Microenvironment”. October 2019, *Journal of Thoracic Oncology*. DOI:<https://doi.org/10.1016/j.jtho.2019.08.1528>

S. H. Lim, C. M. Kuan, **M. Campisi**, V. Chiono, A. Pavesi “Analyzing immune cell infiltration of cancer spheroids in a 3D cell culture platform”, July 2019, *Cancer Research*. DOI: 10.1158/1538-7445.AM2019-47. https://cancerres.aacrjournals.org/content/79/13_Supplement/47

M. Campisi, S K. Sundararaman, S. Kitajima, V Chiono, R. D. Kamm and D. A. Barbie “Tumor-vascular interactions promote STING-driven inflammation in the tumor microenvironment”, July 2019, *Cancer Research*. https://cancerres.aacrjournals.org/content/79/13_Supplement/958

W.L. Lee S., Paoletti C., **Campisi M.**, Osaki T., Adriani G., Kamm R.D., Mattu C., Chiono V., “MicroRNA delivery through nanoparticles”, Aug. 2019, *Journal of controlled Release*, vol. 313. Elsevier B.V., pp. 80–95, 10-Nov-2019. <https://doi.org/10.1016/j.jconrel.2019.10.007>

Aref A.R., **Campisi M.**, Ivanova E., Portell A., Larios D., Piel B.P., Mathur N., Zhou C., Coakley R.V., Bartels A., Bowden M., Herbert Z., Hill S., Gilhooley S., Carter J., Cañadas I., Thai T. C., Kitajima S., Chiono V., Paweletz C. P., Barbie D.A., Kamm R.D. and Jenkins R.W. “Microfluidic ex vivo culture of organotypic tumor spheroids to model immune checkpoint blockade”. Sept. 2018, *Lab on a Chip*. <https://doi.org/10.1039/C8LC00322J>

Campisi M., Shin Y., Osaki T., Hajal C., Chiono V. and Kamm R.D. “3D Self-Organized Microvascular Model of the Human Blood-Brain Barrier with Endothelial Cells, Pericytes and Astrocytes”. Jul. 2018, Biomaterials. 180, 117–129. <https://doi.org/10.1016/j.biomaterials.2018.07.014>

Hajal C., **Campisi M.**, Mattu C., Chiono V. and Kamm R.D. “In Vitro Models of Molecular and Nano-Particle Transport across the Blood-Brain Barrier”. May 2018, Biomicrofluidics. 12 (4). <https://doi.org/10.1063/1.5027118>

Kitajima S., Ivanova E., Guo S., Yoshida, R., **Campisi M.**, Sundararaman S.K., Tange S., Mitsuishi Y., Thai T.C., Masuda S., Piel B.P., Sholl L.M., Kirschmeier P.T., Paweletz C.P., Watanabe H., Yajima M., Barbie D.A. “Suppression of STING associated with LKB1 loss in KRAS-driven lung cancer”. Oct 2018, Cancer Discovery. <https://cancerdiscovery.aacrjournals.org/content/9/1/34>

Cañadas I, Thummalapalli R, Kim JW, Kitajima S, Jenkins RW, Christensen CL, **Campisi M**, Kuang Y, Zhang Y, Gjini E, Zhang G, Tian T, Sen DR, Miao D, Imamura Y, Thai T, Piel B, Terai H, Aref AR, Hagan T, Koyama S, Watanabe M, Baba H, Adeni AE, Lydon CA, Tamayo P, Wei Z, Herlyn M, Barbie TU, Uppaluri R, Sholl LM, Sicinska E, Sands J, Rodig S, Wong KK, Paweletz BP, Watanabe H, Barbie, DA. “Tumor innate immunity primed by specific interferon-stimulated endogenous retroviruses”. July 2018, Nature Medicine. <https://doi.org/10.1038/s41591-018-0116-5>

T. Osaki, Y. Shin, V. Sivathanu, **M. Campisi**, R.D. Kamm, “In vitro microfluidic models for neurodegenerative disorders. September, 2017, Advanced Healthcare Materials. <https://doi.org/10.1002/adhm.201700489>

Short curriculum vitae

EDUCATION

Polytechnic University of Turin

M.S. in Biomedical Engineering (Major Bionanotechnology) Mar 2014 – Mar 2017

- Score: 110 cum Laude / 110
- Thesis: *Microfluidic platforms mimicking the Blood-Brain Barrier for testing of Nanoparticle delivery to the brain*
- Tutors: Gianluca Ciardelli, Valeria Chiono, Roger Kamm

Polytechnic University of Turin

B.S. in Biomedical Engineering Oct 2010 – Mar 2014

- Score: 92 / 110
- Thesis: *Installation of CT workstation for Breast cancer*
- Tutors: P. Falco (im3D), F. Molinari

RESEARCH EXPERIENCE

Dana-Farber Cancer Institute, Harvard Medical School, Dept. of Medical Oncology

Visiting Ph.D. student, Boston, MA

Research advisor: Prof. M.D., David. A. Barbie July 2017–July 2018 & Feb 2020 – present

Molinette Hospital, University of Turin, Dept. of Molecular Biotechnology and Health Sciences.

Visiting Ph.D. student Turin, IT

Research advisor: Prof. M.D., Roberto Chiarle June 2019– Jan 2020

Polytechnic University of Turin, Dept. of Mechanical Engineering.

Ph.D. student, Turin, IT

Research advisor: Prof. Valeria Chiono Oct. 2017– present

Massachusetts Institute of Technology (MIT), Mechanobiology Lab, Dept. of Biological Engineering

Visiting research student, Cambridge, MA

Research advisor: Prof. Roger Kamm June 2016–June 2017

INTERNATIONAL CONFERENCES & SUMMER SCHOOL

TERMIS YSIS AM & EU webinar series.

Oral webinar presentation, Sept,2020

Talk abstract: “*Microphysiological systems for modelling microvasculature and multicellular-vascular interactions using microfluidic technology*” M. Campisi, T. Osaki, S. Shelton, S. Sundararaman, S.W.L. Lee, C. Mattu, G. Adriani, C. Voena, I. Mota, E. Patrucco, S. Kitajima, R. Chiarle, D. A. Barbie, R. D. Kamm and V. Chiono.

European Congress on Alternatives to Animal Testing (EUSAAT)

Talk: Linz, Austria, Oct 9-13, 2019

Talk abstract: “*Modelling the human Blood-Brain Barrier microvasculature and nanocarrier transport on a microfluidic chip*”. Campisi M., W.L. Lee S., Osaki T., Possenti L., Mattu C., Adriani G., Chiono V, R.D. Kamm.

World Lung Cancer Conference, Annual meeting

Barcelona, Spain, Sept 7-10, 2019

Poster abstract: “*Tumor-stroma interactions promote cGAS-STING-driven inflammation in lung tumor microenvironment*”. Campisi M, Sundararaman S., I. Cañadas, Chiono V, RD Kamm, S.K, Kitajima DA Barbie.

Summer School -Drug delivery, Denmark Technical University

Copenhagen, Denmark, Aug 18-30, 2019

Keystone Symposia: Delivering Therapeutics Across Biological Barriers

Dublin, Ireland, May 6-9, 2019

Talk abstract: “*Model of Nanoparticles Transport Across the human Blood-Brain Barrier*”. Campisi M, Osaki T., Possenti L., Mattu C., Adriani G., Kamm R.D., Chiono V.

American Association for Cancer Research, Annual meeting

Atlanta, Georgia, US, Mar 29-Apr 3, 2019

Talk abstract: “*Tumor-vascular interactions promote STING-driven inflammation in the tumor microenvironment*” Campisi M, Sundararaman S.K, Kitajima S., Chiono V, RD Kamm, DA Barbie.

Poster abstract: “*Analyze immune cell infiltration of cancer spheroids in a 3D cell culture platform*”. S. H. Lim, C. M. Kuan, Campisi, M, Chiono V, Pavesi A.

AWARDS

- Fondazione “Franco and Marilisa Caligara” for post-graduate research abroad, Feb 2021
- Young Scientist Travel Award (EUSAAT), Oct 2019
- Centro 3R “Young Scientist Award” 2019, June 2019
- The Outstanding Young Person for Research, Italy, Junior Chamber International, Mar 2019
- AACR-Pezcoller Foundation Scholar-in-Training Award, Mar 2019
- Award - Ermenegildo Zegna Founder’s scholarship, Aug 2016, Aug 2017
- Scholarship for master thesis abroad (Polytechnic of Turin), Jun 2016
- E.D.I.S.U. scholarship for B.S. and M.S. degree, Sept 2010 and 2014

Contents

ABSTRACT OF THE THESIS	15
THESIS OUTLINE.....	18
SECTION I.....	20
DESIGN AND COMPARISON OF CONVENTIONAL PRECLINICAL MODELS WITH 3-DIMENSIONAL IN VITRO TECHNOLOGIES: FOCUS ON MICROPHYSIOLOGICAL SYSTEMS.....	20
CHAPTER 1 - DESIGN PRINCIPLES OF PRECLINICAL MODELS.....	21
ABSTRACT.....	21
<i>Preclinical in vivo and in vitro models</i>	<i>23</i>
<i>Comparison of current 2D in vitro models</i>	<i>27</i>
<i>Bioengineering approaches for the design of 3-dimensional preclinical models</i>	<i>29</i>
<i>Tissue engineering and 3D bioprinting.....</i>	<i>31</i>
<i>Organoids.....</i>	<i>34</i>
<i>Microfluidic technology and ‘microphysiological systems’</i>	<i>36</i>
CHAPTER 2 - DESIGN PRINCIPLES, MICROFABRICATION AND THERAPEUTIC TESTING APPLICATIONS OF BIO-INSPIRED HUMAN MICROPHYSIOLOGICAL SYSTEMS USING MICROFLUIDIC TECHNOLOGY	41
ABSTRACT.....	41
<i>Bio-inspired Microphysiological systems</i>	<i>43</i>
<i>Microfluidic technology and microfabrication processes of micro and macro systems</i>	<i>44</i>
<i>Microphysiological systems for vessel formation in vitro: modelling microvasculature and multicellular-vascular interactions</i>	<i>46</i>
<i>Patterned microchannel: 3D macro-vessels</i>	<i>48</i>
<i>Self-assembled microvessels: vasculogenesis</i>	<i>49</i>
<i>Preclinical modeling of drug efficacy and nanoparticle transport with Microphysiological systems</i>	<i>50</i>
<i>Nanoparticles as drug delivery systems</i>	<i>51</i>
AIM OF THE WORK.....	56
REFERENCES	57
SECTION II	65
3-D MICROPHYSIOLOGICAL MODEL OF THE BLOOD-BRAIN BARRIER.....	65
CHAPTER 3 – CURRENT ADVANCES AND CHALLENGES IN THE MODELLING OF HUMAN BLOOD-BRAIN BARRIER	66
ABSTRACT.....	66
INTRODUCTION.....	68
<i>Structures and components of the Blood-Brain Barrier.....</i>	<i>68</i>
<i>Cellular components of the human Blood-Brain Barrier.....</i>	<i>68</i>
<i>Functions and regulation of the Blood-Brain Barrier</i>	<i>70</i>
<i>Transport mechanisms across the Blood-Brain Barrier</i>	<i>73</i>
<i>Blood-Brain Barrier in the pathology of neurological disease.....</i>	<i>77</i>
<i>Nanoparticle as a delivery system across the Blood-Brain Barrier.....</i>	<i>78</i>
<i>In vitro and in vivo modelling of the Blood-Brain Barrier for testing nanocarrier transport efficacy</i>	<i>81</i>
<i>Other in vitro Blood-Brain Barrier models.....</i>	<i>83</i>
<i>Microphysiological models of the Blood-brain Barrier.....</i>	<i>84</i>

DISCUSSION	90
CONCLUSION	91
CHAPTER 4 - MODELLING NANOPARTICLE TRANSPORT USING A 3D MICROPHYSIOLOGICAL MODEL OF THE HUMAN BLOOD-BRAIN BARRIER MICROVASCULATURE	92
ABSTRACT	92
INTRODUCTION	95
MATERIAL AND METHODS	98
<i>Material and reagents</i>	98
<i>Fabrication of the microfluidic device: Photolithography and Soft lithography</i>	98
<i>Fabrication of the macro device (Laser cutting)</i>	99
<i>Preparation of nanoparticles</i>	100
<i>Characterization of Nanoparticles</i>	101
<i>3D Microphysiological BBB model</i>	101
<i>Immunostaining and confocal imaging</i>	103
<i>BBB microvascular parameters characterization</i>	103
<i>Quantitative RT-PCR</i>	104
<i>Transwell permeability assay</i>	105
<i>3D permeability measurements and quantification</i>	106
<i>Quantification of 2D cellular nanoparticle uptake</i>	107
<i>3D intensity map of spatial-temporal NPs distribution</i>	107
<i>Cell viability assay</i>	108
<i>Statistical analysis</i>	108
RESULTS	109
<i>Characterization of the 3D Microphysiological BBB model</i>	109
<i>Protein and gene expressions of the Microphysiological BBB model</i>	114
<i>Specific cell contributions to BBB microvascular permeability</i>	121
<i>Testing of NPs transport in the 3D Microphysiological BBB model</i>	124
<i>Physical Characterization of Transferrin-functionalized PS and PU</i>	124
<i>Cytocompatibility assay and Cell Uptake of PS and PU NPs</i>	124
<i>2D Transwell BBB Model for NP Permeability</i>	125
<i>NPs microvascular Permeability Across a 3D Microphysiological BBB model</i>	128
<i>3D Biodistribution of NPs in the BBB Microphysiological model</i>	129
DISCUSSION	132
CONCLUSION	135
ACKNOWLEDGMENTS	136
SUPPLEMENTARY METHODS	139
REFERENCES	141
SECTION III –	152
3D MICROPHYSIOLOGICAL MODELS OF TUMOR-VASCULAR INTERACTIONS IN KRAS/LKB1 NON-SMALL CELL LUNG CANCER AND ALK⁺ ANAPLASTIC LARGE CELL LYMPHOMA	152
CHAPTER 5 – MODELLING cGAS-STING DRIVEN INNATE IMMUNITY AND T-CELL INFILTRATION/EXCLUSION IN THE NON-SMALL CELL LUNG TUMOR MICROENVIRONMENT	153
ABSTRACT	153
INTRODUCTION	155
<i>Lung cancer biology</i>	155
<i>KRAS/LKB1 mutant Non-Small Cell Lung Cancer</i>	158
<i>Innate immunity and cGAS-STING pathway</i>	158
<i>Lung Tumor microenvironment</i>	160

<i>In vitro</i> Preclinical models of lung cancer	162
DISCUSSION	164
CONCLUSION	165
CHAPTER 6 – A MICROPHYSIOLOGICAL VASCULAR-TUMOR MODEL UNCOVERS TUMOR-DERIVED cGAMP EXPORT TO PROMOTE cGAS-STING DRIVEN MICROVASCULAR INFLAMMATION IN THE TUMOR MICROENVIRONMENT	166
ABSTRACT	166
INTRODUCTION	169
MATERIALS AND METHODS	170
Materials and reagents	170
Cell culture	170
Immunohistochemical (IHC) Staining and analysis	170
Genetic engineering and CRISPR/Cas9 systems	171
RT-PCR	171
Immunoblotting	172
Immunohistochemistry	172
dsDNA Stimulation	173
3D microfluidic device	173
3D Microphysiological system: Lung cancer - microvasculature model	174
3D Migration assay	175
3D perfusion and adhesion assay	176
Permeability measurements	177
Immunofluorescence and confocal imaging	178
Multiplexed cytokine/chemokine profiling	178
ELISA	179
Cell Sorting by CD31	179
Statistical analysis	179
RESULTS	180
3-D spheroids microphysiological system reveals STING-driven cytokine /chemokine production after LKB1 reconstitution	180
Innate immune signaling changes captured in a 3-D Microphysiological system of lung tumor-vasculature interactions	183
The cooperative production of cytokines in the Microphysiological tumor-vasculature interaction is not dependent on cancer cell intrinsic STING	185
Endogenous activation of TBK1 in the tumor vasculature	186
Export of 2',3'-cGAMP by tumor cells activates STING in neighboring endothelial cells	190
2'3'-cGAMP and IFN- β prime the endothelium for immune cell extravasation	192
DISCUSSION	195
CONCLUSION	197
ACKNOWLEDGMENTS	198
CHAPTER 7 – ALK-POSITIVE ANAPLASTIC LARGE CELL LYMPHOMA - VASCULAR INTERACTIONS PROMOTE RESISTANCE TO ALK INHIBITOR VIA CCL19/21-CCR7 SIGNALING AXIS	199
ABSTRACT	199
INTRODUCTION	201
Anaplastic Lymphoma Kinase (ALK) in the pathogenesis of cancer	201
ALK as therapeutic target in Anaplastic Large Cell Lymphoma	203
Preclinical modeling of microphysiological ALK-vascular interactions	204
MATERIALS AND METHODS	205
Materials and reagents	205
Cell culture	205
Genetic engineering and CRISPR/Cas9 systems	205

<i>ALCL-vascular microphysiological model</i>	205
<i>Immunocytochemistry and Imaging</i>	206
<i>Cell viability assays</i>	206
RESULTS	207
DISCUSSION	209
CONCLUSIONS	210
ACKNOWLEDGMENTS	211
REFERENCES	213
SECTION IV	218
BIOARTIFICIAL POLYMER NANOPARTICLES	218
FOR SYNTHETIC OLIGONUCLEOTIDE RELEASE	218
IN THE TUMOR MICROENVIRONMENT	218
CHAPTER 8 – NANOCARRIERS AS DELIVERY SYSTEMS FOR OLIGONUCLEOTIDE RELEASE	219
ABSTRACT	219
INTRODUCTION	221
<i>Oligonucleotide as therapeutic strategies</i>	221
<i>Design principles of bioartificial nanocarriers</i>	222
<i>Lipid-based nanoparticle delivery systems</i>	225
<i>Polymer-based nanoparticles delivery systems</i>	226
<i>Synthetic polymers</i>	228
<i>Natural Polymers</i>	230
DISCUSSION	232
CONCLUSION	234
CHAPTER 9 - BIOARTIFICIAL PLGA-CHITOSAN NANOPARTICLES FOR MIRNA AND SIRNA RELEASE	
.....	235
ABSTRACT	235
INTRODUCTION	237
MATERIAL AND METHODS	238
<i>Materials and reagents</i>	238
<i>Fabrication process of bioartificial nanoparticles</i>	238
<i>Size and zeta potential by dynamic light scattering (DLS)</i>	239
<i>Morphological characterization: scanning electron microscopy (SEM)</i>	240
<i>Entrapment efficiency and payload release</i>	240
<i>Production yield</i>	240
<i>Cell culture</i>	241
<i>Flow cytometry</i>	242
<i>Statistical analysis</i>	242
RESULTS	243
<i>Physicochemical characterization of complexes and miRNA-loaded NPs</i>	243
<i>Entrapment efficiency, payload release and morphological characterization</i>	247
<i>Biological characterization and transfection efficacy of miRNA and siRNA- loaded NPs</i>	249
DISCUSSION	255
CONCLUSION	257
ACKNOWLEDGMENTS	258
REFERENCES	259
SECTION V	264
FINAL DISCUSSION, MAIN ACHIEVEMENTS AND FUTURE PERSPECTIVES	264

CHAPTER 10 - GENERAL DISCUSSION	265
<i>Design of in vitro preclinical models and 3D microphysiological systems</i>	266
<i>Microphysiological systems for modeling multicellular-vascular interactions using microfluidic technology</i>	267
<i>Microphysiological systems for blood-brain barrier modeling</i>	268
<i>Microphysiological models of the tumor – vascular interactions in KRAS/LKB1 Non-Small Cell Lung Cancer and ALK⁺ Anaplastic Large Cell Lymphoma</i>	269
<i>Nanomedicine and Nanoparticle transport using microphysiological systems</i>	270
<i>Translational application of microphysiological systems for personalized medicine</i>	271
<i>Advanced bioengineering tools for microphysiological systems</i>	273
<i>Microphysiological systems: a pharma perspective</i>	274
CONCLUSIONS	276
REFERENCES	277

List of figures

Graphical abstract 1: Engineered microphysiological systems of multicellular-vascular interactions using microfluidic technology for modelling nanoparticles transport and drug efficacy.	17
Graphical abstract 2: Preclinical models for biomedical research.	22
Graphical abstract 3: Preclinical microphysiological systems for biomedical research.	42
Graphical abstract 4: Modelling the BBB microvasculature.	67
Graphical abstract 5: Preclinical 3D microphysiological BBB model and testing of nanoparticles (NPs) transport across the model.	93
Graphical abstract 6: cGAS-STING driven innate immunity in the non-small cell lung tumor microenvironment comprising tumor cells, fibroblasts, ECM, microvasculature and immune cells.	154
Graphical abstract 7: Preclinical models of KRAS/LKB1 tumor spheroids and microvasculature to model the tumor microenvironment.	167
Graphical abstract 8: Preclinical models of Anaplastic large cell lymphoma and vascular interactions to model the tumor microenvironment and the perivascular niche in the lymph node.	200
Graphical abstract 9: Nanoparticles as delivery systems for oligonucleotide release.	220
Graphical abstract 10: Uptake and cytosolic release of bioartificial PLGA-Chitosan nanoparticles for miRNA and siRNA release.	236
Figure 1.1: Preclinical in vivo mouse models.	26
Figure 1.2: traditional preclinical in vitro culture systems.	28
Figure 1.3: Transwell systems.	29
Figure 1.4: Advanced 3D preclinical models.	30
Figure 1.5: Tissue engineering applications of 3D bioprinting.	33
Figure 1.6: Preclinical organoids culture systems.	35
Figure 1.7: Advanced 3D microphysiological systems.	37
Figure 1.8: Microfabrication of microfluidic device by photolithography and soft lithography.	45
Figure 1.9: Vascular network formation in vivo.	47
Figure 1.10: Engineering vascular formation in microphysiological systems.	50
Figure 1.11: Biological barriers and precision medicine.	52
Figure 1.12: Classes of NPs and surface property for enhanced delivery.	55
Figure 2.1: Structure, functions and transport mechanisms of the Blood-Brain Barrier.	72
Figure 2.2: Transport mechanisms of the Blood-Brain Barrier.	76
Figure 2.3: <i>Transport mechanisms of the Nanoparticle delivery across the Blood-Brain Barrier.</i>	80
Figure 2.4: In vitro models of the Blood-Brain Barrier.	83
Figure 2.5: Design of microfluidic devices.	100
Figure 2.6 : Blood-Brain Barrier (BBB) and 3D Microphysiological BBB model.	111
Figure 2.8: Microvascular conditions and iPSC-ECs - PCs/ACs contact interactions.	113
Figure 2.9: Quantification of microvascular parameters of 3D BBB Microphysiological model.	116
Figure 2.10: iPSC-ECs-PCs/ACs contact interactions and microvascular parameters.	117
Figure 2.11: BBB junctions and ECM expression analysis by immunocytochemistry.	119
Figure 2.12: Immunocytochemistry analysis of tight junctions and ECM protein deposition.	120
Figure 2.13: Quantitative RT-PCR of 3D Microphysiological BBB model in microfluidic system.	120
Figure 2.14: Microvascular permeability quantification in BBB model.	122
Figure 2.15: Perfusion ability and permeability assay in BBB microphysiological model.	123

Figure 2.16: Polymer Nanoparticle Testing in 2D culture systems.	127
Figure 2.17: Nanoparticle experiments in 2D transwell systems.....	128
Figure 2.18: Nanoparticles permeability testing in 3D Microphysiological BBB model.....	130
Figure 2.19: Biodistribution of Nanoparticles in 3D Microphysiological BBB model.	131
Figure 3.1: The biology of lung cancer.....	156
Figure 3.2: The biology of lung cancer.....	158
Figure 3.3: The cGAS-STING pathway.	160
Figure 3.4: <i>The lung microenvironment</i>	162
Figure 3.5: Design of microfluidic devices.....	174
Figure 3.6: <i>LKB1 reconstitution of 3-D KL spheroids and response to dsDNA in microfluidic culture</i> . .	181
Figure 3.7: Immune infiltration in 3-D KL model and response to dsDNA in microfluidic culture.	182
Figure 3.8: Impact of LKB1 reconstitution on dsDNA sensing in co-culture with MVNs.	185
Figure 3.9: <i>MVN co-culture enhances dsDNA-induced cytokines/chemokines even in the absence of tumor cell STING</i>	188
Figure 3.10: Activation of STING-TBK1 signaling in tumor vasculature and lymphocyte infiltration...	189
Figure 3.11: 2'3'-cGAMP exported by cancer cells activates STING signaling in endothelial cells.....	192
Figure 3.12: 2'3'-cGAMP and IFN- β promote vascular permeability and upregulation of adhesion molecules.....	194
Figure 3.13: Anaplastic lymphoma kinase (ALK) signaling.	202
Figure 3.14: Modelling ALK ⁺ Anaplastic Large Cell Lymphoma (ALC) interaction with blood vessel. .	208
Figure 4.1: Biological barriers and challenges of oligonucleotide (miRNA/siRNA) therapy.	225
Figure 4.2: Viral and non-viral delivery systems for oligonucleotide release.	228
Figure 4.3: Fabrication process of complexes and nanoparticle (NPs) delivery systems.	239
Figure 4.4: Physicochemical characterization of complexes and nanoparticles (NPs).....	247
Figure 4.5: Physicochemical and morphological characterization of nanoparticles (NPs) and viability assay.	248
Figure 4.6: Transfection efficiency of siRNA- and miRNA-loaded nanoparticle (NPs).....	251
Figure 4.7: Transfection efficiency of nanoparticles (NPs) in anaplastic large cell lymphoma (ALCL) cell models and NPs stability.	254

List of tables

Table 1: Advantages and limitations of in vitro and in vivo preclinical models.	38
Table 2. BBB microphysiological model.....	87
Table 3. Physical characterization of size and zeta potential of NPs.....	125
Table 4. Primer sequences for quantitative real time RT-PCR.....	137
Table 5. Antibodies for immunocytochemistry.	138
Table 6. Primers for real-time RT-PCR.....	212
Table 7. PLGA/CS/NPs characteristics for miRNA release.	257

Abstract of the thesis

Improving the effectiveness of preclinical models of living human tissues in the prediction of drug responses is critical to reducing costly failures in clinical trials. To date, most preclinical models exhibit limitation in faithfully recapitulating the local tissue and organ microenvironment, and in certain circumstances, this can lead to misleading outcomes.

Recent advances in bioengineering, microfabrication and microfluidic technologies have driven considerable progress in the design of microengineered models of functional units of human organs and pathophysiology with 3-dimensional tissues on chips. These offer the possibility to more closely recapitulate multi-cellular architectures, dynamic cell-cell interaction and tissue interfaces, physicochemical microenvironments and local vascular perfusion of the human body than with conventional 2D culture systems. *In vitro* 2D preclinical models have represented an invaluable tool for complex biological interactions, drug efficacy and pharmacodynamics but they have been limited in their translatability. Instead, 3D advanced models could provide the basis for preclinical experimentation with greater predictive power, and potentially represent alternative models in agreement with the 3Rs principle. Commonly referred to as microphysiological systems, such biomimetic *in vitro* models contain living human cells integrated in extra-cellular matrix, arranged into multi-cellular architectures to simulate *in vivo* tissue-specific microenvironments.

In this work, we propose the design of three different bio-inspired 3D microphysiological models to study multicellular-vascular interactions in a microfluidic device. This includes a model of the human blood-brain barrier (BBB), as well as two clinically relevant cancer models: KRAS/LKB1 lung carcinoma and ALK-positive anaplastic large cell lymphoma (ALCL) models. These three models have in common an advanced perfusable microvasculature, developed by different strategies: self-assembled vasculogenesis that reproduces capillary-size microvascular networks, or patterned microchannels, an endothelial cells-based 3D macro-vessel to recreate large blood vessels. Dynamic culture supported cell-cell contact interactions and continuous secretion of signaling factors to accurately recapitulate *in vivo* organization and functional unit.

The BBB model, which contains iPS-derived endothelial cells, brain pericytes and astrocytes self-organized into microvascular network to accurately replicate neurovascular construct. Gene expression analysis, computational analysis of geometrical structures and quantitative immunocytochemistry consistently confirmed increased maturation toward BBB-like structures.

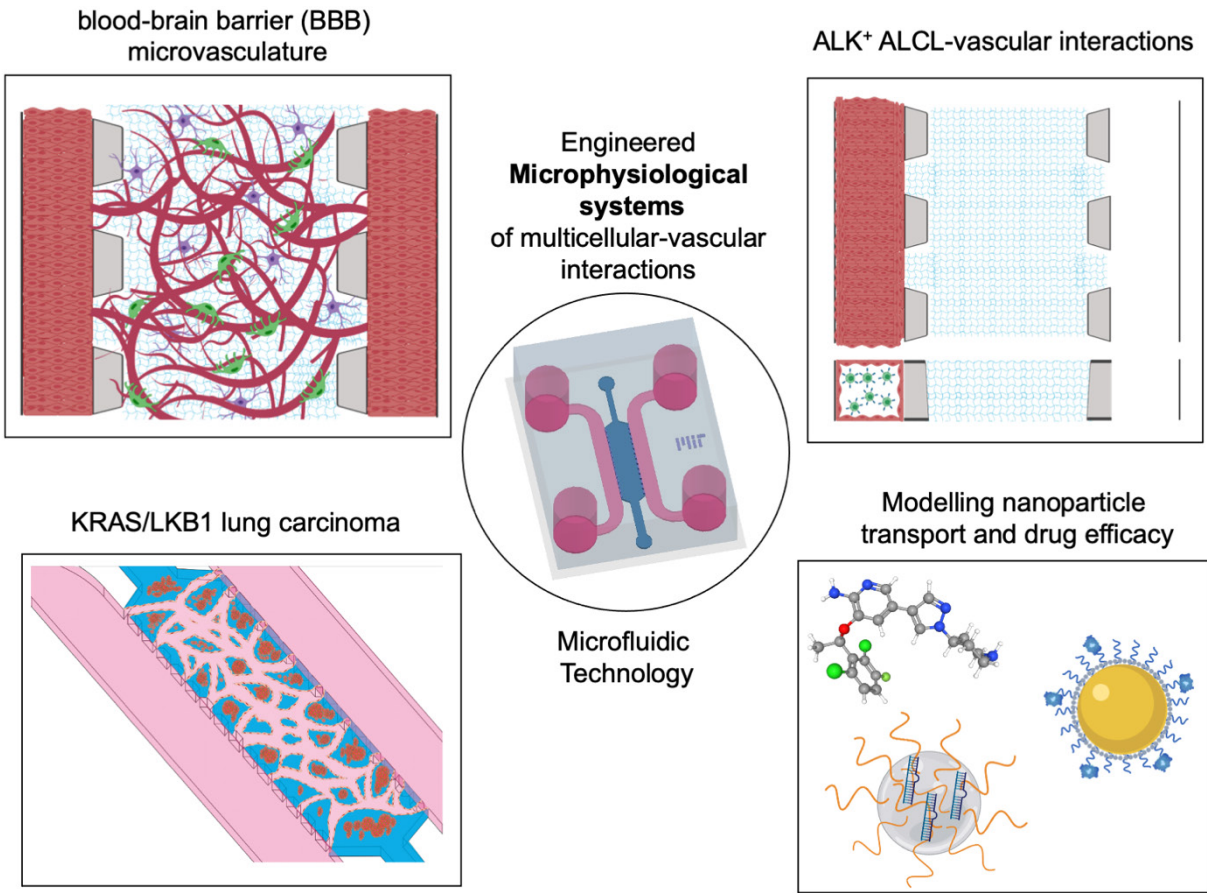
BBB microvasculature exhibited vascular permeability lower than conventional *in vitro* systems, and similar to *in vivo* measurements in the rat brain. The BBB system was used to test transport of innovative carriers, such as polymer nanoparticles, which have been shown to effectively deliver drugs across the BBB. Interestingly, holo-transferrin (a brain endothelial cells ligand) functionalized polystyrene (PS) and polyurethane (PU) nanoparticles (NPs) displayed increased permeability compared to blank NPs.

With the advent of immunotherapies, the lung tumor-microvascular model was critical in understanding the dynamic biology of immune cell recruitment and exclusion in the lung cancer microenvironment. Interestingly, the KRAS/LKB1 mutant genotype yields a phenotype, that is resistant to PD-1 blockade, which we found to be partially mediated by the cGAS/STING pathway. We used this model to determine that extracellular export of 2',3'-cGAMP by cancer cells plays an important role in activating STING signaling in endothelial cells and increasing vascular permeability and expression of E selectin, VCAM-1, and ICAM-1, facilitating T cell adhesion to the endothelium.

Finally, the ALK-positive ALCL-vascular model was exploited to unveil a molecular mechanism of tumor drug resistance to ALK inhibitors primed by the interaction of lymphoma cells and endothelial cells via the CCL19/CCL21/CCR7 axis. At the same time, preliminary experiments were performed to encapsulate miRNAs and siRNA into PLGA/Chitosan nanoparticles for gene silencing and potential treatment of a number of diseases, including cancer. Preliminary nanocarrier characterization demonstrated high stability, efficient payload encapsulation and uptake, enhanced intracellular delivery, and low cytotoxicity.

Altogether, these microengineered microphysiological systems have the capability to more reliably predict therapeutic vulnerabilities and study drug transport across biological barriers, thereby expediting drug discovery, and providing important new insights into fundamental biological processes to expand our understanding of several currently incurable diseases.

Overall, our findings suggest that microphysiological systems are robust and physiologically-relevant models, with the ability to overcome current preclinical limitations, potentially revolutionize drug research and development, and providing more effective preclinical assays.



Graphical abstract 1: *Engineered microphysiological systems of multicellular-vascular interactions using microfluidic technology for modelling nanoparticles transport and drug efficacy.*

Schematic created with biorender.com

Thesis outline

The present work is divided in five main sections, whose contents are summarized below.

Section 1 is an introduction section focused on preclinical models including conventional or more sophisticated *in vivo* mouse studies and 2D and 3D *in vitro* systems.

Advantages and limitations of these systems are highlighted, and the major challenges are described. Advances and future perspectives of microengineering technologies for innovative models are defined. Rational design strategies for microphysiological models using microfluidic technology are proposed, together with innovative design principles for vascular formation in those systems. Lastly, recent applications and future perspectives of microphysiological systems as preclinical testing platforms for drugs and nanocarriers are outlined.

Section 2 focuses on the *in vitro* modelling of the blood-brain barrier (BBB).

It begins with detailed description of structure, functions and transport mechanisms of the BBB and its cellular components, with a comprehensive list of existing *in vitro* and *in vivo* models. In the following chapter, extensive biological and computational characterization of the BBB microphysiological model is provided. Innovative methodology is defined to extrapolate vascular permeability and spatiotemporal biodistribution of polymer nanoparticles in the BBB microvasculature, which furnishes the first insights towards more reliable preclinical prediction of drug transport efficacy.

Section 3 elaborates different designs of microphysiological cancer models using microfluidic devices to study tumor-vascular interactions, namely a lung tumor-microvascular model cancer and an anaplastic large cell lymphoma vascular model, respectively.

In both cases, a brief introduction of the sub-category of cancers and current *in vitro* modelling with subsequent description of each model and its findings are presented. Microphysiological cancer models were characterized in terms of structural aspects by confocal imaging and functional features as vascular permeability, gene expression and cell viability. Interestingly, the lung tumor vascular model was employed to uncover a biological mechanism of immune cell exclusion from

the tumor microenvironment, and the ALCL-vasculature model unveiled a molecular drug resistance phenotype primed by interaction of lymphoma and endothelial cells.

Section 4 explores the design of novel bioartificial nanoparticles as delivery systems of oligonucleotides (miRNAs and siRNAs) for gene silencing and potential treatment of diseases, including cancer and tissue regeneration. Physicochemical characterization, transfection efficiency and cytocompatibility of nanoparticles, based on chitosan (CS) and poly(lactic-co-glycolic acid) (PLGA) are discussed.

Section 5 provides a general discussion of the main achievements of the experimental work, followed by conclusions and future developments.

Section I

Design and comparison of conventional preclinical models with 3-Dimensional in vitro technologies: Focus on microphysiological systems

Chapter 1 - *Design principles of preclinical models*

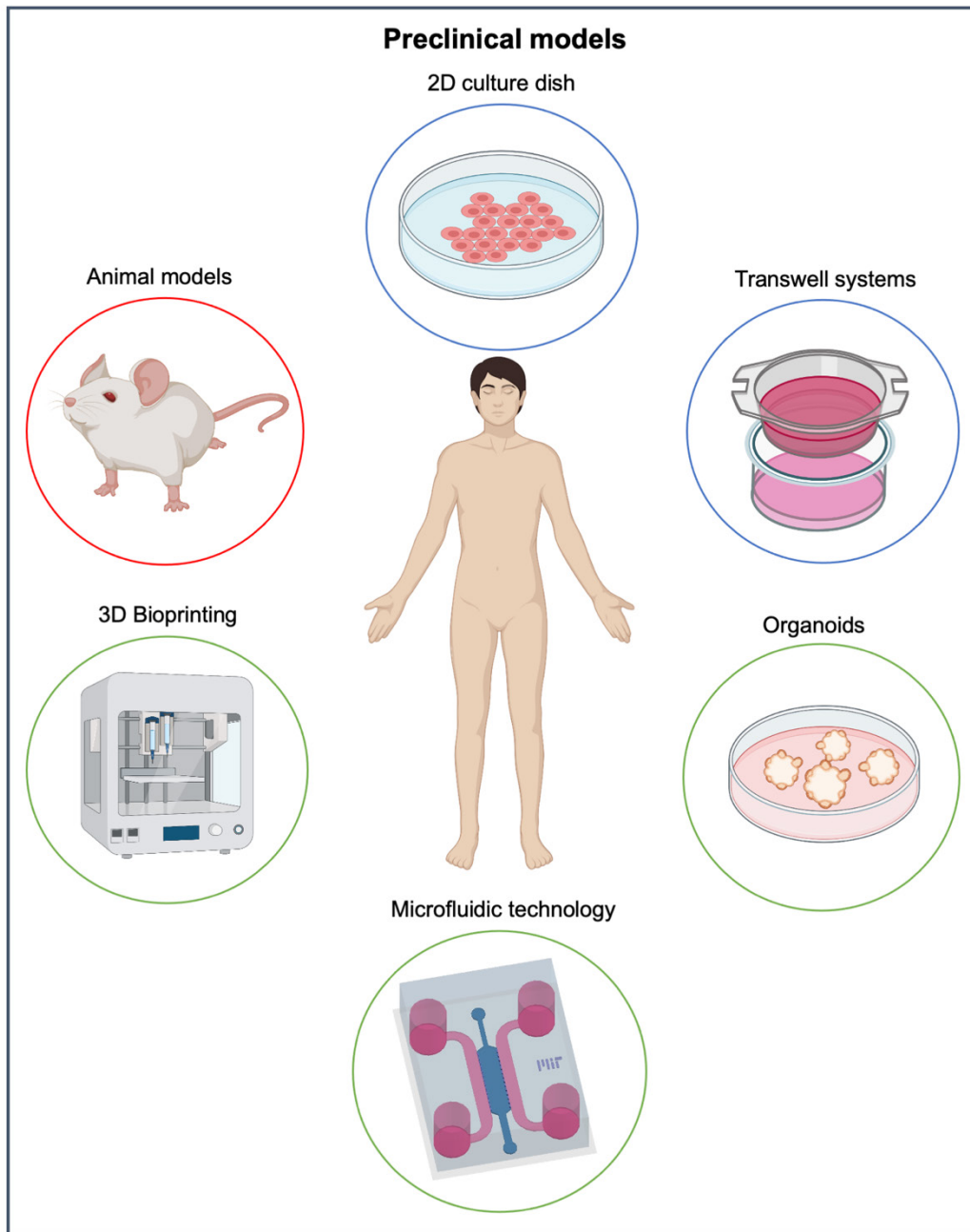
Abstract

Preclinical *in vivo* and *in vitro* models are widely employed for unveiling biological mechanisms and studying therapeutic efficacy and toxicity. Despite their enormous contribution to basic and translational research, to date, most preclinical models exhibit genetic variabilities and limitation in faithfully recapitulating the local tissue microenvironment, leading to misleading outcomes in clinical settings. Improving the effectiveness of preclinical models is crucial to reduce costly failures in clinical trials and improve patient outcome.

As an alternative to 2-Dimensional culture systems and *in vivo* mouse models, Tissue engineering and 3D bioprinting, organoids and microphysiological systems have the potential to recapitulate key microenvironmental characteristics of human organs and mimic their primary functions.

The advent of more advanced 3D systems is attributed to progresses in biomaterials, micro/nanotechnologies, and stem cell biology, which enable to precisely replicate the 3-dimensional microarchitecture and spatial distribution of multiple cells to emulate *in vivo* tissue-specific microenvironment. These microdevices could be employed as specialized *in vitro* models to emulate or unveil complex mechanism and predict pharmacological efficacy of drugs and nanocarriers.

In Chapter 1, advantages and limitations of *in vivo* mouse models, and 2D conventional culture systems are discussed. Then, bioengineering approaches and design principles of 3-dimensional preclinical models are described. Finally, 3D *in vitro* models are presented and recent advances in tissue engineering, 3D bioprinting, organoids and 'Microphysiological systems using microfluidic technology for blood-brain barrier and cancer research are outlined.



Graphical abstract 2: Preclinical models for biomedical research.

Schematic created with biorender.com

Preclinical in vivo and in vitro models

Preclinical development of drug candidates for the treatment of cancer or neurodegenerative diseases commonly involves testing of potential therapeutic agents in conventional two-dimensional (2D) cell culture systems. Further, drug development does not advance into the clinical stage without assessing therapeutic efficacy using *in vivo* animal models [1].

Despite unprecedented investment in pharmaceutical research and development (R&D), the number of new drugs approved worldwide, targeting neurodegenerative diseases and cancers, has remained low [2]. Several *in vivo* and *in vitro* models have largely shaped our knowledge and are currently used in biomedical research. Cell line-derived models defined our understanding of cancer and its hallmarks [3], [4], in basic and translational oncology and neurodegenerative research. These 2D *in vitro* models are based on the establishment of long-term *in vitro* culture of cell lines in Petri dishes derived from mice or patient donors, stored in cell line banks and commercialized. Once derived, cell lines are low-cost and easy to manipulate, enabling rapid evaluation of drug candidates [5].

Cell line models have two major disadvantages: 1) loss of genetic heterogeneity and irreversible changes in gene expression are imposed by long-term *in vitro* propagation of selected sub-clones and might be different between laboratories, and 2) despite their demonstrated value, they cannot support the tissue-specific, differentiated functions of many cell types or accurately predict *in vivo* tissue functions and drug efficacy [6]. Besides 2D *in vitro* culture, the two broadest applications of cell line models are: 1) allotransplantation of mouse cell lines into syngeneic immunocompetent mice models (autografts) [7][8] and 2) xenotransplantation of human cells into immunocompromised mice (xenografts) [9].

In both types of models, tumor cells can be injected ectopically (mostly subcutaneously), orthotopically to mimic tumor growth in its organ of origin or systemically (mostly intraperitoneally, intravenously or intracardially) to study metastatic ability [10]. Although cell lines can often predict efficacy of cytotoxic agents, these models unfortunately fail to faithfully predict clinical activity for many targeted therapies [1][11]. Also, cell lines have a rapid non-autochthonous growth in mice compared with their human counterparts, display a dramatically perturbed tissue architecture with a severely altered microenvironment, including changes in the vascular, lymphatic and immune compartments [10]. The main advantage of syngeneic mouse

models is that tumor rejection by alloreaction does not occur, because transplantation is performed using cell lines previously established through isolation of a specific genetic background, such as C57BL/6 or Balb/c, back into the same inbred immunocompetent mouse strain. While this does allow characterization of murine anti-tumor immune responses, the system does not fully recapitulate human immune-oncology [1][5] (Fig. 1.1a).

Recently, a particular subtype of xenograft which has gained importance is patient-derived xenografts (PDXs). PDXs are typically generated by subcutaneous implantation of fresh, surgically-derived human tumors into immunodeficient mice (mice without an immune system) [9], [12], [13] (Fig. 1.1b). PDXs have been shown to stably retain molecular, genetic and histopathological features of original patients' tumors, over limited passages of *in vivo* expansion [14], modelling inter-patient heterogeneity. Several retrospective comparisons have provided strong evidence that PDXs can precisely predict therapy responses: "co-clinical" trials of therapies in PDXs, derived from patients enrolled in clinical trials, have shown strong correlations [15][16][17]. However, despite promises of personalized medicine, PDX studies remain severely limited by high costs and logistical difficulties, including limitations in the engraftment rates [18]. Additionally, even though human stroma is initially present, it is ultimately replaced by mouse stromal components following *in vivo* passaging, modifying paracrine tumor microenvironmental interactions, by introducing cross-species signaling incompatibilities, restricting the utility of PDXs for examining human-specific microenvironment-targeted therapy [19]. Finally, the immunocompromised background required for successful engraftment of PDXs precludes their use in studying immune cell function and immunotherapeutic strategies [20] and fails to reflect cancer immunoediting and immunosurveillance [21].

The understanding of the genetic mutations underlying tumorigenesis has engendered the generation of diverse genetically engineered mouse models (GEMMs), which are the most sophisticated models that accurately mimic human pathogenesis [10][22] (Fig. 1.1c). GEMMs reproduce the genetic and molecular events in an autochthonous *in vivo* setting, allowing *de novo* disease formation in a native immune-proficient microenvironment. GEMMs can be simply classified as either transgenic or endogenous [23]. Transgenic GEMMs are mutant mice that express target genes, such as oncogenes or dominant-negative tumor-suppressor genes in a non-physiological manner, caused by ectopic promoter and enhancer elements. To recapitulate the genetic features, transgenic mice are generated by pronuclear injection of cDNA constructs of

fertilized oocytes or through gene targeting and lentiviral transduction in stem cells. These systems are constitutive or inducible, controlled by an exogenous promoter to reversibly control target-gene expression with exogenous ligands (doxycycline[24] and tetracycline systems or so called (Tet) on or off [25][26]). Transgenic GEMMs were used to study the concept of oncogene addiction [10][24], however, gene expression may be seen as excessively artificial, resulting in a reduced clonal heterogeneity compared with human tumors. Endogenous GEMMs allow a spatially and temporally controlled introduction of human-relevant mutations [22] [27] [28] [10] [23]. Inducibility is achieved via exogenous site-specific recombinase (SSR) delivery (*Cre-loxP* and *FIP-FRT systems*) in the form of adenovirus, to an accessible somatic tissue. GEMMs not only faithfully recapitulate molecular and histopathological features of human disease but also have a strong predictive power for drug response and resistance [29]. However, germline mutations in GEMMs are constitutively present throughout the mouse and might lead to developmental defects and/or undesirable effects outside the tissues of interest. Although GEMM models recapitulate mouse immunoediting, this is limited to few oncogenes or tumor suppressor genes and fails to reproduce the intrinsic neoantigen repertoire derived from an extensive tumor mutation burden. Third, the generation of GEMM models is very expensive and time consuming.

Of notice, novel strategies aimed at accelerating *in vivo* cancer gene validation via genetic engineering include CRISPR-Cas9 technology [30]. This is now considered a breakthrough for facilitating rapid germline and somatic cancer modelling [31]–[33].

Finally, humanized mice models have emerged as a tool to study the human immune system by engraftment in severe combined immunodeficiency (SCID) mice with human fetal tissues, hematopoietic stem cells, or peripheral-blood mononuclear cells [34] (Fig. 1.1d). These models have dramatically improved the ability to study human diseases from an immunological perspective more relevant to humans. Although these models represent an important advance, the establishment of function human immune system in mice, with the transgenic expression of human molecules such as Human Leukocyte Antigen (HLA) in humanized model is still suboptimal and does not fully recapitulate a robust human immune system [35], including many limitations such as the potential for xeno-reactive graft-versus-host disease, limited lifespan and incomplete human immune functions [34] [35] [20].

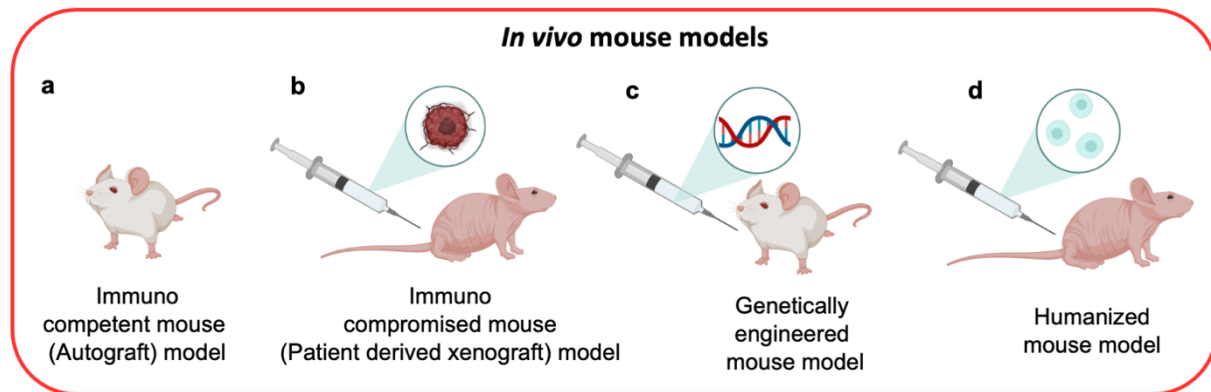


Figure 1.1: Preclinical in vivo mouse models.

a) Immunocompetent mouse model (autograft) is generated by injecting cell line with the same mouse background **b)** immunocompromised mouse model. This model is used to generate patient derived xenograft (PDXs) by implantation of surgically-derived specimens into immunodeficient mouse **c)** Genetically engineered mouse models generated by injection of cDNA to induce the expression of an oncogene or de-repression of tumor suppressor gene **d)** humanized mouse models generated by injection of human hematopoietic stem cell transplant in severe combined immunodeficiency (SCID) mice to generate an humanized mouse model with a human-like immune system. Schematics created with BioRender.com.

To summarize, *in vivo* animal models can emulate physiological complexity at the whole-organism level and have been considered the gold standard in research, however successful drug candidates for neurodegenerative diseases tested in animal models have largely failed in clinical trials [36]. Animal surrogates of human diseases are now facing increased scrutiny and skepticism regarding their scientific validity and translatability to humans [37].

In cancer research, traditional animal models have faced many challenges, including the inability to predict human onco-immunology [5]. Failures in clinical trials are primarily due to the poor predictive power and inefficiency of existing preclinical drug screening models. In summary, *in vivo* animal models allow study of cellular, tissue, organ and systemic level functions as well as pharmacodynamics and pharmacokinetics in a complex organism. However, they are costly, laborious, ethically contentious, have limited translatability and often lack predictive value to answer complex biological questions of cell-cell interactions.

To recapitulate, some of the major limitations of conventional *in vivo* and *in vitro* models are:

- the dissimilarity between 2D *in vitro* cell culture systems and *in vivo* models with the patient target;
- genetic and immunologic differences between humans and animal models
- failure to accurately recapitulate native tissue-specific microenvironment, which substantially contributes to the complex pathophysiology of the disease [38] [39].

The higher failure rates, lack of strong prediction of human efficacy of drugs and ethical concerns, have led to the development of guiding principles underpinning the humane use of animals in scientific research, called the three Rs (refinement, replacement, reduction) to find alternatives to animal testing [1][5]. However, animal models are still an indispensable intermediate for preclinical research [5]. It appears that more reliable models are needed to mimic the complexity of human cancer as an evolutionary process of mutated cells that are in intimate crosstalk with their local microenvironment including different immune cells [5][40]. In this context, surrogate *in vitro* 3D models that can reproduce the complex structure and functionality of living human organs are indispensable for understanding diverse biological responses of the human body for a variety of biomedical, pharmaceutical, chemical and environmental applications.

Comparison of current 2D in vitro models

In vitro modelling of human biology has commonly relied on conventional primary or immortalized culture of cell lines *in vitro* [41]. Simple 2D cultures on Petri dishes of brain endothelial cells or tumor cells have been useful to assess efficacy and cytotoxicity of drug candidates for over 50 years (Fig. 1.2a). 2D cell cultures of cancer cell lines helped to establish the initial investigation of cancer in humans. However, while valuable resources, cell lines cultured in 2D monolayers only represent a subclone of the original tissue, adapted to grow in artificial conditions [42]. Although cell lines have been considered standard and shared tools in the scientific community, some skepticism has arisen, given that genetic variations in the same cell lines used by different research groups have led to different or even opposite results [6]. These models are

often too simple to answer complex biological questions of cell interactions or physicochemical characterization of biological parameters, such as drug transport through the BBB.

To enable more functional studies, an advanced culture setup, called a transwell-based assay has been developed, enabling the investigation of cell migration and invasion through the microscale pores of a membrane [43], and/or the study of drug transport and vascular permeability in blood-brain barrier models [44]. Transwell models are composed of 2 chambers divided by a semipermeable microporous membrane, allowing independent access to both chambers [45] (Fig. 1.2b, 1.3a). Membranes coated with collagen or Matrigel are covered with confluent monolayer of brain endothelial cells before initiating the experiment. These systems have been widely used for compartmentalized cultures, including brain pericytes and astrocytes on the opposite side of the membrane [46]. These simple cultures still often fail to replicate the key features of the BBB, such as shear stress resulting from blood flow and the BBB microenvironment, which makes their predictive value for human responses questionable [47]. Transwell systems have also been exploited to study immune cells and tumor cell trans-endothelial migration in a similar fashion [48]–[50]. However, they do not provide information about the complex interactions between all the cellular components of the tissue-specific microenvironment in human organs in diseased or healthy states [51].

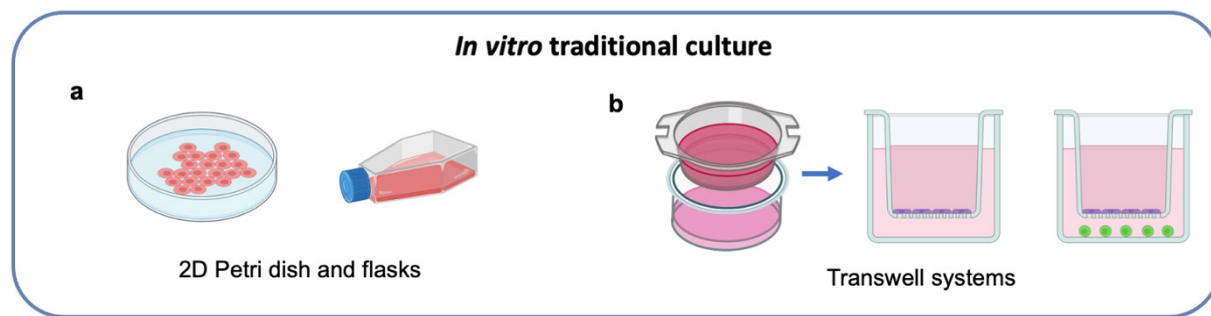


Figure 1.2: traditional preclinical in vitro culture systems.

a) 2D culture system of cell lines and **b)** Transwell systems containing mono-culture or co-culture of cells. Schematics created with BioRender.com.

Neither 2D culture nor Transwell models reproduce the complexity observed in the 3D tissue architecture of living organs or incorporate mechanical forces (for example, fluid shear stress, hydrostatic pressure and tissue deformation) that can substantially influence cell behaviors [52]–[55][51]. Moreover, migration studies using Transwells are mostly affected by gravity which

results in a lack of important tissue–tissue interactions and an inability to study recruitment of circulating immune cells, as well as physiological dosing of test therapeutic agents [39]. In summary, current *in vitro* models are more reproducible, easy to analyze and more fit for high-throughput screening than animal models, and allow the study of human cells and tissues. However, they are often too simplistic to answer complex research questions, especially those interrogating multifaceted cell-cell interactions or the role of mechanical forces.

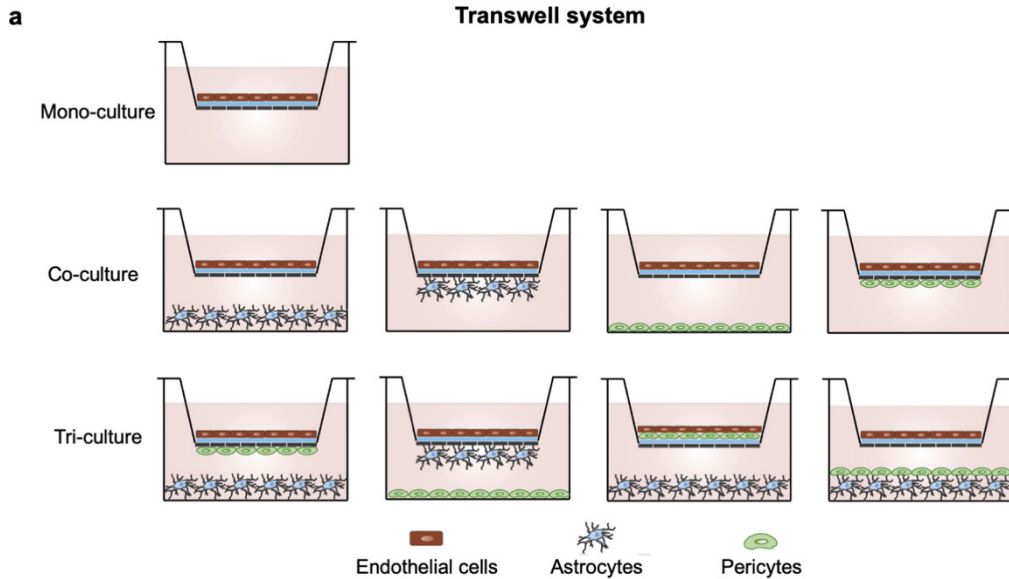


Figure 1.3: Transwell systems.

a) Schematic representation of Transwell systems of mono-culture of endothelial cells, co-culture or tri-culture with astrocytes and pericytes to model the blood-brain barrier. Reproduced with permission from [46].

Bioengineering approaches for the design of 3-dimensional preclinical models

To better uncover human biology and improve preclinical translation into effective therapies, there is a need for more accurate preclinical model systems. The drug discovery community has identified the critical need for new testing approaches to generate reliable predictions of drug efficacy and safety in humans [57][60]. Recent advances in bioengineering, cell biology and microengineering techniques, such as microfabrication and microfluidics have enabled the development of microengineered models of the functional units of human organs. There are several potential approaches to this unmet need that have reached a sustainable cost, reliability and robustness. Some of these technologies have begun to tackle major technical challenges at the

critical steps of conventional and emerging drug discovery processes, while others are still under development. These systems, which have been developed to perform the primary function of human organs *in vitro*, are composed of living cells and tissues organized in such a way that produces novel functionalities by design. It is thus paramount to recapitulate closely characteristics of human organs. Design principles of advanced *in vitro* systems converge into three main areas: anatomy, physiology, and cell sources.

The anatomical structure of a tissue or organ is essential to its function, and structural change could result in organ dysfunction and disease. Additionally, the physiological characteristics (physical, mechanical, and biochemical factors) of human organ have profound influences on the functions of cells and organs [61]. Appropriate cell sources are critical to the success of microphysiological systems and the cell types are determined according to the organ of interest and its function.

Their physical integration will then produce the final structural architecture of the organ and reproduce the mechanobiology of cell interaction. The design of these systems must also include evaluation of the final read-out of the experimental platform and usually the design is suitable for convenient real-time monitoring and analysis. Innovative 3D experimental models (tissue engineering, 3D bioprinting, organoids and microphysiological systems) (Figs. 1.4a-c) including their design principles are listed below.

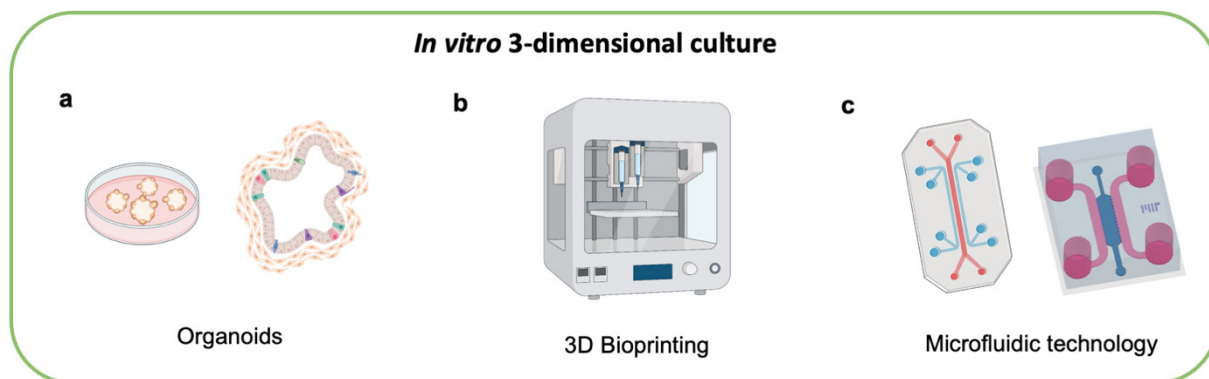


Figure 1.4: Advanced 3D preclinical models.

Schematic representation of a) Organoids, b) 3D bioprinting system and c) microphysiological system using microfluidic technology. Schematics created with BioRender.com

Tissue engineering and 3D bioprinting

Tissue engineering is “an interdisciplinary field and branch of biomedical engineering that integrates cell biology with engineering, nanotechnology and biomaterials toward development of biological substitutes that restore or improve tissue function or a whole organ” [62]. Critical components of tissue engineering strategies are: biomaterials and tissue architectures (scaffolds, patches, etc.) developed with different techniques [63][64]; cell sources (such as stem cells) and environmental cues such as growth factors [65][66]. Among all the techniques, additive manufacturing techniques, including three-dimensional (3D) printing methods, have driven innovations in the field. Particularly, 3D bioprinting [67], a 3D printing technique for biocompatible and biological materials, including living cells, is one of the most promising for fabricating complex tissue constructs. In 3D bioprinting, materials and living cells are precisely positioned layer-by-layer with tailored spatial control of the placement and consequently, functional biological components and mechanical properties [68] [69]. Information about the architecture of tissues is provided by medical imaging, such as computer tomography, and modelled through computer-aided design (CAD). This poses a potential advantage of exactly reproducing tissue-specific architectures derived from patients with non-invasive technologies. Tissue engineering is aimed at the regeneration of tissues and organs function [70], but it can also be applied for development of *in vitro* experimental models [71]. Indeed, 3D bioprinting have enabled scientists to build 3D functional living tissue models for *in vitro* drug screening and disease modeling [65], [72]. Nevertheless, 3D bioprinted *in vitro* models face several complexities, such as the choice of materials, cell types, growth and differentiation factors, and technical challenges related to the sensitivities of living cells to the printing process, and the biocompatibility and stability construction of tissues [73]. Advances in hardware and bioprinting processes have facilitated the fabrication of many tissues, including neural tissues [74] and tumor microenvironments with different levels of complexities [75], [76] [67] (Fig. 1.5a,b). A basic prerequisite for the survival of 3D engineered tissue constructs is the establishment of blood vessels. The development of perfusable vascular networks is also gaining importance for drug testing, as vasculature plays a fundamental barrier in drug transport (BBB, tumor microenvironment). 3D bioprinting of vasculature with hierarchical biomimetic structures has allowed blood circulation within thick macro-tissue constructs, accelerating vascularization and enhancing tissue regeneration[77]. Successful rapid vascularization of tissue constructs requires

synergy between fabrication of perfusable channels and functional bioinks that induce angiogenesis and capillary formation within constructs [72] [77]. Notably, 3D bioprinting of vasculature at the macroscale (centimeters to millimeters in diameter) has been quite successful. Despite the current attempts to achieve one or a few features of the tissue type, great challenges remain in simultaneously incorporating all physiologically-relevant features to recapitulate a tissue microenvironment [78]. Moreover, additional technological challenges, including higher printing resolution and speed, should be faced for the design of single-cell structures, like capillary networks [71]. Currently, only light-assisted bioprinting techniques, such as laser assisted bioprinting (laser induced forward transfer) [79] and biological laser bioprinter [80] can achieve cell-scale resolution. Briefly, Light-assisted bioprinters are comprised of a pulsed laser source, a target, and a substrate that receive the printed material. The target is made of a thin layer of gold or titanium coated onto a laser transparent support (i.e. glass). Cells are prepared in a liquid solution (i.e. culture media), and deposited at the surface of the metal film. The laser pulse induces vaporization of the metal film, resulting in the production of a jet of liquid solution which is deposited onto the facing substrate. Light-assisted bioprinting allows printing of capillary-size vessels (10-50 μm), but mostly limited to 2D applications [76][78] (Fig. 1.5c). Future advancements in bioprinting technology will facilitate the process of establishment of more physiologically relevant models, including vascular components in a tissue-specific microenvironment [68]. Further optimization and technological advances are required to enlarge this application into large scale production of *in vitro* models in biomedical labs and companies [81][71].

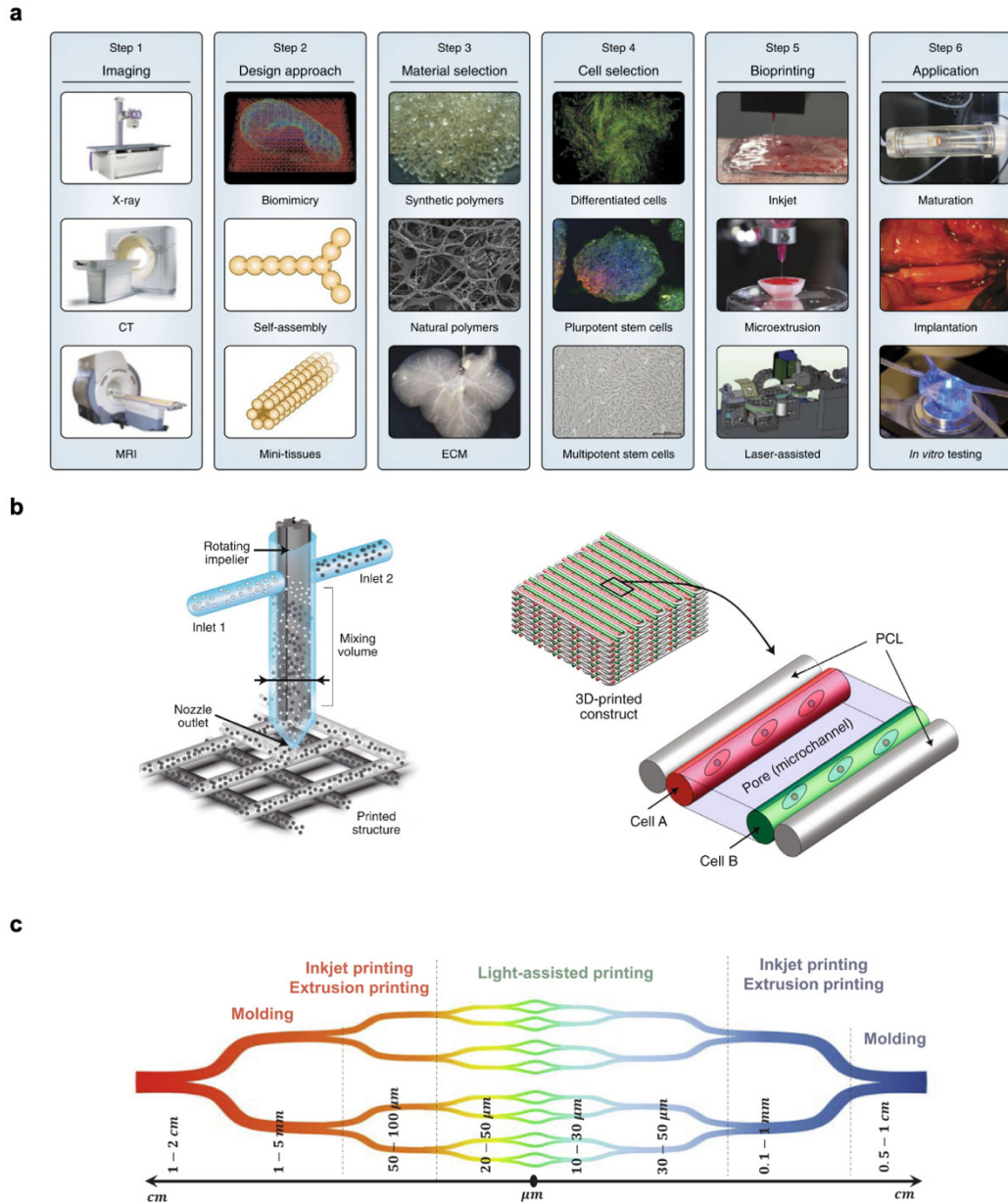


Figure 1.5: Tissue engineering applications of 3D bioprinting.

a) A typical process for bioprinting of 3D tissues. Imaging of tissue can be used to guide the design of bioprinted tissues. The choice of materials and cell source is essential and depends on the specific tissue and function. Common materials include synthetic or natural polymers and decellularized ECM. Cell sources are also fundamental and depend on the application. These components have to integrate with bioprinting system. **b)** Schematic of a mixing nozzle that can be used to print materials at the microscale. A 3D architecture that includes multiple cells embedded in polycaprolactone (PCL) polymer. **c)** The summary of current fabrication bioprinting techniques to generate blood vessel from arteries to capillaries. Reproduced with permission from **a)** [67] **b)**[82], [72] **c)**[77].

Organoids

Organoids are 3D self-organizing organotypic structures that resemble organs *in vivo*, and generally contain ECM materials, such as laminin-rich Matrigel [83]. Organoid cultures are established by self-assembled aggregation into low attachment cultures and grown embedded in hydrogel (Matrigel). Cells for organoids are derived from normal, pre-malignant or malignant tissues, and have shown to retain hierarchical organization and genomic features of their originating organs [81] [82]. Organoids can be maintained in culture for extended periods of time, on the order of months, and can be classified not only based on their tissue of origin, but also on the type of cells used for their generation such as: adult tissues (also called patient-derived organoids), pluripotent embryonic stem cells (ESCs), induced pluripotent stem cells (iPSCs) and adult stem cells [86]. Moreover, organoids are further distinguished into distinct classes corresponding to the diverse culture techniques, which can be used to generate organoids: i) submerged culture and ii) air-liquid interphase culture.

Submerged culture organoids consist of cells grown within a large drop of solid ECM gel submerged beneath tissue culture medium. Organoids might be grown in ultra-low attachment dishes in suspension before being immersed into a solid gel (Fig. 1.6a). In the air-liquid interphase system, cells are cultured into a type I collagen matrix, on the top of an inner transwell insert (Fig. 1.6b), with culture medium provided through a permeable membrane, thereby facilitating oxygen diffusion [84] [85] [89]. In cancer research, organoid culture involves either normal or malignant epithelial stem cells isolated from patients [90]. For brain research, organoids are mostly derived using ESCs or iPS cells that spontaneously differentiate to precisely recapitulate neurogenesis of the central nervous system [41]. Organoid systems recapitulate the normal developmental processes of an organ, as well as homeostasis and pathophysiology of the original tissues. However, organoids are commonly closed structures, which precludes direct experimental access to the epithelial lumen, and lack the tissue–tissue interfaces between epithelial tumor cells and surrounding vasculature and stroma, that are important contributors to cancer control and progression [90]. Furthermore, they do not retain the normal mechanical stimuli, which cells experience within whole organs (for example, breathing motions in lungs or cyclic peristaltic deformations in intestine), that also can contribute to tumor behavior [88] [89]. Recently, many research groups explored the use of CRISPR-Cas9 genome-editing system to introduce multiple mutations into cells that become organoids derived from normal human intestinal epithelium or

from stem cells. Recently, organoids have emerged as a new *in vitro* tool for drug discovery and personalized medicine, as an *ex vivo* high-throughput screening platform for testing efficacy and toxicity of drug compounds.

Although some limitations, such as risk of contamination from high handling level and low-to-medium throughput screening, organoids still represent an attractive model to recapitulate human tumor biology. However, though organoids enable interactions between neoplastic cells, they exclude most of the cells of the tumor microenvironment, lacking the native immune system and stromal/vascular component.

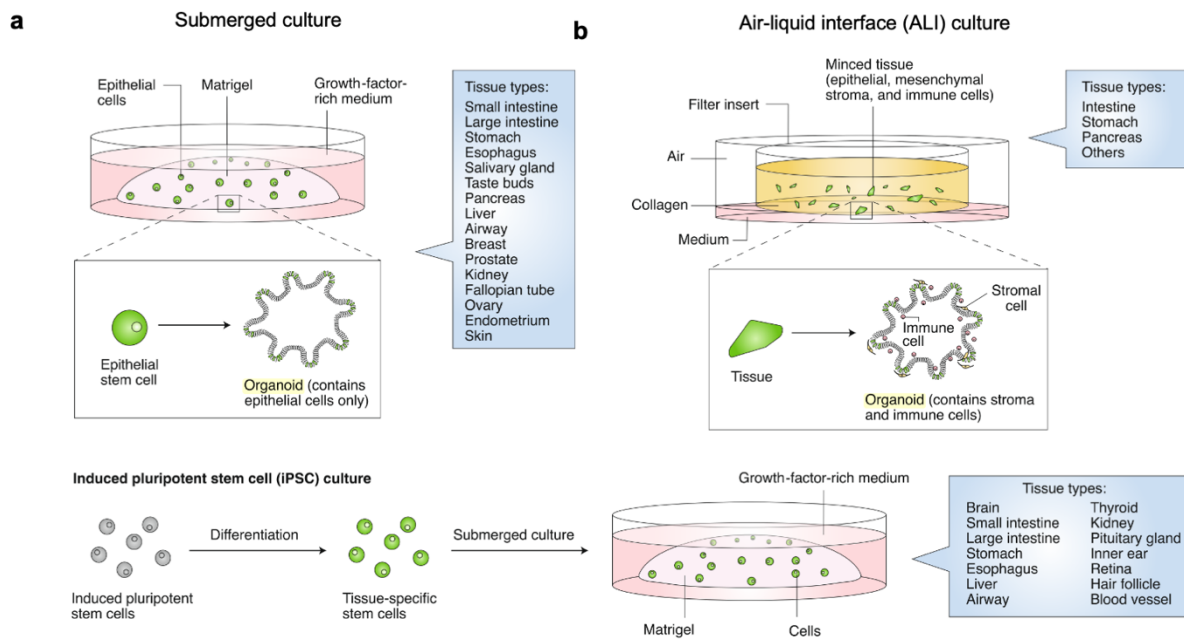


Figure 1.6: Preclinical organoids culture systems.

Organoid methodologies are **a)** submerged culture and **b)** air-liquid interface (ALI) culture which is combined with Transwell systems. Reproduced with permission from [89].

Microfluidic technology and ‘microphysiological systems’

The advent of microfabrication and biotechnology has given rise to the design and fabrication of new “microfluidic technology” systems, able to process small volumes of fluids (microliters to nanoliters) through microchannels. The first applications were in many scientific fields, ranging from molecular biology, such as high-throughput laboratory analysis of molecules (DNA, proteins etc.), to chemical analysis and silicon microelectronics, such as microelectromechanical systems (MEMS)[93]. Cell biology is a research area into which microfluidic technology has brought a new capability for culturing living cells in continuously perfused, micrometer-sized chambers in order to model physiological functions of tissues and organs. For these purposes, microfluidic devices for culturing cells in 3D systems are based on easy-to-fabricate microchannels, that can range from hundreds of micrometers up to millimeters in size, in a transparent biocompatible soft elastomer support. A wide range of possible designs are constructed by engineers through CAD-based systems and transferred into a device by lithography and molding systems [94]. Custom systems for particular applications, including microchannels or layer-by-layer deposition, can be made using different biocompatible materials [95][96], such as polydimethylsiloxane (PDMS), and different nanofabrication techniques [95]. PDMS is a soft silicon-based polymer with desirable properties, such as thermo-electric insulation, biocompatibility, high chemical inertness and impermeability. It has excellent optical transparency, low toxicity and high permeability to oxygen and carbon dioxide, allowing the fabrication of microchambers in which to grow and observe cells. These devices can be fabricated in microfabrication facilities to satisfy specific design requirements. It is also becoming common to purchase standardized commercially available chips, fabricated with simplified design, for a broader range of applications [90] [94][96].

Such microchannels are filled with hydrogels (typically collagen, Matrigel, fibrin) able to polymerize at 37 °C, embedding several type of cells [100]. Cells with 10-100 µm sizes are well suited for microfluidic devices. These systems contain living cells and tissues that have been organized into compartmentalized channels or self-assembled tissues. The goal is not to build a whole living organ but rather to reproduce a few functional units that recapitulate tissue- and organ-level functions. These systems are called “Organs-on-chip” or “microphysiological systems”. Microphysiological systems using microfluidic technology may recapitulate 3D tumor microenvironment (TME) [39][38][101][102], study metastasis and immune-tumor interactions, and model complex TME and ECM [103] [101] [102].

From the Human Body to Microphysiological systems

The human body consists in multiple systems working together to maintain homeostasis, while each cell plays unique functions.

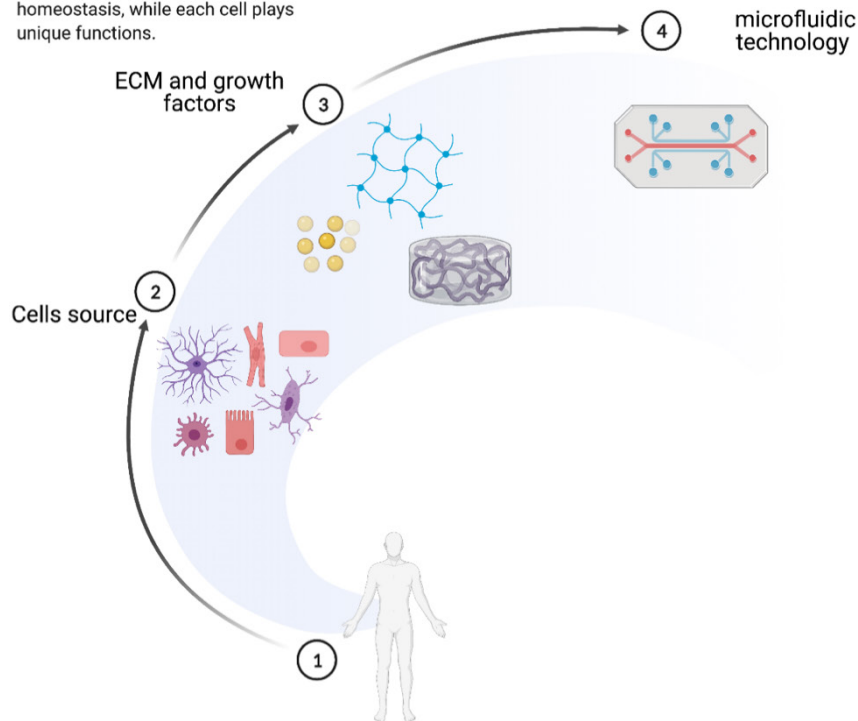


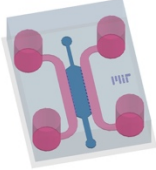
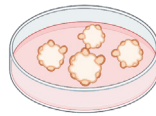
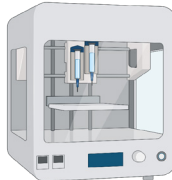
Figure 1.7: Advanced 3D microphysiological systems.


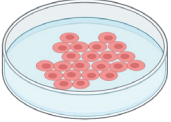

Schematic representation of microphysiological system: cells, extra-cellular matrix (ECM) growth factors and microfluidic technology. Schematics created with BioRender.com

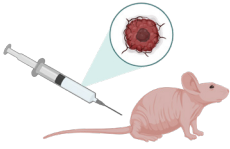
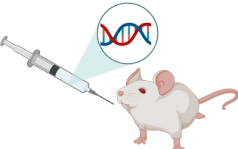
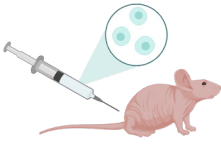
3D cancer cell spheroids have also been developed to recapitulate cell–cell and cell–ECM interactions between tumor cells. Microphysiological systems could include cell line spheroids, as well as patients’ or mouse-derived organotypic tumor spheroids (PDOTS, MDOTS) for a personalized medicine approach [83]. Such dynamic multicellular co-culture could reproduce paracrine and contact interactions and account for 3D cell growth, mimicking the local *in vivo* organization. One of the advantages is the possibility of medium-term culture (1-2 weeks) [108]. Given their scalable size, microfluidic devices make use of a low number of cells and use low quantities of culture medium and other needed reagents, which results in a low cost technology [109]. Ultimately, they can be produced in large quantities and in a sufficiently robust manner, thereby making them reliable and amenable to large-scale manufacture. In microfluidic devices, it might be possible to integrate more sophisticated technologies, such as sensors to monitor cell parameters [110], [111]. The main advantage of microphysiological systems compared to traditional culture is the potential to mimic more complex anatomic structures and cell-cell

interactions for several days. Below, Table 1 shows the advantages and limitations of preclinical models.

Table 1: *Advantages and limitations of in vitro and in vivo preclinical models.*

Type of culture	Preclinical model	Characteristics	Advantages	Limitations
<i>in vitro</i>	<p>3D Microphysiological systems (microfluidic device)</p> 	<p>Use of patient-derived specimens, stem cells or cell lines</p> <p>Dynamic multicellular co-culture</p> <p>Mimics local in vivo organization and structure</p> <p>Medium-term culture</p> <p>Microfluidic devices are scalable (size, number of cells)</p> <p>Imaging in real-time</p>	<p>Ideal to study immune–tumor and vascular interaction in 3D microenvironment</p> <p>Requires low number of cells</p> <p>Ability to modulate cytokine/gradients and reduces reagents</p> <p>Possibility to include fluid flow stimuli with pump</p> <p>Reproduces paracrine and contact interactions</p> <p>Model 3D ECM</p>	<p>Inability to recapitulate biological interactions in vivo within an entire animal</p> <p>Maintain long-term culture (months)</p> <p>Risk of contamination during handling</p> <p>Difficulty in providing correct cell culture Medium for all cell types</p>
<i>in vitro</i>	<p>3D Organoids</p> 	<p>Use of patient-derived specimens, stem cells or cell lines</p> <p>Ideal to recapitulate the pathophysiology of the original tissue</p> <p>Single/multicellular co-culture</p> <p>Mimic organization in vivo</p> <p>Medium- to long-term culture</p> <p>Imaging in real-time</p> <p>Low to medium costs</p>	<p>Ideal to recapitulate the pathophysiology of the original tumor</p> <p>Reproduces paracrine and contact interactions</p> <p>Model 3D ECM</p>	<p>Lack native immune and stromal elements</p> <p>Require time to propagate sufficient material for drug screening/testing</p> <p>Difficult to provide correct protocols/cell culture medium</p> <p>Risk of contamination for high handling level</p>
<i>in vitro</i>	<p>3D Bioprinting</p> 	<p>Use of stem cells or cell lines</p> <p>High costs for equipment with high resolution and wide range of processing possibilities</p> <p>Low to Medium-term culture</p>	<p>living cells are precisely positioned</p> <p>reproducing tissue-specific architectures derived from patients' bioimages (custom design)</p>	<p>Printing with high resolution (μm) and speed (depending on printing technology)</p> <p>Biocompatibility of bioink and printing process parameters (e.g. shear stress) might affect cell viability</p> <p>Require time for printing 3D structure with high thickness</p>

		<p>Multicellular co-culture</p> <p>Mimics local <i>in vivo</i> organization and structure</p>		<p>Risk of contamination for high handling Level</p>
<i>in vitro</i>	<p>Transwell culture</p> 	<p>Use of patient-derived specimens, stem cells or cell lines</p> <p>Single/multicellular co-culture</p> <p>Modulate cytokine gradients</p> <p>Low cost</p>	<p>Study paracrine signaling, chemotaxis (immune cells) and vascular permeability</p> <p>Simple technical culture</p>	<p>Inability to recapitulate biological <i>in vivo</i> Interaction</p> <p>Gravity force (g) may affect results</p> <p>Difficulty in imaging (depends on membrane transparency)</p> <p>Lack of biomimetic microenvironment</p>
<i>in vitro</i>	<p>2D cell culture</p> 	<p>Ideal to study single cancer cell autonomous processes</p> <p>Use of patient-derived, stem cells or cell line</p> <p>Low to medium culture time</p> <p>Low costs</p>	<p>Reproducible experiments in a single cell component</p> <p>Simple technical culture</p>	<p>Inability to recapitulate biological <i>in vivo</i> interactions</p> <p>Potential genetic changes of cancer cells over time</p> <p>Lack of the ECM and microenvironment</p> <p>Fails to account for 3-dimensional cell growth</p> <p>Require cells, cell culture medium and culture dishes</p> <p>Lack of immune cells</p> <p>No multicellular co-culture</p>
<i>in vivo</i>	<p>Immuno-competent mouse (Autograft)</p> 	<p>Ideal to study biological <i>in vivo</i> interaction within the entire animal</p> <p>Syngeneic cell lines with the same mouse background</p> <p>Biological interaction <i>in vivo</i> within the entire animal</p> <p>Long-term culture (over months)</p> <p>High costs</p>	<p>Include immune cells interactions (mouse)</p> <p>Reproduce <i>in vivo</i> organization</p> <p>Mouse-derived organotypic tumor spheroids (MDOTS) derived from this model can be cultured in 3D microfluidic device or as organoids</p>	<p>Challenging imaging in real-time</p> <p>Lack of human immune cells interactions</p>
<i>in vivo</i>	<p>Immuno compromised mouse (Patient derived xenograft)</p>	<p>Ideal to study biological <i>in vivo</i> interaction within the entire animal</p> <p>Culture system using patient-derived specimens</p>	<p>Reproduce <i>in vivo</i> organization</p> <p>(PDXs) derived from this model can be cultured in 3Dmicrofluidic</p>	<p>Challenging imaging in real-time</p> <p>Lack of immune cells compartment</p>

		<p>High costs</p> <p>Require animal facility</p> <p>Long-term culture (over months)</p>	device or as organoids	<p>Genetic differences between species</p> <p>Lack of human vasculature after several passages</p>
<i>in vivo</i>	<p>Genetically engineered mouse models</p> 	<p>Ideal to study biological in vivo interaction within the entire animal</p> <p>High costs</p> <p>Require animal facility</p> <p>Long-term culture (over months)</p>	<p>Include immune cells interactions (mouse)</p> <p>Inducible (On/off) systems of oncogenes and tumor suppressor genes</p>	<p>Challenging imaging in real-time</p> <p>Genetic differences between species</p> <p>Inducible systems is limited to few oncogenes</p> <p>Not recapitulate tumor mutation burden</p>
<i>in vivo</i>	<p>Humanized mouse model</p> 	<p>Ideal to study biological in vivo interaction within the entire animal</p> <p>High costs</p> <p>Require animal facility</p> <p>Long-term culture (over months)</p>	Include immune cells interactions (humanized version)	<p>Challenging imaging in real-time</p> <p>Close/identical similarity to human genes</p> <p>Not fully recapitulate a robust human immune system</p> <p>Limited incomplete human function</p>

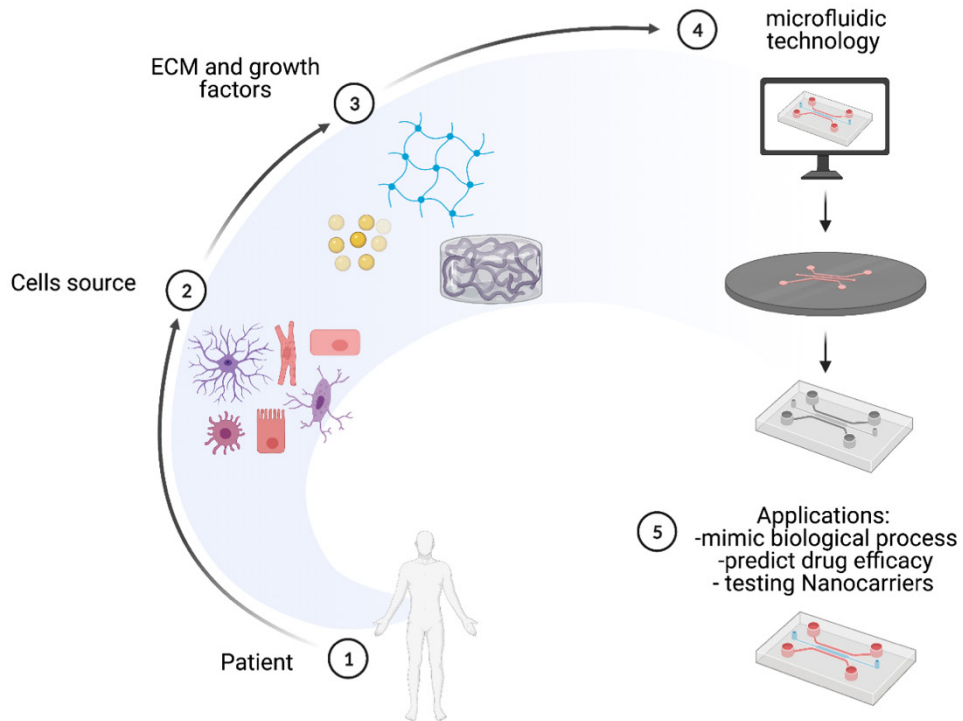
Chapter 2 - Design principles, microfabrication and therapeutic testing applications of bio-inspired human microphysiological systems using microfluidic technology

Abstract

Microphysiological systems are 3-dimensional microengineered and bioinspired platforms created with the use of microfluidic technology, which contain living human primary cells, stem cells and induced pluripotent stem cells (iPS) embedded in extracellular matrix (ECM)-like biomimetic hydrogel organized to represent key functional units of living human organs and reconstitute human pathophysiology. These microdevices replicate the 3-dimensional microarchitecture defined spatial distribution of multiple cells to emulate *in vivo* tissue-specific microenvironment. Microphysiological systems could be employed as specialized *in vitro* models that permit simulation of complex biological processes and predict pharmacological efficacy of drugs and nanocarriers. Thus, these microsystems potentially represent low-cost alternatives to 2D culture systems and conventional animal models in agreement with the 3Rs principle (reduction, refinement, replacement), to improve preclinical testing of innovative pharmaceutical therapies, and expand our understanding of several currently incurable diseases.

In chapter 2, the design and the micro-engineered tools for microfabrication of bio-inspired human micro-physiological living systems and their potential uses are discussed with a focus on microfluidic technology for modelling microvasculature and multicellular-vascular interactions. Finally, some potential applications of the microfluidic technology for therapeutic testing are illustrated, particularly focusing on testing nanoparticles (NPs) as delivery systems.

Microphysiological systems



Graphical abstract 3: Preclinical microphysiological systems for biomedical research.

Schematic created with biorender.com

Bio-inspired Microphysiological systems

As described in the previous Chapter, microphysiological systems contain living cells that have been organized into compartmentalized single or multiple channels. The main goal of microphysiological system modelling is to reproduce minimal functional units that recapitulate tissue- and organ-level functions in a more physiologically-relevant model. “Bio-inspired microphysiological systems” refers to design principles that involve a deep understanding of the morphogenetic biology and tissue structures, for faithful reproduction of functional tissues. Fundamental aspects of the technology are: (i) the selection of appropriate cell types, able to undergo self-organization into complex architectures; (ii) the design of proper ECM composition to enable cell polarization and development through complex morphogenic steps, converging into precise anatomical structures. Hence, microengineering techniques should guide the process of cell self-organization into 3D multicellular structures [112]. Both ESCs and iPSCs have the capacity of spontaneous self-organization, when cultured in 3D hydrogels, reproducing pluripotent stem cell arrangement during embryogenesis [113]. Indeed, in microphysiological systems, ESCs and iPSCs undergo differentiation with higher genetic expression of tissue-specific markers, suggesting a more physiological behavior of pluripotent stem cells. In this thesis, iPSCs self-organization will be exploited for blood-vessel formation in microphysiological systems.

The dynamic reciprocal interactions between cells involve exogenous stimuli, given by the growth factors contained in the culture medium, paracrine stimulation and direct cell interactions, improving self-organization into structures of increasing complexity that recapitulate the main stages of tissue development *in vivo*.

Microengineered devices, by providing spatial boundary conditions and control over these parameters, have proved capable of directing these processes, and therefore appear well suited to guide complex tissue self-organization. Important advancements in this field are self-assembled structures as a part of living systems. In addition, microphysiological systems could potentially expedite drug discovery and provide important new insights into fundamental disease processes.

Microfluidic technology and microfabrication processes of micro and macro systems

Microfluidic systems are fabricated using high-precision soft lithographic methods using polydimethylsiloxane (PDMS), that is a transparent, inert and biocompatible polymeric substrate. The protocol that is related to microfabrication process of the microfluidic device can be divided in three phases: design of the device pattern (**mask design**) master fabrication (**photolithography**) and mold fabrication (**soft lithography**)[94][99].

Mask preparation are opaque plates (glass or quartz) or film (polyester base) with transparent areas to allow ultraviolet (UV) light to shine through in a defined pattern. The pattern is realized by following the instruction from a computer-aided design (CAD) file. [95], [99].

Photolithography is a microfabrication process used to pattern elements of a thin film (photoresist) in a substrate (silicon wafer). It makes use of UV light passing through a mask to transfer a geometric pattern onto a photoresist, a light sensitive material, coating the substrate. Usually, the resolution of the transparency (20 μm) is enough for microfluidic application. Two types of photoresist exist: positive and negative. In positive photoresist the portion that is exposed to UV light becomes soluble to the photoresist developer. The portion of the photoresist that is unexposed remains insoluble. Instead, a negative photoresist is a type of photoresist in which the portion that is exposed to UV light becomes insoluble to the developer, instead unexposed portion of the photoresist is dissolved by the photoresist developer (Fig. 1.8a). SU-8 (negative photoresist) is a viscous liquid epoxy-based photoresist solution designed for micromachining and microelectronic applications is used in this application. Due to exposition to UV-light (350-400 nm) and subsequent crosslinking portions of the film become insoluble to liquid photoresist developers.

Subsequently, a series of chemical treatments and baking at 65 and 95 °C allows to finalize the pattern or to potentially embed more layer by deposition of a new material in the desired pattern upon the material already present. In summary, photolithography for thin film deposition is realized through the following steps: mask preparation, application of photoresist, exposure, development. The master is the final patterned structure produced by photolithography (Fig. 1.8b). After master fabrication, **soft-lithography** process is used to prepare PDMS mold [94]. Briefly, PDMS is supplied in two components, a silicon elastomeric base and curing agent mixed 10:1 weight ratio (base : curing agent) mixed and degassed to remove bubbles.

The PDMS solution is then poured onto the master and baked into an oven at 80 °C. After punching holes to make gel inlet and reservoirs, devices are sterilized and then plasma treated to a bonded to a glass cover slip[94] (Fig. 1.8c).

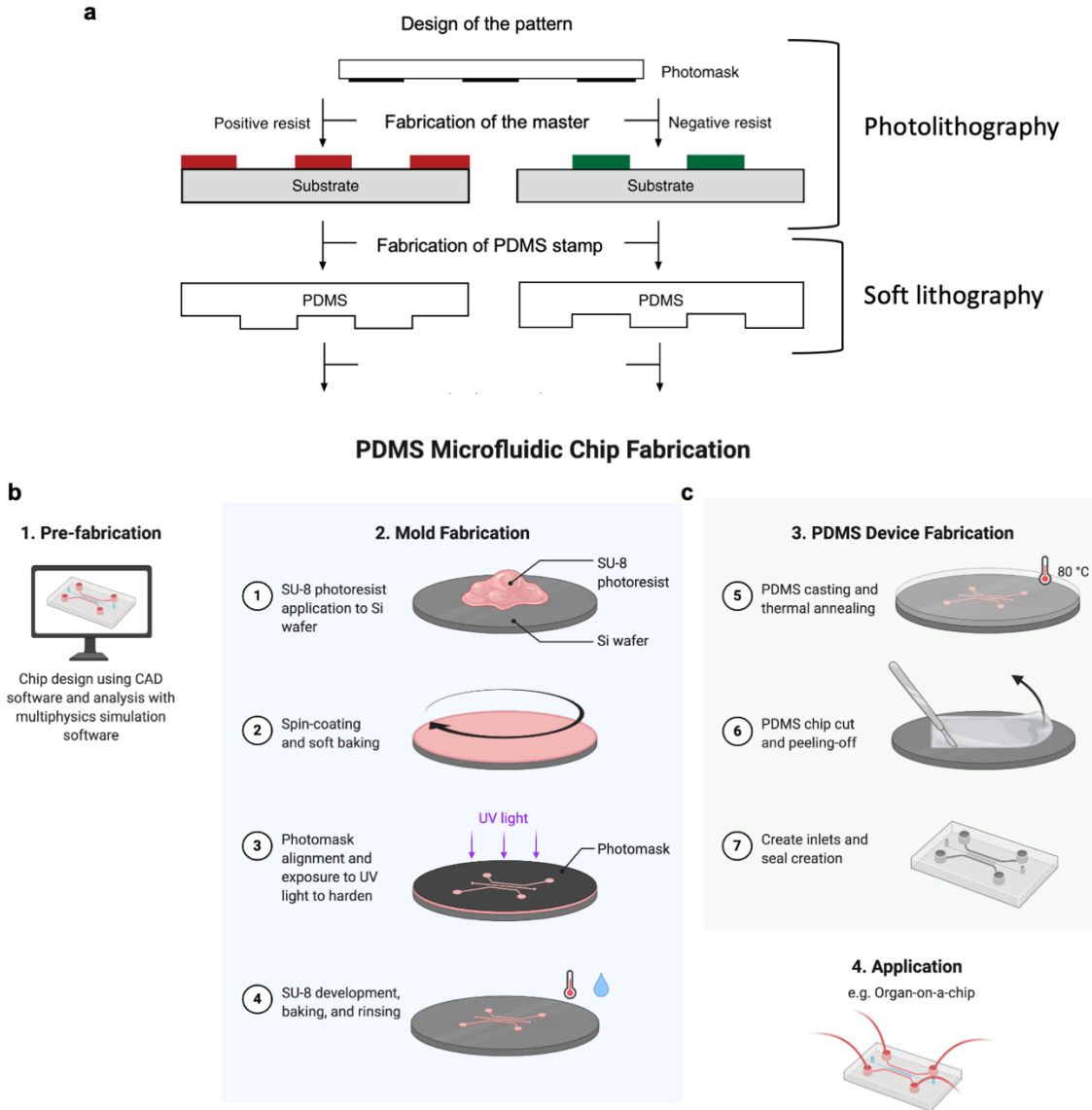


Figure 1.8: Microfabrication of microfluidic device by photolithography and soft lithography.

a) Schematics of the photolithography including positive and negative photoresist and soft lithography **b)** Photolithography procedures in a microfluidic device. SU-8 is spin-coated and prebaked on a bare wafer. UV light is exposed on the SU-8 covered by a transparency photomask (black). Exposed SU-8 is then baked after exposure and developed to define channel patterns. **c)** PDMS mixed solution is poured on the wafer and cured. Cured PDMS is then peeled from the wafer. The device is trimmed, punched and autoclaved ready for assembly. Reproduced with permission from a) [99]. **b)** and **c)** Schematics created with BioRender.com.

In this thesis, microphysiological systems described in Chapter 4 - Section II were prepared based on PDMS chips, while those in Chapters 6 and 7 - Section III were made use of the commercial ‘3-D cell culture chip’ (DAX-1, AIM Biotech, Singapore) which is fabricated using a cyclic olefin polymer (COP). The design and fabrication of the microfluidic devices will be illustrated in detail in the experimental parts of the relative Chapters.

Microphysiological systems for vessel formation in vitro: modelling microvasculature and multicellular-vascular interactions

The formation and maintenance of vasculature is of crucial importance for tissue engineering. During early embryogenesis, blood vessels are formed by mesoderm-derived endothelial progenitors (angioblast cell) coalescence followed by the formation of hollow lumens. Capillary-like networks contain angioblasts that then differentiate into ECs, a process known as vasculogenesis [114]. Vasculogenesis also occurs during adulthood through recruitment of endothelial progenitor cells from bone marrow. During development, and following the formation of a primary network, expansion and sprouting occurs from existing vessels, by a process known as angiogenesis [115][116] (Fig. 1.9a, b).

In vitro modelling exploits similar physiological mechanisms for blood vessel formation. Modelling vascularization and multicellular-vascular interactions is of key importance for a variety of reasons: 1) replication of the angiocrine functions of organ-specific ECs [117], which deploy sets of growth factors that actively participate in the maintenance of homeostasis; 2) mimicry of organ-specific barriers, such as the blood–brain barrier, that limits the transport of therapeutics into brain tissue, or the tumor-vasculature barrier impairing immune cells infiltration into solid tumor microenvironments.

Lastly, the tissue construct can be maintained in culture for longer by vascularization and diffusion of oxygen and appropriate nutrient delivery and waste elimination, thus improving the relevance and long-term stability of the *in vitro* models. From a tissue engineering prospective, the combination of microfluidic modelling and pre-vascularization for *in vivo* implantation is one promising strategy toward the bioengineering of functional tissues.

Angiocrine cues participate actively in the induction, patterning and guidance of organ formation, regeneration, as well as in the maintenance of homeostasis and metabolism [115][117]. ECs regulate complex tasks by supplying stimulatory or inhibitory growth factors, produce ECM components and collectively release cytokines that consequently affect the tissue-specific microenvironment, such as in the brain [121], lung tumor microenvironment [122] and anaplastic-large cell lymphoma niche[123]. Notably, cancers are not composed merely of cancer cells alone; instead, they are complex ‘ecosystems’ comprising many different cell types and noncellular factors. It has been demonstrated that the complexity and diversity of the tumor microenvironment (TME) influences the patient response to immunotherapy. The tumor stroma, including ECs, pericytes, fibroblasts, is a critical component of the TME, and it has crucial roles in tumor initiation, progression, metastasis and therapy resistance [124][125] (Fig. 1.9c, d)

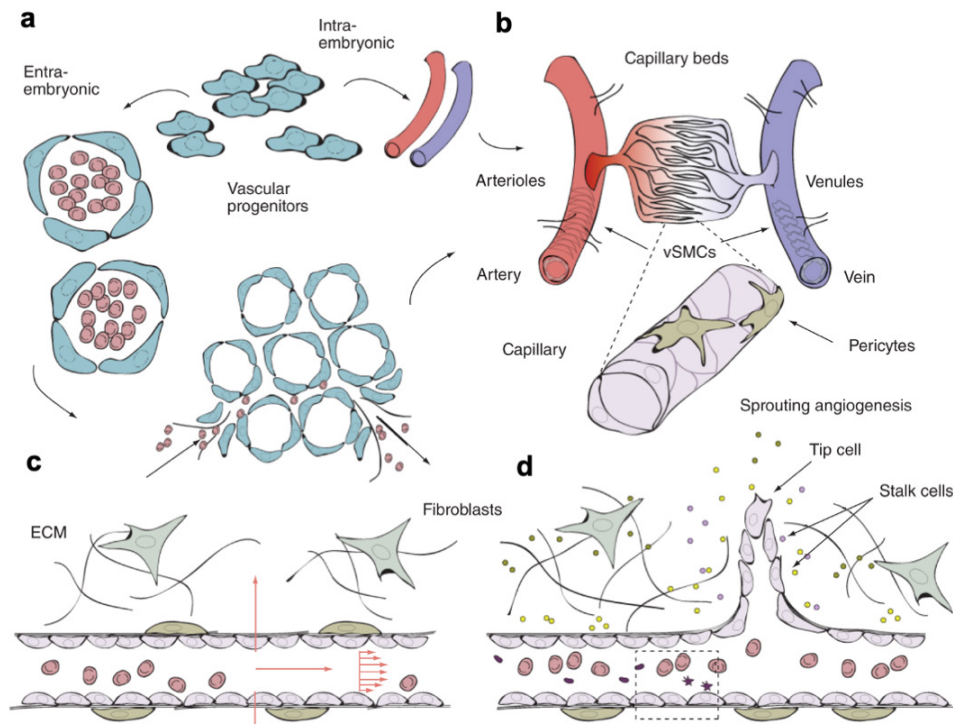


Figure 1.9: Vascular network formation in vivo.

a) Vascular progenitor cells merge into endothelial cells islands, which subsequently form together a microvasculature b) Schematic of a vascular systems of connected arterioles and venules after vasculogenesis vessels mature and remodel, directed by a variety of angiogenic factors and cytokines. c) Section of a blood vessels showing mechanical factors such as wall shear stress and axial strain also direct angiogenesis. d) EC-secreted factors recruit mural cells during angiogenic remodeling pro-angiogenic factors are released from stromal cells such as fibroblast directing migration and sprouting of ECs. Reproduced with permission from [127].

In many tumors, the vasculature is abnormal, and dysfunctional imbalance between the levels of pro-angiogenic and antiangiogenic factors promotes rapid but aberrant vascular formation. Morphologically, tumor blood vessels are tortuous, dilated and unevenly distributed with unpaired perfusion. Fibroblasts also have multiple functions: (i) they shape the ECM, which in turn provides structure and support to cells, and (ii) they contribute to paracrine cellular signaling with cytokine productions [126]. The vasculature is also essential for immune response: immune cells circulate within the bloodstream and the production of cytokines or adhesion molecules by tissues are critical for the recruitment of immune cells. This process is especially relevant in tissue- immune cell interactions and during tumor cell transmigration.

In vitro vascular networks are generated by two distinct approaches: via endothelial-lined patterned channels, or by self-assembled networks [127][128]. Both systems are developed using microfluidic technology. In this context, microfluidic systems allow the possibility to include microvasculature [129], which has many advantages such as: provide oxygen and nutrient exchange to extend the days of culture, to study extravasation of metastatic cancer cells [130] [131][132], to reach a more physiologically-relevant mimicking the tissue-specific microenvironment. The engineering of 3D macro-vessels by patterned microchannels is described in the following paragraph.

Patterned microchannel: 3D macro-vessels

The patterned microchannel method consists of the 3D culture of cells on the walls of micropatterned chips. Using this method, the designed channels determine the size and architecture of the newly-formed vessels. To develop hollow-lumen 3D macro-vessels, ECs are made to adhere on microfluidic channel walls, pre-coated with cell adhesive materials, such as fibronectin, Matrigel or collagen. The microfluidic channel will act as a mold of the blood vessel, giving the final shape to adherent ECs. After microchannel coating, solutions containing ECs will be injected in the fluidic channel and the device will be rotated twice to allow cell attachment onto all channel wall surfaces. Adherent ECs will form a confluent monolayer. (Fig. 1.10b). Depending on the design of the microfluidic device, the 3D macro-vessel has one or multiple sides with shared borders with the gel channels. The gel channels contain cell-hydrogel or hydrogel only (depending on the application) and are filled at the beginning of the culture process. During hydrogel injection, capillary effect, surface tension and post structures will prevent their spread into the entire

microfluidic chip. The size of the 3D macro-vessel depends on the size of the fluidic channels, typically ranging between 100-2000 μm [94]. The 3D macro-vessel is suitable for mimicking large blood vessel circulation, permeability and cell extravasation, and cell-cell interactions [133].

Using the macro-vessels is possible to model angiogenesis process. Angiogenesis is the expansion and remodeling of a blood vessel via the sprouting of ECs from pre-existing vessels. It results from a sequence of events influenced by cell-cell and cell-ECM interactions. Angiogenesis sprouting *in vitro* is led by ANG-1 and VEGF gradients stimulations, created within the device. Recombinant cytokines are added to the culture medium, or may be produced by stromal cells loaded in flanked gel channel [131] [132], which constantly releases pro-angiogenic factors [136][137].

Self-assembled microvessels: vasculogenesis

In vitro formation of microvascular network relies on careful mixing of ECs such as HUVECs or combination of HUVECs and stromal cells (fibroblasts or pericytes) in fibrin gel by self-assembled vasculogenesis- like process [135]–[137]. This approach does not require an extra structure to guide vasculatures: vascular cells are seeded within hydrogels in the chip device, where the cells reconstitute 3-D vascular networks by self-assembly as to generate a more physiological vasculature than the ones in other methods. Coalescence of cells form intussusceptions and vacuoles, and organize themselves into endothelial tubes into well-formed blood vessels. This process usually takes place into 3-5 days up to 7 days. Vascular networks quickly regress in the absence of stromal cells, demonstrating the usefulness of their paracrine signaling. Variants include culture of fibroblasts in the parallel gel channel [140] (Fig. 1.10a).

Perfusability is an important function and is confirmed by flow of fluorescent fluorophores (fluorescent dextran) or beads [127]. Self-assembled micro-vessels can reach 100 μm capillary diameter (even down to $<20 \mu\text{m}$). The ability to generate perfusable microvascular network in a relatively short period of time has allowed the observation of physiologically relevant events in real-time, such as trans- endothelial extravasation of tumor cells [141][142][143], as well as the modelling of vascularized microtumors [144].

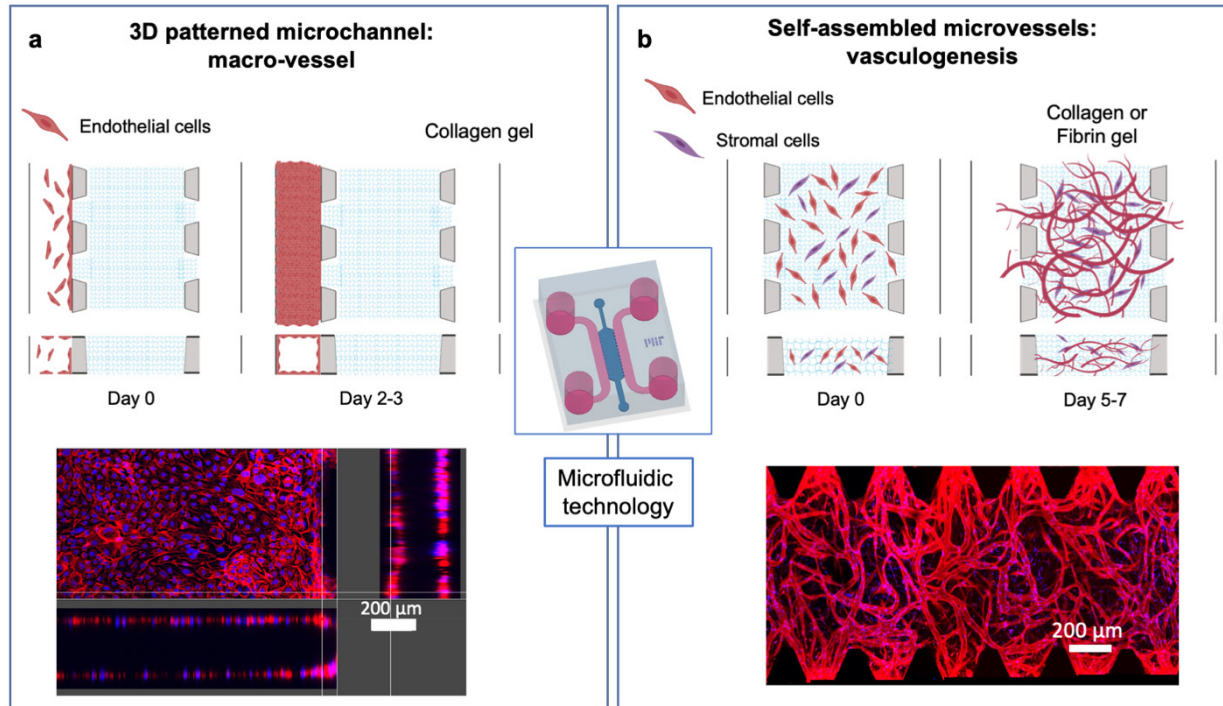


Figure 1.10: Engineering vascular formation in microphysiological systems.

a) Schematic patterned microchannel: macro-vessel formation in the microfluidic device using endothelial cells (ECs) in 2-3 days. Confocal image of F-actin (red, ECs) and DAPI (blue, nuclei) at day 3 **b)** Self-assembled microvessels by vasculogenesis. Schematic of the microvascular network formation after 7 days. Cells (ECs and stromal cells) self-organized into microvasculature. Confocal image of F-actin (red, ECs) and DAPI (blue, nuclei) at day 7. Schematics created with BioRender.com.

Preclinical modeling of drug efficacy and nanoparticle transport with Microphysiological systems

As the biotechnology industry continues to develop new classes of biopharmaceuticals, improved fundamental understanding of how drug delivery affects safety and efficacy, along with new delivery technologies seems to be necessary. However, it remains difficult to accurately predict patient drug response and organs interactions in standard systems. Consequently, innovative testing platforms are needed to evaluate and predict pharmaceutical delivery in more physiologically-relevant settings. In addition/alternative to traditional and animal preclinical models, which have the limitation discussed in previous chapters, microphysiological models have been widely studied recently as a novel *in vitro* model of organs. Since it is possible to create a more reliable mimic of the tissue-specific microenvironment by using microfluidic device technology, these devices could provide the basis for more cost-effective preclinical drug

screening with greater predictive power. By improving the effectiveness of preclinical predictions of human drug responses is critical to reducing costly failures in clinical trials. Several studies have demonstrated the potential of microphysiological systems on studying efficacy, toxicity, pharmacokinetics, transport and distribution properties across biological barriers of novel drugs therapeutics, including nanomaterials used as nanocarriers, such a nanoparticles (NPs), leading to the discovery of new targets and drug candidates.

Nanoparticles as drug delivery systems

The delivery of pharmaceutical agents to a specific tissue/organs or cells is critical for patient's diagnosis and treatments. There are several biological barriers that limit drugs reaching the therapeutic target site, while interacting with different molecules, cells, tissues and organs as they are transported through the body. functional delivery is determined by large-scale issues such as biodistribution, stability and clearance to smaller-scale barriers such as intracellular trafficking, uptake pathways through cell-specific targeting and molecular transport to specific organelles[145] (Fig. 1.11a). At the systemic level, circulation in the bloodstream is an important factor which affect drug stability. Clearance from the circulation due to enzymatic digestions or phagocytosis from monocytes and dendritic cells is an important factor that affects clearance of drug delivery systems[146]–[148] as well as the heterogeneity of tissue-specific microenvironment and its conditions with altered pH[148]. Moreover, drugs lose their pharmacological activity due to changes in environmental factors such as moisture, temperature, and pH, which can occur in the tissue microenvironment or during storage. The tissue microenvironment affects drug delivery, and could be overcome using delivery systems tunable with pH variations. Moreover, cellular delivery is challenging in terms of discriminating the correct target cells by targeting specific receptors on the cells by surface coating/functionalization of delivery systems containing a proper functionalization targeting specific ligands. This also helps with the uptake of the delivery system and the payload release. In this regard, nanomedicine, a branch of nanotechnology, and precision medicine, an emerging field could enable to overcome the limitations of conventional free-drug delivery treatment with customizable in a manner that depends on patient-specific characteristics [149]. Among nanomedicine tools, engineered nanomaterials can be tuned to display different physical and chemical properties that influence their interactions with their biological environments and delivery destinations[146].

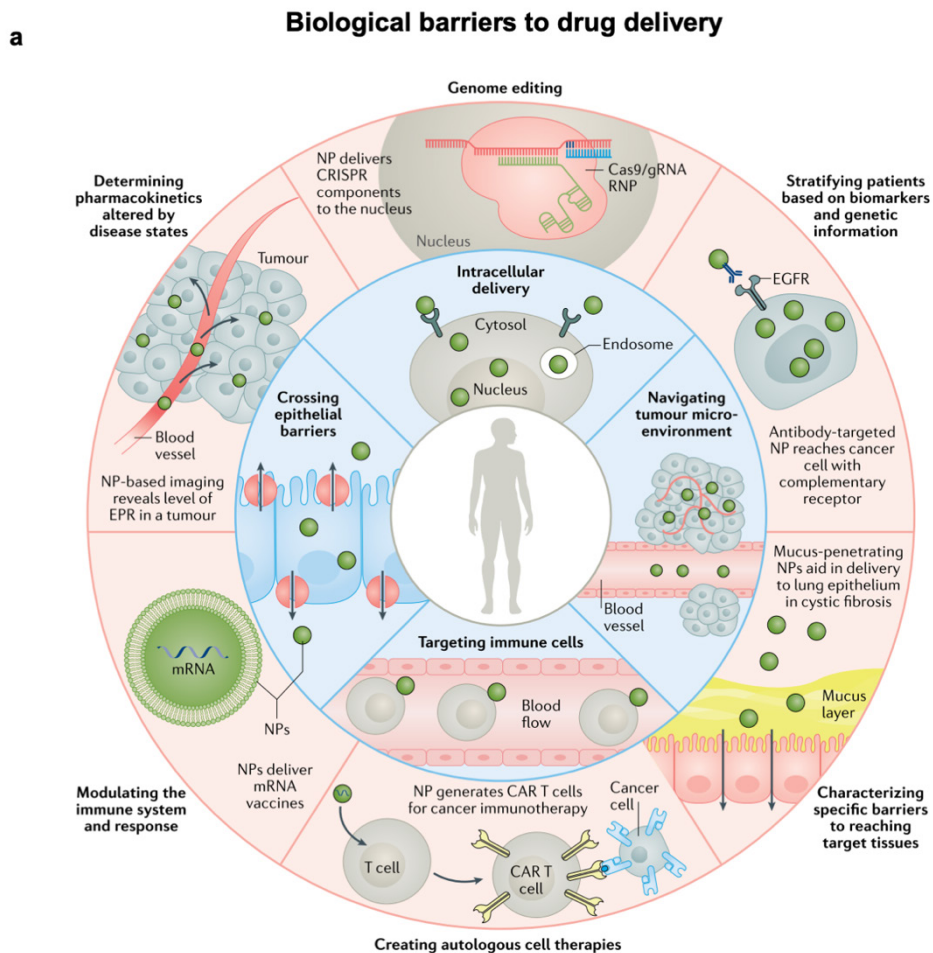


Figure 1.11: Biological barriers and precision medicine.

a) Schematic overview of the biological barriers that nanoparticles (NPs) can potentially overcome (inner ring), including crossing endothelial barriers, intracellular delivery with targeted functionalization, overcome the immune system clearance. The outer ring of the schematic expresses the precision medicine applications that may benefit from NPs design. Reproduced with permission from [148].

Nanomaterial-based delivery systems significant promise to improve treatment specificity, stability and solubility of encapsulated cargos. Delivery can vary depending on the size, shape, surface chemistry, stiffness, and chemical composition of the delivery vehicles to define the optimal design to reach a specific biological target. Drug delivery affects numerous factors that contribute to therapeutic efficacy, including pharmacokinetics, distribution, cellular uptake and metabolism, excretion and clearance, as well as toxicity [150].

Among all drug delivery systems, nanoparticles (NPs) constitute a significant portion of research. NPs indicate solid colloidal particles with a size range of 1 – 1000 nm, have been developed to overcome the limitations of free therapeutics and facilitate crossing through all the physical biological barriers: systemic, microenvironmental and cellular, that are heterogeneous across patient populations and diseases[148]. Early studies on NP biological iterations were unable to overcome these biological barriers to delivery, but more recent NP designs have utilized advancements in controlled synthesis strategies to incorporate complex architectures, bio-responsive moieties and targeting agents to enhance delivery[148]–[150]. Indeed, the NPs size is also an important design parameter that defines NP delivery across biological barriers such as tumor vasculature or the BBB [147]. NPs have the potential to revolutionize the diagnosis and treatment allowing targeted delivery of drugs, contrast agents, immunotherapies, and gene editor systems, by improving the stability and solubility of encapsulated cargos, promote transport across membranes and prolong circulation times to increase safety and efficacy.

NPs offers many advantages in their design, such as non-invasiveness, low cost, good biodegradability and long-term stability, ease of synthesis, high targeting efficiency, and high controllability on encapsulation and release of the payload NPs can therefore be utilized as more complex systems, including combination therapies, imaging or theranostic applications[148], [151], [152]. NPs improve the protection and release of poorly water soluble drugs and allow a controlled-spatio-temporal and sustained release, eventually triggered on demand such as enzyme-, pH-, temperature and redox- responsive delivery systems.

There are several NPs classes including polymeric, inorganic and lipid-based NPs. Each class of NPs has several advantages and disadvantages that are showed in figure (Figs. 1.12a, b, c).

Lipid-based NPs are structures comprising one or two self-assembled lipid bilayers, such as liposomes composed of phospholipids. Lipid-based NPs are able to deliver hydrophilic, hydrophobic and lipophilic drugs[153][146].

Polymer-based NPs are synthesized from synthetic or natural polymers synthesized by using various techniques such as emulsification (solvent displacement or diffusion), nanoprecipitation, ionic gelation and microfluidics[154]–[156][157].

Inorganic materials such as gold, iron oxide and silica have been used to synthesize nanostructured systems with a variety of sizes, structures and geometries (nanospheres, nanorods, nanostars, nanoshells, NPs), inorganic NPs have unique physical, electrical, magnetic and optical properties,

which have been used for different drug delivery, diagnosis, photothermal and imaging applications (contrast agents). Most NPs have good biocompatibility and stability, however, due to their low solubility and toxicity at high doses, are limited in their clinical application.

To date, a large number of delivery systems have been developed to treat diseases, including lipid-based, polymer-based, inorganic, which have already been FDA-approved or are under clinical trials[148][158]. To allow an enhanced delivery, surface properties of NPs are commonly engineered and tailored for a specific target tissue. NPs can be functionalized with proteins, antibodies, carbohydrates and other ligands on the NP surface, (Fig. 1.12d), characterized by high specificity towards selected receptors overexpressed by the membrane of cancer cells or towards selected components of the tissue-specific microenvironment, can induce a more specific and efficient NP uptake[159]. In certain cases, to avoid rapid excretion based on surface properties and increase long-term circulations, NPs are covered with FDA-approved Polyethylene glycol (PEG) which improves the circulation time by altering the NP size and solubility while shielding the NP surface from enzymes and antibodies that may induce degradation, secretion and clearance, but does not completely prevent recognition by macrophages or other cells of the immune system[148]. NPs might also be designed to overcome many limitations regarding traditional therapies towards more personalized and precision medicine[96], and NPs development has expanded into a broad range of clinical applications, such as cancer therapy, immunotherapy, neurological disease genome editing including release of oligonucleotides[152], [159]–[164].

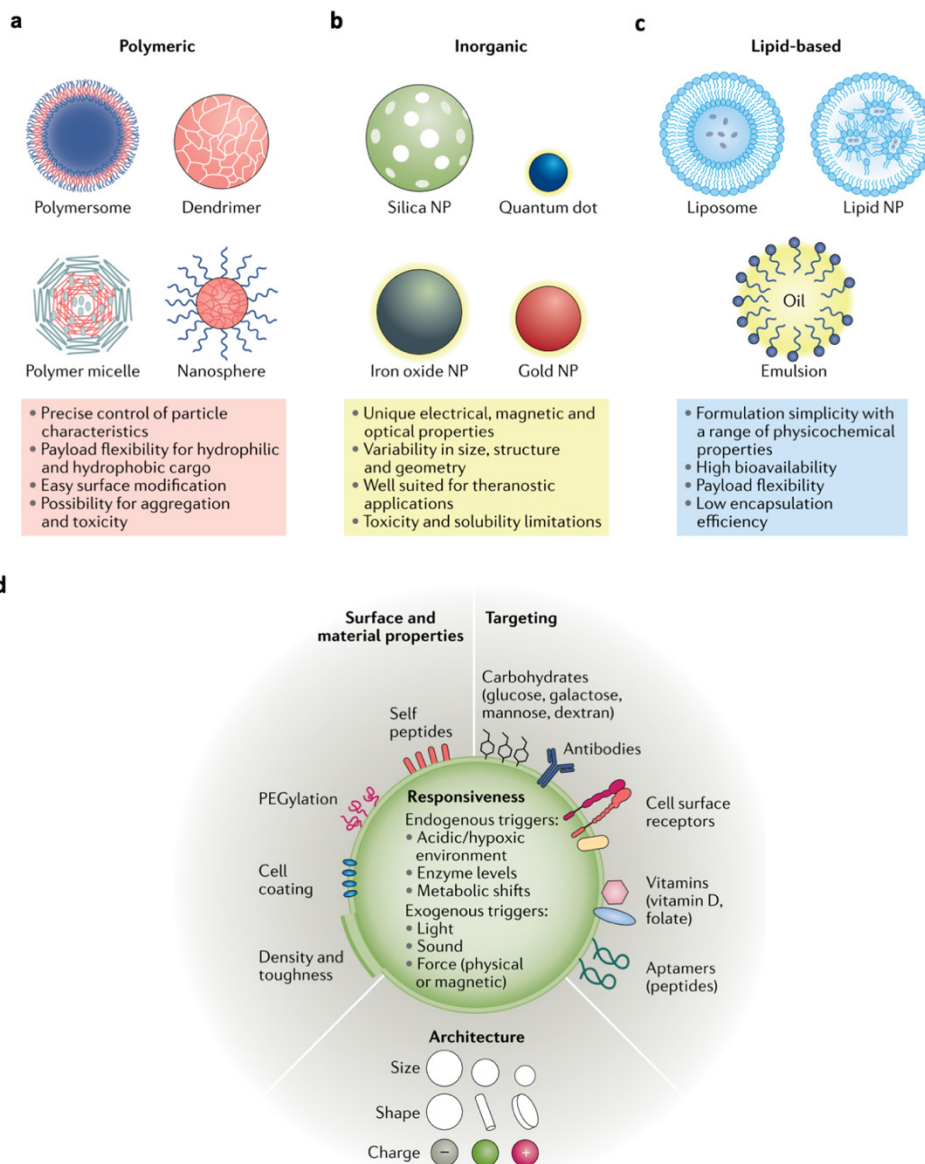


Figure 1.12: Classes of NPs and surface property for enhanced delivery.

Classes of nanoparticle (NPs) a) polymeric b) inorganic c) lipid, with some of their common subclasses. Several advantages and disadvantages are listed below: d) Surface and material properties, architecture, targeting moieties and responsiveness for NPs that can be altered in combination for intelligent designs to tailor the delivery systems to a specific application. Reproduced with permission from [148].

Aim of the work

The aim of this thesis is to design and develop microengineered microphysiological systems to study multicellular-vascular interactions in a microfluidic device and testing of drugs and nanoparticle transport. In particular, this thesis focuses on three different bio-inspired 3D microphysiological models of multicellular-vascular interactions in a microfluidic device:

- human blood-brain barrier (BBB) model
- KRAS/LKB1 lung carcinoma
- ALK-positive anaplastic large cell lymphoma (ALCL) models

These three models have in common an advanced perfusable microvasculature created by self-assembled vasculogenesis and patterned microchannel. The application of BBB microphysiological model systems as preclinical testing platforms for drugs and nanocarriers is described.

The vascularized KRAS/LKB1 lung carcinoma was used to determine that extracellular export of 2',3'-cGAMP by cancer cells plays an important role in activating STING signaling in endothelial cells. Similarly, the ALK-positive ALCL model was used to study tumor-vascular interactions.

In the final section of the thesis, bioartificial nanoparticles were engineered by nanoprecipitation containing chitosan (CS) and poly(lactic-co-glycolic acid) (PLGA) and miRNAs or siRNAs, and their physicochemical characterization are discussed.

Overall, these microengineered microphysiological and drug delivery have the capability to more reliably predict therapeutic vulnerabilities and study drug transport across biological barriers, thereby expediting drug discovery, and providing important new insights into fundamental biological processes to expand our understanding of several currently incurable diseases.

References

- [1] C. P. Day, G. Merlino, and T. Van Dyke, “Preclinical Mouse Cancer Models: A Maze of Opportunities and Challenges,” *Cell*, vol. 163, no. 1, pp. 39–53, 2015.
- [2] B. Munos, “Lessons from 60 years of pharmaceutical innovation,” *Nat. Rev. Drug Discov.*, vol. 8, no. 12, pp. 959–968, 2009.
- [3] D. Hanahan and R. A. Weinberg, “Hallmarks of cancer: The next generation,” *Cell*, vol. 144, no. 5, pp. 646–674, 2011.
- [4] D. Hanahan and R. A. Weinberg, “The hallmarks of cancer,” *Cell*, vol. 100, no. 1, pp. 57–70, 07-Jan-2000.
- [5] N. Gengenbacher, M. Singhal, and H. G. Augustin, “Preclinical mouse solid tumour models: Status quo, challenges and perspectives,” *Nat. Rev. Cancer*, vol. 17, no. 12, pp. 751–765, 2017.
- [6] U. Ben-David *et al.*, “Genetic and transcriptional evolution alters cancer cell line drug response,” *Nature*, vol. 560, no. 7718, pp. 325–330, 2018.
- [7] T. Voskoglou-Nomikos, J. L. Pater, and L. Seymour, “Clinical predictive value of the in vitro cell line, human xenograft, and mouse allograft preclinical cancer models,” *Clin. Cancer Res.*, vol. 9, no. 11, pp. 4227–4239, 2003.
- [8] J. P. A. Ioannidis, B. Y. S. Kim, and A. Trounson, “How to design preclinical studies in nanomedicine and cell therapy to maximize the prospects of clinical translation,” *Nat. Biomed. Eng.*, vol. 2, no. 11, pp. 797–809, 2018.
- [9] C. L. Morton and P. J. Houghton, “Establishment of human tumor xenografts in immunodeficient mice,” *Nat. Protoc.*, vol. 2, no. 2, pp. 247–250, 2007.
- [10] K. K. Frese and D. A. Tuveson, “Maximizing mouse cancer models,” *Nat. Rev. Cancer*, vol. 7, no. 9, pp. 645–658, 2007.
- [11] J. I. Johnson *et al.*, “Relationships between drug activity in NCI preclinical in vitro and in vivo models and early clinical trials,” *Br. J. Cancer*, vol. 84, no. 10, pp. 1424–1431, 2001.
- [12] V. C. Daniel *et al.*, “A primary xenograft model of small-cell lung cancer reveals irreversible changes in gene expression imposed by culture in vitro,” *Cancer Res.*, vol. 69, no. 8, pp. 3364–3373, 2009.
- [13] A. T. Byrne *et al.*, “Interrogating open issues in cancer precision medicine with patient-derived xenografts,” *Nat. Rev. Cancer*, vol. 17, no. 4, pp. 254–268, 2017.
- [14] M. Hidalgo *et al.*, “Patient-derived Xenograft models: An emerging platform for translational cancer research,” *Cancer Discov.*, vol. 4, no. 9, pp. 998–1013, 2014.
- [15] M. R. Girotti *et al.*, “Application of sequencing, liquid biopsies, and patient-derived xenografts for personalized medicine in melanoma,” *Cancer Discov.*, vol. 6, no. 3, pp. 286–299, 2016.
- [16] D. Siolas and G. J. Hannon, “Patient-derived tumor xenografts: Transforming clinical samples into mouse models,” *Cancer Res.*, vol. 73, no. 17, pp. 5315–5319, 2013.
- [17] J. J. Tentler *et al.*, “Patient-derived tumour xenografts as models for oncology drug development,” *Nat. Rev. Clin. Oncol.*, vol. 9, no. 6, pp. 338–350, 2012.
- [18] J. G. Clohessy and P. P. Pandolfi, “Mouse hospital and co-clinical trial project—from bench to bedside,” *Nat. Rev. Clin. Oncol.*, vol. 12, no. 8, pp. 491–498, 2015.
- [19] D. Delitto *et al.*, “Patient-derived xenograft models for pancreatic adenocarcinoma demonstrate retention of tumor morphology through incorporation of murine stromal elements,” *Am. J. Pathol.*, vol. 185, no. 5, pp. 1297–1303, 2015.
- [20] L. Zitvogel, J. M. Pitt, R. Daillère, M. J. Smyth, and G. Kroemer, “Mouse models in oncoimmunology,” *Nat. Rev. Cancer*, vol. 16, no. 12, pp. 759–773, 2016.
- [21] G. P. Dunn, L. J. Old, and R. D. Schreiber, “The immunobiology of cancer immunosurveillance and immunoediting,” *Immunity*, vol. 21, no. 2, pp. 137–148, 2004.
- [22] D. A. Tuveson and T. Jacks, “Technologically advanced cancer modeling in mice,” *Curr. Opin.*

- Genet. Dev.*, vol. 12, no. 1, pp. 105–110, 2002.
- [23] J. Jonkers and A. Berns, “Conditional mouse models of sporadic cancer,” *Nat. Rev. Cancer*, vol. 2, no. 4, pp. 251–265, 2002.
- [24] K. Schönig, F. Schwenk, K. Rajewsky, and H. Bujard, “Stringent doxycycline dependent control of CRE recombinase in vivo,” *Nucleic Acids Res.*, vol. 30, no. 23, p. e134, 2002.
- [25] and J. A. E. Zhou Zhu, Tao Zheng, Chun G. Lee, Robert J. Homer, “Tetracycline-controlled transcriptional regulation systems: advances and application in transgenic animal modeling,” *Semin. Cell Dev. Biol.*, vol. 13, no. 02, pp. 121–128, 2002.
- [26] D. W. Gaylor, “Are tumor incidence rates from chronic bioassays telling us what we need to know about carcinogens?,” *Regul. Toxicol. Pharmacol.*, vol. 41, no. 2, pp. 128–133, 2005.
- [27] Kirk R. Thomas and Mario Capecchi, “Site-directed mutagenesis by gene targeting in mouse embryo-derived stem cells,” vol. 51, pp. 503–512, 1987.
- [28] K. Kersten, K. E. Visser, M. H. Miltenburg, and J. Jonkers, “Genetically engineered mouse models in oncology research and cancer medicine,” *EMBO Mol. Med.*, vol. 9, no. 2, pp. 137–153, 2017.
- [29] M. Singh, C. L. Murriel, and L. Johnson, “Genetically engineered mouse models: Closing the gap between preclinical data and trial outcomes,” *Cancer Res.*, vol. 72, no. 11, pp. 2695–2700, 2012.
- [30] F. J. Sánchez-Rivera and T. Jacks, “Applications of the CRISPR-Cas9 system in cancer biology,” *Nat. Rev. Cancer*, vol. 15, no. 7, pp. 387–395, 2015.
- [31] H. Wang *et al.*, “One-step generation of mice carrying mutations in multiple genes by CRISPR/cas-mediated genome engineering,” *Cell*, vol. 153, no. 4, pp. 910–918, 2013.
- [32] J. Weber *et al.*, “CRISPR/Cas9 somatic multiplex-mutagenesis for high-Throughput functional cancer genomics in mice,” *Proc. Natl. Acad. Sci. U. S. A.*, vol. 112, no. 45, pp. 13982–13987, 2015.
- [33] R. Maresch *et al.*, “Multiplexed pancreatic genome engineering and cancer induction by transfection-based CRISPR/Cas9 delivery in mice,” *Nat. Commun.*, vol. 7, 2016.
- [34] L. D. Shultz, F. Ishikawa, and D. L. Greiner, “Humanized mice in translational biomedical research,” *Nat. Rev. Immunol.*, vol. 7, no. 2, pp. 118–130, 2007.
- [35] T. M. Allen *et al.*, “Humanized immune system mouse models: progress, challenges and opportunities,” *Nat. Immunol.*, vol. 20, no. 7, pp. 770–774, 2019.
- [36] T. M. Dawson, T. E. Golde, and C. Lagier-Tourenne, “Animal models of neurodegenerative diseases,” *Nat. Neurosci.*, vol. 21, no. 10, pp. 1370–1379, 2018.
- [37] I. W. Y. Mak, N. Evaniew, and M. Ghert, “Lost in translation: Animal models and clinical trials in cancer treatment,” *Am. J. Transl. Res.*, vol. 6, no. 2, pp. 114–118, 2014.
- [38] J. Ahn, Y. J. Sei, N. L. Jeon, and Y. Kim, “Tumor microenvironment on a chip: The progress and future perspective,” *Bioengineering*, vol. 4, no. 3, pp. 1–17, 2017.
- [39] A. Sontheimer-Phelps, B. A. Hassell, and D. E. Ingber, “Modelling cancer in microfluidic human organs-on-chips,” *Nat. Rev. Cancer*, vol. 19, no. 2, pp. 65–81, 2019.
- [40] S. E. Gould, M. R. Junttila, and F. J. De Sauvage, “Translational value of mouse models in oncology drug development,” *Nat. Med.*, vol. 21, no. 5, pp. 431–439, 2015.
- [41] L. M. E. Glenn C. Begley, “Raise standards for preclinical cancer research,” *Nature*, vol. 483, 2012.
- [42] D. Caballero, S. Kaushik, V. M. Correlo, J. M. Oliveira, R. L. Reis, and S. C. Kundu, “Organ-on-chip models of cancer metastasis for future personalized medicine: From chip to the patient,” *Biomaterials*, vol. 149, pp. 98–115, 2017.
- [43] J. Pijuan *et al.*, “In vitro cell migration, invasion, and adhesion assays: From cell imaging to data analysis,” *Front. Cell Dev. Biol.*, vol. 7, no. JUN, pp. 1–16, 2019.
- [44] R. Cecchelli *et al.*, “Modelling of the blood-brain barrier in drug discovery and development.,” *Nat. Rev. Drug Discov.*, vol. 6, no. 8, pp. 650–661, 2007.
- [45] “The Transwell Migration Assay,” *JoVE Sci. Educ. Databas*, vol. Cell Biolo, 2020.
- [46] J. Banerjee, Y. Shi, and H. S. Azevedo, “In vitro blood–brain barrier models for drug research:

- state-of-the-art and new perspectives on reconstituting these models on artificial basement membrane platforms,” *Drug Discov. Today*, vol. 21, no. 9, pp. 1367–1386, 2016.
- [47] M. W. van der Helm, A. D. van der Meer, J. C. T. Eijkel, A. van den Berg, and L. I. Segerink, “Microfluidic organ-on-chip technology for blood-brain barrier research,” *Tissue barriers*, vol. 4, no. 1, p. e1142493, 2016.
- [48] P. J. Stewart-Hutchinson, T. P. Szasz, E. R. Jaeger, M. D. Onken, J. A. Cooper, and S. C. Morley, “Technical Advance: New in vitro method for assaying the migration of primary B cells using an endothelial monolayer as substrate,” *J. Leukoc. Biol.*, vol. 102, no. 3, pp. 941–948, 2017.
- [49] K. Berencsi *et al.*, “In vitro migration of cytotoxic T lymphocyte derived from a colon carcinoma patient is dependent on CCL2 and CCR2,” *J. Transl. Med.*, vol. 9, pp. 11–13, 2011.
- [50] I. Tavernaro *et al.*, “Modulating Myeloid Immune Cell Migration Using Multivalently Presented Monosaccharide Ligands for Advanced Immunotherapy,” *Adv. Ther.*, vol. 2, no. 12, p. 1900145, 2019.
- [51] C. R. Justus, N. Leffler, M. Ruiz-Echevarria, and L. V. Yang, “In vitro cell migration and invasion assays,” *J. Vis. Exp.*, no. 88, pp. 1–8, 2014.
- [52] P. P. Guan *et al.*, “By activating matrix metalloproteinase-7, shear stress promotes chondrosarcoma cell motility, invasion and lung colonization,” *Oncotarget*, vol. 6, no. 11, pp. 9140–9159, 2015.
- [53] G. Follain *et al.*, “Fluids and their mechanics in tumour transit: shaping metastasis,” *Nat. Rev. Cancer*, vol. 20, no. 2, pp. 107–124, 2020.
- [54] W. J. Polacheck, J. L. Charest, and R. D. Kamm, “Interstitial flow influences direction of tumor cell migration through competing mechanisms,” *Proc. Natl. Acad. Sci. U. S. A.*, vol. 108, no. 27, pp. 11115–11120, 2011.
- [55] C. H. Heldin, K. Rubin, K. Pietras, and A. Östman, “High interstitial fluid pressure - An obstacle in cancer therapy,” *Nat. Rev. Cancer*, vol. 4, no. 10, pp. 806–813, 2004.
- [56] P. K. Chaudhuri, B. C. Low, and C. T. Lim, “Mechanobiology of Tumor Growth,” *Chem. Rev.*, vol. 118, no. 14, pp. 6499–6515, 2018.
- [57] J. W. Scannell, A. Blanckley, H. Boldon, and B. Warrington, “Diagnosing the decline in pharmaceutical R&D efficiency,” *Nat. Rev. Drug Discov.*, vol. 11, no. 3, pp. 191–200, 2012.
- [58] G. Caponigro and W. R. Sellers, “Advances in the preclinical testing of cancer therapeutic hypotheses,” *Nat. Rev. Drug Discov.*, vol. 10, no. 3, pp. 179–187, 2011.
- [59] J. Bowes *et al.*, “Reducing safety-related drug attrition: The use of in vitro pharmacological profiling,” *Nat. Rev. Drug Discov.*, vol. 11, no. 12, pp. 909–922, 2012.
- [60] P. Y. Muller and M. N. Milton, “The determination and interpretation of the therapeutic index in drug development,” *Nat. Rev. Drug Discov.*, vol. 11, no. 10, pp. 751–761, 2012.
- [61] T. Mammoto and D. E. Ingber, “Mechanical control of tissue and organ development,” *Development*, vol. 137, no. 9, pp. 1407–1420, 2010.
- [62] R. Langer and J. P. Vacanti, “Tissue engineering,” *Science (80-.)*, vol. 260, no. 5110, pp. 920–926, 1993.
- [63] J. A. Hubbell, “Biomaterials in tissue engineering,” *Bio/Technology*, vol. 13, no. 6, pp. 565–576, 1995.
- [64] S. J. Hollister, “Porous scaffold design for tissue engineering,” *Nat. Mater.*, vol. 4, no. 7, pp. 518–524, 2005.
- [65] P. K. Chandra, S. Soker, and A. Atala, *Tissue engineering: current status and future perspectives*. INC, 2020.
- [66] D. Howard, L. D. Buttery, K. M. Shakesheff, and S. J. Roberts, “Tissue engineering: Strategies, stem cells and scaffolds,” *J. Anat.*, vol. 213, no. 1, pp. 66–72, 2008.
- [67] S. V. Murphy and A. Atala, “3D bioprinting of tissues and organs,” *Nat. Biotechnol.*, vol. 32, no. 8, pp. 773–785, 2014.
- [68] C. Mota, S. Camarero-Espinosa, M. B. Baker, P. Wieringa, and L. Moroni, “Bioprinting: From Tissue and Organ Development to in Vitro Models,” *Chem. Rev.*, 2020.

- [69] C. F. Guimarães, L. Gasperini, A. P. Marques, and R. L. Reis, “The stiffness of living tissues and its implications for tissue engineering,” *Nat. Rev. Mater.*, vol. 5, no. 5, pp. 351–370, 2020.
- [70] A. C. Fonseca *et al.*, “Emulating Human Tissues and Organs: A Bioprinting Perspective Toward Personalized Medicine,” *Chem. Rev.*, 2020.
- [71] X. Ma *et al.*, “3D bioprinting of functional tissue models for personalized drug screening and in vitro disease modeling,” *Adv. Drug Deliv. Rev.*, vol. 132, pp. 235–251, 2018.
- [72] S. V. Murphy, P. De Coppi, and A. Atala, “Opportunities and challenges of translational 3D bioprinting,” *Nat. Biomed. Eng.*, vol. 4, no. 4, pp. 370–380, 2020.
- [73] S. Mehrotra, J. C. Moses, A. Bandyopadhyay, and B. B. Mandal, “3D Printing/Bioprinting Based Tailoring of in Vitro Tissue Models: Recent Advances and Challenges,” *ACS Appl. Bio Mater.*, vol. 2, no. 4, pp. 1385–1405, 2019.
- [74] L. Papadimitriou, P. Manganas, A. Ranella, and E. Stratakis, “Biofabrication for neural tissue engineering applications,” *Mater. Today Bio*, vol. 6, no. January, p. 100043, 2020.
- [75] Y. S. Zhang, M. Duchamp, R. Oklu, L. W. Ellisen, R. Langer, and A. Khademhosseini, “Bioprinting the Cancer Microenvironment,” *ACS Biomater. Sci. Eng.*, vol. 2, no. 10, pp. 1710–1721, 2016.
- [76] Y. Kang, P. Datta, S. Shanmughapriya, and I. T. Ozbolat, “3D Bioprinting of Tumor Models for Cancer Research,” *ACS Appl. Bio Mater.*, vol. 3, no. 9, pp. 5552–5573, 2020.
- [77] A. K. Miri, A. Khalilpour, B. Cecen, S. Maharjan, S. R. Shin, and A. Khademhosseini, “Multiscale bioprinting of vascularized models,” *Biomaterials*, vol. 198, no. August 2018, pp. 204–216, 2019.
- [78] C. Mandrycky, Z. Wang, K. Kim, and D. H. Kim, “3D bioprinting for engineering complex tissues,” *Biotechnol. Adv.*, vol. 34, no. 4, pp. 422–434, 2016.
- [79] B. Guilloin *et al.*, “Laser assisted bioprinting of engineered tissue with high cell density and microscale organization,” *Biomaterials*, vol. 31, no. 28, pp. 7250–7256, 2010.
- [80] F. Guillemot *et al.*, “High-throughput laser printing of cells and biomaterials for tissue engineering,” *Acta Biomater.*, vol. 6, no. 7, pp. 2494–2500, 2010.
- [81] H. S. Santana *et al.*, “Microfluidic Devices and 3D Printing for Synthesis and Screening of Drugs and Tissue Engineering,” *Ind. Eng. Chem. Res.*, vol. 59, no. 9, pp. 3794–3810, 2020.
- [82] T. J. Ober, D. Foresti, and J. A. Lewis, “Active mixing of complex fluids at the microscale,” *Proc. Natl. Acad. Sci. U. S. A.*, vol. 112, no. 40, pp. 12293–12298, 2015.
- [83] H. Clevers, “Modeling Development and Disease with Organoids,” *Cell*, vol. 165, no. 7, pp. 1586–1597, 2016.
- [84] M. A. Lancaster and J. A. Knoblich, “Organogenesis in a dish: Modeling development and disease using organoid technologies,” *Science (80-.)*, vol. 345, no. 6194, 2014.
- [85] M. A. Lancaster and M. Huch, “Disease modelling in human organoids,” *DMM Dis. Model. Mech.*, vol. 12, no. 7, 2019.
- [86] D. Dutta, I. Heo, and H. Clevers, “Disease Modeling in Stem Cell-Derived 3D Organoid Systems,” *Trends Mol. Med.*, vol. 23, no. 5, pp. 393–410, 2017.
- [87] X. Li *et al.*, “Oncogenic transformation of diverse gastrointestinal tissues in primary organoid culture,” *Nat. Med.*, vol. 20, no. 7, pp. 769–777, 2014.
- [88] J. T. Neal *et al.*, “Organoid Modeling of the Tumor Immune Microenvironment,” *Cell*, vol. 175, no. 7, pp. 1972–1988.e16, 2018.
- [89] Y.-H. Lo, K. Karlsson, and C. J. Kuo, “Applications of organoids for cancer biology and precision medicine,” *Nat. Cancer*, vol. 1, no. 8, pp. 761–773, 2020.
- [90] J. Drost and H. Clevers, “Organoids in cancer research,” *Nat. Rev. Cancer*, vol. 18, no. 7, pp. 407–418, 2018.
- [91] P. K. Chaudhuri, B. C. Low, and C. T. Lim, “Mechanobiology of Tumor Growth,” *Chem. Rev.*, vol. 118, no. 14, pp. 6499–6515, 2018.
- [92] K. Bhadriraju and C. S. Chen, “Engineering cellular microenvironments to improve cell-based drug testing,” *Drug Discov. Today*, vol. 7, no. 11, pp. 612–620, 2002.
- [93] G. M. Whitesides, “The origins and the future of microfluidics,” *Nature*, vol. 442, no. 7101, pp.

- 368–73, 2006.
- [94] Y. Shin *et al.*, “Microfluidic assay for simultaneous culture of multiple cell types on surfaces or within hydrogels,” *Nat. Protoc.*, vol. 7, no. 7, pp. 1247–59, 2012.
- [95] D. C. Duffy, J. C. McDonald, O. J. A. Schueller, and G. M. Whitesides, “Rapid prototyping of microfluidic systems in poly(dimethylsiloxane),” *Anal. Chem.*, vol. 70, no. 23, pp. 4974–4984, 1998.
- [96] B. A. Aguado, J. C. Grim, A. M. Rosales, J. J. Watson-Capps, and K. S. Anseth, “Engineering precision biomaterials for personalized medicine,” *Sci. Transl. Med.*, vol. 10, no. 424, 2018.
- [97] G. M. Whitesides, E. Ostuni, X. Jiang, and D. E. Ingber, “Soft Lithography in Biology,” *Annu. Rev. Biomed. Eng.*, vol. 3, pp. 335–73, 2001.
- [98] J. C. McDonald and G. M. Whitesides, “Poly(dimethylsiloxane) as a material for fabricating microfluidic devices,” *Acc. Chem. Res.*, vol. 35, no. 7, pp. 491–499, 2002.
- [99] D. Qin, Y. Xia, and G. M. Whitesides, “Soft lithography for micro- and nanoscale patterning,” *Nat. Protoc.*, vol. 5, no. 3, pp. 491–502, 2010.
- [100] R. D. Kamm *et al.*, “Perspective: The promise of multi-cellular engineered living systems,” *APL Bioeng.*, vol. 2, no. 4, p. 040901, 2018.
- [101] A. Malandrino, R. D. Kamm, and E. Moeendarbary, “In Vitro Modeling of Mechanics in Cancer Metastasis,” *ACS Biomater. Sci. Eng.*, vol. 4, no. 2, pp. 294–301, 2018.
- [102] Y. S. Zhang, Y. N. Zhang, and W. Zhang, “Cancer-on-a-chip systems at the frontier of nanomedicine,” *Drug Discov. Today*, vol. 22, no. 9, pp. 1392–1399, 2017.
- [103] R. Portillo-Lara and N. Annabi, “Microengineered cancer-on-a-chip platforms to study the metastatic microenvironment,” *Lab Chip*, vol. 16, no. 21, pp. 4063–4081, 2016.
- [104] A. Pavesi *et al.*, “A 3D microfluidic model for preclinical evaluation of TCR-engineered T cells against solid tumors,” *JCI insight*, vol. 2, no. 12, pp. 1–18, 2017.
- [105] G. Adriani, A. Pavesi, A. T. Tan, A. Bertolotti, J. P. Thiery, and R. D. Kamm, “Microfluidic models for adoptive cell-mediated cancer immunotherapies,” *Drug Discov. Today*, vol. 21, no. 9, pp. 1472–1478, 2016.
- [106] A. R. Aref *et al.*, “3D microfluidic *ex vivo* culture of organotypic tumor spheroids to model immune checkpoint blockade,” *Lab Chip*, 2018.
- [107] R. W. Jenkins *et al.*, “Ex vivo profiling of PD-1 blockade using organotypic tumor spheroids,” *Cancer Discov.*, vol. 8, no. 2, pp. 196–215, 2018.
- [108] F. Zheng, F. Fu, Y. Cheng, C. Wang, Y. Zhao, and Z. Gu, “Organ-on-a-Chip Systems: Microengineering to Biomimic Living Systems,” *Small*, vol. 12, no. 17, pp. 2253–2282, 2016.
- [109] B. Zhang and M. Radisic, “Organ-on-A-chip devices advance to market,” *Lab Chip*, vol. 17, no. 14, pp. 2395–2420, 2017.
- [110] M. M. Alvarez *et al.*, “Emerging Trends in Micro- and Nanoscale Technologies in Medicine: From Basic Discoveries to Translation,” *ACS Nano*, vol. 11, no. 6, pp. 5195–5214, 2017.
- [111] H. Im, K. Lee, R. Weissleder, H. Lee, and C. M. Castro, “Novel nanosensing technologies for exosome detection and profiling,” *Lab Chip*, vol. 17, no. 17, pp. 2892–2898, 2017.
- [112] J. Laurent *et al.*, “Convergence of microengineering and cellular self-organization towards functional tissue manufacturing,” *Nat. Biomed. Eng.*, vol. 1, no. 12, pp. 939–956, 2017.
- [113] A. Deglincerti, G. F. Croft, L. N. Pietila, M. Zernicka-Goetz, E. D. Siggia, and A. H. Brivanlou, “Self-organization of the in vitro attached human embryo,” *Nature*, vol. 533, no. 7602, pp. 251–254, 2016.
- [114] S. P. Herbert and D. Y. R. Stainier, “Molecular control of endothelial cell behaviour during blood vessel morphogenesis,” *Nat. Rev. Mol. Cell Biol.*, vol. 12, no. 9, pp. 551–564, 2011.
- [115] L. Lamallice, F. Le Boeuf, and J. Huot, “Endothelial cell migration during angiogenesis,” *Circ. Res.*, vol. 100, no. 6, pp. 782–794, 2007.
- [116] R. H. Adams and K. Alitalo, “Molecular regulation of angiogenesis and lymphangiogenesis,” *Nat. Rev. Mol. Cell Biol.*, vol. 8, no. 6, pp. 464–478, 2007.
- [117] S. Rafii, J. M. Butler, and B. Sen Ding, “Angiocrine functions of organ-specific endothelial cells,”

- Nature*, vol. 529, no. 7586, pp. 316–325, 2016.
- [118] J. M. Butler, H. Kobayashi, and S. Rafii, “Instructive role of the vascular niche in promoting tumour growth and tissue repair by angiocrine factors,” *Nat. Rev. Cancer*, vol. 10, no. 2, pp. 138–146, 2010.
- [119] B. Ghesquière, B. W. Wong, A. Kuchnio, and P. Carmeliet, “Metabolism of stromal and immune cells in health and disease,” *Nature*, vol. 511, no. 7508, pp. 167–176, 2014.
- [120] P. Carmeliet and R. K. Jain, “Molecular mechanisms and clinical applications of angiogenesis,” *Nature*, vol. 473, no. 7347, pp. 298–307, 2011.
- [121] Z. Zhao, A. R. Nelson, C. Betsholtz, and B. V. Zlokovic, “Establishment and Dysfunction of the Blood-Brain Barrier,” *Cell*, vol. 163, no. 5, pp. 1064–1078, 2015.
- [122] D. Lambrechts *et al.*, “Phenotype molding of stromal cells in the lung tumor microenvironment,” *Nat. Med.*, vol. 24, no. 8, pp. 1277–1289, 2018.
- [123] M. Campisi, C. Voena, I. Mota, E. Patrucco, R. D. Kamm, and R. Chiarle, “Abstract PO-17: Microphysiologic model of ALK+ anaplastic large cell lymphoma and vascular interactions predicts drug efficacy in a 3D microfluidic chip,” *Blood Cancer Discov.*, vol. 1, no. 3 Supplement, p. PO-17 LP-PO-17, Nov. 2020.
- [124] N. K. Altorki *et al.*, “The lung microenvironment: an important regulator of tumour growth and metastasis,” *Nat. Rev. Cancer*, vol. 19, no. 1, pp. 9–31, 2019.
- [125] K. C. Valkenburg, A. E. De Groot, and K. J. Pienta, “Targeting the tumour stroma to improve cancer therapy,” *Nat. Rev. Clin. Oncol.*, vol. 15, no. 6, pp. 366–381, 2018.
- [126] Y. Huang, B. Y. S. Kim, C. K. Chan, S. M. Hahn, I. L. Weissman, and W. Jiang, “Improving immune–vascular crosstalk for cancer immunotherapy,” *Nat. Rev. Immunol.*, vol. 18, p. 195, Jan. 2018.
- [127] K. Haase and D. Roger Kamm, “Advances in on-chip vascularization,” *Regen. Med.*, vol. 12, pp. 285–302, 2017.
- [128] S. Kim, W. Kim, S. Lim, and J. S. Jeon, “Vasculature-on-a-chip for in vitro disease models,” *Bioengineering*, vol. 4, no. 1, 2017.
- [129] A. Hasan *et al.*, “Microfluidic techniques for development of 3D vascularized tissue,” *Biomaterials*, vol. 35, no. 26, pp. 7308–7325, 2014.
- [130] M. B. Chen, J. A. Whisler, J. Fröse, C. Yu, Y. Shin, and R. D. Kamm, “On-chip human microvasculature assay for visualization and quantification of tumor cell extravasation dynamics,” *Nat. Protoc.*, vol. 12, no. 5, pp. 865–880, May 2017.
- [131] A. Sobrino *et al.*, “3D microtumors in vitro supported by perfused vascular networks,” *Sci. Rep.*, vol. 6, no. July, pp. 1–11, 2016.
- [132] D. Caballero, S. M. Blackburn, M. De Pablo, J. Samitier, and L. Albertazzi, “Tumour-vessel-on-a-chip models for drug delivery,” *Lab Chip*, vol. 17, no. 22, pp. 3760–3771, 2017.
- [133] Y. T. Ho, G. Adriani, S. Beyer, P. T. Nhan, R. D. Kamm, and J. C. Y. Kah, “A Facile Method to Probe the Vascular Permeability of Nanoparticles in Nanomedicine Applications,” *Sci. Rep.*, vol. 7, no. 1, pp. 1–13, 2017.
- [134] C. Kim, J. Kasuya, J. Jeon, S. Chung, and R. D. Kamm, “A quantitative microfluidic angiogenesis screen for studying anti-angiogenic therapeutic drugs,” *Lab Chip*, vol. 15, no. 1, pp. 301–310, 2015.
- [135] Y. Shin *et al.*, “In vitro 3D collective sprouting angiogenesis under orchestrated ANG-1 and VEGF gradients,” *Lab Chip*, vol. 11, no. 13, pp. 2175–2181, 2011.
- [136] G. S. Jeong *et al.*, “Sprouting angiogenesis under a chemical gradient regulated by interactions with an endothelial monolayer in a microfluidic platform,” *Anal. Chem.*, vol. 83, no. 22, pp. 8454–8459, 2011.
- [137] N. Kosyakova *et al.*, “Differential functional roles of fibroblasts and pericytes in the formation of tissue-engineered microvascular networks in vitro,” *npj Regen. Med.*, vol. 5, no. 1, 2020.
- [138] X. Wang, D. T. T. Phan, A. Sobrino, S. C. George, C. C. W. Hughes, and A. P. Lee, “Engineering anastomosis between living capillary networks and endothelial cell-lined microfluidic channels,”

- Lab Chip*, vol. 16, no. 2, pp. 282–290, 2016.
- [139] S. Kim, H. Lee, M. Chung, and N. L. Jeon, “Engineering of functional, perfusable 3D microvascular networks on a chip,” *Lab Chip*, vol. 13, no. 8, pp. 1489–1500, 2013.
- [140] J. A. Whisler, M. B. Chen, and R. D. Kamm, “Control of perfusable microvascular network morphology using a multiculture microfluidic system,” *Tissue Eng. - Part C Methods*, vol. 20, no. 7, pp. 543–552, 2014.
- [141] M. B. Chen, J. A. Whisler, J. Fröse, C. Yu, Y. Shin, and R. D. Kamm, “On-chip human microvasculature assay for visualization and quantification of tumor cell extravasation dynamics,” *Nat. Protoc.*, vol. 12, no. 5, pp. 865–880, 2017.
- [142] M. B. Chen, J. A. Whisler, J. S. Jeon, and R. D. Kamm, “Mechanisms of tumor cell extravasation in an in vitro microvascular network platform,” *Integr. Biol.*, vol. 5, no. 10, pp. 1262–1271, Oct. 2013.
- [143] A. Boussommier-Calleja, Y. Atiyas, K. Haase, M. Headley, C. Lewis, and R. D. Kamm, “The effects of monocytes on tumor cell extravasation in a 3D vascularized microfluidic model,” *Biomaterials*, vol. 198, pp. 180–193, 2019.
- [144] A. Sobrino *et al.*, “3D microtumors in vitro supported by perfused vascular networks,” *Sci. Rep.*, vol. 6, no. August, pp. 1–11, 2016.
- [145] E. Blanco, H. Shen, and M. Ferrari, “Principles of nanoparticle design for overcoming biological barriers to drug delivery,” *Nat. Biotechnol.*, vol. 33, no. 9, pp. 941–951, 2015.
- [146] O. S. Fenton, K. N. Olafson, P. S. Pillai, M. J. Mitchell, and R. Langer, “Advances in Biomaterials for Drug Delivery,” *Adv. Mater.*, vol. 30, no. 29, pp. 1–29, 2018.
- [147] T. C. Roberts, R. Langer, and M. J. A. Wood, “Advances in oligonucleotide drug delivery,” *Nat. Rev. Drug Discov.*, vol. 19, no. 10, pp. 673–694, 2020.
- [148] 7
- [149] J. Wolfram and M. Ferrari, “Clinical cancer nanomedicine,” *Nano Today*, vol. 25, pp. 85–98, 2019.
- [150] W. Poon, B. R. Kingston, B. Ouyang, W. Ngo, and W. C. W. Chan, “A framework for designing delivery systems,” *Nat. Nanotechnol.*, vol. 15, no. 10, pp. 819–829, 2020.
- [151] M. E. Davis, Z. Chen, and D. M. Shin, “Nanoparticle therapeutics: An emerging treatment modality for cancer,” *Nat. Rev. Drug Discov.*, vol. 7, no. 9, pp. 771–782, 2008.
- [152] R. A. Petros and J. M. Desimone, “Strategies in the design of nanoparticles for therapeutic applications,” *Nat. Rev. Drug Discov.*, vol. 9, no. 8, pp. 615–627, 2010.
- [153] L. Sercombe, T. Veerati, F. Moheimani, S. Y. Wu, A. K. Sood, and S. Hua, “Advances and challenges of liposome assisted drug delivery,” *Front. Pharmacol.*, vol. 6, no. DEC, pp. 1–13, 2015.
- [154] R. Karnik *et al.*, “Microfluidic platform for controlled synthesis of polymeric nanoparticles,” *Nano Lett.*, vol. 8, no. 9, pp. 2906–2912, 2008.
- [155] A. Zielinska *et al.*, “Polymeric Nanoparticles: Production, Characterization, Toxicology and Ecotoxicology,” *Molecules*, vol. 25, no. 16, 2020.
- [156] J. P. Rao and K. E. Geckeler, “Polymer nanoparticles: Preparation techniques and size-control parameters,” *Prog. Polym. Sci.*, vol. 36, no. 7, pp. 887–913, 2011.
- [157] S. Debnath, R. Suresh Kumar, and M. Niranjana Babu, “Ionotropic gelation - A novel method to prepare chitosan nanoparticles,” *Res. J. Pharm. Technol.*, vol. 4, no. 4, pp. 492–495, 2011.
- [158] A. C. Anselmo and S. Mitragotri, “Nanoparticles in the clinic: An update,” *Bioeng. Transl. Med.*, vol. 4, no. 3, pp. 1–16, 2019.
- [159] A. Ahmad, F. Khan, R. K. Mishra, and R. Khan, “Precision Cancer Nanotherapy: Evolving Role of Multifunctional Nanoparticles for Cancer Active Targeting,” *J. Med. Chem.*, vol. 62, no. 23, pp. 10475–10496, 2019.
- [160] B. Yu, X. Zhao, J. L. Lee, and R. J. Lee, “Targeted delivery systems for oligonucleotide therapeutics,” *AAPS J.*, vol. 11, no. 1, pp. 195–203, 2009.
- [161] A. R. Jones and E. V. Shusta, “Blood-brain barrier transport of therapeutics via receptor-

- mediation,” *Pharm. Res.*, vol. 24, no. 9, pp. 1759–1771, 2007.
- [162] A. Flemming, “Autoimmunity: Nanoparticles engineered for antigen-specific immunotherapy,” *Nat. Rev. Drug Discov.*, vol. 15, no. 4, p. 233, 2016.
- [163] R. S. Riley, C. H. June, R. Langer, and M. J. Mitchell, “Delivery technologies for cancer immunotherapy,” *Nat. Rev. Drug Discov.*, vol. 18, no. 3, pp. 175–196, 2019.
- [164] A. M. Grabrucker *et al.*, “Nanoparticle transport across the blood brain barrier,” *Tissue Barriers*, vol. 4, no. 1, 2016.

Section II

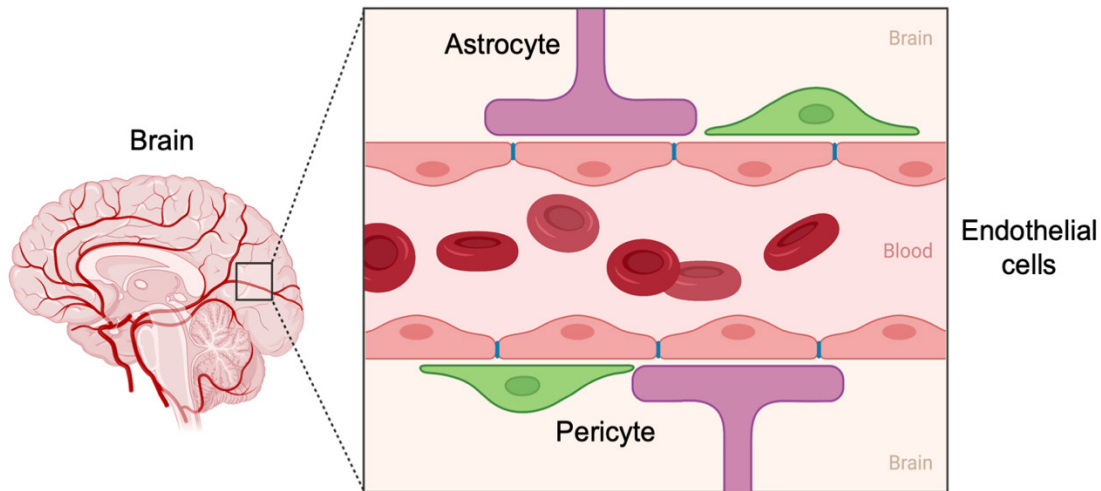
3-D Microphysiological model of the Blood-Brain Barrier

Chapter 3 – Current advances and challenges in the modelling of human Blood-Brain Barrier

Abstract

The blood-brain barrier (BBB) is the first interface between blood circulation and brain tissues and represent the tightest barrier in the human body. The BBB consists of endothelial cells which form tight and adherens junctions, surrounded by brain pericytes and overlapped by astrocytes. Despite BBB main role in maintaining brain homeostasis by controlling solute transit, its protective barrier constitutes a nearly-impenetrable obstacle against therapeutic drug delivery into the brain parenchyma from blood. To date, efficient drug delivery to the brain is restricted and, consequently, treatment strategies and neuro-pharmaceutical development are limited for many brain pathological processes, including neurodegenerative diseases. The lack of reliable preclinical models, able of reproducing human anatomical complexity and predicting molecular mechanisms of drug transport through the BBB, partially contributes to the misleading results in clinical trials. Understanding the different traffic routes adopted by drugs is, therefore, critical in the development of pre-clinical models to test targeted therapies.

In this chapter 3, fundamentals about the structure, components and cellular functions of the BBB are provided, focusing on the main mechanisms of molecule transport through the BBB. Then, innovative drug delivery systems, such as nanoparticles, are presented. Finally, current advances in preclinical BBB design model *in vitro* are discussed focusing on literature examples of BBB models, including organoids, 3D printing and the emerging 3D microphysiological systems using microfluidic technology. Potential opportunities, current challenges and future perspectives on modelling the BBB through *in vitro* preclinical models are further discussed.



Graphical abstract 4: *Modelling the BBB microvasculature.*

Schematic created with biorender.com

Part of the work described in this chapter has been previously published in:

<https://doi.org/10.1002/adhm.201700489>

“In vitro microfluidic models for neurodegenerative disorders”.

September, 2017, *Advanced Healthcare Materials*.

T. Osaki, Y. Shin, V. Sivathanu, **M. Campisi**, R.D. Kamm.

<https://doi.org/10.1063/1.5027118>

“In Vitro Models of Molecular and Nano-Particle Transport across the Blood-Brain Barrier”.

May 2018, *Biomicrofluidics*.

Hajal C., **Campisi M.**, Mattu C., Chiono V. and Kamm R.D

Introduction

Structures and components of the Blood-Brain Barrier

The blood-brain-barrier (BBB) is a highly selective and semipermeable barrier that separates the bloodstream circulation from the neural cells of the central nervous system (CNS), maintains the homeostasis of the brain microenvironment protecting it from pathogens and harmful compounds[1]. BBB is a fundamental anatomic structure present in organisms with a well-developed CNS that regulates ion exchanges and allows the transport of nutrients and oxygen to the brain[2]. In early 1900s, the Nobel Prize Paul Ehrlich firstly reported the discovery of a sort of brain barrier while performing an intravenous injection of an aniline blue, and surprisingly found no staining in the CNS[3]. At that time, this lack of staining was simply attributed to the inability of the brain to absorb the dye. The experiment was repeated by one of his students, Edwin Goldmann, demonstrating a compartmentalization existing between cerebral fluid and vasculature, suggesting the presence of a barrier [4]. A few years later, due to the invention of the electron microscope in the 1960s, the anatomical structure of the BBB was observed and described, followed by increased understanding of its structure and functions [5].

Structurally, BBB is formed by endothelial cells (ECs), pericytes (PCs) and astrocytes (ACs) strongly connected with the main role of conceiving a physical and functional protection regulating the selective active and passive transport that restricts the passage of solutes (Figs. 2.1a, 2.1b).

Cellular components of the human Blood-Brain Barrier

Endothelial cells (ECs) establish the formation of brain capillaries and are the first interface of biotransport exchanges between the bloodstream and the brain[6]. Brain ECs differ from peripheral ECs in several characteristics, such as higher mitochondrial density, higher tight junctions (TJs) proteins and reduced pinocytotic activity[7]. ECs adhesion is characterized by the overlapping of TJs and adherens junctions (AJs) maintaining structural support [8] by a complex system that cover the space between ECs. The TJs are regulated via the intracellular/membrane proteins zonula occludens (ZO) ZO-1, ZO-2 and ZO-3, Claudin 3 and 5, and Occludin. AJs are mediated by VE-cadherin, PECAM-1 and Nectin [7][9]. Therefore, junction efficiency in reducing ion passage

increases exponentially with the number of strands, which is formed by a collection of transmembrane proteins with extracellular domains. Alterations in intra and extra-cellular calcium concentration modulate junction assembly[10]. Junctions provide structural integrity and adhesion between cells and regulate transport mechanisms[11]. Both TJs and AJs are responsible for restriction of the paracellular diffusional pathway to ions and other polar solutes, and effectively block diffusion of macromolecules[12]. ECs also allow a rapid diffusion of oxygen and carbon dioxide[13]. The resistance to ions exchanges is due to high trans-endothelial electrical resistance and low paracellular conductance [14]. Moreover, neuronal cells release vasoactive agents and cytokines, modifying barrier permeability, the expression and formation of junctional processes [15][16]. It has been demonstrated that TJ expression might be induced by the use in culture of conditioned medium from pericytes and astrocytes[17][18] . On the other hand, disruption of TJs is generally correlated to BBB breakdown [19] and associated with brain disorders which may cause alterations in the expression or loss of TJs and AJs [20].

Pericytes (PCs) are vascular mural cells and embedded in the basement membrane of the blood vessels enveloping brain microvessels [21]. PCs play an important role in the formation of a permeable interface between the circulatory system and CNS [19]. PCs coordinate and process signals from their neighboring cells, regulate vascular permeability, BBB integrity, and are involved in BBB formation during embryogenesis[22]. PCs express several contractile and cytoskeletal proteins (for example, α -smooth muscle actin, vimentin, desmin, myosin) and cell surface antigens (Platelet-derived growth factor receptor beta (PDGFRB)), cluster of differentiation 145, (CD146))[23] in the cytoplasmic membrane[21][24]. They inhibit vascular permeability and coordinate signaling in cooperation with ACs[25]. PCs contribute to the formation and alignment of TJs, play an active role in regulating angiogenesis and controlling the flow within blood capillaries and the brain [6][15], and also mediate leukocyte adhesion and transmigration into the CNS[26][27]. Furthermore, PCs effectively lead clearance of tissues debris and proteins released by neighboring cells, as well as neurotoxins[28][33]. However, their degeneration might causes BBB breakdown and accumulations of neurotoxins[15], causing synaptic dysfunction and neuronal injury [45]. Moreover, a PCs dysfunction also contributes to neurodegenerative diseases such as Alzheimer's and Parkinson's diseases through the breakdown of the BBB, or related to contractile issues of brain microvessels[29] [30] [31].

Astrocytes (ACs), also known as glial cells, are star-shaped cells localized in close contact with the abluminal surface of BBB vessels [32]. The ACs endfeet provide biochemical support for those cells that form the neurovasculature through the production of cytokines, neutrophic factors and angiopoietin-1 that helps maintain the TJs[17], and contribute into modulate the expression of transport receptors and transcytosis in the ECs [16][33]. ACs endfeet envelop neuron synapses modulating the synaptic transmission, vasoconstriction and dilatation of brain capillaries[34], and maintaining BBB integrity[35], as well produce isoforms of laminin found into parenchymal basal membrane[36]. Activated ACs are important regulators of brain inflammation, involved in the pathogenesis of many neurodegenerative diseases[37] [35], [38], but seems not to be involved in BBB vascular permeability regulation[39]. Around brain capillaries, there is some space between ECs and neurons forming the perivascular space[40], also called Virchow-Robin space, fluid-filled in which perivascular immune cells such as macrophages engage the immune surveillance of the CNS[41].The BBB includes two different basement membranes layers [25][42]. Separately, ECs secrete the endothelial basal membrane that incorporates ECs and PCs, and ACs secrete the parenchymal basement membrane that separates ACs from blood vessels[43]. In close contact with the BBB, in the brain microenvironment, there are proteins of the extracellular matrix (ECM). Key ECM components are: several isoform of laminins glycoproteins, collagen type IV, nidogen, fibronectin, and heparin sulfate proteoglycans [42] (Fig. 2.1c). The ECM forms a matrix network of proteins that support and mediate cellular activities and signaling [44]. ECM proteins possess natural ligands for cell surface receptors, such as integrins [45]. Receptor-ligand binding induces cell signaling pathways on vascular endothelium and mediates mechano-transduction to the cytoskeleton[46], and represent a target for numerous diseases [47]. Hereupon, ECM molecules are relevant in healthy and diseased human tissue modelling to mimic and reproduce physiologically-relevant microenvironment *in vitro* [48].

Functions and regulation of the Blood-Brain Barrier

The physiological function of BBB is coordinated by a series of physical, transport and metabolic properties. This anatomic structure preserves brain homeostasis, regulates influx and efflux transport, exchanges molecules and ions, and protects from exogenous harmful compounds[42]. BBB also regulates cell trafficking and supplies nutrients to the brain, which is the most metabolically active organ in the body. In addition to providing a stable environment for brain

functions, BBB also maintains molecules exchange and optimal ionic composition for synaptic signaling by a sequence of specific ionic channels and transporters [38]. BBB provides a regulated impermeable interface and it has low passive permeability to many essential water-soluble nutrients and metabolites required by nervous tissue[2] [58].

The main BBB function is to act as a barrier to prevent inflammatory insults and pathogens from one of the most immunologically susceptible organs[30][49], as well monitoring alterations of the inflammatory processes due to the local microenvironment changes (immunosurveillance)[50]. Indeed, infections in the brain are very rare. However, when the brain is affected by an infection, the treatment is very difficult: only few antibiotics are able to pass through the BBB, while most of them cannot reach the brain due to their relatively high molecular weight. In some cases, antibiotics need to be administered into CNS directly into the cerebrospinal fluid (CSF), where they can enter the brain by crossing the blood-cerebrospinal barrier and the BBB [51] (Fig. 2.1d). BBB also plays an essential role in molecules transport and ion regulation. It contributes to preserve the brain from neurotoxins and prevents plasmatic macromolecules, such as albumin, prothrombin and plasminogen [1], from easily entering into the brain [52]. These macromolecules may damage nervous tissue causing cellular activation and leading to apoptosis[53], in addition to contributing to greater vascular permeability[54]. BBB permeability is also affected during inflammation, when it becomes more permeable, allowing some antibiotics and immune cells to move through the BBB to the brain; as an outcome it can also allow unwanted viruses and bacteria to penetrate the brain.

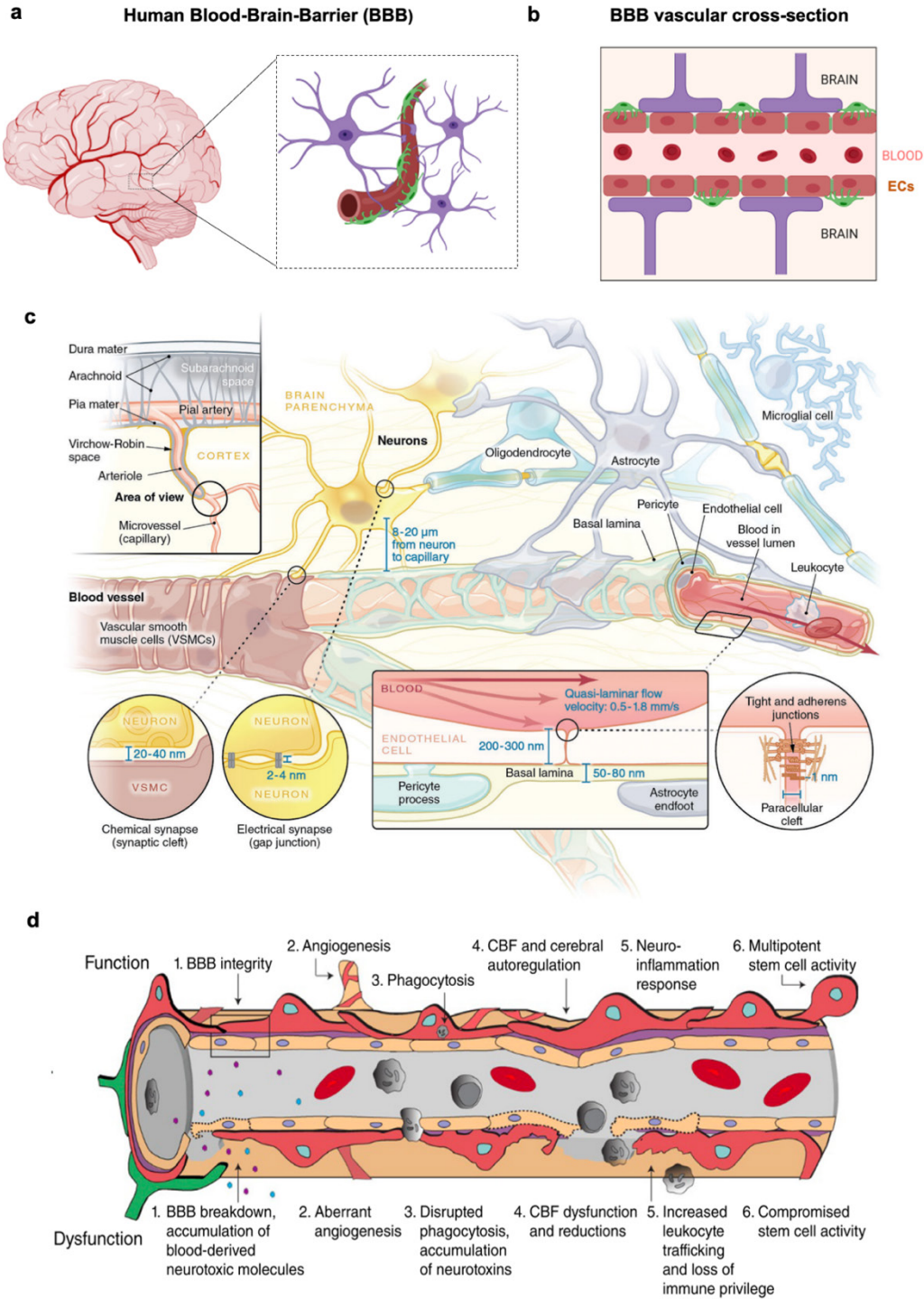


Figure 2.1: Structure, functions and transport mechanisms of the Blood-Brain Barrier.

a) Schematic of the human BBB composed of brain Endothelial cells (ECs), capillary overlapped by brain pericytes (PCs, green) and astrocytes (ACs, violet) endfeet and **b)** Schematic of BBB vascular cross-section. **c)** Schematic of the brain microenvironment and cross-talk between cells. Reproduced with permission from [55] **d)** Functions of the BBB during health and disease states. Reproduced with permission from [19]. Schematics created with BioRender.com

Transport mechanisms across the Blood-Brain Barrier

In order to design innovative drug delivery strategies to cross the BBB and enter the brain, it is fundamental to unveil the different types of ECs membrane transporters and their classifications[56]. The brain is a delicate organ which BBB protects from harmful compounds and precisely controls its microenvironment. However, the same mechanisms represent a stringent hurdle in the development of efficient therapeutics treating the brain. Design of drugs targeting the cellular pathways across an intact BBB is an unsolved medical need for many neurological disorders and an improved understanding of the blood-brain interfaces may provide novel and more effective strategies to treat CNS pathologies [56]–[58].

The main factors that restrict the passage of drugs through the BBB are its molecular weight and composition. Compounds with a high polar surface area that can form more than 6 hydrogen bonds need high free energy to cross the cell lipid membrane from the aqueous phase[59]. Computational *in silico* predictions of BBB permeability have demonstrated that an increase number of rotatable bonds is associated with reduced BBB permeability[60]. Rotatable bonds are defined as any single bond, not in a ring bound to a non-terminal heavy (i.e., non-hydrogen) atom[61]. Compounds with many rotatable bonds might have a more complex structure and undergo potential conformational changes in molecular shapes that would reduce their BBB permeability. Moreover, compounds with affinity for plasma proteins present in the blood are not able to penetrate through the BBB [62][63]. *In silico* and *in vitro* predictions suggest that lipophilic and cationic molecules may cross BBB more easily than anionic molecules due to their ability to interact with the negatively charged phospholipid heads of cells [59][64]. As the brain is shielded from many essential nutrients, the BBB endothelium contains several specific solute carriers (transporters) to supply glucose and amino acids to the brain compartment [59].

The knowledge of physiological mechanisms on transmembrane passage of substances across the BBB allows the design of efficient drug carriers [65]–[67]. Most brain cells are located far less than 25 μm from capillaries, so once the BBB has been crossed, the diffusion of drugs or nanocarriers to neurons and glial cell bodies is fully accessible [68]. In general, diffusion and transcellular bidirectional transport across the BBB can be classified into five main categories: passive diffusion, active efflux transport, carrier-mediated transport, ion transport and receptor-mediated transport (Fig. 2.2a).

Passive diffusion is an energy-independent process triggered by concentration gradients that allows blood gasses, such as oxygen and carbon dioxide, to cross the BBB [60]. Furthermore, many lipid-soluble molecules and non-polar molecules can diffuse through the BBB cell membrane, cross the endothelium and passively enter the brain. There is a positive correlation between the lipid solubility of the solute and the rate at which it enters to the CNS [13].

Active efflux transport may intercept some of the penetrating lipids that enter the brain by passive diffusion and pump them out of the ECs. Many substances are actively pumped out of the brain capillaries forming the BBB by efflux pumps called ABC transporters (ATP-binding cassette family), that actively (by consuming ATP) transport a diverse range of lipid-soluble molecules out of the CNS. ABC transporters carry out a vital neuroprotective and detoxifying function by removing potentially neurotoxic endogenous or xenobiotic molecules [69]. There are several ABC transporters in human brain (they are a family of 48 proteins), some of which have been found throughout the body. The MDR1-encoded multidrug resistance transporter P-glycoprotein (P-GP) is an ATP-dependent efflux pump that intercepts many solutes and mediates rapid removal of toxic lipophilic metabolites that have been ingested, like many amphipathic cationic drugs, ultimately associated with drug resistance. In addition to PG-P, several multidrug resistance-associated proteins (MRPs) are expressed in brain capillaries. MRPs regulate the efflux of anionic compounds and include a breast cancer resistance protein (BCRP), the organic anion transporting polypeptide (OATP) family and the organic anion transporter (OAT) family. P-GP and BCRP are strategically placed in the luminal membrane of the BBB [4]. These transporters have also been found in PCs and ACs and work together to reduce the transport of many drugs and increase their efflux from the brain[70][71]. MRPs are inserted in either luminal or abluminal membranes, with some species differences between humans and animals, in both the polarity and the isoforms of MRPs expressed at the BBB. The ABC family is important for the development of innovative strategies for release of therapeutics to the brain, because many of the current drugs are substrates for these ABC efflux transporters and their brain penetration is significantly reduced by this transport activity. P-GP is fundamental in the transmission to the brain of drugs and compounds, it also affects the permeability of BBB.

Carrier-mediated transport of solute is mediated by transport proteins expressed by ECs specialized to supply a range of essential solutes and nutrients, such as glucose, galactose; neutral, basic, and acidic amino acids and monocarboxylic acids (ketone bodies); nucleotides, vitamins,

fatty acids and hormones. Specifically, carrier-mediated transport systems are regulated by brain metabolic needs, to facilitate the transport of nutrients. Some solute carriers are: GLUT1 (glucose), MCT1 (ketone bodies, such as R-beta-hydroxybutyrate and acetoacetate, which are energy sources for the brain), LAT1 and EAAT1 (amino-acids and sodium dependent systems)[1][4][6][72]. In most cases, vitamins, such as B1, B3, B5, or E are transported through the BBB or choroid plexus by facilitated diffusion. Instead, the sodium-dependent multivitamin transporter facilitate transport of biotin, pantothenic acid, and lipoic acid[73].

Ion transport mechanism plays critical roles in regulating the intracellular pH of blood vessels. ECs and TJs form a continuous hurdle that restricts diffusion of molecules between blood and brain interstitial fluid and vice versa. To allow the transport of ions, the BBB has two main ion transporters: the sodium/potassium pump and the sodium-potassium-two chloride transporter. The sodium pump is located on the abluminal membrane, regulating the sodium influx into the brain ISF in exchange for potassium. Na^+, K^+ -ATPase maintains the high concentration gradient for Na^+ at the BBB (extracellular \gg intracellular), so that Na^+ dependent transport can occur. The high energy demands for active ATP-dependent transporters is due to the high BBB mitochondrial density. The sodium-potassium-two chloride ($\text{Na}^+ - \text{K}^+ - 2\text{Cl}^-$) co-transporter resides predominantly in the luminal BBB, transports sodium, potassium, and chloride from blood to the brain blood vessels. Sodium-hydrogen exchanger is presented on the luminal membrane, whereas chloride-bicarbonate exchanger is showed at each side. The chloride-bicarbonate exchanger also regulates active secretion of bicarbonate through the BBB[74].

Receptor-mediated and adsorptive-mediated transcytosis of high molecular weight molecules across the BBB via endocytosis mechanisms provides the main route by which proteins and peptides can enter into the CNS. Although the majority of large and high molecular weight molecules are physically prevented from entering the brain by the presence of the TJs, specific and some non-specific transcytosis mechanisms exist to transport a variety of large molecules and compounds across the BBB. These vesicular mechanisms contain both receptor-mediated transcytosis (RMT) or adsorptive-mediated transcytosis (AMT). In RMT, macromolecular ligands bind to specific receptors on the cell surface triggering uptake events. Both the ligand and receptor form a caveolae that is internalized as a vesicle and transported across the cytoplasm through the opposite pole of the cell and released. Dissociation of the ligand and receptor presumably occurs during cellular transit or during the exocytotic event[75]. The adsorptive-mediated transcytosis

(AMT) requires an excess of positive charge and cationic molecules to activate the endocytic pathway. Then, interaction with cell surface binding sites induces endocytosis and subsequent transcytosis [63]. Large proteins such as transferrin, lactoferrin, insulin, low density lipoproteins (LDL), immunoglobulin (IgG) are RMT dependent [64]. RMT transport systems have been adopted as targets for drug delivery to the brain via “Trojan horse” strategy: different agents that normally do not cross the BBB can be conjugated to monoclonal antibodies against one of the BBB receptors (e.g., transferrin or insulin receptors). The monoclonal antibodies therefore act as surrogate ligands and can be used to carry conjugated neurotherapeutics across the BBB [51][76].

a

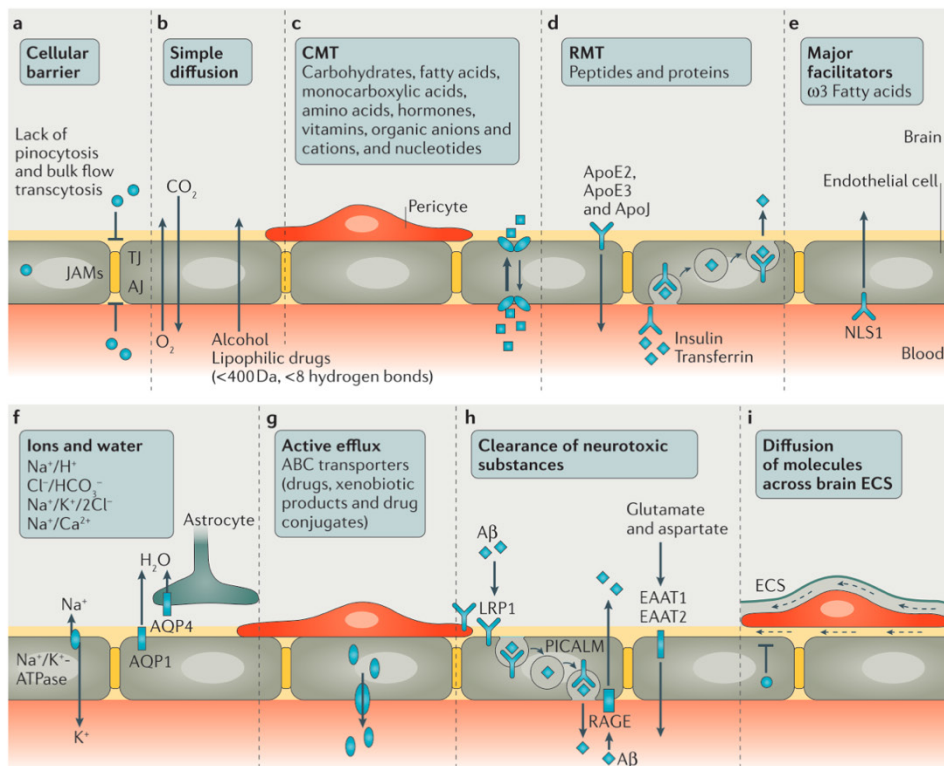


Figure 2.2: Transport mechanisms of the Blood-Brain Barrier.

a) Overview of BBB transport mechanisms. Reproduced with permission from [77].

Blood-Brain Barrier in the pathology of neurological disease

BBB disruption, dysfunction and inflammation are associated with the pathogenesis of most CNS disorders and neurodegenerative diseases. The barrier dysfunction is primarily caused by loss of integrity and enlargement of tight junction and consequently changes in transport systems and accumulation of blood-derived neurotoxic molecules[19]. Indeed, BBB breakdown allows influx of neurotoxic blood-derived contents, cells and microbial pathogens into the brain and is associated with inflammation and immunogenicity, which can initiate multiple pathways of neurodegeneration[78]. Also, abnormal vascular architecture caused by a pathological PCs deficiency[15] [79] might lead to onset forms of neurodegeneration, with a more permeable vasculature with increased leukocyte trafficking, loss of immune privilege and contributing to the disease pathogenesis. Dysfunction in the EC membrane transporters is also correlated with BBB breakdown. Some evidence has shown that ABC transporters are involved in the pathogenesis and treatment of different brain disorders. For example, one-third of patients with epilepsy have drug-resistant epilepsy which is associated with polymorphism in the MDR1 gene [6][4].

Cerebrovascular dysfunction and pathology might contribute to cognitive decline and neuronal damage in Alzheimer's disease, in addition to beta amyloid pathology[29][80], pathogenesis of Parkinson's Disease [81], and traumatic brain injury [82]. Brain cancer and metastasis to the brain are also associated with BBB disruption[83], loss of integrity, abnormal function and dysfunctional blood flow [84]–[86]. The strategies for crossing the BBB to delivery pharmaceutical compounds are totally different in a healthy BBB compared to pathological conditions. In a healthy BBB, drug transport mainly relies on receptor and carrier mediated transport, or combination of advanced nanocarriers with transient opening techniques of the BBB, such as using focused ultrasound. Under pathological conditions, the BBB breakdown enables the accumulation of toxic compounds in the perivascular spaces. These accumulations prevent the normal biodistribution of molecules through the CNS by concentration and gradient-driven diffusion through the extracellular spaces of the brain and interrupt the regional formation of interstitial fluid flow, which prevents therapeutic antibodies, proteins, peptides, gene therapies and other drugs from efficiently reaching their targets.

Nanoparticle as a delivery system across the Blood-Brain Barrier

The design of innovative strategies to deliver therapeutic agents across the BBB has become a major research topic in neuroscience. BBB represents a nearly impenetrable barrier against efficient therapeutics delivery to the CNS, limiting treatment options and drug development against many brain pathologies, including neurodegenerative diseases.

Only few lipophilic small molecules, such as alcohol, caffeine or opioids (morphine, heroin), few analgesics, antibiotics or antipsychotics, typically with a molecular weight below 400-500 Da, have the ability to cross the BBB reaching the CNS by passive or carrier-mediated mechanisms. Some of these molecules are reported here [87].

For example, in Parkinson's disease (PD), a prodrug for dopamine replacement, L-DOPA, is a small molecule that crosses the BBB via neutral amino acid transporter. However, in Alzheimer disease (AD), 98% of small molecule drugs and ~100% of biologic drugs do not cross the BBB, requiring further studies and development [88]. Since the passage of the drugs through the BBB is primarily restricted, several approaches have been applied to allow drugs passage across the BBB, including osmotic disruption of the BBB [87], chemical modification of drugs [89] and nanoparticles-mediated delivery[90].

Nanoparticle (NP) delivery platforms are solid colloidal particles with a size range of 1 – 1000 nm. NPs have also been studied in brain scenario [91], whereby NPs with an effective hydrodynamic diameter of approximately 100 nm are often associated with favorable delivery capabilities [91]–[95]. In fact, the size of NPs is also an important design parameter that defines NP delivery across the BBB. NPs offer many advantages, such as non-invasiveness, low cost, good biodegradability and long-term stability, ease of synthesis, high targeting efficiency and high controllability to load and release drugs throughout the BBB [96]. NPs, due to their small size, tunable properties and ease of surface functionalization, have emerged as solutions to reach relatively inaccessible brain tissue [97]. In terms of drug species, the first drug delivered by NPs to the brain was the hexapeptide dalargin (Tyr-D-Ala-Gly-Phe-Leu-Arg)[98].

To date, drugs delivered with NP carriers have covered peptides [99], proteins[100], nucleic acids [101], antibodies[102] , and anticancer drugs[103] [104]. Several types of NPs have been developed for drug delivery though the BBB [97], including polymeric, lipidic [105] and inorganic materials such as gold, silver and zinc oxide NPs [106]–[108].

Polymeric NPs can be prepared both from natural and synthetic materials[109]. One example is the synthetic polymer poly(butyl cyanoacrylate) (PBCA)[102], which was the first material used for drug delivery to the CNS. Polyesters, such as poly(lactic acid) (PLA), poly(glycolic acid) (PGA), and their copolymer poly(lactic-co-glycolic acid) (PLGA)[110], have been explored for delivering several payloads, such as diagnostic agents [103], nucleotides [111][112], proteins [113] and traditional small molecules to the brain [114]. Therefore, PLGA, PLA or PGA NPs have been classified as biodegradable and have been approved by the U.S. Food and Administration (FDA) and European Medicines Agency (EMA) as effective carriers for drug delivery in humans [109]. Polymeric NPs offer peculiar versatility thanks to their stability, drug encapsulation capabilities and easy production [109], [115], [116]. Several types of polymer NPs with high density of positive charges have been reported to cross the BBB, such as NPs based on Chitosan, a biodegradable and biocompatible polysaccharide [117][118]. Additionally Chitosan NPs have also been applied for delivery of drugs (e.g. dopamine) to the CNS across the BBB, as high dose of dopamine where found in rat striatum [119].

Similar to chitosan, poly(ethylenimines) (PEIs) are a family of cationic polymers that are well-suited for nucleic acid delivery. Recently, PEI nanoparticles surface functionalized with rabies virus glycoprotein (RVG) have been shown to deliver microRNAs to the CNS pre-treated with mannitol to disrupt the BBB for improved delivery[120], [121].

Lipid-based NPs include a large subset of lipidic structures, usually spherical platforms of lipid bilayers[122]. They offer many advantages in terms of simplicity of formulation, biocompatibility and ability to carry large payloads, representing the most common class of FDA approved nanomedicines[123]. Lipid-based NPs, such as liposomes are composed of phospholipids, forming self-assembled mono or multi layered vesicular structures, capable of carrying hydrophilic and hydrophobic drugs[124].

Inorganic materials such as gold, silver and zinc oxide have been also used to prepare NPs with 10-100 nm size. They have unique electrical, magnetic and optical properties that have been applied for *in vivo* diagnostics and therapeutic applications or their combination called “theranostic” [97][124].

The mechanisms of BBB penetration can be divided into active and passive transport. The passive transport does not require energy to move substances through the BBB, as in passive diffusion, which allows the diffusion of small NPs or lipophilic molecules through ECs[87]. On the other

hand, active transport includes receptor- and adsorption-mediated endocytosis and carrier-mediated transport, which require hydrolysis of adenosine triphosphate (ATP)[125] (Fig. 2.3a). Different ligands, proteins and antibodies have been conjugated to NPs in order to decorate its surface and facilitate BBB penetration through active transport mechanisms [116][126]–[130].

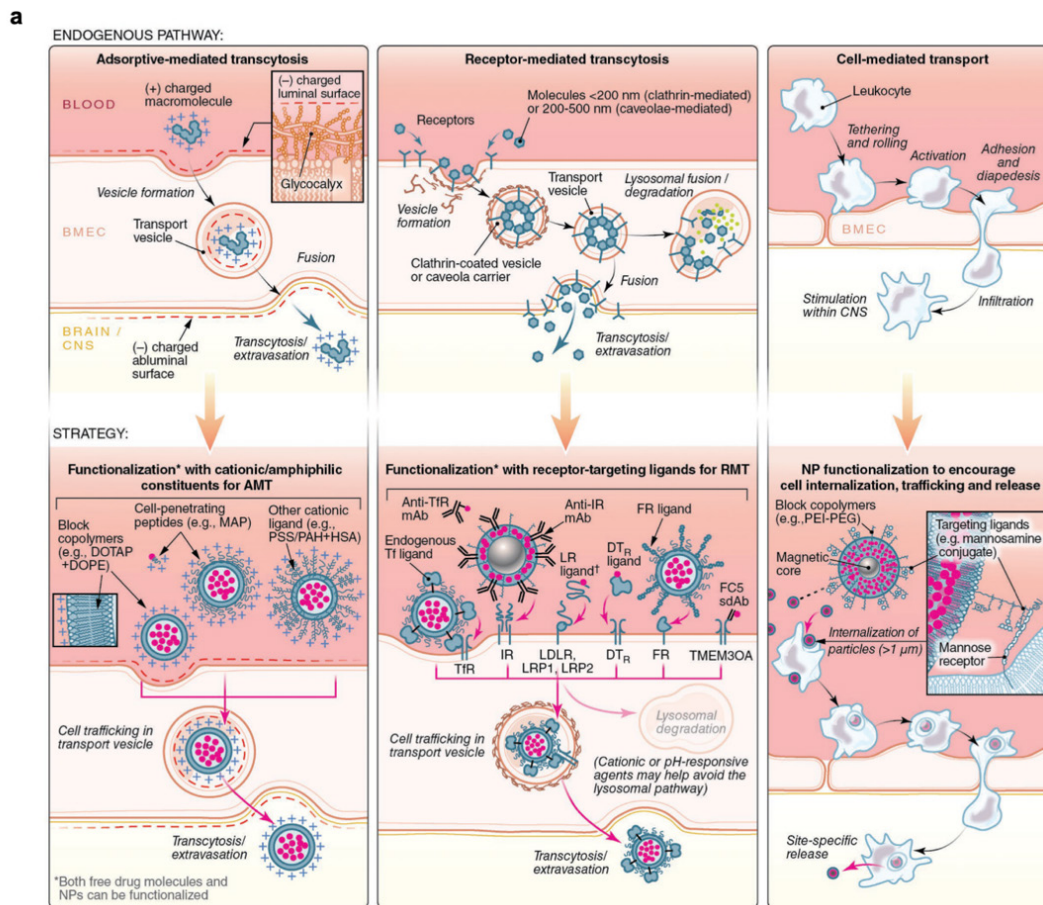


Figure 2.3: Transport mechanisms of the Nanoparticle delivery across the Blood-Brain Barrier. *a)* Overview of drug-delivery strategies to the brain that exploit endogenous pathways across the BBB, including adsorptive-mediated transcytosis (AMT), receptor-mediated transcytosis (RMT), and cell-mediated transport. Drug molecules and NPs can be specifically functionalized to exploit these mechanisms of transport across the BBB. Reproduced with permission from[55].

Most common substrates for BBB receptors include transferrin (Tf) and lactoferrin (Lf) for their specific receptors; low-density lipoproteins, such as ApoE, ApoB and Angiopep-2 for lipoprotein receptors; folic acid for folate receptors (FR); insulin for insulin receptors[55] [131][132]. Moreover, transporters such as Glucose transporter protein (GLUT), LAT1 and P-GP have also been exploited to aid drug delivery to brain [55][133]–[135].

Surface-functionalized NPs act as “Trojan horses” through the use of specific ligands targeting BBB ECs receptors: ligands are bound to drugs or used to decorate NPs [136][137], [138]. However, several neuroactive peptides are already active at low concentrations in the brain. Thus, slow transport rates from blood to the brain may limit the accumulation in the brain interstitial fluid. Among these ligands, Tf has been one of the most widely studied for NP functionalization [139]. The Tf receptor (TfR) regulates iron transport into the brain for iron homeostasis which is important for metabolism, neural conductivity and other general brain functions [140]. The TfR has been one of the primary targets studied for BBB delivery because of its abundant and high expression by the brain endothelium [141], [142]. Numerous research groups have demonstrated the capability of TfR-targeting NPs to improve drug delivery into brain tissue [143]–[149]. Indeed, Tf has proven to be a unique ligand for grafting onto NPs for delivery across BBB [138], [150]–[152].

In vitro and in vivo modelling of the Blood-Brain Barrier for testing nanocarrier transport efficacy

Modelling the human BBB is fundamental to study the physiopathology and biological mechanisms of the brain, the transport of neurological drugs to the brain and its altered permeability during pathological states. Modelling is also important to unveil cellular pathways and drug targets during diseases. From a pharmaceutical perspective, BBB models are tools for the discovery of new drug compounds that are capable of effectively penetrate into the brain. There are two main types of experimental models: *in vitro* and *in vivo* models. Among *in vitro* models, there are two major classes of BBB experimental models: 2D and 3D models[153].

In vitro 2D models, such as 2D petri dish culture, have been used for high-throughput screening to assess toxicology or cytotoxicity and cellular uptake of thousands of novel compounds [154], either to replicate basic features of BBB cells environments to deeply understand cellular mechanisms. Usually, this step does not require a BBB mimic and permeability assay [155][156]. Conventional approaches to assess drug transport studies through the BBB are 3D culture assays called Transwell systems. This system consists of a cylindrical lower compartment, usually a standard well plate of any size between 6-24 wells, where a porous semipermeable membrane (or filter membrane) of different materials is embedded in an insert, which separates the upper

compartment from the lower compartment [36],[103][157]. Transwell has been employed in BBB research to study the permeability of brain ECs monolayer co-cultured with ACs and PCs, both during static or recirculating flow condition [158]. The insert is usually coated with collagen, laminin or hydrogel matrix to mimic the ECM of the microenvironment. At the top of the transwell insert, ECs are grown to create a confluent monolayer. Other cellular components can be cultured in contact with ECs, at the opposite site of the membrane, or in non-contact on the bottom of the well [159]. Several cell sources have been used for transwell cultures, such as primary human cells[160] and other species, such as mice or porcine [156], [161], [162], or stem cells and induced pluripotent stem cells (iPSCs)[163][164][165] (Fig. 2.4a, b).

Advances in the culture system have been made in order to ensure models that are very easy to produce and widely used to evaluate drug transport across the BBB model. Although, these cultures are often too simple and fail to replicate key characteristics of BBB, such as genetic expressions of the brain, shear stress resulting from blood flow and the BBB microenvironment, which makes their predictive value questionable for human responses. While this system is reproducible and easy to use, limitations have occurred in mimicking fundamental BBB features and complexities, such as cell-cell or cell-matrix interactions, compromising its ability to accurately model brain blood vessels in terms of their genetic expression of junctional proteins and membrane transporters. The lack of reproducible alternatives makes transwell systems widely used for target validation and screening of several compounds that will finally be tested in animal models [164].

In vivo animal models, such as mice models, including genetically engineered mice models (GEMM), have traditionally been considered as reliable platforms for evaluating NP delivery and are still considered the gold standard [157]. Even though the *in vivo* model recapitulates the complexity of BBB microenvironment, however, crucial genetic, cellular, immunologic and molecular variations between mice and humans, restraining their ability to reproduce human pathophysiology and their capability to effectively screen for human CNS therapeutics [166]–[168] finally affecting the translational clinical potential.

Mouse models are generally used at the end of the drug discovery pipeline to test and approve 2-5 candidates to be included in a clinical trial. However, despite successful preclinical tests in mice, more than 80% fail in phase I and II clinical trials [155], [169], and only 50% that eventually reach

phase III are approved for clinical use [170]. This emphasizes the lack of tools to test drugs before the clinical trials [171]. Furthermore, costs and ethical constraints also limit their use [172].

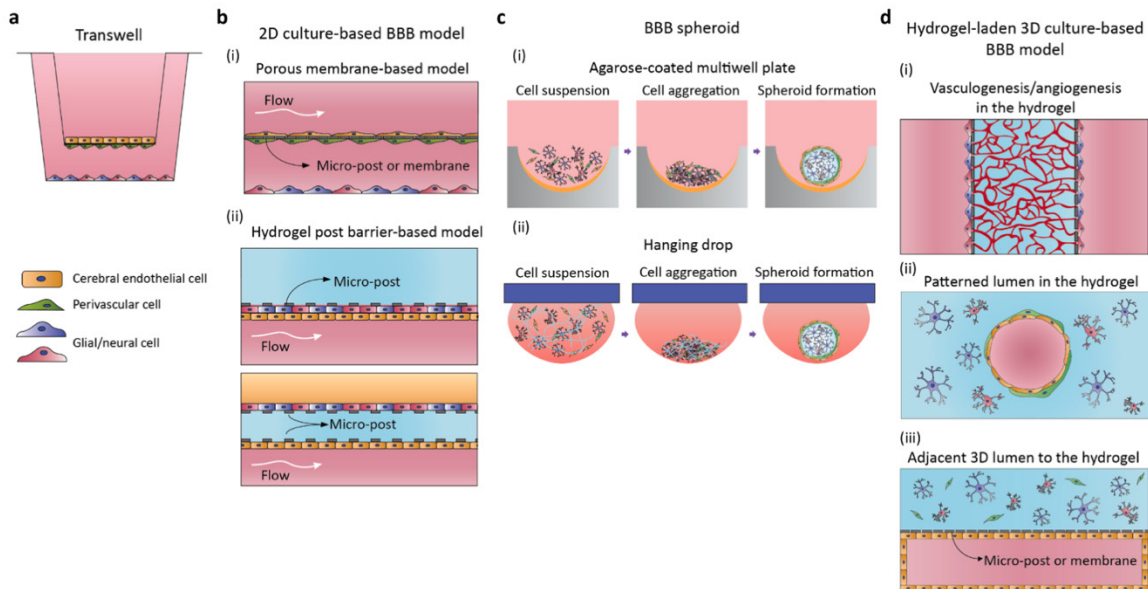


Figure 2.4: *In vitro* models of the Blood-Brain Barrier.

Schematic overview of a) transwell systems b) 2D culture systems c) BBB spheroids or organoids and d) 3D culture based microphysiological systems. Reproduced with permission from [153].

Other in vitro Blood-Brain Barrier models

As an alternative to *in vivo* testing and 2D *in vitro* models, 3D *in vitro* models, such as organoids and 3D printing BBB models, have been designed and improved.

Organoids and spheroids have been used to develop self-organized BBB cells under low adhesion dishes [173]–[175] to screen brain penetrating agents using matrix-assisted laser desorption/ionization mass spectrometry imaging (MALDI MSI). Brain organoids contain neurons, PCs, ACs and the outer layer of BBB organoids are usually ECs, but still lacking capillary-like blood vessels inside the organoid [173], [175]. To mimic the brain vasculature, organoids were transplanted into the cortex of the mouse brain to induce the outgrowth of murine vessels into the human tissue, increasing cell survival and maturation [176] (Fig. 2.4c).

Additional examples of BBB models derived from 3D bioprinting. This technology potentially mimics essential physiological and pathological features and has been applied to BBB modelling. 3D-bioprinted constructs enable the investigation of cellular and ECM interactions in a potential

high-throughput and reproducible manner[177]. A biohybrid system containing microporous tubular structures of 10 μm diameter and 1 μm pores mimicking capillaries fabricated with the two-photon lithography technology. Mouse brain ECs (bEnd.3 cells) were seeded directly on top of the capillaries to recreate an endothelial barrier. Human glioblastoma cells (U87) were loaded closely to microvessels[178]. Recently, same biohybrid system included human brain ECs hCMEC/d3, primary ACs and glioblastoma cells was designed to mimic the brain tumor microenvironment including the BBB[179]. Numerical simulations demonstrated uniform and physiologically relevant flow rates in the microcapillaries. Another BBB model contained microvessels was generated by extrusion-printed frame, combining bEnd.3 ECs in hollow channel to form microvessels embedded in a collagen matrix. 3D printing was used to fabricate the main frame of the BBB design, containing a dissolvable and non-dissolvable resin[180][177]. Another research group has recently developed a 3D printed BBB vasculature. A sacrificial template, constituted by gelatin and alginate was printed and subsequently coated with porous poly-caprolactone/poly (DL-lactide-co-glycolide) (PCL/PLGA) was used to create the “skeleton” of the vessels. The bEnd.3 cells were perfused within the channels, while other primary rat cells, including PCs, ACs and neurons, were co-cultured in a collagen matrix wrapping the 3D vasculature[181].

Microphysiological models of the Blood-brain Barrier

In addition to organoids or spheroids, 3D printing BBB model and advanced microfluidic models have been designed and improved. These models consist of cell culture devices created using microchips, usually produced in polydimethylsiloxane (PDMS)[182], [183]. PDMS microchips are gas-permeable and optically transparent devices that generally contain continuously perfused chambers containing living cells that are arranged in way to simulate tissue and organ level physiology[48]. Fabricated with lithography and soft lithography, the design is adapted according to specific applications. Microphysiological models may closely replicate brain microenvironment, showing physiological-like cell behavior and predictive outputs of human tissue in response to treatments, reducing animal experimentation and research costs[184]. It can also show the replication of organ-level functions and physiological responses to stimuli that are not possible with conventional 2D or 3D culture systems[185]. Such systems are relatively robust, reproducible, suitable for any cell type amenable to culture, enabling the use of patient derived

cells for drug transport studies [186], with the potential ability to accelerate the *in vitro* pre-clinical evaluation and screening of nanocarriers for effective therapeutic strategies (Fig. 2.4d).

New examples of microphysiological models are rapidly emerging. The most recently published advanced 3-Dimensional BBB models were proposed by:

- Both et al. [187], who developed a platform with two perpendicular flow channels. Rat endothelial cells were cultured as a 2D monolayer in contact with a polycarbonate membrane that divided the rat astrocytes channels.
- Herland et al. [188], who fabricated a PDMS-collagen device by viscous fingerprinting [189] to obtain a hollow tube channel. Human brain endothelial cells were introduced by recirculating fluid flow forming a macrovessel of 200 to 600 μm in diameter. Pericytes or astrocytes were co-cultured in the same device in the surrounding collagen region. From same group, a similar BBB model was further engineered by Park et al. [190] to evaluate shuttling of drugs and antibodies. Cells were differentiated under hypoxia condition which increased barrier functionality and enhanced BBB mimic of transport.
- Bang et al. [191] who defined a BBB model culturing HUVECs and normal human lung fibroblasts in contact interactions with rat cortical neurons loaded in the side channel.
- Adriani et al. [192], developed a single layer PDMS microfluidic device with two gel channels regions and two fluidic channels. In one fluidic channel, 3-Dimensional human HCMEC/D3 monolayer was obtained. In the other two channels, mouse ACs and neurons were cultured.
- Shin et al. [193], developed a single layer PDMS microfluidic device with a similar pattern compared to Adriani et al. [192]. In this case, all cells used, human cerebral microvascular endothelial cells (hCMEC/D3) and neural progenitor cells (ReN cells), were derived from humans. A 3-Dimensional human HCMEC/D3 monolayer was formed in the fluidic channel. A gel channel was loaded with human neural progenitor cell line, with the ability to differentiate into neurons and glial cells. This model was used to study the effect of Alzheimer's Disease on the BBB.
- Ahn et al. [194], developed a double layer BBB chip system with the upper layer containing a monolayer of human brain microvascular endothelial cells (HBMEC) on one side, human

brain vascular PCs on the other side, and ACs in the lower layer. This device was used to screen nanoparticles biodistribution.

- Maoz et al. [190], developed a linked organ on a chip model of neurovascular unit (including BBB and neuronal cells) to study the effect of intravascular administration of psychoactive drugs.
- Vatine et al. [195] realized a human iPSC-derived BBB model for disease modeling and personalized medicine applications, where whole blood was perfused in the capillary to test the ability of the monolayer to protect neural cells from plasma-induced toxicity.
- Lee et al. [196] defined a CNS-like angiogenesis model. HBMEC were cultured on one side of the device, and sprouted into a gel region containing human PCs and ACs. Fibroblasts were cultured on the other side of the device to promote angiogenesis.
- Chung et al. [197] compared HUVECs, hMVEC and hCMEC/D3 that formed a 3D monolayer as models of BBB. Cell penetrating peptides permeability was evaluated.

These models have been developed with various cell sources and design concepts for a range of applications. The multicellular complexity was reproduced by compartmentalized culture of each cell type of the BBB in separate microfluidic channels, where the size and anatomic features of brain capillaries were not fully recapitulated. Several combinations of cells including cross-species composition were used. Only in one case [191] the model showed similar capillary structures to the BBB, with more accurate *in vitro* reproduction of physiological characteristics, but contained a combination of cells (HUVECs, lung fibroblasts and rat cortical neurons) which is far from identical to the human BBB. In the table below (Table 2), a compelling list of the BBB microphysiological models is listed and their features including device fabrication, cell components, permeability and physiological function mimicked in their systems and consequently results are described.

Table 2. BBB microphysiological model.

Table modified with permission from [228]

Ref.	Devices Fabrication	Endothelial cells	Co-culture cells	Physiological function	Results	Permeability measurements
Adriani et al. 2017 [192]	3D Single layer PDMS-device with 4 channels	HUVEC or hCMEC/D3	Primary brain astrocytes Rats cortical neurons E18	N.A.	N.A.	6.58×10^{-5} to 3.3×10^{-6} cm ² /s 10 70 kDa dextran, 4 and 7 days culture
Herland et al. 2016 [188]	3D PDMS device-Viscous fingerprinting procedure	Human brain microvascular endothelial cells (hBMVEC)	human brain pericytes Human brain astrocytes	TNF- α mediated inflammation	G-CSF and IL-6. IL 8 release increased compare to static transwell culture and between co-cultures	$2 - 5 \times 10^{-6}$ cm ² /s 3 kDa dextran Different co-culture systems
Wang et al. 2016 [198]	3D Printed microfluidic chamber Polycarbonate insert	hiPS-derived BMEC	Primary rat astrocytes	Exposure to small drugs molecules (caffeine, cimetidine, doxorubicin)	Permeable to molecules	4, 20, 70 kDa dextran 10^{-7} to 10^{-8} cm ² /s
Cho, H. et al. 2015 [199]	3D PDMS Composite assembly of horizontal parallel micro channel beside one macro-channel	Rat brain endothelial cells (RBE4)	Human neutrophils	Neutrophils transmigration TNF- α mediated inflammation oxygen-glucose deprivation-Antioxidant treatment	Inhibition of neutrophils transmigration Neuroinflammation response ROS and ROCK activation. Cell death. Limited antioxidant effect	40 kDa, visual diffusion comparison
Deosarkar et al. 2015 [200]	PDMS circular device Independent vascular channel	Rat brain endothelial cells (RBEC)	Neonatal rat astrocytes	N.A.	N.A.	40 kDa under flow condition: $41-1.1 \times 10^{-6}$ cm ² /s for co-culture condition
J.D. Wang et al. 2016 [201]	two layered microfluidic channels-porous membrane	Mouse brain endothelial cells (b.End3)	Mouse astrocyte (C8D1A) Immortalized mouse pericytes	P-gp efflux pump functional expression by Dexamethasone	Increased by cultures days, P-GP expression in mono e co-cultures	Urea 1.1×10^{-6} Mannitol $0.3-0.6 \times 10^{-6}$ cm ² /s Dexamethasone 2.9×10^{-6} permeability
Brown et al. 2015 [202]	3 PDMS layers 1 polycarbonate filter membrane	Human brain microvascular endothelial cells (hBMVEC)	Primary Human brain pericytes Primary astrocytes humancortical glutamatergic	Exposition to glutamate ascorbate -Cold shock	Increased permeability to ascorbate Disruption of TJs	24h fluid flow of 10, 70 kDa dextran - Compare diffusion across the membrane

			neurons from hiPSCs			
Kim et al. 2015 [180]	3D printed collagen gel and channels	Immortalized mouse brain endothelial cells (b.end3)	N.A.	BBB disruption by hyperosmotic D-mannitol exposure	Increase of permeability And recovery after treatment	40 kDa dextran 2.27×10^{-7} cm ² /s 6.5×10^{-10} cm ² /s Mannitol 3.9×10^{-6} cm ² /s
Booth et al. 2012 [187]	PDMS subLayer Polycarbonate membrane	Immortalized mouse brain endothelial cells (b.end3)	C8D1A astrocytes	Histamine exposition	Response after histamine, initial value in 6-15 min	4, 20,70 kDa Propidium iodide
Partyka et al. 2016	1 hydrogel reservoir up on 2 microchannels	HCMEC/D3	Human astrocytes	TNF- α mediated inflammation with without shear stress	Permeability increase in cocultures	4 kDa -dextran -Flow $0.6-1.2 \times 10^{-6}$ cm/s -TNF- α $4-9 \times 10^{-6}$ cm/s
Achyuta et al.	2 PDMS chamber and polycarbonate membrane	Rat brain EC RBE4	E18 neural cells Differentiate in neurons, astrocytes, microglia	TNF- α mediated Inflammation	Hyperpermeability TNF- α induced ICAM-1 and glial activation	3 kDa dextran Relative comparisons
Walter et al. 2015	PDMS-PETmembrane-glass- device assembly	hCMEC/D3 or primary rat brain endothelial cells	Primary brain pericytes Primary brain astrocytes	N.A.	N.A.	Sodium fluorescein 376 Da dextran 4,4 kDa Evans blue-labeled albumin 67 kDa $0.4 -1.57 \times 10^{-6}$ cm/s
Sellgren et al. 2015 [203]	Two-compartment PDMS device and PTFE membrane	murine brain endothelial (b.end3)	Astrocytes (C8D1A, ATTC)	N.A.	N.A.	dextran 70 kDa 6×10^{-7} cm/s
Merkel et al. 2016 [204]	Cell culture insert PET membrane 0.3 um	hBMVEC isolated from temporal of hippocampal tissue	Human primary astrocytes	Comparison of Adeno-associated virus vectors AAV9 AAV2 Trafficking the BBB	-AAV9 more efficiently cross the barrier - TJs expression	3 kDa dextran 16000 RU 40 kDa dextran 800 RU
Bang. et al. 2017 [191]	3D Single layer PDMS-device with 4 channels	HUVEC	Normal lung fibroblast Rat cortical neurons E17	Conditioned medium effect on neural culture and permeability		20 kDa FITC-dextran, $0.45 \pm 0.11 \times 10^{-6}$ cm/s; 70 kDa FITC-dextran, $0.36 \pm 0.05 \times 10^{-6}$ cm/s
Shin et al. 2019 [193]	3D Single layer PDMS-device with 5 channels	HcMEC/D3	Neural progenitor cells (ReN): wild Type and producing A β amyloid (ReN-AD)	Effect of Alzheimer disease on BBB breackdown	increased BBB permeability in AD decreased expression of tight junctions	AD model (1.4×10^{-5} cm s ⁻¹ for 3 kDa, and 6.45×10^{-6} cm s ⁻¹ for 40 kDa) WT model (7.46×10^{-6} cm s ⁻¹ for 3

						kDa, and $1.96 \times 10^{-6} \text{ cm s}^{-1}$ for 40 kDa)
Park. et al. 2019 [205]	3D double layer PDMS-device with 2 bonded channels separated by PET membrane	Human iPS IMR90-4 differentiated into hBMVEC	Human pericytes Human astrocytes	Verapamil, Rhodamine 123 DiOC2 Citalopram Doxorubicin, Angiopep-2-coated Qdots under normoxia or hypoxia	Increased barrier functionality under hypoxic condition	Ratio of Papp
Maoz et al. 2018 [190]	Polycarbonate microfluidic device containing two parallel channels PDMS- separated by polycarbonate membrane	hBMVEC	Human hippocampal neural stem cells HIP-009 human astrocytes human pericytes	metabolic coupling of endothelial and neuronal cells Methamphetamine effect on BBB	Dynamic interaction between neural and endothelial cells Methamphetamine transiently open the BBB	CB; 530 Da; Papp = $11.2 \pm 0.8 \times 10^{-6} \text{ cm/s}$ BSA-555; ~67 kDa; Papp = $2.7 \pm 0.2 \times 10^{-7} \text{ cm/}$
Ahn et al. 2020 [194]	3D double layer PDMS-device with 2 bonded channels separated by polycarbonate membrane	HBMEC	Human brain vascular pericytes Human astrocytes	High density lipoprotein (HDL) Nanoparticles transport	Nanoparticles cross the BBB via scavenger receptor class B type (SR-B1) mediated transecytosis	4 kDa dextran $1 \times 10^{-6} \text{ cm/s}$ 40 kDa dextran $1 \times 10^{-6} \text{ cm/s}$
Lee et al. 2020 [196]	3D Single layer PDMS-device with 4 channels	HBMEC HUVEC	Primary human pericytes Primary normal human astrocytes Normal lung fibroblasts	Reconstituting the functional efflux transporter system, (P-GP)	Calcein accumulation in P-GP inhibitor treated cells	10 kDa dextran $0.86 \times 10^{-6} \text{ cm/s}$ 70 KDa dextran $0.31 \times 10^{-6} \text{ cm/s}$
Vatine et al. 2019 [195]	3D double layer PDMS-device with 2 bonded channels separated by PDMS membrane	iPSCs differentiated into iBMECs	Primary human brain astrocytes human primary brain vascular pericytes IPS-derived neural progenitor cells	Patient derived model Perfusion with whole blood	BBB Protect neural cells from plasma-induced toxicity	3 KDa dextran $1 \times 10^{-7} \text{ m s}^{-1}$
Chung et al. 2020 [196]	3D Single layer PDMS-device with 5 channels	HUVEC hMVEC hCMEC/D3	N.A.	Evaluate cell penetrating peptides (ApoE and angiopep-2) targeting lipoprotein receptor protein 1 (LRP1)	ApoE showed higher penetration than angiopep-2	$0.36 \times 10^{-6} \text{ m s}^{-1}$

Discussion

BBB, present in the CNS, is the most impenetrable barrier of the human body: it restricts the transport of several molecules, including the efficient delivery of therapeutics to the brain[42].

Over several years, preclinical *in vivo* and *in vitro* systems have been developed to mimic the BBB. Traditional systems, such as Transwell assays, are well-suited for high-throughput screening but oversimplify the physiological reproduction of human BBB[206]. Likewise, *in vivo* animal models have been widely used for small molecules screening and have proven to insufficiently reproduce human BBB pathophysiology for more advanced therapies targeting specific transport mechanisms, due to significant cross-species differences (genetic, cellular, protein expressions)[207].

The lack of reliable preclinical models able to reproduce the human anatomical complexity and predicting molecular mechanisms of drug transport across the BBB, partially contributed to the misleading results of novel therapeutics in clinical trials[13]. For these reasons, therapeutic options for CNS disorders remain currently limited. As conventional models failed, enormous research efforts were spent to develop innovative *in vitro* 3D models, such organoids, bio-printed systems for BBB modelling and, lastly, micro-physiological models using microfluidic technology[208]. For instance, organoid platforms have become increasingly relevant, but still lack an accurate reproduction of the vasculature. This technology system can advance in synergy with 3D printing and microfluidic-based technologies[174][209].

Furthermore, advances in 3D bioprinting facilitate the generation of models using several strategies that accurately recapitulate ECM and cell interaction using natural and synthetic biomaterials. Although in its early stage, this technology has great potential to revolutionize this field. Future implementation including precise control, reproducibility and versatile printing resolution is necessary to enable a broader application of bioprinting to recap the size and anatomical features of brain capillaries and their surrounding microenvironment [210].

An additional modelling design, which may overcome the above limitations in mimicking the microvasculature, is represented by 3D micro-physiological systems based on microfluidic technology[211]. Although its development is still at early stage, recent progress in BBB-chips has allowed the reproduction of the essential biological functions of BBB and also the capability to screen targeted therapeutic approaches with an unprecedented level of physiological relevance

in vitro. The microfabrication techniques used in BBB-chips can help address some of the challenges of organoid generation, such as nutrient supply and spatiotemporal control of morphogenetic signaling pathway activation[206]. These techniques can be combined with 3D printing for optimization and standardization of barrier functions. However, more efforts are still needed to define completely reliable models that will become the current standards in preclinical applications. In order to support their implementations, it might be essential to realize a systematic and compelling comparison of *in vitro* systems with *in vivo* studies and correlation with patients responses to therapies.

Conclusion

In this chapter the essential concepts of BBB biology, including a compelling list of cellular components and transport mechanisms were introduced, emphasizing their characteristics and functions. Alterations in brain homeostasis, which causes BBB disruption in neurological disease was also examined. Then, innovative strategies for delivering therapeutic agents across the BBB nanoparticles as delivery systems were introduced, followed by an overall outline of traditional *in vitro* and *in vivo* modelling of the BBB to test the nanocarrier transport efficacy. Finally, different designs of *in vitro* models were described, including organoids, 3D printing and emerging micro-physiological models using microfluidic devices.

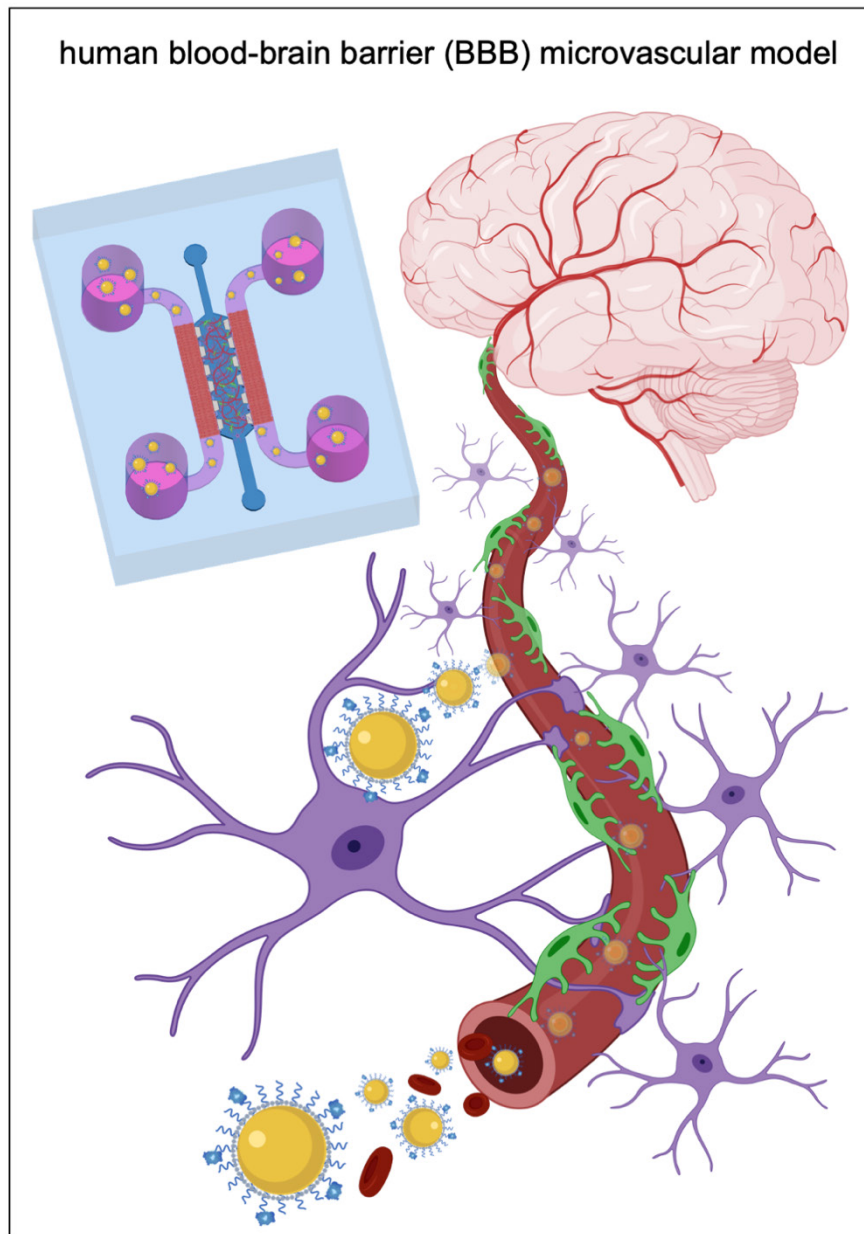
Remaining challenges for the current BBB models include a faithful reproduction of all BBB components on the same platform with more physiologically-relevant gene and protein expression. Also, faithful reproduction of brain vessels in terms of anatomical structure would be beneficial to mimic the bio-transport and fluid dynamic typical of brain capillaries, which consequently might produce better prediction of drug transport across the BBB. Recent advances in microengineering and nanotechnologies will help address these technical difficulties by combining technologies such as organoids, bioprinting and microphysiological models. Their combination will be crucial to further advance reliability and significance of BBB models, and their application as test platforms for innovative therapeutics, including nanomaterials-based nanocarriers, such a NPs.

Further studies will be performed to improve its physiological relevance for translational application in drug screening and development.

Chapter 4 - *Modelling nanoparticle transport using a 3D microphysiological model of the human Blood-Brain Barrier microvasculature*

Abstract

In this chapter, an engineered 3-dimensional Microphysiological BBB human model on a microfluidic chip was developed, consisting of self-organized microvascular networks derived via vasculogenesis, to accurately replicate the anatomical neurovascular organization observed *in vivo*. Specifically, this *in vitro* model includes human iPS cell-derived endothelial cells, primary pericytes and astrocytes embedded in the same 3D ECM-like microenvironment. Confocal microscopy imaging showed that iPS cells self-organized into microvasculature with the size of capillaries, overlapped by pericytes and in physical contact-interaction with astrocytes as occurs *in vivo*. Computational analysis was used to evaluate geometrical microvascular parameters, such as diameter and capillary branching, and confirm the improved morphological relevance of the model. Gene expression of membrane transporters, tight junctions and extracellular matrix proteins from cells on the microfluidic chip indicated BBB-like maturation and differentiation. Then, the established 3D microphysiological BBB model was exploited to develop a method to predict the transport of functionalized polymeric NPs across human BBB. Specifically, the effect of functionalizing the surface of polystyrene (PS)- and polyurethane (PU)-NPs with holo-transferrin (Tf) on NP transport efficacy was investigated. Fluorescently-labelled NPs were perfused through the BBB microvasculature and confocal images were acquired. Spatial distribution and permeability of NPs in the 3D model were quantified by computational analysis. The system showed similar permeability of PS and PU NPs, which increases after surface-functionalization with Tf. In comparison with conventional Transwell systems, this microphysiological models of the BBB enables rapid analysis of NP permeability in a physiologically relevant setting. Therefore, Chapter 4 presents the design of a new microphysiological BBB model and proof-of-principle insight of a methodology approach to predict transport of NPs in a reliable model of the human BBB.



Graphical abstract 5: *Preclinical 3D microphysiological BBB model and testing of nanoparticles (NPs) transport across the model.*

Schematic created with biorender.com, adapted with permission from [226].

This work was performed at the Roger Dale Kamm Laboratory, “Mechanobiology Lab” at the Massachusetts Institute of Technology (MIT) as part of the collaboration between MIT and the Politecnico di Torino, during an exchange period at MIT for the doctoral candidate.

Part of the work described in this chapter has been previously published in:

<https://doi.org/10.1016/j.biomaterials.2018.07.014>

“3D Self-Organized Microvascular Model of the Human Blood-Brain Barrier with Endothelial Cells, Pericytes and Astrocytes”.

Biomaterials. Jul. 2018

Campisi M., Shin Y., Osaki T., Hajal C., Chiono V. and Kamm R.D

<https://doi.org/10.1002/adhm.201901486>

“Modeling Nanocarrier Transport Across a 3D In Vitro Human Blood-Brain-Barrier Microvasculature”., Advanced Healthcare Materials, Feb. 2020.

W.L. Lee S.*, **Campisi M.***, Osaki T., Possenti L., Mattu C., Adriani G., Kamm R.D., Chiono V.

* shared first-authorship

<https://doi.org/10.4081/bse.2019.105>

“In vitro microfluidic modelling of the human blood-brain-barrier microvasculature and testing of nanocarrier transport”.

Biomedical Science and Engineering, 2020.

Campisi M., W. L. Lee S., Osaki T., Possenti L., Mattu C., Adriani G., Chiono V., Kamm R.D.

https://doi.org/10.1007/978-1-0716-1174-6_14

“3D self-organized human Blood-Brain Barrier in a microfluidic chip”

Programmed morphogenesis: Methods and Protocols. Methods in Molecular Biology, Book Chapter. 2021.

Campisi M.*, Lim S.H.* , Chiono V., Kamm R.D.

* shared first-authorship

Introduction

The blood-brain-barrier (BBB) regulates molecular trafficking to maintain a dynamic balance between the brain and blood circulation and protects against harmful compounds and pathogens [14]. BBB is formed by brain endothelial cells (ECs), which are specialized cells connected by tight junctions (TJs) and adherens junctions (AJs), with specific transport mechanisms that are able to restrict the passage of substances from bloodstream compared to other body locations [14]. The endothelium is surrounded by pericytes (PCs) which are equally distributed in vessel surfaces, enveloping ECs [15], present at 1:3 ratio (PCs : ECs ratio) [22] [28]. In close proximity to the vessels, the astrocytes (ACs) provide biochemical support to other BBB cells, forming an additional continuous layer that isolates blood vessels from brain tissue [212].

BBB function is also coordinated by neuronal interactions, whose projections are in contact with both ACs and vessels directly, to transmit vasoactive signaling and generates a well-known structure called the neurovascular unit[10], [213], [214]. The BBB restricts the diffusion of most molecules by various transport mechanisms, it also prevents neurotoxins compounds from entering the brain by an active transport mechanism mediated by P-glycoprotein (P-GP) while allowing the diffusion of water and lipid-soluble molecules or hydrophobic molecules like oxygen and carbon dioxide [215][216][14][4].

TJs hinder paracellular permeability of brain capillaries, suggesting that hydrophilic molecules must cross the endothelium by transcellular pathway to reach their neuronal targets or leave the brain [215]. Some exceptions are represented by small molecules with a molecular weight below 400-500 Daltons or lipophilic compounds with less than 8 hydrogen bonds that typically cross the brain endothelium [13]. In addition, BBB creates a pharmacokinetic obstacle against 100% of high molecular weight molecules and 98% of small molecules[59], and constitutes a nearly impenetrable obstacle against therapeutic delivery to the CNS. Consequently, it limits treatment strategies and neuro-pharmaceutical development in many brain pathological processes, including neurodegenerative diseases. Several pre-clinical BBB models have been developed to understand their role in brain pathogenesis and to screen drug efficacy[211]. 2D culture cell monolayers have traditionally been used to evaluate drug transport; however, in particular for the brain, these models exhibit non-physiological permeability and lack the anatomical architecture of the human *in vivo*

brain structure, limiting the ability to mimic the brain barrier [36]. In contrast, animal models more accurately replicate the complexity of a biological microenvironment.

According to a recent European Union (EU) report from 2017 about the use of experimental animals, a large portion of animal studies involves research on the nervous system. Every year (2015-2017) about 900,000 mice and 1,3 million animals were used in basic, translational and applied research on the CNS and mental disorders[217][218]. Although considered the gold standard, 80% of candidates for successful neurotherapeutic in mouse models subsequently failed in clinical trials[13]. These data underline that the development of a more advanced human BBB model *in vitro*, validated to test drug transport *in vivo*, may be the key to reduce animal testing and, thus, solve a critical unmet medical need. To optimize the design of innovative therapies and drug carriers, a robust, reliable, and cost-effective *in vitro* BBB model that adequately reflects human *in vivo* conditions is needed. As an alternative to *in vivo* testing and 2D *in vitro* models, BBB organoids were developed to study transport of brain penetrating agents[173], [175]. Additional examples of BBB models derived from 3D bioprinting, mimicking capillaries fabricated with the two-photon lithography technology, where mouse brain ECs (bEnd.3 cells) were seeded directly on top. Although these systems are cost-effective, they are limited in their ability to recreate a realistic BBB morphology and microenvironment.

As an alternative, microfluidic technology offers a promising tool to reconstitute the BBB with several advantages: 1) precise control of the 3D cellular and ECM microenvironment, 2) provide a platform for the study of cellular and structural responses to various stimuli, 3) mimic the complex cellular interactions and structures found in many tissues or organs *in vivo*. These platforms are referred as Microphysiological systems or Organ on chip. The systems so far have relatively large diameters (~600-800 μm) [188],[190], [205] compared to the dimension of human BBB vasculature *in vivo* (arterioles and venules 10-90 μm ; capillaries 7-10 μm)[96][68]. While they are able to recapitulate the BBB microvasculature morphology and the development in terms of mature cell-cell interactions via natural biological processes, they fail to incorporate relevant cell models, combining human umbilical vein endothelial cells (HUVECs), human or rat ECs with rat neurons and ACs. However, cross-species compatibility remains a concern regarding the relevance of these results to human physiology[15]. Moreover, HUVECs offer a poor model for cerebral vasculature, while PCs, recognized to be a key component of the BBB [15], have not been considered in these models [32,34].

To overcome these limitations, advanced microphysiological models or using microfluidic technology have demonstrated the potential to accelerate the *in vitro* pre-clinical evaluation and screening of novel drugs for effective therapeutic strategies, as shown in the previous chapter (Chapter 3).

In addition, polymer nanoparticles (NPs) have been explored for their tunable properties to release therapeutics across the BBB. Additionally, it has been demonstrated that surface modification of NPs, such as using ligands for specific binding to BBB cells enhances NP accumulation in the brain through receptor-mediated endocytosis[55]. Several models have been used to evaluate NPs efficacy toxicity, pharmacokinetics, transport and distribution properties across biological barriers of novel drugs therapeutics, as shown in previous chapter (section I - Chapter 1 and 2, section II - Chapter 3). Traditional *in vitro* systems failed to mimic the BBB complexity, and *in vivo* models have crucial genetic differences to finally have realistic predication of human response to drugs targeting the brain. In Alternative, microphysiological systems will broaden the possibility of testing the effectiveness of NPs in a more relevant BBB reproduction *in vitro*, Despite the fact that only a few examples are now present in the literature[194], more efficient platforms are needed.

Accordingly, this chapter reports on the development, characterization and testing of a microphysiological BBB model realized by combining human induced pluripotent stem cell-derived endothelial cells (iPSC-ECs), primary brain vascular pericytes (PCs) and astrocytes (ACs) forming microcapillaries by self-assembled vasculogenesis-like processes, with vascular permeability similar to *in vivo* measurements in rat brain. After characterizing the model in terms of genetic and protein expression, vascular formation and permeability, the microphysiological BBB model was used to test the transport of polymer-based nanoparticles (NPs), (polystyrene NPs and synthesized polyurethane NPs), which emerged as a potential solution to deliver therapeutics through the BBB due to its small size and surface functionalization. Since transport across the BBB represents a fundamental indication of the NP delivery capabilities, the development of an *in vitro* BBB model and the design of a reliable method to quantify the NP transport behavior represent fundamental tools for assessing NP efficacy. Here, the NP permeability across the developed microphysiological BBB model was compared to the Transwell 2D models. Differences in 3D NP permeability and transport were observed between commercially available polystyrene NPs and synthesized polyurethane NPs. The method was also capable of quantifying the effect of surface-functionalizing NPs with human holo-transferrin (Tf), an attractive brain-associated

ligand, on their permeability across the BBB. Importantly, the work presents initial findings on the use of a self-assembled 3D microphysiological BBB model to assess polymer NP transport and provides proof-of-principle insight on a new methodology for pre-clinically screen nanocarrier candidates that optimally cross the human BBB.

Material and Methods

Material and reagents

For microfluidic technology: Polydimethylsiloxane (PDMS) (Sylgard 184 silicone elastomer kit, Dow Corning). Fibronectin (C010), Fibrinogen (F8630), poly-L-lysine (P4707) and thrombin (cat. no. T9549) (Sigma-Aldrich, USA).

For PU synthesis and preparation: Poly(ϵ -caprolactone)-diol (PCL-diol (2,000 g/mol), Poly(ethylenglicole) (PEG 2000 g/mol), n-BOC Serinol, Dibutyl Dilaurate (DBTL), and 1,6 Hexamethylene diisocyanate (HDI) were purchased from Sigma Aldrich. L- α -phosphatidylglycerol (EGG-PG), 1,2-distearoyl-sn-glycero-3-phosphoethanolamine-N-[carboxyl(polyethylene glycol)-2000] (DSPE-PEG-COOH) and L- α -phosphatidylethanolamine-N-(lissamine-rhodamine B-sulfonyl) (Egg-Liss-Rhod PE) were purchased from Avanti Polar Lipids (Alabaster, AL, USA). Holo-Tf Human (T4132), N-(3-Dimethylaminopropyl)-N'-ethylcarbodiimide hydrochloride (EDC), N-Hydroxysuccinimide (NHS), 2-(N-morpholino)ethanesulfonic acid (MES) hemisodium salt were purchased from Sigma Aldrich.

For commercially-available nanoparticles: Fluorescent carboxylate PS-NPs (F8801, F8810, FluoSpheres) was purchased from Life Technologies and Spherotech (CFP-0562-2, USA).

Fabrication of the microfluidic device: Photolithography and Soft lithography

Microfluidic systems (micro-device) are fabricated using high-precision soft lithographic methods[183] using polydimethylsiloxane (PDMS) that is an optically transparent polymeric substrate, impermeable, inert and biocompatible [182]. The fabrication process of a microfluidic device is divided into two steps: master fabrication (photolithography) and copy mold fabrication (soft lithography) [219]. The design of microfluidic devices was generated with AutoCAD (Autodesk) which contains a gel region flanked by two fluidic channels. Pillar-like posts delimitate fluidic channel from the gel region. (height: 150 μm , width of the fluidic channel: 1340 μm , width

of the gel channel: 2200 μm , post distance: 150 μm (Fig. 2.5a). After the design of the microfluidic pattern, the CAD file was sent out for mask preparation (CAD/Art Services, Inc.) and then, the master was fabricated with photolithography. Briefly, SU-8, a negative photoresist based on epoxy resin, was used. Negative photoresist is a photoresist which parts exposed to UV are cross-linked, while the remaining parts are soluble and may be removed during development. SU-8 was applied on silicon wafer surface through spin coating. The wafer with SU-8 on top was exposed to UV light (350-400 nm), using a mask aligner. The parts that were not exposed to UV were developed and removed from the surface using methanol bath under agitation. Then, the master was ready for fabrication of the devices and could be stored and reused. Soft lithography method was used to fabricate devices as described previously[220]. Briefly, silicone elastomer and curing agent (Sylgard 184 elastomer kit, Dow Corning) were mixed at a 10:1 ratio, the mixture was degassed in a desiccator, poured into a petri dish that contained the silicon wafer mold and placed in an oven at 70 °C for 2 h. Devices were cut from the PDMS replica, punched for inlet/outlet ports using 1 and 2 mm diameter biopsy punches to create gel and media ports, before sterilization by dry cycle autoclave for 20 min. After drying at 80 °C overnight, PDMS layers were treated with oxygen plasma that allows simple oxidation of the surface of both PDMS and glass substrates to create strong siloxane bonds (Si-O-Si) for reliable bonding of PDMS to glass. Devices were then bonded to 25 \times 25 mm² glass cover slips and left at 80 °C for at least 24 h for hydrophobicity to be restored.

Fabrication of the macro device (Laser cutting)

Macro-devices contain a gel region flanked by two fluidic channels were designed using AutoCAD and master molds were cut from 0.5 mm cast Clarex (polymethylmethacrylate) sheet (Astra Products) using an Epilogue laser cutter (height: 1000 μm , width of the fluidic channels: 3000 μm , width of the gel channel: 3000 μm). Two semi-walls alongside the gel channel delimitate the border with fluidic channels in order to guide gel insertion (as opposed to typical posts) (Fig. 2.5b). Thin molds were bonded by acetone to a larger acrylic sheet surrounded by the same height lip in order to generate a device with reproducible thickness size. PDMS device fabrication was performed by soft-lithography as described above. Poly-D-lysine (Sigma-Aldrich) was injected into the devices at 1 mg/mL concentration, left within the device for 2-3 hours and then rinsed with sterile cell culture water (Lonza) and finally incubated at 80 °C for drying.

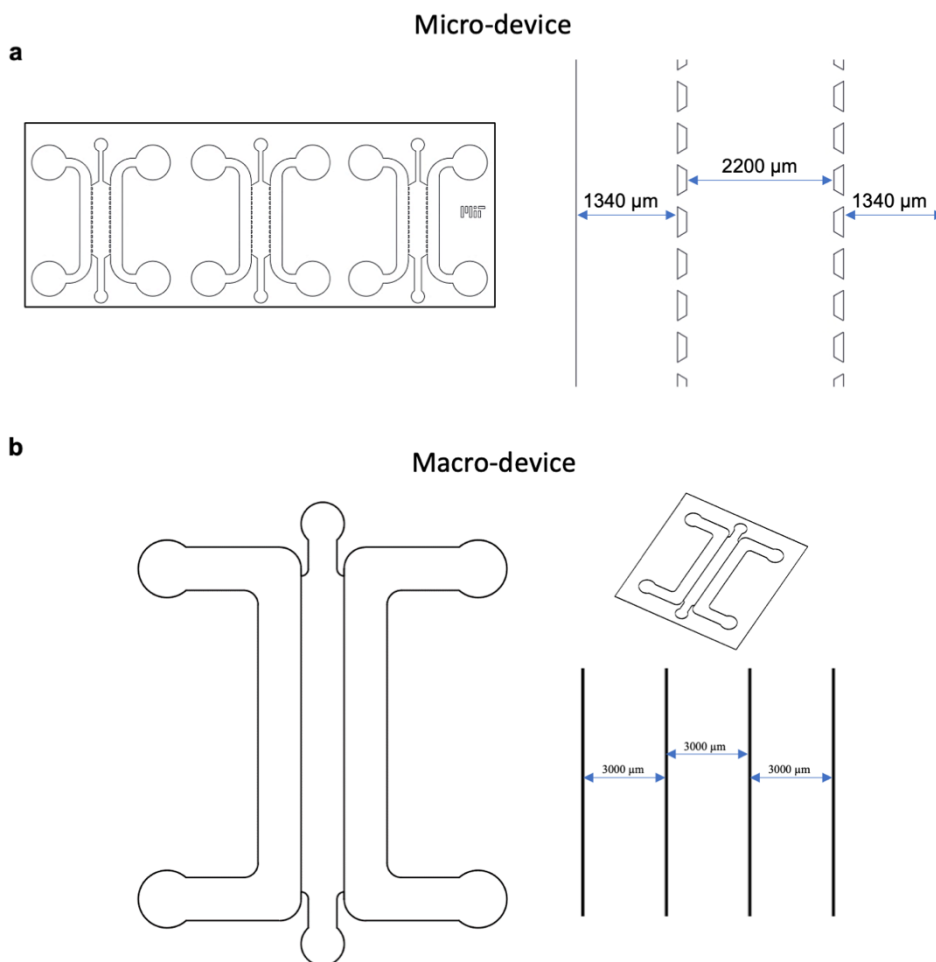


Figure 2.5: Design of microfluidic devices.

microfluidic devices (micro-device, macro-device) were designed using Autocad (Autodesk) and were comprised of a central gel region, two fluidic channels and four reservoirs. a) Micro-device dimensions are: 150 μm (height), 1000 μm (width of fluidic channel) and 1300 μm (gel channel). 200 μm is the distance between posts, which delimitate the gel region from the fluidic channel b) Macro-device dimensions were: 1000 μm (height), 3000 μm (width of fluidic channel) and 3000 μm (width of gel channel), with semi-walls that delimitate gel region from fluidic channels of 300-400 μm to separate the gel from the media channel. Devices were bonded to glass coverslips (25 mm x 25 mm (a), 45 mm x 50 mm (b)). Reproduced with permission from [221].

Preparation of nanoparticles

Commercially available PS-NPs of different sizes (100, 200, 400 nm) were exploited for surface grafting with human holo-Tf following a method that was previously described[222]. Briefly, bare carboxylic-modified 100 nm PS-NPs (2.2 mg/ml) were incubated with Tf (2.2 mg/mL) in 50 mM 2-(N-morpholino)ethanesulfonic acid (MES) buffer at room temperature (RT) for 2 hours.

Nanoprecipitation method was used to prepare PU-NPs which as previously described [223]. Briefly, synthesized PU was dissolved in acetonitrile and dropped into a solution of water and lipids, containing 200 µg of L- α -phosphatidylglycerol (Egg-PG), 240 µg of 1,2-distearoyl-sn-glycero-3-phosphoethanolamine-N-[carboxy(polyethylene glycol) (Mw 2000 Da) (DSPE-PEG-COOH) and 5 µl of L- α -phosphatidylethanolamine-N-(lissamine-rhodamine B-sulfonyl) (Egg-Liss-Rhod PE). The NPs suspension was spun down at 3200 rpm. For Tf functionalization, NPs were obtained, resuspended in MES buffer, containing EDC and NHS (1:2.5 molar ratio) and incubated at RT for 30 min for the activation of the carboxyl groups on the surface. Activated NPs were quickly collected by centrifugation, mixed in PBS containing Tf (1:16 molar ratio to COOH), and incubated at 4 °C overnight. Tf-conjugated NPs were obtained and stored at 4 °C for further use.

Characterization of Nanoparticles

The hydrodynamic diameter, polydispersity index and zeta potential of NPs were measured using Malvern ZS90 zeta-sizer (Nano ZS, Malvern, UK). NPs were analyzed by 3 technical replicate measurements repeated on 3 different batches of NPs. Data shown as mean values, error bars \pm SD. Cryo TEM and TEM was performed by dropping a PU-NP solution (7 µl, 0.5 mg/ml) onto a carbon-coated copper mesh grid.

3D Microphysiological BBB model

Human iPSC-ECs (Cellular Dynamics International, CDI) were cultured on flasks coated with 30 µg/mL human fibronectin (Millipore) in vascular medium (VascuLife VEGF Medium Complete Kit, Lifeline with iCell media supplement, CDI). HBMECs (ScienCell) and HUVECs (Lonza) were cultured under manufacturer's protocols with endothelial cell medium from their company respectively. Human primary astrocytes and pericytes (ScienCell) were cultured on a poly-L-lysine coated flask with culture medium (ScienCell) in a humidified incubator (37 °C, 5% CO₂). Culture medium was refreshed every 2 days (Fig. 2a).

The 3D microphysiological BBB model containing iPSC-ECs + PCs + ACs was developed as indicated below[221]. Briefly, fibrinogen (6 mg/mL in phosphate-buffered saline (PBS)) and thrombin from bovine plasma (Sigma-Aldrich) (4 U/mL in VascuLife) were first prepared and

placed on ice. All cells were detached using TrypLE (Gibco), spun down at 1200 rpm for 5 min, counted, resuspended in medium with 4 U/mL thrombin at 6×10^6 cells/ml, iPSC-ECs, 2×10^6 cell/ml PCs and 2×10^6 cells/ml ACs (final cell density), and left on ice. A volume of 20 μ L of the tri-cellular suspension was mixed with 20 μ L fibrinogen (final concentration 3 mg/mL), and the mixture was immediately injected into the gel channel using the filling port. Devices were rotated and collocated upside-down in a humidified chamber. After 15 min at RT for hydrogel polymerization, medium was injected into both fluidic channels via the inlet ports. Two growth factor-enriched media were used for 3D microphysiological BBB culture:

- Medium A (day 0 to day 5): endothelial medium (Vasculife) enriched with 50 ng/mL vascular endothelial growth factor (VEGF) and 1% (v/v) Astrocyte growth factor supplement;
- Medium B (day 6 and day 7): endothelial medium (Vasculife) enriched with 1% v/v Astrocyte growth factor supplement.

After 2-3 days of culture, medium was aspirated from one fluidic channel, replaced with 30 μ L of 30 μ g/mL fibronectin and left in the incubator for 30 min, before rinsing 2 times with DPBS. iPSC-ECs were detached and resuspended at 2×10^6 cells/mL in tri-culture medium. 30 μ L iPSC-EC suspension was injected to the coated fluidic channel and the device was tilted upside-down at a 60° angle to allow cells to spread evenly over the gel interface by gravity. The device remained tilted for 15 min, before medium was gently added to fluidic channel. The following day, non-adherent iPSC-ECs were removed by replacing with fresh medium and the above procedure was performed for the other fluidic channel. Other two conditions were made: iPSC-ECs mono-culture and iPSC-ECs + PCs co-culture to be compared to the 3D microphysiological BBB model tri-culture of iPSC-ECs + PCs + ACs, maintaining the same final cell density. Devices were kept in the incubator for 7 days, with media refreshed daily. Due to the absence of brain astrocytes in iPSC-ECs mono-culture and iPSC-ECs + PCs co-culture, astrocyte growth factor supplement was not supplemented to medium A and B.

Immunostaining and confocal imaging

To perform immunostaining inside of the microfluidic channel after 7 days of culture, the microphysiological models were rinsed with PBS and fixed in 4% paraformaldehyde (PFA, Electron Microscopy Sciences) at RT for 15 min. Cellular membrane was permeabilized using 0.1% Triton X-100 (Sigma-Aldrich) for 5 min at RT followed by rinsing with PBS twice. Primary antibodies (1:100, volume ratio) against CD31, Glial Fibrillary Acidic Protein (GFAP), (Abcam), F-actin (Rhodamine Phalloidin, Molecular Probes), 4,6-Diamidino-2-Phenylindole (DAPI Thermo Fisher Scientific) were used to identify iPSC-ECs, ACs, PCs, and nuclei. F-actin is expressed by all cells, whereas only iPSC-ECs are CD31 positive and GFAP is only expressed by ACs. Double staining of CD31/F-actin and GFAP/F-actin was used to identify iPSC-ECs and ACs respectively, which enabled to identify PCs as those cells that only expressed F-actin.

For the evaluation of TJs and ECM proteins expression by immunocytochemistry, primary antibodies against ZO-1 (Invitrogen), occludin, claudin-5, laminin and collagen IV (Abcam) were used. Secondary antibodies (1:200, volume ratio) were antirabbit or anti-mouse IgG conjugated with Alexa Fluor (488, 555, or 647) (Invitrogen). All antibodies are listed in Table 5. Devices were incubated with primary and secondary antibodies overnight at 4 °C, in a shaker. Devices were washed with PBS and imaged using a confocal laser scanning microscope (FV-1000, Olympus, Japan; aspect ratio 1024×1024) by high resolution images at 10 ms/pixel scan velocity. Postprocessing and stitching of tiled confocal data were computed using Imaris (Bitplane, Switzerland) and Fluoview (Olympus, Japan). Fold change average immunofluorescence (IF) intensity for iPSC-ECs was normalized by the cell boundary length (ZO-1, occludin, and claudin-5) or by microvascular area (laminin, collagen IV). Region of interests (ROIs) were chosen to contain only vessel portions to exclude gel regions from the computations.

BBB microvascular parameters characterization

To identify and describe microvascular parameters, confocal images were processed using ImageJ software (<http://rsbweb.nih.gov/ij/>) and plugins (Trainable Weka Segmentation 3D, 3D geometrical measure). Briefly, noise was removed from images and contrast was enhanced. To produce binarized images, an automatic threshold was defined. From 2D projections, lateral vessel area (*Alateral*), and total branch length (*Lbranch*) were analyzed by ImageJ. Percentage of area

coverage was calculated dividing $A_{lateral}$ by the entire area of the region of interest. Taking advantage of the observation that most vessels are oriented in a plane parallel to the device, lateral sizes, parallel to the devices, were computed as the ratio of the projected lateral vessel area to the total branch length (Fig. 2.9d). Transverse diameters, perpendicular to the device, were computed using the 3D vessel volume (V) and the surface area of the vessels in 3D ($A_{surface}$). Average cross-section area and circularity were computed using lateral and transverse diameters. The equations used to compute both diameters, cross-section area, lateral and surface areas and circularity are reported below.

$$A_{lateral} = D_{lateral}L_{branch}$$

$$A_{surface} = \pi \sqrt{\frac{D_{transverse}^2 + D_{lateral}^2}{2}} L_{branch}$$

$$V = \frac{\pi D_{lateral} D_{transverse} L_{branch}}{4}$$

$$D_{lateral} = 2R_{major} = \frac{A_{lateral}}{L_{branch}}$$

$$D_{transverse} = \sqrt{\frac{D_{lateral}^2}{\frac{A_{surface}^2 D_{lateral}^2}{8V^2} - 1}}$$

$$A_{cross} = \pi \frac{D_{transverse} D_{lateral}}{4}$$

$$Circularity = \frac{D_{transverse}}{D_{lateral}}$$

Quantitative RT-PCR

To measure junctions, ECM and transporter proteins, total RNA isolation was performed using TRIzol reagent (Life Science) that also dissolved fibrin gel. Reverse transcription was performed using SuperScript VILO cDNA synthesis kit (Invitrogen). Quantitative Real-time RT-PCR (RT-

PCR) using SYBR Premix Ex Taq (Takara) or Power SYBR Green PCR Master Mix, was performed with a 7900HT Fast Real-Time PCR System (Applied Biosystems). mRNA of endothelial cell adhesion molecule (PECAM also known as CD31, glyceraldehyde 3-phosphate dehydrogenase (GAPDH) and Ribosomal Protein S18 (RPS18) were used as housekeeping genes, set to 100% as the internal standard. RT-PCR experiments were repeated at least 3 times for cDNA prepared from 6 devices. Primer sequences (Integrated DNA technology) are listed in Table 4. A macro device was used for RT-PCR experiment in order to collect higher amount of total RNA.

Transwell permeability assay

iPSC-ECs were cultured on a transwell membrane (1 μm pore size; Corning) and grown to confluency. Monolayer formation including confluency and TJ formation, was assessed by evaluating trans-endothelial electrical resistance (TEER) using EVOM2 (World precision instrument) with silver/silver-chloride chopstick electrodes (STX2) between the transwell insert and bottom surface of the culture well plate where the TEER probe was fully submerged in culture medium during measurement. The confluent EC monolayer was incubated with 300 μl of 50 $\mu\text{g}/\text{mL}$ fluorescent NP suspensions in the transwell insert and 200 μL of culture medium in the well for 1 h and 3 h. At each timepoint, medium in the insert and well was separately collected. The total fluorescence signal of each medium sample was measured by a fluorescence plate reader (Molecular Devices). In some experiments, a solution of only 70 kDa FITC-dextran (1:100) or fluorescent NPs (50 $\mu\text{g}/\text{ml}$) was suspended in PBS. After formation of iPSC-EC monolayer, culture medium was removed and 200 μl of PBS was added to the bottom well. Then, 200 μl of FITC-dextran solution was added to the transwell insert. 3D z-stacks images of the region above and below the insert membrane (interspace: 500 μm) were captured using a confocal microscope (FV-1000, Olympus, Japan) (800 \times 800 pixels, 20X magnification) at 0 min (t_1) and 5 min (t_2). 2D monolayer permeability was calculated using Fiji software by considering the fluorescence intensities of both regions, bottom (b) and top (t) at 0 min (I_{T1} and I_{B1}) and at 5 min (I_{T2} and I_{B2}) for the green (dextran) and red (NPs) fluorescence channels, using the following equation:

$$P = \frac{(I_{B2} - I_{B1})V_g}{A_v \Delta t (I_{T2} - I_{T1})}$$

where g and v referred to gel region and vascular region, I is the mean intensity of the signal within the region of interest (ROI), V_g is the volume of bottom solution in the observation area, A_v is the lateral surface of the transwell membrane (3.2 mm \times 3.2 mm) and $\Delta t = t_2 - t_1$ is the duration of the test (5 min). The total fluorescence was measured by VMax micro plate reader (Molecular Devices).

3D permeability measurements and quantification

10, 40 and 70 kDa FITC-dextran were diluted 1:100 in culture medium for permeability tests.

The microvascular permeability was evaluated as the flux of solute across microvasculature walls. Using mass conservation, the quantity of FITC-dextran crossing the microvasculature corresponds to the rate at which it accumulates outside the microvasculature in the gel region.

To dilute NPs solution, a 70 kDa FITC-dextran was used. All NPs (50 $\mu\text{g/ml}$ final concentration) were freshly prepared for each experiment and vortexed for 10 s before their use. To measure NP microvascular permeability, medium was first aspirated from both fluidic channels of each device. In one fluidic channel, 15 μl of NP-containing solution was added, while 15 μl of solution without NP was added simultaneously in the other fluidic channel. 3D z-stacks of the gel channel was imaged at intervals of 5 min by confocal microscopy (512 \times 512 pixels, 20X magnification) (Olympus model FV1000) for at least 3 different ROIs. According to a previously described method [224], microvascular permeability and NP permeability were quantified by considering the increase in fluorescence intensity within the gel using eq. (1):

$$P = \frac{(I_{g,t2} - I_{g,t1})}{A_v \Delta t} \frac{V_g}{(I_{v,t1} - I_{g,t1})}$$

where the subscripts g and v stand for the gel region and vascular region, respectively, I is the mean intensity of the signal within the ROI, V_g is the volume of the gel, A_v is the lateral surface of the microvascular network and $\Delta t = t_2 - t_1$ is the duration of the test (30 min to 1 h). Geometrical parameters such as *Alateral* and *volume* of the microvasculature were computed using Fiji software by segmenting the images using vascular borders obtained with the dextran signal using the 3D

Trainable Weka Segmentation plugin and an ad-hoc classifier. The above-described variable were derived by the 3D analysis of the confocal image stacks as described previously[225].

To simplify the equation, following parameters can be used: $A_{lateral}$, L_{branch} , mean intensity of tissue I_T at different time points and mean intensity of vessels I_V , t (time between 2 images). Hence, permeability calculation can be made using the following simplified equation:

$$P_v = \frac{1}{(I_V^{t1} - I_T^{t1})} \frac{(I_T^{t2} - I_T^{t1})}{\Delta t} \frac{A_{lateral}}{L_{branch}}$$

Quantification of 2D cellular nanoparticle uptake

iPSC-ECs were plated on 2D culture glass-bottom dishes (MatTek, cat#. P35G-0-14-C) and allowed to grow to confluency (~ 80%). In order to be visualized, cells were stained with Cell Tracker Green (CMFDA at 2 μ M) following the manufacturer's instructions. 50 μ g/mL of NPs were added to the labelled cells before their incubation for up to 4 h. The, cells were rinsed with PBS twice to wash out the excess of NPs before fixation with 4% paraformaldehyde and counterstained with DAPI (1:1000). Cells were imaged using confocal microscopy (1024 \times 1024 pixels, 60X magnification) for at least 3 different ROIs.

NP uptake was evaluated by quantifying the NP fluorescent intensity within two different 3D regions: (i) a region that is close to the nuclei (includes the nucleus and a 1 μ m-thick layer surrounding the nucleus) and (ii) the cytoplasm. Regions were generated using Fiji software by selecting the Trainable Weka Segmentation plugin and previously trained classifiers. The NP channel image was filtered to remove noise and background with a rolling radius of 15 pixels. The amount of fluorescence signal (a.u.) was resolved in each region by multiplying the volume-averaged value of the signal by the volume of the respective region. A ratio was obtained by normalizing data of the nuclei-associated region by the signal within the cytoplasmic region.

3D intensity map of spatial-temporal NPs distribution

3D maps were generated from the using the 3D confocal images to evaluate the spatial distribution of NPs within the microvasculature and ECM gel region of the BBB microphysiological model.

The 3D confocal stacks were converted to VTK files using a Matlab code (<https://it.mathworks.com/matlabcentral/fileexchange/58819-write-2d-and-3d-arrays-into-vtk>), before displaying the final 3D intensity maps using Paraview (<https://www.paraview.org/>) and NPs fluorescent intensity were plotted. Biodistribution analysis was defined using Fiji software (<http://rsbweb.nih.gov/ij/>). Briefly, sections of the confocal images of permeability measurements were sampled using line scan measurements at different time points. Then, the intensity profile histograms of the vascular cross-section were plotted.

Cell viability assay

The cell viability assay (MTS assay) was executed following the manufacturer's instructions (CellTiter 96 AQueous One Solution Cell Proliferation Assay, Promega). iPSC-ECs were cultured in 96-well plates and grown to confluency (~ 80%). NPs were resuspended in culture medium using different concentrations (0 - 500 $\mu\text{g/mL}$), added to cells up to 4 hours incubation time. Then, cells were washed twice with PBS before adding the MTS reagent. Absorbance measurements were performed using the Vmax micro plate reader (Molecular Devices).

Statistical analysis

All data were plotted as the mean \pm SD using Prism (GraphPad software). Statistical analysis was determined using a two-tailed Student's t-test and where appropriate, one-way ANOVA with Holm-Sidak's multiple comparisons test. P values and adjusted P values (ANOVA) of less than 0.05 were taken as evidence of a statistically significant difference. For permeability measurements, data were analyzed using a two-tailed Student's t-test and where appropriate, one-way ANOVA with Holm-Sidak's multiple comparisons or Kruskal-Wallis H test with Dunn's multiple comparisons test.

Results

Characterization of the 3D Microphysiological BBB model

The 3D Microphysiological BBB model was established by tri-culture of human induced pluripotent stem cell-derived endothelial cells (iPSC-ECs), human brain vascular pericytes (PCs) and human brain astrocytes (ACs) in 3D fibrin hydrogel (iPSC-ECs + PCs + ACs), to mimic the structural organization of the brain microcirculation and BBB interface found in *in vivo* human brain (Figs. 2.1a, b, Chapter 2), (Fig. 2.5a). After injection of cell-gel suspension on the inlet port, iPSC-ECs elongated and formed intracellular interconnections; vacuoles appeared after 24 hours followed by lumen organization and capillary structures after 2-3 days. Combinations of two different media enriched with growth factors (VEGF (50 ng/ml) and 1% v/v of Astrocyte Growth Supplement) were used (Fig. 2.6b). Then, iPSC-ECs spontaneously formed a microvascular network (μ VN) with highly interconnected microvasculature by day 7 of the microfluidic culture (Fig. 2.6b).

The 3D microphysiological BBB model formed by vasculogenesis-like process, consisted of perfusable and well-connected, self-organized μ VN in a microfluidic system (Fig. 2.6c). iPSC-ECs seeded in the side channels created an interconnected and perfusable macrovessel that reduced possible leakage through the side barrier of the microfluidic channel of the central gel region and promoted the connection of vessels to the media channels, facilitating flow into the microvasculature (Fig. 2.6d). Apart the complete BBB tri-culture condition iPSC-ECs + PCs + ACs, the other two conditions, iPSC-ECs mono-culture and iPSC-ECs + PCs co-culture were tested to unveil the single cell component contribution (Figs. 2.7a - c). A typical BBB characteristic is its stratified organization with cell layers around blood vessels under contact interactions. Through high-resolution confocal microscopy imaging, spontaneous self-organization into multicellular BBB-like structures was observed. PCs spontaneously overlapped with endothelial vasculature at multiple locations recapitulating BBB-like structures. Indeed, PCs (F-actin, red, Fig. 2.6d) adhered to both sides of the EC surface, surrounding the vessel (CD31, green, Fig. 2.7d-f). For example, tracing the intensity profiles of EC and PC in confocal images (Fig. 2.7e), F-actin signal was detected outside the vessel, clearly outlining the presence of PCs (Figs. 2.8f, 2.9a). These images displayed that PC partially overlapped the external surface of the EC walls

exhibiting a BBB-like organization. Compared to a culture of iPSC-ECs that formed large microvasculature, these results suggested that interactions with PCs effectively facilitated endothelial organization, by stabilizing a mature microvasculature with closer morphology to that of *in vivo* brain capillaries. 3D images of capillary bifurcations showed PCs in contact with the endothelium at multiple locations (Fig. 2.7f). Furthermore, direct contact of astrocytic end feet and abluminal vascular surface was also observed. ACs addition further assisted in the evolution of complex cell-cell connections and branches similar to those present in the native microvasculature. Additionally, direct cell body contacts were observed between AC endfeet (Glial Fibrillary Acidic Protein, (GFAP), violet) and the abluminal surface of the brain vessels (CD31, green, Fig. 2.7g, 2.9b, 2.9c). In all model conditions cells self-assembled into complex cell organization and recapitulated vascular brain morphogenesis. As geometrical parameters of the μ VN, microvascular capillary diameters and branch length were quantified from confocal images of the μ VN (Figs. 2.7c, 2.8a-c).

In each condition, iPSC-ECs mono-culture, iPSC-ECs + PCs co-culture and iPSC-ECs + PCs + ACs tri-culture, μ VN were formed. However, in the iPSC-ECs mono-culture, microvessels fused and formed large vessel diameters (average lateral diameter $108 \pm 14 \mu\text{m}$, and transverse diameter $29 \pm 10 \mu\text{m}$) expressed as mean \pm SD, and slowly regressed at 7 days end-point (Fig. 2.8d, g). The diameters were significantly smaller in the case of iPSC-ECs + PCs co-cultures (average lateral diameter: $64 \pm 13 \mu\text{m}$, average and transverse diameter: $27 \pm 7 \mu\text{m}$) (Fig. 2.8 e, g). The model also exhibited higher tortuosity and random orientation in the 3D gel region. Finally, iPSC-ECs + PCs + ACs tricultures allowed the formation of μ VN with the following size features: $42 \pm 13 \mu\text{m}$ (lateral size); $25 \pm 6 \mu\text{m}$ (transverse size) expressed as mean \pm SD, showing a cross-section, circularity and a diameter similar to those of *in vivo* human brain microcirculation (arterioles and venules have 10-90 μm size; capillaries have 7-10 μm size) (Fig. 2.8f, g).

Moreover, μ VN branch length average was reduced in the 3D microphysiological BBB model ($136 \pm 24 \mu\text{m}$) compared to mono-culture of iPSC-ECs ($226 \pm 40 \mu\text{m}$) and co-culture of iPSC-ECs + PCs ($179 \pm 31 \mu\text{m}$) (Fig. 2.8h), proving a more intertwined μ VN. Therefore, the microvascular model conditions covered gradually less surface area in the projected confocal image (62% and 42%, respectively) (Fig. 2.8i), reaching 28% covered area in the case of iPSC-ECs + PCs + ACs triculture. Indeed, the BBB model showed more physiological morphology, with decreased capillary diameters and branch length, probably due to the secretion of angiogenic factors from

PCs and ACs. These μ VN also exhibited more random interconnections and tortuosity and a more similar structure to the *in vivo* cerebral microvessel morphology.

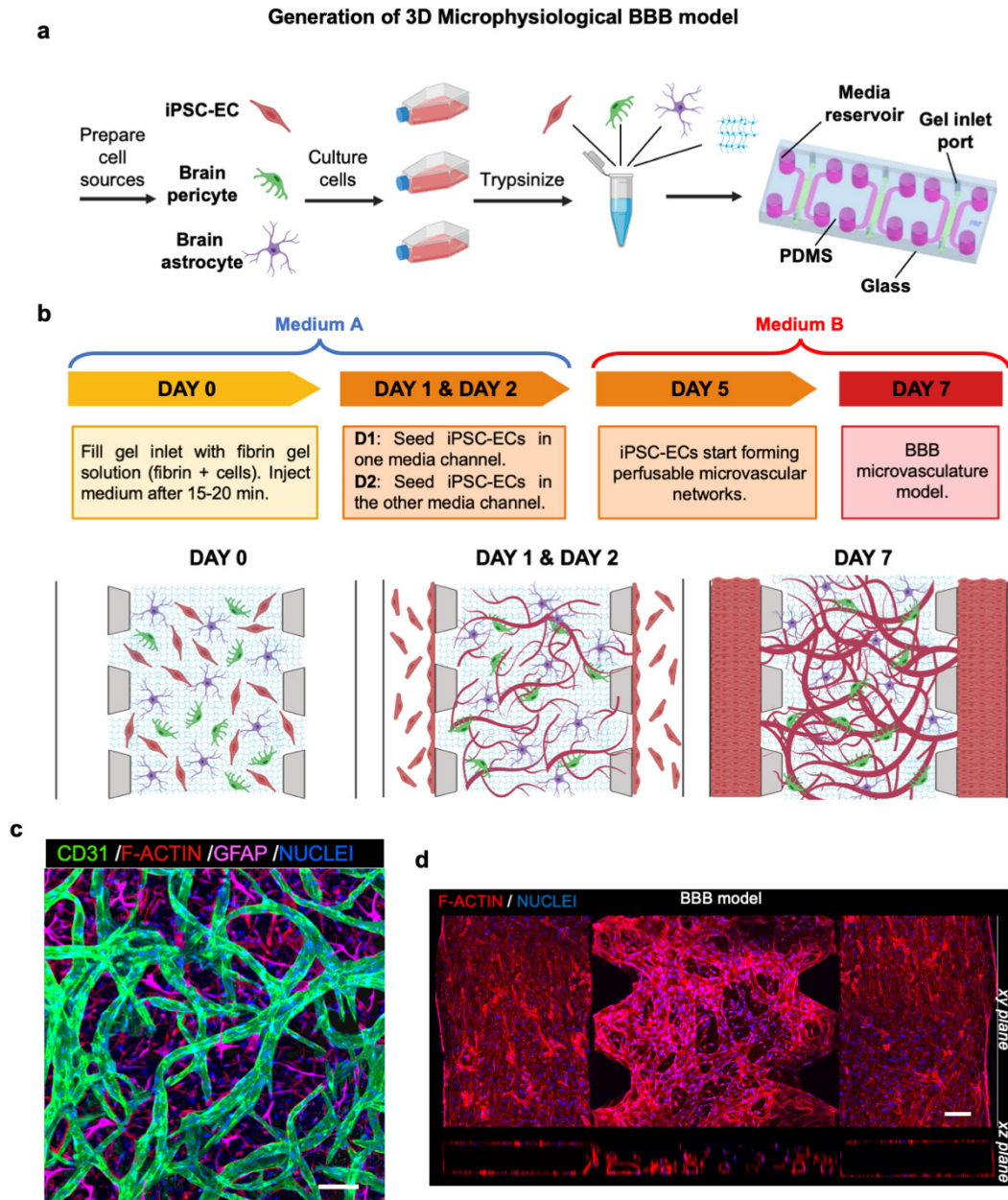


Figure 2.6 : Blood-Brain Barrier (BBB) and 3D Microphysiological BBB model.

a) Schematic explanation of BBB model and protocol, from 2D culture of induced pluripotent stem cells-derived endothelial cells (iPSC-ECs), brain pericytes (PCs) and brain astrocytes (ACs) to generate a 3D Microphysiological BBB model by self-assembled vasculature within a microfluidic device. The PDMS microfluidic platform was fabricated using soft lithography techniques and designed with inlet ports for injecting cell-gel suspensions, and large medium reservoirs and fluidic channels for culture medium. **b)** Experimental protocol and timeline with details on culture

*medium procedure to realize the 3D Microphysiological BBB model. Schematic of dynamic culture of the Microphysiological BBB model over time in a section of 3D microfluidic system. Experimental steps and seeding configuration and of vasculogenesis process of Microphysiological BBB model including iPSC-ECs + PCs + ACs as self-assembled microvascular network that undergoes maturation within 7 days of culture. 3-dimensional ECs layer covering top, bottom and side surfaces of the fluidic channels. **c)** Confocal image of self-assembled μ VN of the Microphysiological BBB model including iPSC-ECs (CD31, green), PCs (F-actin, red) and ACs (GFAP, magenta), and nuclei (DAPI, blue). **d)** Confocal images of xy and xz (cross-section) planes of the 3D Microphysiological BBB model with iPSC-ECs + PCs + ACs, including EC layers in the side channels. Scale bars 200 μ m. **c, d)** Reproduced with permission from [221]. All schematics were created with BioRender.com.*

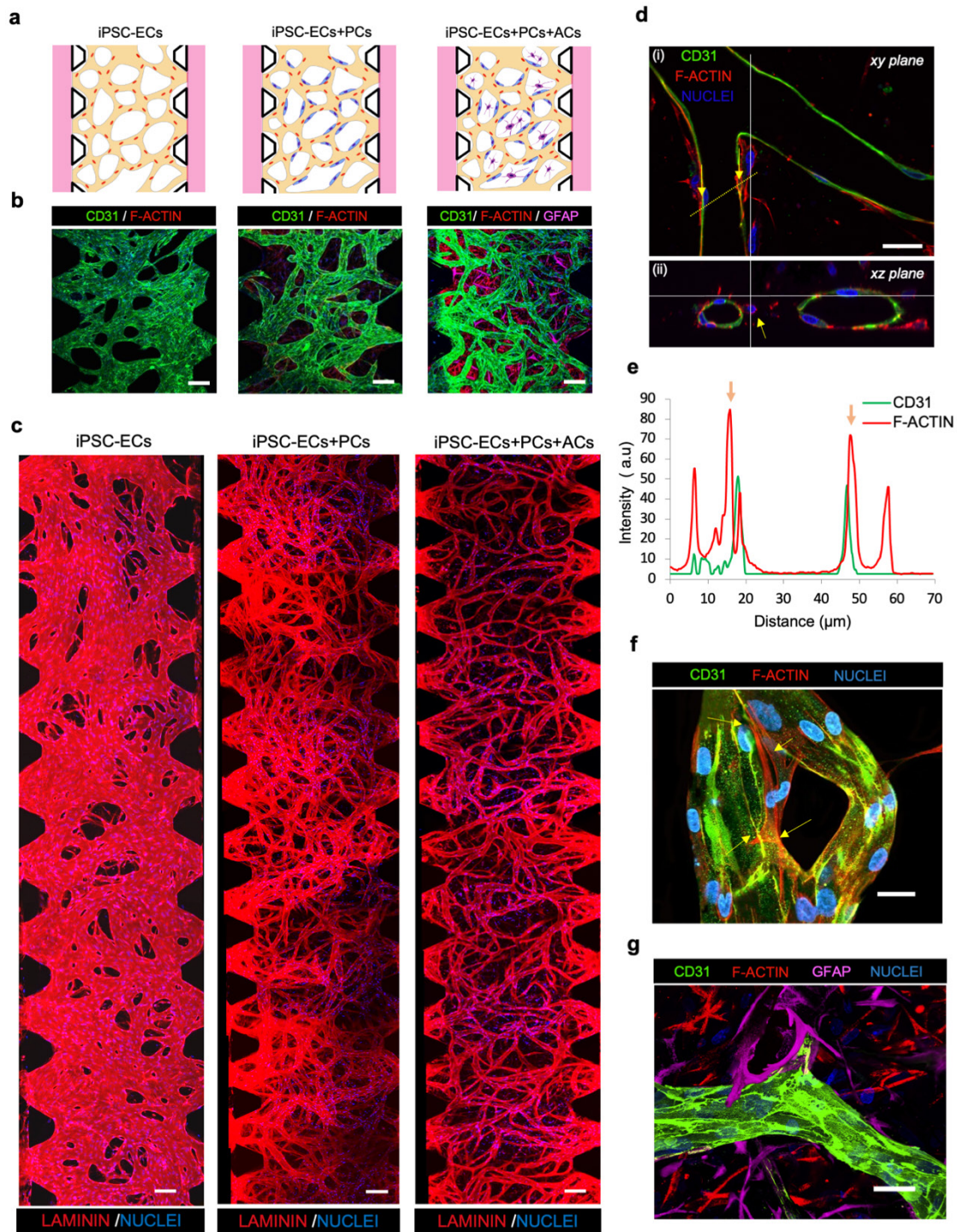


Figure 2.7: Microvascular conditions and iPSC-ECs - PCs/ACs contact interactions.

a) Schematic representation and **b)** confocal images of iPSC-ECs mono-culture (CD31, green), co-culture with PCs (F-actin, red), and tri-culture with PCs and ACs (GFAP, magenta), after 7 days of culture in the microfluidic system. **c)** Confocal images of microvascular network conditions of the entire microfluidic system of iPSC-ECs, iPSC-ECs+PCs and iPSC-ECs+PCs+ACs at day 7. **d)** Confocal images of blood microvessels and cross-sections showed hollow lumens. PCs adhered to and partially covered blood microvessel. Confocal images of cross-sectional blood

microvessels showed iPSC-ECs surrounded by PCs. The yellow line shows how a section was sampled using a line scan measurement producing generation of intensity profile histogram. **e)** Intensity profile analysis of CD31/F-actin in iPSC-ECs -PCs interaction corresponding to the yellow line scan. Contact interaction/overlapping between ECs and PCs are shown by distinct yellow arrow matching with the same peak at the intensity profile. CD31 expression (green) was low when F-actin expression (red) was highly expressed, further indicating that detected F-actin belonged only to brain PCs outside the vessels. Region of low green intensity corresponds to the vascular bed of the vessel. **f)** Contact interactions of PCs enveloping and adhering to a blood brain capillary. **g)** Confocal image of iPSC-ECs, PCs and ACs in the Microphysiological BBB system. Scale bars indicate 100 μm , (b), Scale bars 200 μm , (c). and 20 μm (d, f, g). Reproduced with permission from [221].

Protein and gene expressions of the Microphysiological BBB model

In order to analyze whether the engineered 3D Microphysiological BBB model constituted a functional barrier interface and exhibited physiological features typical of the BBB present *in vivo*, quantitative real-time RT-PCR and immunocytochemistry analyses were performed.

The endothelial-specific junction proteins ZO-1, occludin and claudin-5 (Fig. 2.10a-c, Fig. 2.11a), and ECM proteins such as laminin (Fig. 2.10d) and collagen IV (Fig. 2.10e) expressions were evaluated by confocal microscopy (Figs. 2.11b-f). Continuous ECs cell-cell junctions disposed as rhomboidal boundaries along lumens were observed in co-culture and tri-culture conditions, as demonstrated by the clear presence of ZO-1 along the cell-cell border. Interestingly, an increase of TJ protein expression between μVN models was observed. Therefore, the BBB microphysiological model obtained by iPSC-ECs + PCs + ACs tri-culture expressed relatively higher level of ZO-1 as well as occludin and claudin-5, in comparison to mono-culture and co-culture control conditions. Another sign of microvascular maturation was the production of basement membrane proteins, such as laminin and collagen IV exhibiting a similar trend to junctional proteins. The immunofluorescence intensity of laminin and collagen approximately doubled in the case of the iPSC-ECs + PCs + ACs (Fig. 2.11d-f). To confirm immunocytochemistry results of protein expression, bulk RNA was extracted and purified from the entire cell population from the microfluidic systems (Fig. 2.12a). Three different conditions were compared at several time points (day 0, 4, and 7). RT-PCR analysis was conducted considering gene markers of junctional proteins, ECM deposition and several EC membrane transporters such as passive diffusion, active efflux, carrier-mediated, ion and receptor-mediated transport. Microvascular maturation was examined in terms of their gene expression and compared

to control conditions (iPSC-ECs). The mRNA was reported as relative to CD31 and GAPDH expression (fold change). TJ proteins such as ZO-1, occludin, and claudin-5 were highly upregulated in tri-culture conditions at day 7 compared to iPSC-ECs + PCs and iPSC-ECs conditions suggesting higher level of maturation. Indeed, ZO-1 expressions were well defined and clearly presented at the intersection between cells forming a rhomboidal grid, characteristic of mature and well-organized capillaries. Instead, mono-culture exhibited low expression of TJ proteins with no accumulation at cell-cell boundaries. Similar trend was shown by occludin (Fig. 2.10b) and claudin-5 (Fig. 2.10c). Interestingly, the expression of TJ markers in the BBB microphysiological model increased as a function of the time of culture (Fig. 2.1-a-c, Figs. 2.11a-e). As expected, GFAP was only expressed in the presence of ACs. PDGFR gene expression was slightly higher in the tri-culture condition while alpha-smooth muscle actin (aSMA) expression was reduced, possibly due to the increased proliferation of all cell components. Additionally, ECM proteins (collagen IV, laminin) were highly expressed over time in the triculture condition compared to the mono- and co-culture cases. In addition, compared to iPSC-ECs + PCs and iPSC-ECs models, gene expression of transport mechanisms specific of the BBB, such as P-GP, MRP1, MRP4, TF-R, LRP1, LAT-1, GLUT-1, CAT1, MCT1, ABCA1, and BCRP was upregulated and increased over time in the tri-culture BBB model (iPSC-ECs + PCs + ACs). Overall, after 7 days, the triculture condition displayed a constantly increased maturation and up-regulation of all examined genes (Fig. 2.12b, Primer sequences in Table 4). Overall, the immunostaining results were in agreement with RT-qPCR data of BBB-related gene expression demonstrating that the tri-culture of iPSC-ECs + PCs + ACs gave rise to a BBB microphysiological model with closer BBB-like features and maturation.

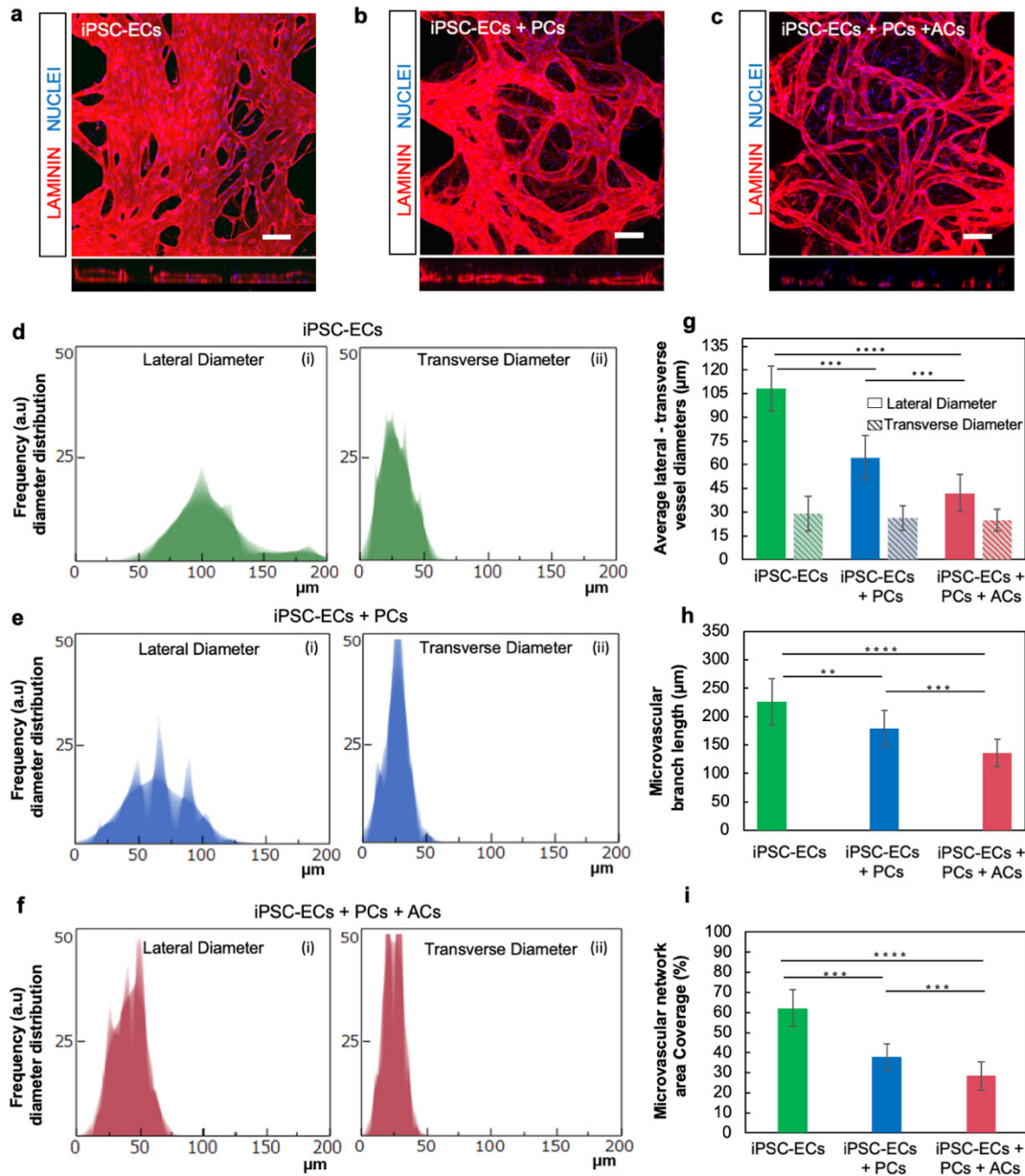


Figure 2.8: Quantification of microvascular parameters of 3D BBB Microphysiological model.

Confocal images of 3D BBB μVN conditions showing laminin expression (red) and cell nuclei (DAPI, blue) **a)** monoculture of iPSC-ECs, **b)** co-culture of iPSC-ECs + PCs and **c)** tri-culture of iPSC-ECs + PCs + ACs (scale bar: 100 μm). Distribution of lateral and transverse vessel diameter measurements of 3D Microphysiological BBB conditions formed by vasculogenesis, for **d)** monoculture of iPSC-ECs, **e)** co-culture with brain PCs, **f)** tri-culture with brain PCs and ACs. **(g, h, i)** Quantification of microvascular parameters: **g)** average lateral and transverse capillary diameters of each condition, **h)** average microvascular branch length and **i)** percentage ratio of microvascular network area coverage to the total area. $*p < 0.05$, $**p < 0.01$, $***p < 0.001$, $****p < 0.0001$. Average values \pm SD, $n = 30$. Reproduced with permission [221].

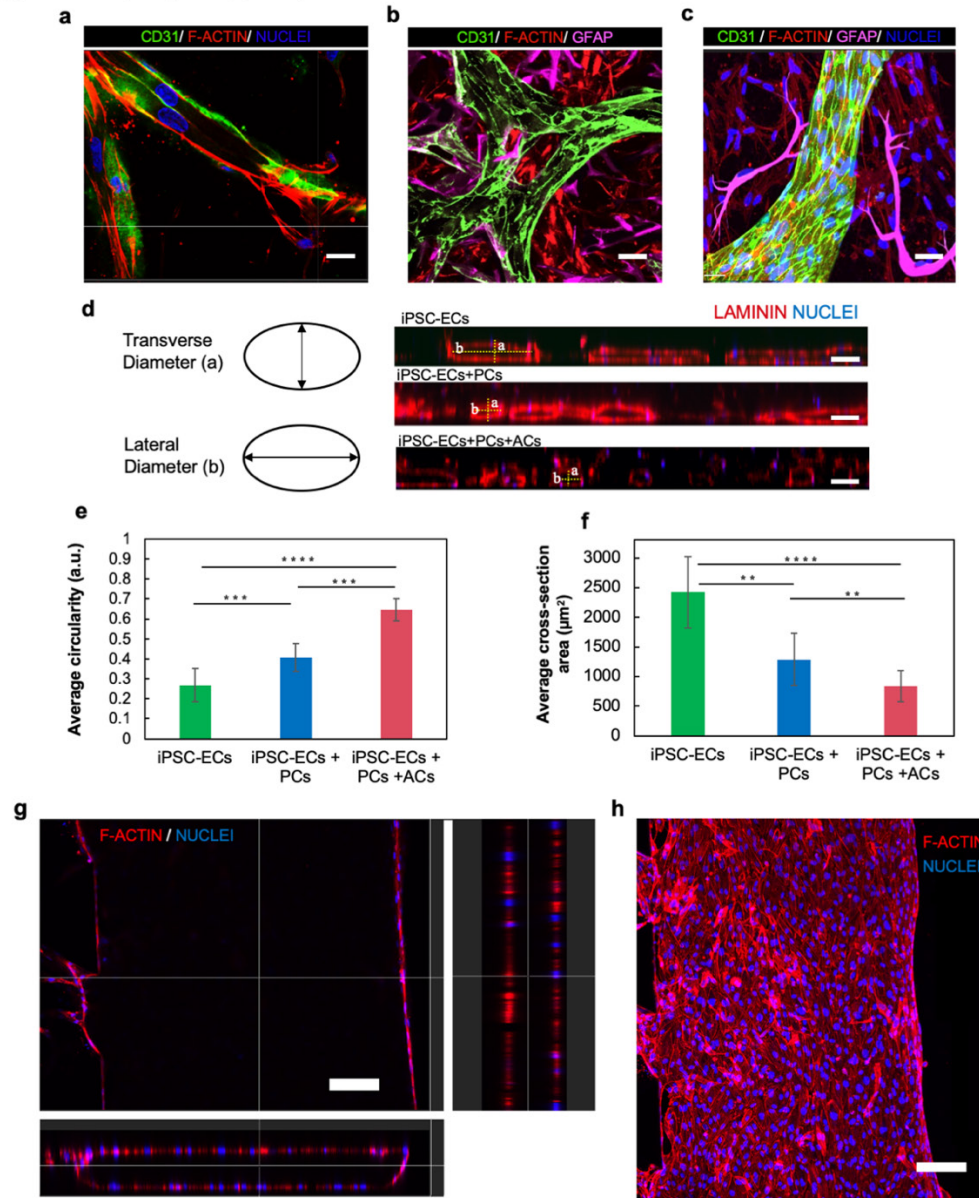


Figure 2.9: iPSC-ECs-PCs/ACs contact interactions and microvascular parameters.

a) images of a blood microvessel showing a hollow endothelial cells lumen, where PCs adhere and partially envelop brain microvessel. **b-c)** Cross-sectional images of a blood microvessel showing a lumen enclosed by ACs and PCs. **d-e)** Circularity is the ratio between transverse and lateral diameters. **f)** Average vascular cross-section area for iPSC-ECs, iPSC-ECs + PCs, and iPSC-ECs + PCs + ACs at day 7. 3D iPSC-ECs monolayer in the side channel. **g)** Maximum projection confocal images and **h)** cross section of 3D endothelial cells layer. Scale bar indicate 25 μm (a, b, c), and 50 μm (e). Data shows * $p < 0.05$, ** $p < 0.01$, *** $p < 0.001$, **** $p < 0.0001$. Day 7, Average values SD, $n = 20$. Reproduced with permission from [221].

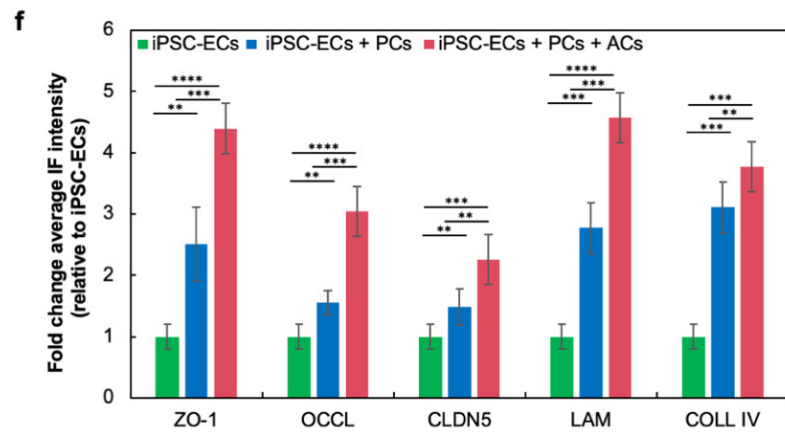
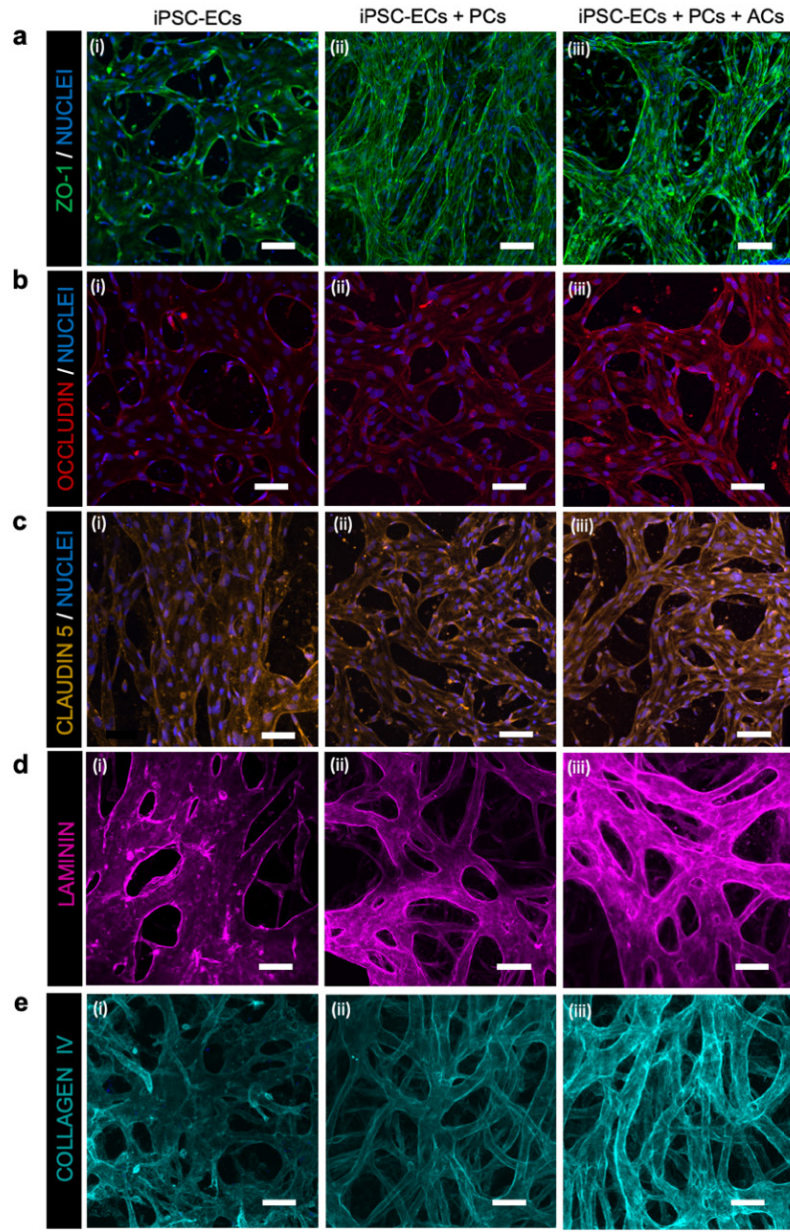


Figure 2.10: BBB junctions and ECM expression analysis by immunocytochemistry.

a) Confocal images showing the expression of tight junction ZO-1 protein, **b)** occludin (OCCL) and **c)** claudin-5 (CLDN 5); **d)** ECM production of laminin (LAM) and **e)** collagen IV (COLL IV)) in the case of **(i)** mono-culture of iPSC-ECs, **(ii)** co-culture with PCs and **(iii)** tri-culture with PCs and ACs. BBB microvascular model with PCs and ACs expressed higher intensities of junctional proteins, laminin and collagen IV compared to monoculture and co-culture, providing evidence, by qualitative ROI analysis of intensity, that PCs and ACs improved vascular function. **f)** Quantification of IF intensity (relative to iPSC-ECs) of protein expression from confocal images. Intensities were normalized by the ROI area. * $p < 0.05$, ** $p < 0.01$, *** $p < 0.001$, **** $p < 0.0001$. Average values \pm SD, $n = 8$. Scale bar: 50 μ m. Reproduced with permission from [221].

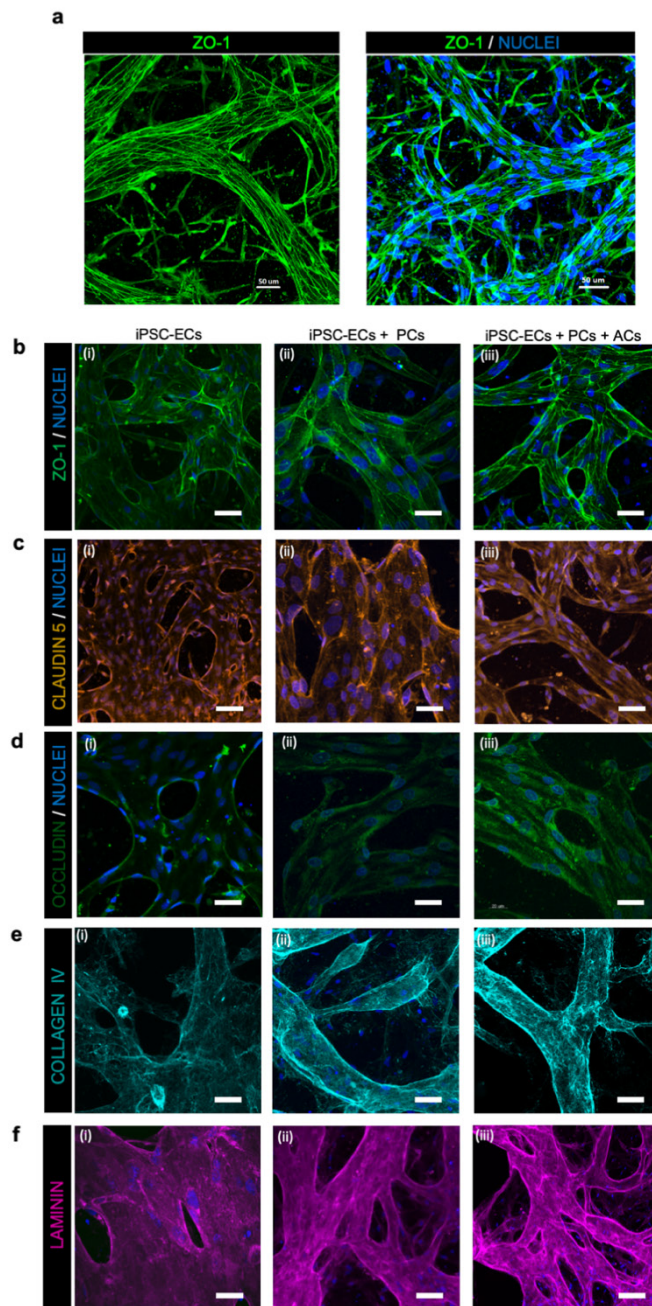


Figure 2.11: Immunocytochemistry analysis of tight junctions and ECM protein deposition.

a) Typical rhomboidal tight junction boundaries (ZO-1) between cells forming microvasculature (i) with and (ii) without nuclei. **b)** Confocal images of tight junctions ZO-1, c) occludin (OCCL) and d) claudin-5 (CLDN 5)), e) expression of ECM proteins such as laminin (LAM) and f) collagen IV (COLL IV)), (i) mono-culture of iPSC-ECs, (ii) co-culture with PCs and (iii) tri-culture with PCs and ACs. Confocal images were acquired at day 7, 60X magnification. Scale bars are: (a) 50 μm and (b-f) 20 μm . Reproduced with permission from [221].

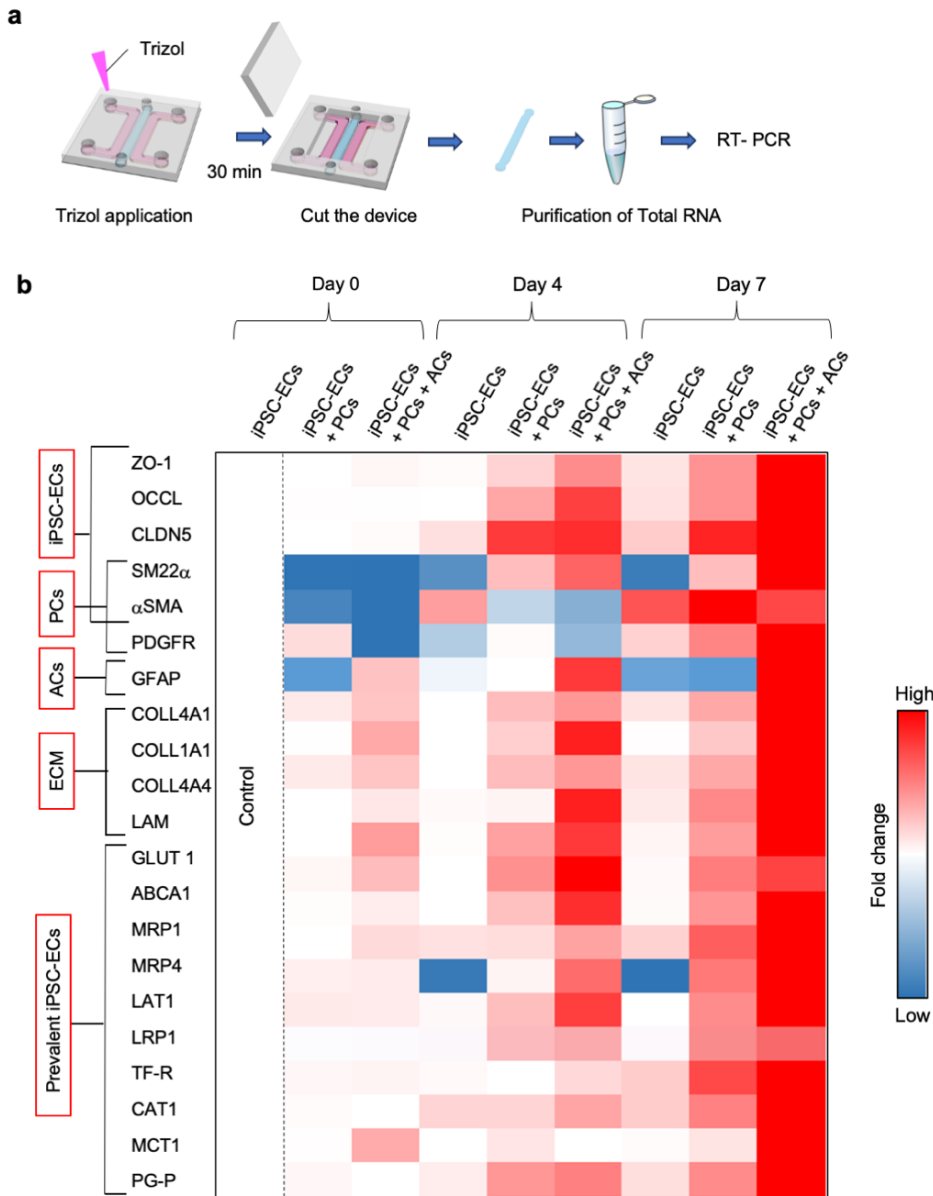


Figure 2.12: Quantitative RT-PCR of 3D Microphysiological BBB model in microfluidic system.

a) Schematic RT-PCR experiments: extraction of cell and gel and purification of bulk RNA from a microfluidic culture. **b)** RT-PCR heatmap of iPSC-ECs mono-culture, co-culture with PCs, and tri-culture with PCs and ACs at several time points (0, 4, 7 days) of mRNA expression of BBB microvascular maturation and other typical BBB-specific features. RT-PCR analysis showed gene

expression of typical markers of 1) ECs, 2) PCs, 3) ACs, 4) ECM proteins, and 5) factors expressed predominantly by ECs, but also by the other two cell types in smaller amounts. Fold change was relative to control (iPSC-ECs mono-culture, day 0). The internal housekeeping gene was CD31. $0.01 < p < 0.05$, $n = 3$. Reproduced with permission from [221].

Specific cell contributions to BBB microvascular permeability

The distinct contribution of brain PCs and ACs to the vascular permeability and perfusability of the 3D Microphysiological BBB was investigated. The assessment of microvascular permeability is a fundamental feature for modelling drug transport and mimick the BBB as to assess the practical ability of the microfluidic culture platform to mimic molecular transport *in vivo*. Firstly, it was shown that all BBB conditions contained well-formed and completely perfusable capillaries by day 7 (Fig. 2.14d). Vascular permeability coefficients were evaluated by perfusing solutions containing FITC-dextran molecules in the microvasculature (10 and 40 kDa), and confocal images were captured every 5 min for 30 min, confirming a functional barrier with high selectivity and size-dependence related to the molecular weight of the fluorescent probe (Figs. 2.13a-d, Figs. 2.14a-d). The contribution of the distinct cell to BBB permeability has been revealed. In the presence of the 3D iPSC-ECs monolayer on the side channels, permeability of 40 kDa FITC-dextran across the microvasculature model progressively decreased from monoculture, to co-culture and triculture: 6.6, 2.5, and 0.89×10^{-7} cm/s (Fig. 2.13e). A similar trend was observed for the permeability values of 10 kDa FITC-dextran which decreased from monoculture to co-culture and triculture: 12, 4.8 and 2.2×10^{-7} cm/s, respectively (Fig. 2.13f). The presence of EC monolayer on the fluidic channels was necessary to hinder the leakage of solutes through the sidewalls of the gel region, avoiding artifacts in the permeability measures. The ECs seeded in the side channels improved the coverage of the exposed vascular-gel region, filled gaps that can sometimes form at the gel-post borders, and increased the contacts between the microvasculature and the main channel, forming a structure similar to capillary ramification connected to a main blood vessel.

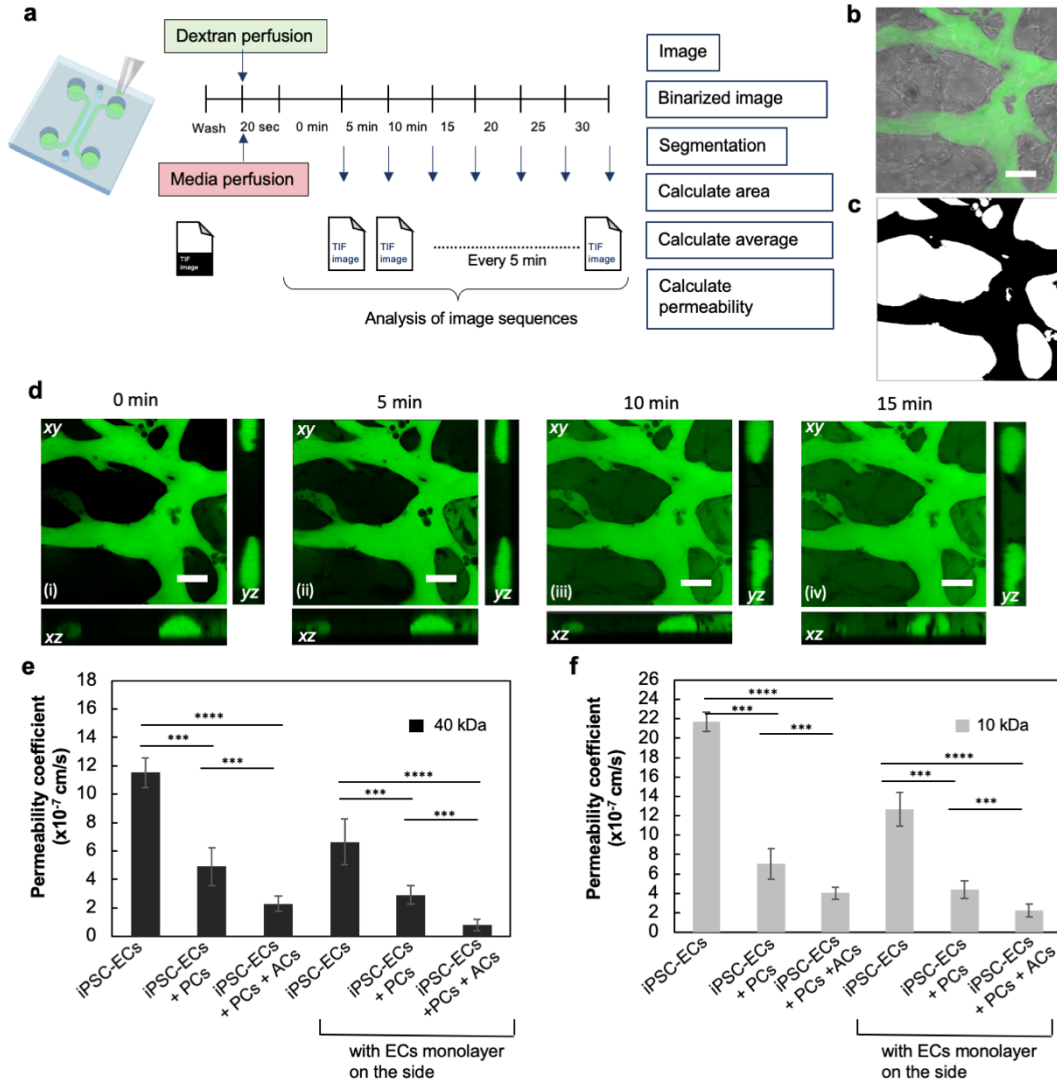


Figure 2.13: Microvascular permeability quantification in BBB model.

a) Microvascular permeability measurement in the microfluidic system: dextran solution was injected in the medium channel after removing medium, and devices were imaged every 3-5 min for 30 min. The figure shows a schematic representation of the workflow for measurement of the permeability coefficient. **b)** Merged confocal- bright field images during dextran fluorescein flux along vasculature. **c)** Image thresholding and binarization after microvessel boundaries identification. **d)** 3D projection and cross-sections including xy, xz and yz planes at 4 timepoints. Vascular permeability coefficients of mono-culture of iPSC-ECs, co-culture of iPSC-ECs + PCs, and tri-culture of iPSC-ECs + PCs + ACs, (with or without ECs monolayer seeded in the side channels) using **e)** 40 kDa and **f)** 10 kDa FTIC-dextran. Data are shown as mean value, error bars \pm SD, $n = 10$, * $p < 0.05$, ** $p < 0.01$, *** $p < 0.001$, **** $p < 0.0001$, scale bars $50 \mu\text{m}$. Reproduced with permission from [221].

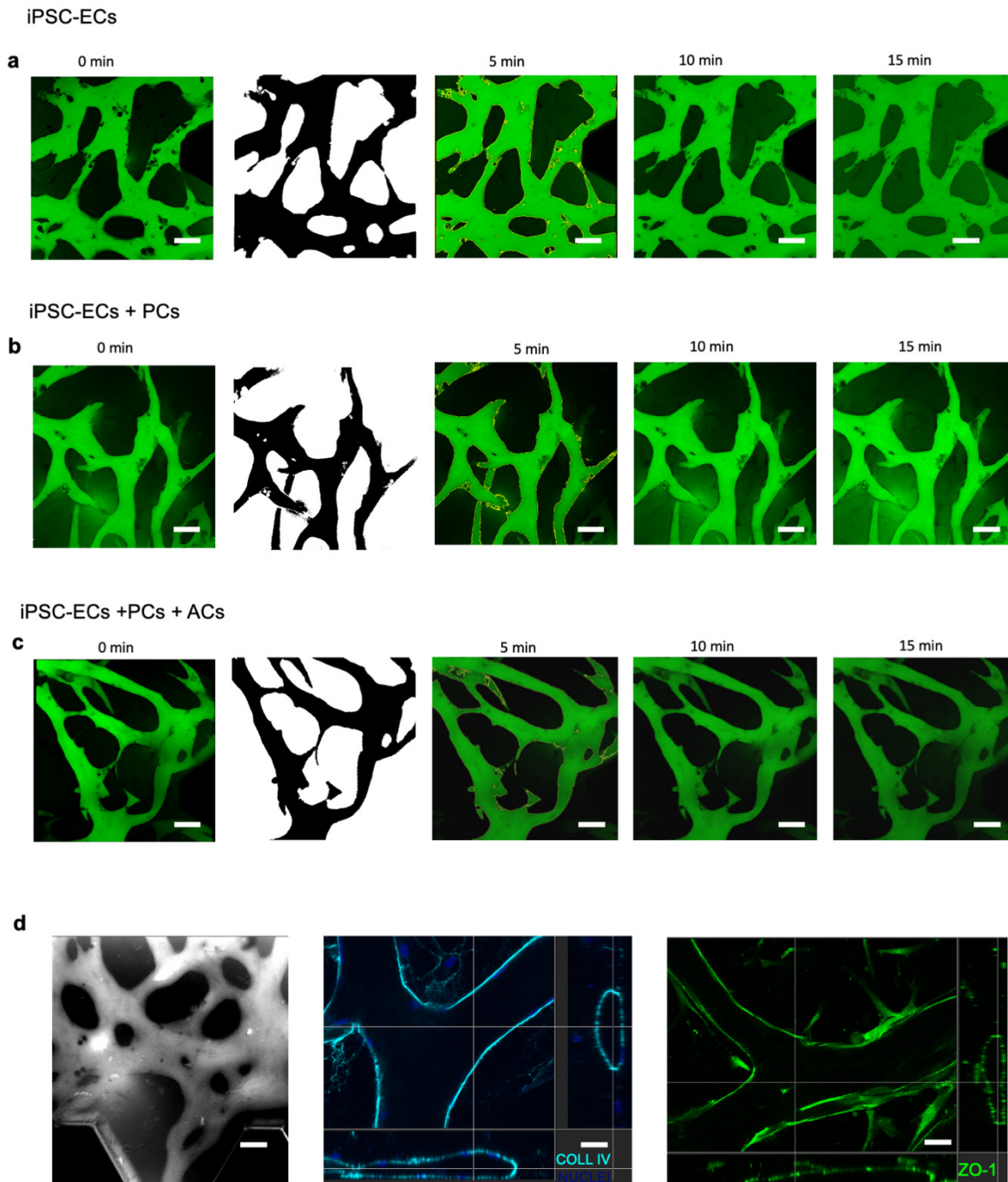


Figure 2.14: Perfusion ability and permeability assay in BBB microphysiological model.

Permeability measurements in different microvascular conditions and at different timepoints. **a)** iPSC-ECs, **b)** co-culture of iPSC-ECs + PCs, and **c)** tri-culture of iPSC-ECs + PCs + ACs, Day 7. **d)** Examples of perfusable microvascular networks with empty lumens. Scale bars are: 50 μm **d)**, 50 μm (**a-c**). Reproduced with permission from [221].

Testing of NPs transport in the 3D Microphysiological BBB model

The 3D Microphysiological BBB model was then explored as a test platform for evaluating NP transport. To identify the right ligand for NPs functionalization, several types of ECs were used: iPSC-ECs, HBMECs and HUVECs (used a control). The cells were 2D-cultured and screened by RT-PCR (Fig. 2.15a). Comparison of HUVECs and iPSC-ECs showed that the transferrin receptor (TfR) was one of the most highly expressed amongst other BBB-specific transporters in iPSC-ECs (2.91 fold higher than HUVECs), but also LAT1 and MRP4 were upregulated (Fig. 2.15a). Although HBMECs highly express junction proteins and mediate several BBB and brain-related transport mechanisms (Fig. 2.15a), HBMECs have previously been observed to organize into irregular *in vitro* microvasculature with large diameters, while iPSC-ECs form well-organized and perfusable capillaries [221]. Based on these results and considerations, the TfR was considered an appropriate transporter model for evaluating NP transport. Additionally, an *in vitro* screening platform based on iPSC-ECs can facilitate the translation of basic research results for clinical application in the context of personalized treatment, also called patients' specific studies. For these reasons, iPSC-ECs were used to design a functional 3D Microphysiological BBB model to test Tf-functionalized NPs.

Physical Characterization of Transferrin-functionalized PS and PU NPs

Initially it was confirmed that PS- and PU-NPs displayed a narrow size distribution by dynamic light scattering (DLS) (Fig. 2.15b). all NPs were functionalized with Tf (PS NPs and synthesized PU NPs), following a previously established method, exploiting carbodiimide-mediated grafting (Figs. 2.15 b-e)[222]. PS and PU NPs showed narrow size distribution (Fig. 2.15f), however, their size and zeta potential increased after Tf-functionalization (Fig. 2.15f and Table 3), as shown in the literature [222], [223].

Cytocompatibility assay and Cell Uptake of PS and PU NPs

Cell viability assays confirmed that NPs were not cytotoxic at several concentrations (0-500 $\mu\text{g/mL}$), as shown by MTS cell viability assay. Particularly, iPSC-ECs treated with NPs showed $81.7 \pm 5.8\%$ of viability compared to control (Fig. 2.15g).

Moreover, 3D confocal images of 2D cultures of iPSC-ECs treated with NPs (Fig. 2.15h) confirmed that NPs were internalized by the cells (Fig. 2.15i and 2.15k) and they were detected in the cell cytoplasm close to cell nuclei (Fig. 2.15j).

Table 3. *Physical characterization of size and zeta potential of NPs.*

NP type	Size [nm]	PDI	ZP [mV]
100 nm (PS)	109.0 ± 0.8	0.0377 ± 0.02	-43.7 ± 0.3
200 nm (PS)	233.0 ± 0.6	0.0373 ± 0.03	-37.0 ± 2.4
400 nm (PS)	457.0 ± 16.5	0.122 ± 0.07	-37.4 ± 2.0
100 nm (PS-Tf)	203.0 ± 3.1	0.215 ± 0.04	-0.04 ± 0.2
PU	112.0 ± 1.0	0.0940 ± 0.01	-44.9 ± 4.0
PU-Tf	118.0 ± 1.4	0.157 ± 0.01	-32.2 ± 0.5

2D Transwell BBB Model for NP Permeability

To evaluate the permeability of NPs, a 2D BBB transwell model was also developed (Fig. 12l), and TEER was measured as a function of culture time, showing values from $130.0 \pm 8.3 \Omega \text{ cm}^2$ after 24 h, to $189.0 \pm 3.4 \Omega \text{ cm}^2$ after 2-3 days (Fig. 2.15m). The PS NPs showed similar permeability and no size dependency after 1 hour (Fig. 2.15n), while PU NPs showed significantly increased permeability compared to PS NPs (Figs. 2.16f).

Permeability of PS-Tf NPs showed a 2.06-fold higher level compared to non-functionalized PS NPs after 3 hours (Fig. 2.15n). In contrast, there were no significant differences in permeability values between functionalized PU-Tf NPs and PU NPs at 2 time point). Additionally, FITC-dextran and NPs permeability remained without changes while tested in combination (Fig. 2.16 d,e). Although the transwell model could recapitulate the theoretical effects of Tf-functionalization on NP permeability, at least 3 h was required for Tf-functionalized PS-NPs to display significant increased in permeability over non-functionalized PS-NPs. On the other hand, the Tf-induced increase in permeability at 1 h, was short-lived for PU-NPs, and differences in permeability was no longer observed at 3 h (Figure 2.16 d,e). Such findings suggest that 2D transwell assays may

not facilitate direct comparisons between NPs from different materials. The results also suggest that alternative platforms should be developed to reduce the time needed to evaluate the efficacy of NP delivery.

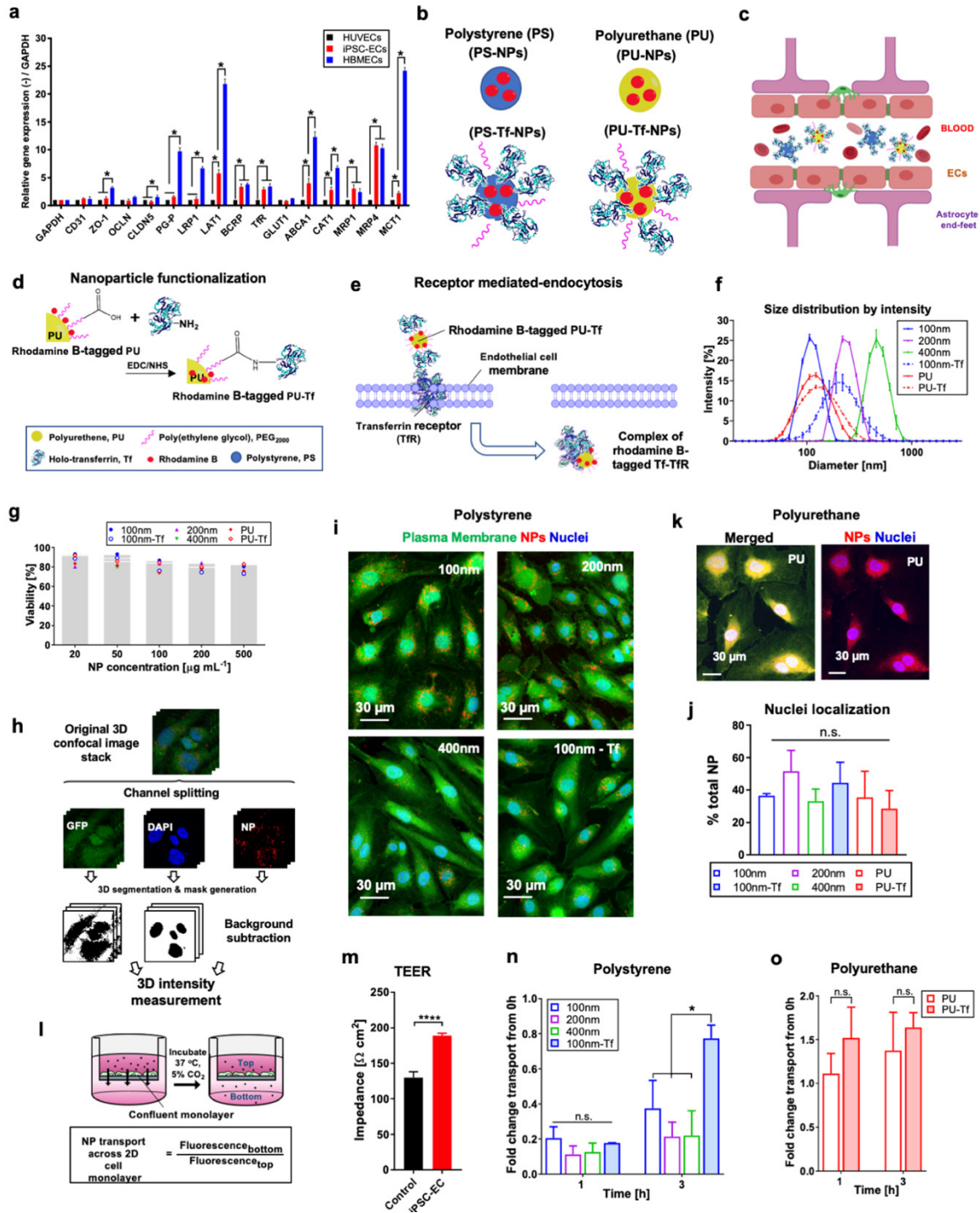


Figure 2.15: Polymer Nanoparticle Testing in 2D culture systems.

a) Gene expression of EC transporters and tight junctions of BBB maturation features by different 2D culture of ECs over 7 days. RT-PCR is plotted as relatively expressed respect to HUVEC, and GAPDH as the internal housekeeping gene. **b)** Schematics of PU and PS NPs, **c)** BBB section and NPs circulating inside BBB blood vessel. **d)** Preparation of Tf-functionalized PU NPs and **e)** schematic of TfR-mediated endocytosis of Tf-functionalized NPs. **f)** Size distribution of NPs +/- Tf functionalization by DLS characterization. **g)** iPSC-EC viability for several NP concentrations compared to control. **h)** Method for NPs uptake quantification and localization of NPs in the cellular compartment or close to the nuclei. Confocal images of NPs cell uptake of **i)** PS NPs +/- Tf and **k)** PU NPs. **j)** Percentage of NPs localized at nuclei boundaries over the total NPs per cell. **l)** Transwell experimental setting for NP transport evaluation across an iPSC-EC monolayer. Permeability was assessed as ratio of fluorescence intensity measured from media collected from the bottom and top of a Transwell system. **m)** TEER measurement of iPSC-EC monolayer. Total amount of NPs movement across an iPSC-EC monolayer in the transwell system from 0 h for **n)** PS and **o)** PU NPs. Data are shown as the mean \pm SD, $n \geq 3$ independent experiments, with $* p \leq 0.05$. (n.s.: not significant). Reproduced with permission from [226].

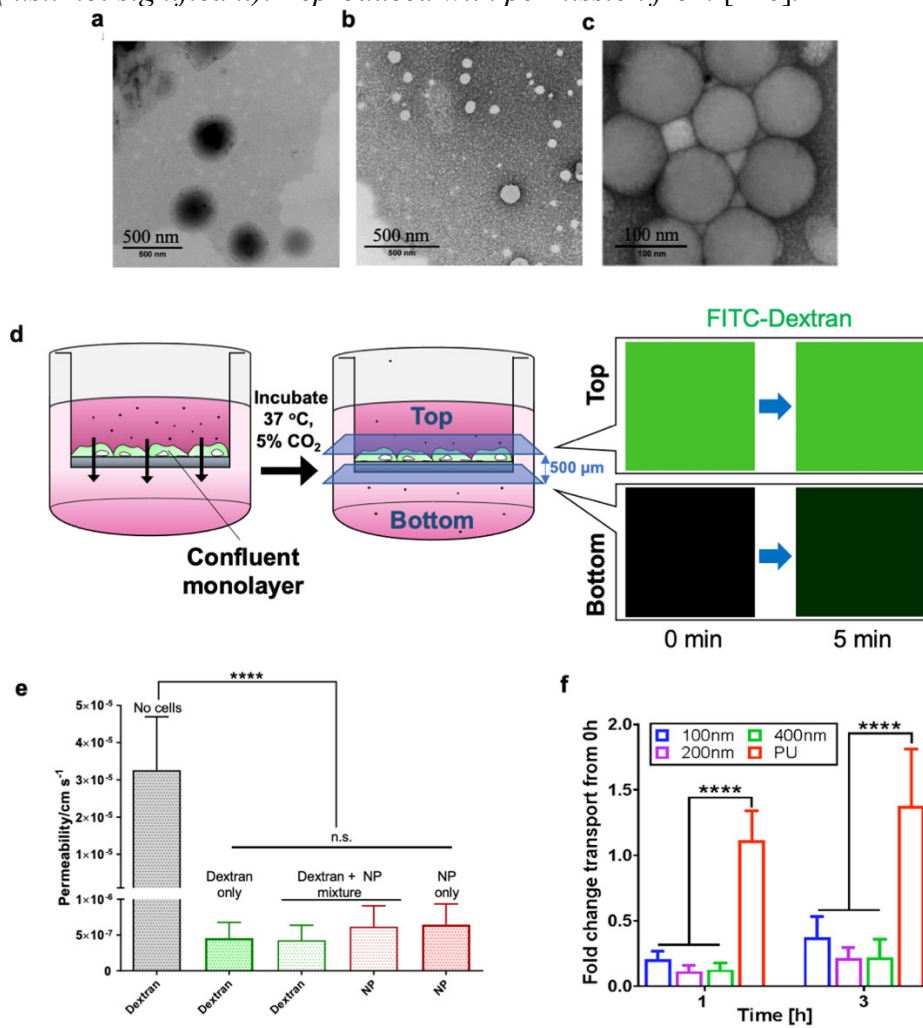


Figure 2.16: Nanoparticle experiments in 2D transwell systems.

a, b) Morphology of PU (polyurethane nanoparticles (NPs) as observed by transmission electron cryomicroscopy (Cryo TEM) and TEM, respectively. PU NPs display a spherical shape **c)** Commercial PS NPs displayed a spherical shape. Reproduced with permission from [227]. In a transwell setting, to measure NP transport at each timepoint, medium in the insert and bottom well was separately collected. Net movement of NPs across the iPSC-EC monolayer was calculated by the ratio of measured fluorescence intensity of media collected from the bottom and top of the transwell insert. **e)** Relative permeability of 70 kDa FITC-dextran and 100 nm PS NPs across an iPSC-EC monolayer in a transwell setting. The x-axis shows the reagent being measured in the added solution which include (from left) only FITC-dextran, a mixture of FITC-dextran and PS NPs, and only PS NPs. Permeability was calculated by analyzing the fluorescence intensity of confocal images that were taken at 5 min intervals of the region above and below the transwell insert (interspace: 500 μm). **f)** PU NP transport across the 2D iPSC-EC monolayer is significantly enhanced compared to PS NPs. Data are presented as the fold change in net movement of NPs across an iPSC-EC monolayer at 0 h, and are shown as the mean \pm SD, $n = 3$, with **** $p \leq 0.0001$. Reproduced with permission from [226].

NPs microvascular Permeability Across a 3D Microphysiological BBB model

The 3D Microphysiological BBB model was used for vascular permeability measurements of polymer NPs. Briefly, solution of NPs and culture medium with dextran were injected in the medium reservoirs and let stabilize for few seconds. Then, merge confocal images were acquired every 5 minutes at each timepoint, for 30 min. Confocal images were split into single channels and 3D volume generated. After network segmentation, vascular permeability to fluorescent tracers and NPs was calculated (Fig. 2.17 b, c). Firstly its capability to differentiate the microvascular permeability of 10, 40 and 70 kDa fluorescent FITC-dextran was characterized observing a decrease in permeability measurements (2.21 ± 1.96 , 0.83 ± 0.86 , $0.62 \pm 0.39 \times 10^{-7} \text{ cm s}^{-1}$, respectively) (Figure 2.17c) that was consistent with previous characterization, which was decreased with an increase in dextran molecular weight (10 kDa: $2.21 \pm 1.96 \times 10^{-7} \text{ cm}\cdot\text{s}^{-1}$; 40 kDa: $0.83 \pm 0.86 \times 10^{-7} \text{ cm}\cdot\text{s}^{-1}$; 70 kDa: $0.62 \pm 0.39 \times 10^{-7} \text{ cm}\cdot\text{s}^{-1}$) (Fig. 14c), as previously shown [221]. There was no significant difference in the microvascular permeability values of several PS NPs with different sizes (100 nm: $1.64 \pm 1.36 \times 10^{-7} \text{ cm s}^{-1}$; 200 nm: $1.33 \pm 0.87 \times 10^{-7} \text{ cm s}^{-1}$; 400 nm: $1.42 \pm 0.72 \times 10^{-7} \text{ cm s}^{-1}$) (Fig. 2.17d). This suggests that over a relatively short time frame, NP permeability did not depend on size, but possibly on other factors, such as material composition and surface functionalization.

Interestingly, Tf-functionalization resulted in a significant increase for PS-Tf NPs ($3.09 \pm 3.26 \times 10^{-7} \text{ cm s}^{-1}$) over non-Tf-functionalized NPs (Fig. 2.17e). PU NPs displayed a comparable microvascular permeability ($1.58 \pm 1.16 \times 10^{-7} \text{ cm s}^{-1}$) as PS NPs, which was significantly higher for PU-Tf NPs ($3.70 \pm 2.72 \times 10^{-7} \text{ cm s}^{-1}$) (Fig. 2.17f). Vascular permeability to FITC-dextran was not altered in the co-presence of NPs. The same experiments were performed with synthesized PU-NPs which shown to be capable of delivering drug cargo to tumors in an *in vivo* mouse model.

3D Biodistribution of NPs in the BBB Microphysiological model

In an analysis of NP distribution in 3D space inside and outside the microvasculature 3D stack of confocal images acquired from BBB Microphysiological model were perfused with NPs. This analysis allowed evaluation of spatial and time-dependent biodistribution of NPs as 3D intensity measurements (Fig. 2.18a). A 2.5-fold increase was detected in fluorescence intensity in the ROI near the smallest blood vessels over two timepoints (Fig. 2.18b). Minor fluctuations in fluorescence intensity could be detected as far as 100 μm distance from the vessel border, demonstrating that the NPs might reach a cellular target about 100 μm away from the blood vessels (Figs. 2.18c and 2.18d). These results demonstrated the sensitivity of the algorithm to detect precise fluctuations in fluorescence signals that are associated with NPs.

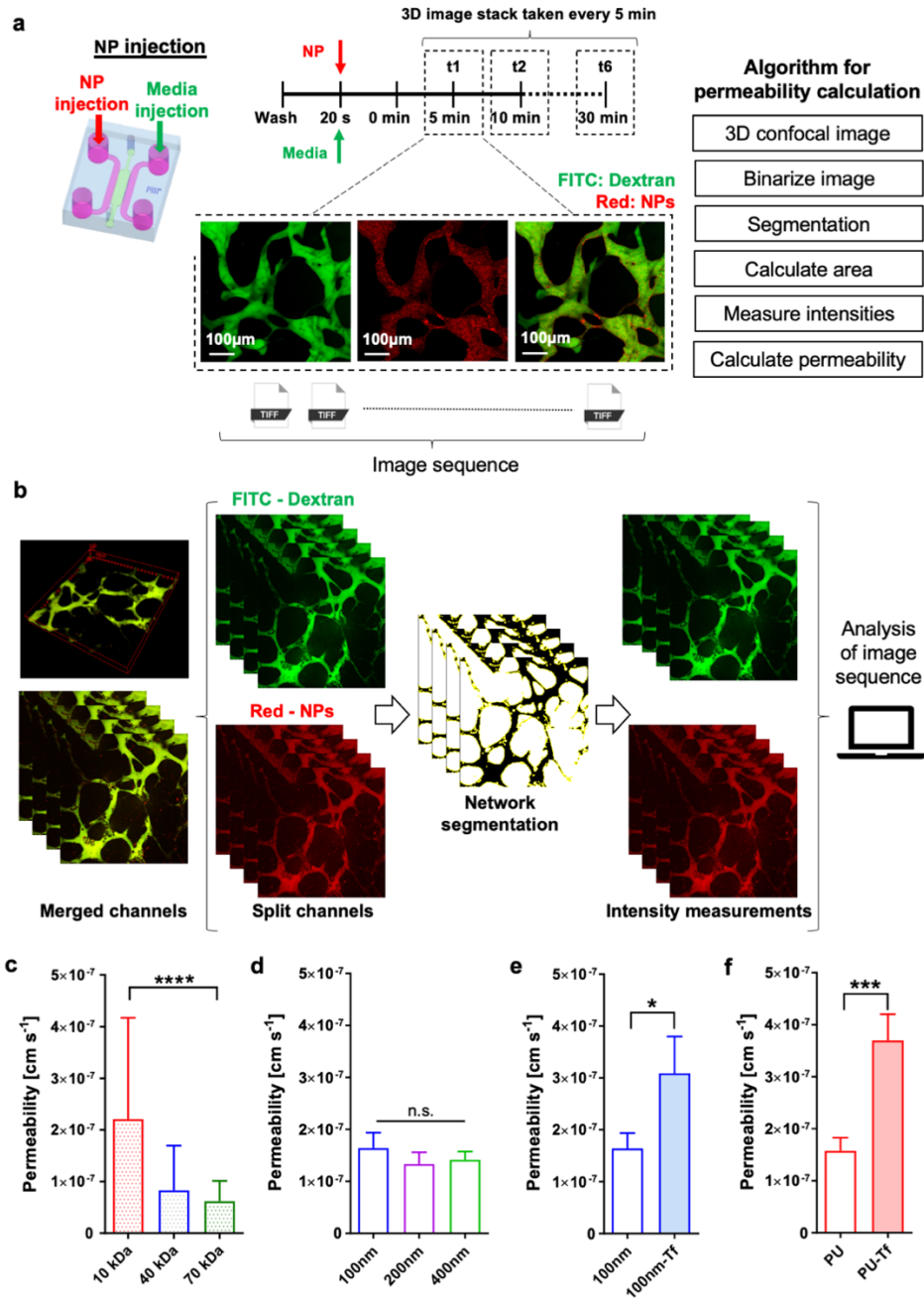


Figure 2.17: Nanoparticles permeability testing in 3D Microphysiological BBB model.

a) Schematic and methods of 3D microvascular permeability measurements. Confocal images of transport of NPs microvasculature (in red) are displayed. **b)** Schematic of intensity of image processing and evaluation of NPs transport across the microvasculature at different timepoints for 3D vascular permeability analysis. 3D microvascular permeability measurements of **c)** FITC-dextran, **d)** PS NPs, **e)** PS NPs and PS-Tf NPs, and **f)** PU and PU-Tf NPs in 3D microfluidic system. Data are shown as the mean \pm SD, $n \geq 3$ independent replicates, with * $p \leq 0.05$, *** $p \leq 0.001$, $p \leq 0.0001$. (n.s.: not significant). Reproduced with permission from [226].

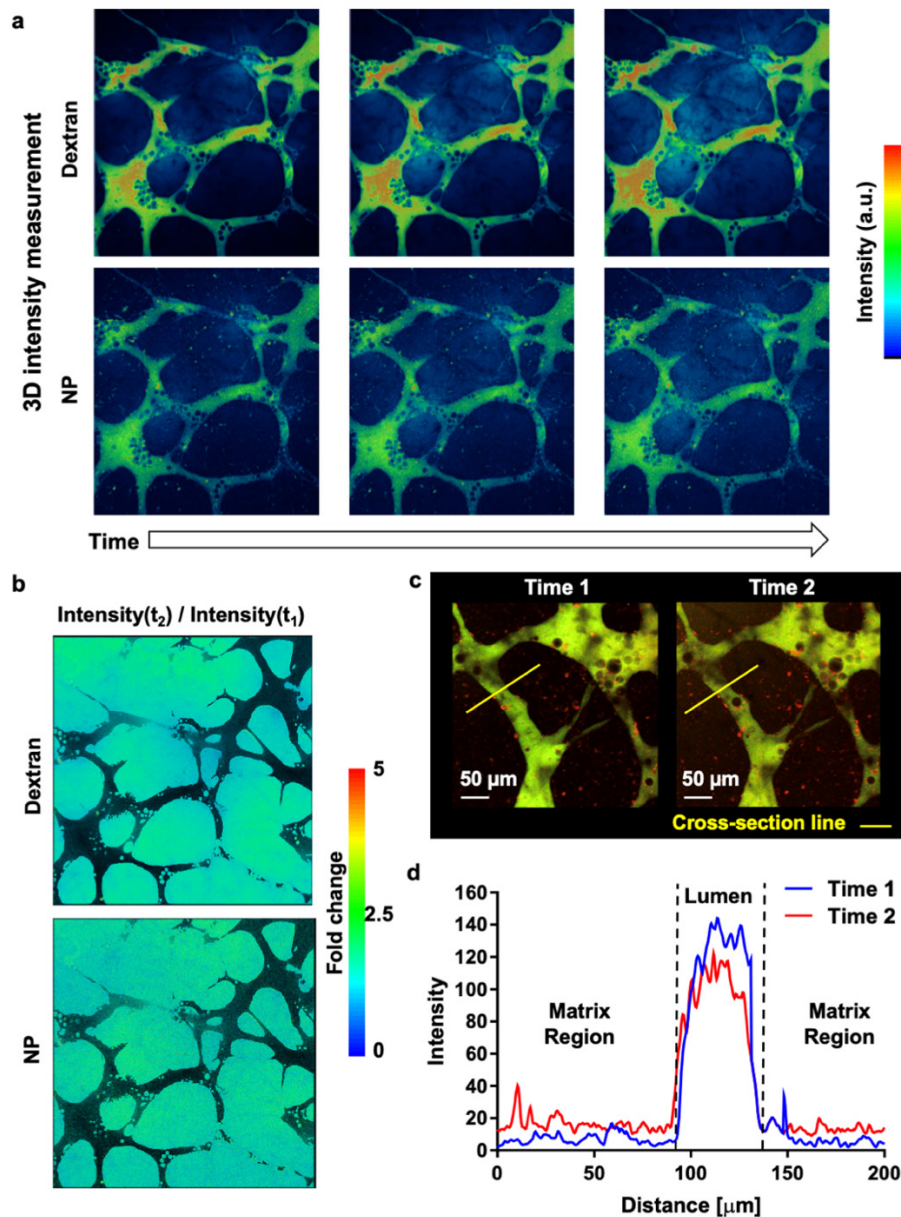


Figure 2.18: Biodistribution of Nanoparticles in 3D Microphysiological BBB model.

a) 3D localization map of NPs density in the microvasculature and in the gel region over time. *b)* Ratio differences in signal intensity of fluorescent FITC-dextran and NPs at two timepoints. *c)* Confocal image of section of microvascular network examined using line scan measurements (yellow line) at different timepoints. *d)* Histogram of fluorescent intensity profile of NPs at two timepoints along the yellow line indicated in (c). Reproduced with permission from [226].

Discussion

In this chapter, an innovative *in vitro* microphysiological model of the human BBB microvasculature was designed. The model consists of a self-assembled microvascular network (μ VN) of iPSC-ECs co-cultured with brain PCs and ACs. The iPSC-ECs were selected as unspecific and immature ECs, capable of organizing themselves in a complex and perfusable vascular network, representing a coherent and relevant replacement of “brain” ECs. Moreover, iPSC cells may be potentially be derived from patients suffering from specific neurodegenerative diseases[228], thereby producing a pathological model for studying disease progression towards precision medicine applications to select optimal personalized therapies. The novelty of microphysiological BBB model arises from the simultaneous seeding of three human cell types into a single gel region, which self-organize into BBB-like structures and producing a perfusable μ VN, comprising small lumens with circular cross-section comparable with *in vivo* human brain microcirculation (arterioles and venules 10-90 μ m; capillaries 7-10 μ m) [68] [229] [96] The model expressed both functional and morphological characteristics present in human BBB, characterized by lower transport selectivity and permeabilities than other published microfluidic models described in chapter 3.

Consistent with previous findings, this morphological change in the final structure of the BBB microphysiological model was induced by the presence of PCs and ACs which secreting pro-angiogenic and vasculogenic growth factors and ECM proteins, but also by juxtacrine signaling [15][17]. In fact, it has already been demonstrated that co-culture of ECs with PCs is required for BBB formation and the maintenance of homeostasis. In particular, PCs not only influence the creation of vascular networks, with significant reduction in lateral diameter, but also induce the differentiation of iPSC-ECs in more brain-specific endothelial cells, as determined by the RT-PCR results[19] (Fig. 2.12). In addition to the contribution of the PCs, the ACs also improved the formation and integrity of the BBB, along with the increase expression of TJ. iPSC-ECs self-assembled into mature vascular networks forming complex structures when interacting with both cell types. The role of ACs was evidenced by an increase in the expression of BBB transporters and TJ proteins, such as ZO-1, occludin, claudin-5, ECM deposition and the corresponding decrease in permeability, similar to previous transwell and microfluidic-based models incorporating ACs[211]. In particular, the upregulation of typical BBB transporters, such GLUT-

1, LAT-1, P-GP, TF-R, LRP1 and MRPs, is fundamental to obtain an *in vitro* BBB model for drug design and testing. Indeed, these specific transporters have been highlighted as potential targets for enhancing the penetration of drugs into the brain. In the model presented here, AC endfeet were in contact interactions with blood vessels, recapitulating a similar physiological arrangement present into the brain. ACs also provide mutual biochemical support through paracrine signaling, regulate influx/efflux, vasodilatation/vasoconstriction by inducing tightening of the endothelium, helping to maintain a BBB-like phenotype[17]. Further investigation is needed to ascertain the relative importance of different biological pathways and factors improving BBB integrity, by quantifying cytokines and chemokines secretions.

As key features in assessing the value of BBB microvascular models for drug transport studies, vascular perfusability and permeability were measured using fluorescent probes. Consistent with the progressive increasing in the model's complexity, corresponding increase in the tightness of junctional proteins, the μ VN, showed decreased permeability. The microphysiological BBB model showed a low value of 8.9×10^{-8} cm/s and 2.2×10^{-7} cm/s for 40 kDa and 10 kDa FITC-dextran, respectively, confirming barrier selectivity, comparable to those measured *in vivo* in rat cerebral microcirculation ($3.1 \pm 1.3 \times 10^{-7}$ cm/s and 1.32 ± 10^{-7} cm/s for 40 and 10 kDa FITC-dextran)[230]. As a side note, the inclusion of an iPSC-EC monolayer, as patterned channel technique in the adjacent fluidic channels, improved vascular perfusability and also reduced the diffusion artifacts associated with tracer leakage across the sidewalls of the gel region.

It is important to note that the present model lacked neurons and microglia, and this might have further effects on barrier functionality. It is known that co-culture of iPSC-ECs with iPS derived neurons causes upregulation of BBB specific transporters and the differentiation of brain-specific ECs. This 3D self-organized BBB system has several advantages compared to the *in vitro* 2D membrane-based monolayer, including its more physiologically-relevant morphology. Certainly, beside model characterization, in this study a new method was proposed to characterize polymer NP transport across the microphysiological BBB model in comparison with the traditional models. Although the conventional transwell model could recapitulate the theoretical effects of Tf-functionalization on NP permeability, at least 3 h were needed to exhibit significantly permeability variations of Tf-functionalized PS-NPs over non-functionalized NPs. In agreement with previous reports, such findings suggest that 2D transwell assays may not facilitate direct comparisons

between NPs made from different materials, also suggesting that alternative platforms should be developed to reduce the time required to assess NP delivery efficacy.

In contrast, the 3D microphysiological BBB model allowed comparisons of vascular permeability coefficients between NPs prepared using different materials, or with Tf surface functionalization, in a shorter time frame (5 min). On the other hand, transcytosis possibly plays a more important role compared to paracellular transport in the microphysiological model. Conversely, in the 2D transwell set-up, transcytosis effects were possibly inferior and paracellular transport prevailed. In addition, transcytosis mechanisms may possibly differ between in vitro 2D monolayers and 3D environment. In the microphysiological BBB model, permeability values of non-functionalized PS NPs measured did not change as a function of NP size in the 100–400 nm range, and non-functionalized PU and PS NPs showed similar permeability values. Interestingly, the Tf-functionalization increased permeability values especially for PU-Tf NPs. Such results are particularly relevant for the future translation of PU NPs to the clinic, considering their demonstrated efficient delivery of drugs to tumors in murine models[223].

Beside toxicology and safety, the transport across the BBB represents an important evidence of NP delivery capabilities. For this reason, the development of a reliable method to quantify NP transport behavior provides an invaluable tool to assess efficacy of NP therapeutic and quantify the effect of surface-functionalizing NPs on their permeability across the BBB.

The methodology presented here represents an opportunity for the design of effective NPs that are able to target damaged areas of the brain. In this scenario, it also contributes toward a better understanding of transport processes and molecular signaling pathways, potentially leading to the discovery of new targets and membrane transporters that are highly upregulated in a pathological BBB condition and improving the delivery of drugs.

Also, although a monolayer may be added to the side channel of the microfluidic device to minimize diffusion artefacts, leakage from the side channels must be checked before measuring permeability values. Therefore, there are multiple experimental factors to consider when comparing data from different methodologies. However, the 3D model is reproducible, as long as the experimental parameters are maintained across multiple experiments. The present findings establish the foundation for future studies to characterization other types of fluorescently-labelled carriers or therapeutics. The methodology of permeability measurement presented could also be employed in combination with other techniques such as fluorescence resonance energy transfer

(FRET) or bimolecular fluorescence complementation (BiFC) to facilitate a more comprehensive comparison between different NPs that are conjugated with appropriate tracers. These comparisons include, but are not limited to, carriers of a wider size range, synthesized with other materials and/or functionalization(s) on their surface, which can also encapsulate cargo. In addition, the 3D microphysiological BBB model could be applied not only to evaluate nanocarriers targeting ECs, but all the cells of the model (PCs and ACs), exploiting the relevant surface functionalization of NPs with specific ligands for cell-specific receptors. Moreover, these studies could be advanced with multiplexed cytokine profiling techniques to analyze molecular mechanisms, thus contributing toward to the identification of genetic targets and drug discovery. Furthermore, the presented BBB model provides a physiologically complex brain microenvironment that can be grown using patient-derived cells and also introduced with specific gene mutations, thus guiding the design of delivery nanocarriers for CNS precision therapy.

Conclusion

In this chapter, the first 3D microphysiological BBB model produced by vasculogenesis was prepared, based on human iPSC-ECs, which self-organize in vascular networks, in contact interaction with human brain PCs and ACs, within a single fibrin gel region. This model exhibits physiologically relevant anatomical structures and provides an effective and reproducible platform compared to traditional models. The model features a perfusable and selective capillary-like microvasculature, formed by iPSC-ECs which differentiate into more BBB-like phenotypes, with lower microvascular permeability compared to conventional *in vitro* BBB models, and similar to *in vivo* measurements in rat brain, as measured by transport of fluorescent probes through capillaries.

In addition, this study reports initial findings of the application of the microphysiological BBB model, to evaluate the transport and spatiotemporal distribution of different polymer NPs (Polyurethane and Polystyrene NPs). The proposed methodology used fluorescently tagged NPs and was able to capture the boost in transport of Tf-functionalized NPs in a few minutes. The results are highly relevant from the perspective of preclinical nanotherapeutic screening according to the 3Rs principle (reduction, refinement, replacement). This model represents a reliable and

valuable next-generation system that promotes understanding of neurovascular function, might enable preclinical development of effective CNS therapeutics. This system can be adapted for high-throughput preclinical screening of innovative therapies targeting specific BBB transporters, to perform drug delivery studies and to investigate the transport of microengineered nanocarriers able to cross the BBB. The model offers a more physiologically relevant BBB microvasculature, which could potentially enable patient-specific assessment of drug-loaded NP delivery to the brain, along with an effective and convenient methodology for quantifying the transport and distribution properties of NPs and potentially predicting neurotherapeutic transport efficacy across BBB.

Acknowledgments

The doctoral candidate would like to thank all the scientists involved in these experiments.

In particular, the candidate would like to acknowledge the contribution of the following:

- Yoojin Shin, designed the microfluidic device and highly contributed to perform immunocytochemistry, permeability assays and vascular parameters analysis.
- Sharon Wei Ling Lee, helped performing NPs permeability measurements in 3D BBB model and Transwell systems.
- Tatsuya Osaki, contributed to design a microfluidic device and assisted with RT-PCR experiments, drawing schematics, statistical analysis and useful discussions.
- Cynthia Hajal, performed vascular parameters analysis and helped in the design of several experiments and permeability measurements.
- Luca Possenti, performed computational analysis of NP uptake and generated the 3D intensity maps of NP spatiotemporal distribution.
- Clara Mattu, prepared PU NPs and analyzed the associated data.
- Giulia Adriani monitored the NPs experiments.
- Valeria Chiono and Roger Dale Kamm supervised the projects and acquired funding.

Table 4. Primer sequences for quantitative real time RT-PCR.

Target gene	Forward primer sequence 5'- 3'	Reverse primer sequence 5'- 3'
GLUT1	GGC CAT CTT TTC TGT TGG GG	CCA GCA GGT TCA TCA TCA GC
GAPDH	TGTGGGCATCAATGGATTGG	ACACCATGTATTCCGGGTCAAT
LAT1	GTC CCT GTT CAC ATC CTC CA	TAG AGC AGC GTC ATC ACA CA
CAT1	CCC TAC TTC TGC CTG GAC AA	ATA ACC CGA GGC ATG GGA AA
CAT3	TTG GGG TCT GGA TGC TGA TT	TTG GCT CTA GAC TTG CGT GA
MCT1	CTT GGG CTT GCC TTC AAC TT	GTA CAG AGG AAC ACA GGG CT
ABCA1	AGC CCT GGA TGT ACA ACG AA	TTT CCT TCC ATA CAG CGG GT
LRP1	CAA CAA CAC CTC AGT CTG CC	GCA GCC ACC GTT ATT CAG AG
BCRP	CTC TTC GGC TTG CAA CAA CT	TTC TCC TCC AGA CAC ACC AC
PGP	CCT TCA CCC AGG CAA TGA TG	GCA CCA AAG ACA ACA GCT GA
MRP1	CAA GGT GGA TGC GAA TGA GG	TGA GGA AGT AGG GCC CAAAG
MRP4	TCC CAT GGA TTC TGT GGC TT	ACT CGT AAC CTC ATC CCA GC
TF-R	AGC CCA CTG TTG TAT ACG CT	TTT CTC AAC TTT GCT GGC CC
CD31	ATT GCA GTG GTT ATC ATC GGA GT	CTGGTTGTTGGAGTTCAGAAGTG
SM22A	AAT GGC GTG ATT CTG AGC AAG	AGT CTT GAT GAC CCC ATA GTC CTC
PDGFR	GAT GAT CTC CAA CGC CTG	TCC TTC TTC CAC GAG CCA
ZO-1	TGG ACA ACC AGA TGT GGA TTT ACC	TCCCGTCTTCATGAGCTGAATT
CLDN5	CTCT GCT GGT TCG CCA ACA T	CAG CTC GTA CTT CTG CGA CA
OCLN	ACA AGC GGT TTT ATC CAG AGTC	GTC ATC CAC AGG CGA AGT TAA T
LAM	GTG ATG GCA ACA GCG CAA A	GAC CCA GTG ATA TTC TCT CCC A
COL4A1	GGA CTA CCT GGA ACA AAA GGG	GCC AAG TAT CTC ACC TGG ATC A
COL4A4	AGAT AAG GGT CCA ACT GGT GT	ACC TTT AAC GGC ACC TAA AAT GA
COL1A1	GAG GGC CAAG ACG AAG ACA TC	CAG ATC ACG TCA TCG CAC AAC
αSMA	ACG GCC GCC TCC TCT TCC TC	GCC CAG CTT CGT CGT ATT CC
RPS18	ACT CAA CAC GGG AAA CCT CA	AAC CAG ACA AAT CGC TCC AC
GFAP	GAT CAA CTC ACC GCC AAC AG	ATA GGC AGC CAG GTT GTT CT

Table 5. *Antibodies for immunocytochemistry.*

Antibody/Probe for immunocytochemistry	Species	Dilution (volume ratio)	Order informations
CD31	Rabbit	1:100	Abcam #ab32457
ZO-1	mouse	1:40	Invitrogen #33-9100
Occludin	Rabbit	1:40	Abcam #ab710192
Claudin 5	Rabbit	1:40	Abcam #ab15106
Laminin	Rabbit	1:100	Abcam #ab11575
Collagen IV	Mouse	1:100	Abcam #ab86042
DAPI (nuclei)		1:1000	Thermo Fisher Scientific #D1306
GFAP	Mouse	1:100	Abcam #ab10062
Rhodamine phalloidin (F-ACTIN)		1:40	Molecular Probes #R415
Anti-mouse alexa fluor 488	Goat	1:200	Thermo Fisher Scientific #A11001
Anti-rabbit alexa fluor 555	Goat	1:200	Thermo Fisher Scientific #A27039
Anti-rabbit alexa fluor 647	Goat	1:200	Thermo Fisher Scientific #A21244
Anti-rabbit alexa fluor 488	Goat	1:200	Thermo Fisher Scientific #A11008
Anti-rabbit alexa fluor 546	Goat	1:200	Thermo Fisher Scientific #A11035
Anti-mouse alexa fluor 647	Goat	1:200	Thermo Fisher Scientific #A21235

Supplementary Methods

1) Quantification of vascular permeability

Acquire confocal images as a 3D stack.

- 1- Open stack on ImageJ
- 2- Analyze → Set measurements → Select measurements section and include Area, mean Intensity, Perimeters ($A_{lateral}$, Intensity, L_{branch})
- 3- Analyze → Set scale → Set measurements in μm (Make sure ImageJ is set to μm)
- 4- Image → Stack → Z-project (image 2D projection)
- 5- Image → Duplicate (duplicate your file)
- 6- Process → Enhance contrast (enhance contrast of duplicated file)
- 7- Process → Binary → Make binary (Binarize your 2D projection)
- 8- Edit → Selection → Create selection (Border between vessel/tissue will be selected in the binarized image that equals the perimeter of the vasculature)
- 9- Edit → Selection → Add to manager (this action shows selected perimeter L_{branch} in first time point)
- 10- In add manager select and add your selection on image that you wish to analyze.
- 11- Analyze → Measure (new tab show parameters such as Area, lateral vessel area ($A_{lateral}$), and branch length (L_{branch}) as perimeter and mean intensity of vessels I_v , inside the vasculature)
- 12- Edit → Selection → Make inverse (select outside part of the vessel)
- 13- Analyze → Measure (consider only the mean intensity of tissue I_T , the region outside of the vasculature)
- 14- Open second time point and create image projection of your z-stack with Image → Stack → Z-project
- 15- Edit → Selection → Add to manager (this action shows the selected perimeter in first time point)
- 16- Repeat points #12 and #13 to quantify the mean intensity of tissue (I_T) at different time points.

2) Characterization of BBB microvascular parameters

- 1- Take confocal images as 3D stack.
- 2- Open stack on ImageJ
- 3- Analyze → Set measurements → Select measurements (Area, Perimeter, Mean Intensity) section and include Area, Intensity, Perimeters
- 4- Analyze → Set scale → Set measurements in μm (Make sure ImageJ is set to μm)
- 5- Image → Duplicate (duplicate your file)

- 6- Image → Adjust → Auto-threshold
- 7- Open plugins from Plugins → Segmentation → Trainable Weka Segmentation 3D
- 8- Segment the stack using plugin
- 9- Train your classifier by selecting regions outside the vasculature
- 10- Load your classifier in the trainable Weka Segmentation 3D system and click "create results"
(this process takes some time)
- When finished, image will look red and green.
- 11- Adjust it to 8-bit. It will turn dark grey and light grey
- 12- Open plugins from Plugins → 3D → 3D geometrical measure
- 13- This will give you vascularized area and volume for two numbers (85 and 155) which correspond to the dark grey color (85) and the light grey color (155). Usually vessels are light grey so you want the area and volume for the 155 row in the measurement box that imageJ outputs.
- 14- Attention! to see the volume and area in dimensional units and not pixels. If you are using proper micrometer units for your initial stack (x,y,z), it will give you the correct number.

3) Compute cell boundary length and vascular area

- 1- Acquire confocal images as 3D stack.
- 2- Open stack in ImageJ
- 3- Analyze → Set measurements → Select measurements (Perimeter) section and include Area, Intensity, Perimeters
- 4- Analyze → Set scale → Set measurements in μm (make sure ImageJ is set to μm)
- 5- Process → Enhance contrast
- 6- Edit → Selection → Select a rectangular selection that contains few cells.
- 7- Process → Binary → Make binary (Binarize your 2D projection)
- 8- Edit → Selection → Create selection (Border between vessel/tissue will be selected in the binarized image that is the perimeter of the vasculature)
- 9- Edit → Selection → Add to manager (this action shows selected perimeter (P) in first time point)
- 10- Analyze → Measure you can define Perimeter as the cell boundary length

Attention! in some regions it might be necessary to draw manually by freehand line selection and then quantify. To compute vascular Area, follow instructions #1-11 and quantify the Area.

Supplementary are reproduced with permission from [221]. Biomaterials. Copyright 2018, Elsevier.

References

- [1] N. J. Abbott, A. A. K. Patabendige, D. E. M. Dolman, S. R. Yusof, and D. J. Begley, "Structure and function of the blood-brain barrier," *Neurobiol. Dis.*, vol. 37, no. 1, pp. 13–25, 2010.
- [2] N. Hagan and A. Ben-Zvi, "The molecular, cellular, and morphological components of blood-brain barrier development during embryogenesis," *Semin. Cell Dev. Biol.*, vol. 38, pp. 7–15, 2015.
- [3] Y. Serlin, I. Shelef, B. Knyazer, and A. Friedman, "Anatomy and physiology of the blood-brain barrier," *Semin. Cell Dev. Biol.*, vol. 38, pp. 2–6, 2015.
- [4] B. V. Zlokovic, "The Blood-Brain Barrier in Health and Chronic Neurodegenerative Disorders," *Neuron*, vol. 57, no. 2, pp. 178–201, 2008.
- [5] T. S. Reese and M. J. Karnovsky, "Fine structural localization of a blood-brain barrier to exogenous peroxidase," *J. Cell Biol.*, vol. 34, no. 1, pp. 207–217, 1967.
- [6] Z. Zhao, A. R. Nelson, C. Betsholtz, and B. V. Zlokovic, "Establishment and Dysfunction of the Blood-Brain Barrier," *Cell*, vol. 163, no. 5, pp. 1064–1078, 2015.
- [7] G. Bazzoni and E. Dejana, "Endothelial cell-to-cell junctions: Molecular organization and role in vascular homeostasis," *Physiol. Rev.*, vol. 84, no. 3, pp. 869–901, 2004.
- [8] R. D. and A. Prat, "The blood brain barrier," *Cold Spring Harb. Lab. - Perspect. Biol.*, pp. 21–38, 2008.
- [9] R. Dermietzel, D. C. Spray, and M. Nedergaard, *Blood-Brain Barriers: From Ontogeny to Artificial Interfaces*, vol. 1. 2007.
- [10] B. T. Hawkins and T. P. Davis, "The blood-brain barrier/neurovascular unit in health and disease," *Pharmacol. Rev.*, vol. 57, no. 2, pp. 173–185, 2005.
- [11] S. Ohtsuki and T. Terasaki, "Contribution of carrier-mediated transport systems to the blood-brain barrier as a supporting and protecting interface for the brain; importance for CNS drug discovery and development," *Pharm. Res.*, vol. 24, no. 9, pp. 1745–1758, 2007.
- [12] C. P. Profaci, R. N. Munji, R. S. Pulido, and R. Daneman, "The blood-brain barrier in health and disease: Important unanswered questions," *J. Exp. Med.*, vol. 217, no. 4, pp. 1–16, 2020.
- [13] W. M. Pardridge, "Blood-brain barrier endogenous transporters as therapeutic targets: A new model for small molecule CNS drug discovery," *Expert Opin. Ther. Targets*, vol. 19, no. 8, pp. 1059–1072, 2015.
- [14] B. T. Hawkins and T. P. Davis, "The Blood-Brain Barrier / Neurovascular Unit in Health and Disease," *Pharmacol. Rev.*, vol. 57, no. 2, pp. 173–185, 2005.
- [15] E. a Winkler, R. D. Bell, and B. V Zlokovic, "Central nervous system pericytes in health and disease.," *Nat. Neurosci.*, vol. 14, no. 11, pp. 1398–1405, 2011.
- [16] S.-W. Lee *et al.*, "SSeCKS regulates angiogenesis and tight junction formation in blood-brain barrier.," *Nat. Med.*, vol. 9, no. 7, pp. 900–906, 2003.
- [17] N. J. Abbott, L. Rönnbäck, and E. Hansson, "Astrocyte-endothelial interactions at the blood-brain barrier," *Nat. Rev. Neurosci.*, vol. 7, no. 1, pp. 41–53, 2006.
- [18] S. Banerjee and M. A. Bhat, "Neuron-Glial Interactions in Blood-Brain Barrier Formation," *Annu. Rev. Neurosci.*, vol. 30, no. 1, pp. 235–258, 2007.
- [19] M. D. Sweeney, S. Ayyadurai, and B. V. Zlokovic, "Pericytes of the neurovascular unit: Key functions and signaling pathways," *Nat. Neurosci.*, vol. 19, no. 6, pp. 771–783, 2016.
- [20] H. Wolburg *et al.*, "Localization of claudin-3 in tight junctions of the blood-brain barrier is selectively lost during experimental autoimmune encephalomyelitis and human glioblastoma multiforme.," *Acta Neuropathol.*, vol. 105, no. 2003, pp. 586–592, 2003.
- [21] A. Armulik, G. Genové, and C. Betsholtz, "Pericytes: Developmental, Physiological, and Pathological Perspectives, Problems, and Promises," *Dev. Cell*, vol. 21, no. 2, pp. 193–215, 2011.
- [22] R. Daneman, L. Zhou, A. A. Kebede, and B. A. Barres, "Pericytes are required for blood-brain barrier integrity during embryogenesis," *Nature*, vol. 468, no. 7323, pp. 562–566, 2010.
- [23] J. Chen *et al.*, "CD146 is essential for PDGFR β -induced pericyte recruitment," *Protein Cell*, vol.

- 9, no. 8, pp. 743–747, 2018.
- [24] B. Obermeier, R. Daneman, and R. M. Ransohoff, “Development, maintenance and disruption of the blood-brain-barrier,” *Nat. Med.*, vol. 19, no. 12, pp. 1584–1596, 2013.
- [25] M. Zonta *et al.*, “Neuron-to-astrocyte signaling is central to the dynamic control of brain microcirculation,” *Nat. Neurosci.*, vol. 6, no. 1, pp. 43–50, 2003.
- [26] A. Armulik *et al.*, “Pericytes regulate the blood-brain barrier,” *Nature*, vol. 468, no. 7323, pp. 557–561, 2010.
- [27] E.-K. Tan, Y.-X. Chao, A. West, L.-L. Chan, W. Poewe, and J. Jankovic, “Parkinson disease and the immune system — associations, mechanisms and therapeutics,” *Nat. Rev. Neurol.*, 2020.
- [28] R. D. Bell *et al.*, “Pericytes Control Key Neurovascular Functions and Neuronal Phenotype in the Adult Brain and during Brain Aging,” *Neuron*, vol. 68, no. 3, pp. 409–427, 2010.
- [29] M. D. Sweeney, A. P. Sagare, and B. V. Zlokovic, “Blood-brain barrier breakdown in Alzheimer disease and other neurodegenerative disorders,” *Nat. Rev. Neurol.*, vol. 14, no. 3, pp. 133–150, 2018.
- [30] J. V. Forrester, P. G. McMenamin, and S. J. Dando, “CNS infection and immune privilege,” *Nat. Rev. Neurosci.*, vol. 19, no. 11, pp. 655–671, 2018.
- [31] C. Iadecola, “The Pathobiology of Vascular Dementia,” *Neuron*, vol. 80, no. 4, pp. 844–866, 2013.
- [32] P. Ballabh, A. Braun, and M. Nedergaard, “The blood-brain barrier: An overview: Structure, regulation, and clinical implications,” *Neurobiol. Dis.*, vol. 16, no. 1, pp. 1–13, 2004.
- [33] M. Ramsauer, D. Krause, and R. Dermietzel, “Cerebral Pericytes and Angiogenesis in vitro,” 2002.
- [34] T. Takano *et al.*, “Astrocyte-mediated control of cerebral blood flow,” *Nat. Neurosci.*, vol. 9, no. 2, pp. 260–267, 2006.
- [35] M. V. Sofroniew and H. V. Vinters, “Astrocytes: Biology and pathology,” *Acta Neuropathol.*, vol. 119, no. 1, pp. 7–35, 2010.
- [36] J. Banerjee, Y. Shi, and H. S. Azevedo, “In vitro blood–brain barrier models for drug research: state-of-the-art and new perspectives on reconstituting these models on artificial basement membrane platforms,” *Drug Discov. Today*, vol. 21, no. 9, pp. 1367–1386, 2016.
- [37] L. E. Clarke and B. A. Barres, “Emerging roles of astrocytes in neural circuit development,” *Nat. Rev. Neurosci.*, vol. 14, no. 5, pp. 311–321, 2013.
- [38] Y. Chen and R. A. Swanson, “Astrocytes and brain injury,” *J Cereb Blood Flow Metab*, vol. 23, no. 2, pp. 137–149, 2003.
- [39] H. H. Tsai *et al.*, “Regional astrocyte allocation regulates CNS synaptogenesis and repair,” *Science (80-.)*, vol. 337, no. 6092, pp. 358–362, 2012.
- [40] J. M. Wardlaw *et al.*, “Perivascular spaces in the brain: anatomy, physiology and pathology,” *Nat. Rev. Neurol.*, vol. 16, no. 3, pp. 137–153, 2020.
- [41] M. M. Esiri and D. Gay, “Immunological and neuropathological significance of the Virchow-Robin space,” *J. Neurol. Sci.*, vol. 100, no. 1–2, pp. 3–8, 1990.
- [42] B. Obermeier, R. Daneman, and R. M. Ransohoff, “Development, maintenance and disruption of the blood-brain barrier,” *Nat. Med.*, vol. 19, no. 12, pp. 1584–1596, 2013.
- [43] B. Engelhardt and L. Sorokin, “The blood–brain and the blood–cerebrospinal fluid barriers: function and dysfunction,” *Semin. Immunopathol.*, vol. 31, no. 4, pp. 497–511, 2009.
- [44] E. Ruoslahti, “Brain extracellular matrix,” *Glycobiology*, vol. 6, no. 5, pp. 489–492, 1996.
- [45] C. C. Visser, L. H. Voorwinden, D. J. A. Crommelin, M. Danhof, and A. G. De Boer, “Characterization and modulation of the transferrin receptor on brain capillary endothelial cells,” *Pharm. Res.*, vol. 21, no. 5, pp. 761–769, 2004.
- [46] T. Tilling, C. Engelbertz, S. Decker, D. Korte, S. Hüwel, and H. J. Galla, “Expression and adhesive properties of basement membrane proteins in cerebral capillary endothelial cell cultures,” *Cell Tissue Res.*, vol. 310, no. 1, pp. 19–29, 2002.
- [47] D. E. Ingber, “Mechanobiology and diseases of mechanotransduction,” *Ann. Med.*, vol. 35, no. 8, pp. 564–577, 2003.

- [48] S. N. Bhatia and D. E. Ingber, "Microfluidic organs-on-chips," *Nat. Biotechnol.*, vol. 32, no. 8, pp. 760–772, 2014.
- [49] A. D. Greenhalgh, S. David, and F. C. Bennett, "Immune cell regulation of glia during CNS injury and disease," *Nat. Rev. Neurosci.*, vol. 21, no. 3, pp. 139–152, 2020.
- [50] J. V. Pluvinaige and T. Wyss-Coray, "Systemic factors as mediators of brain homeostasis, ageing and neurodegeneration," *Nat. Rev. Neurosci.*, vol. 21, no. 2, pp. 93–102, 2020.
- [51] W. M. Pardridge, "Drug targeting to the brain," *Pharm. Res.*, vol. 24, no. 9, pp. 1733–1744, 2007.
- [52] N. Strazielle and J. F. Ghersi-Egea, "Physiology of blood-brain interfaces in relation to brain disposition of small compounds and macromolecules," *Mol. Pharm.*, vol. 10, no. 5, pp. 1473–1491, 2013.
- [53] D. D. Cunningham, "Thrombin induces apoptosis in cultured neurons and astrocytes via a pathway requiring tyrosine kinase and RhoA activities," *J. Neurosci.*, vol. 17, no. 14, pp. 5316–5326, 1997.
- [54] T. Shiobara, T. Usui, J. Han, H. Isoda, and Y. Nagumo, "The reversible increase in tight junction permeability induced by capsaicin is mediated via cofilin-actin cytoskeletal dynamics and decreased level of occludin," *PLoS One*, vol. 8, no. 11, 2013.
- [55] D. Furtado, M. Björnmalm, S. Ayton, A. I. Bush, K. Kempe, and F. Caruso, "Overcoming the Blood–Brain Barrier: The Role of Nanomaterials in Treating Neurological Diseases," *Adv. Mater.*, vol. 30, no. 46, 2018.
- [56] W. M. Pardridge, "Blood-brain barrier drug targeting: the future of brain drug development.," *Mol. Interv.*, vol. 3, no. 2, pp. 90–105, 51, 2003.
- [57] V. K. Gribkoff and L. K. Kaczmarek, "The need for new approaches in CNS drug discovery: Why drugs have failed, and what can be done to improve outcomes," *Neuropharmacology*, vol. 120, pp. 11–19, 2017.
- [58] R. Cecchelli *et al.*, "Modelling of the blood–brain barrier in drug discovery and development," *Nat. Rev. Drug Discov.*, vol. 6, no. 8, pp. 650–661, 2007.
- [59] W. M. Pardridge, "The blood-brain barrier: Bottleneck in brain drug development," *NeuroRx*, vol. 2, no. 1, pp. 3–14, 2005.
- [60] C. Suenderhauf, F. Hammann, and J. Huwyler, "Computational prediction of blood-brain barrier permeability using decision tree induction," *Molecules*, vol. 17, no. 9, pp. 10429–10445, 2012.
- [61] D. F. Veber, S. R. Johnson, H. Y. Cheng, B. R. Smith, K. W. Ward, and K. D. Kopple, "Molecular properties that influence the oral bioavailability of drug candidates," *J. Med. Chem.*, vol. 45, no. 12, pp. 2615–2623, 2002.
- [62] N. Bodor and P. Buchwald, "Brain-Targeted Drug Delivery," *Healthc. Technol. Rev.*, 2003.
- [63] W. A. Banks, "From blood-brain barrier to blood-brain interface: New opportunities for CNS drug delivery," *Nat. Rev. Drug Discov.*, vol. 15, no. 4, pp. 275–292, 2016.
- [64] Z. Bayat, J. Movaffagh, and S. Noruzi, "Development of a computational approach to predict blood-brain permeability on anti-viral Nucleoside Analogues," *Russ. J. Phys. Chem. A*, vol. 85, no. 11, pp. 1923–1930, 2011.
- [65] N. J. Abbott, "Blood-brain barrier structure and function and the challenges for CNS drug delivery," *J. Inherit. Metab. Dis.*, vol. 36, no. 3, pp. 437–449, 2013.
- [66] X. Dong, "Current strategies for brain drug delivery," *Theranostics*, vol. 8, no. 6, pp. 1481–1493, 2018.
- [67] P. J. Gaillard, C. C. Visser, and A. G. de Boer, "Targeted delivery across the blood-brain barrier," *Expert Opin. Drug Deliv.*, vol. 2, no. 2, pp. 299–309, 2005.
- [68] A. D. Wong, M. Ye, A. F. Levy, J. D. Rothstein, D. E. Bergles, and P. C. Searson, "The blood-brain barrier: An engineering perspective," *Front. Neuroeng.*, vol. 6, no. JUL, pp. 1–22, 2013.
- [69] E. Y. Zhang, G. T. Knipp, S. Ekins, and P. W. Swaan, "Structural biology and function of solute transporters: Implications for identifying and designing substrates," *Drug Metab. Rev.*, vol. 34, no. 4, pp. 709–750, 2002.
- [70] D. J. Begley, "Delivery of therapeutic agents to the central nervous system: The problems and the possibilities," *Pharmacol. Ther.*, vol. 104, no. 1, pp. 29–45, 2004.

- [71] R. Bendayan, P. T. Ronaldson, D. Gingras, and M. Bendayan, "In situ localization of P-glycoprotein (ABCB1) in human and rat brain," *J. Histochem. Cytochem.*, vol. 54, no. 10, pp. 1159–1167, 2006.
- [72] R. A. Hawkins, R. L. O’Kane, I. A. Simpson, and J. R. Viña, "Structure of the Blood–Brain Barrier and Its Role in the Transport of Amino Acids," *J. Nutr.*, vol. 136, no. 1, pp. 218S–226S, 2006.
- [73] R. Spector and C. E. Johanson, "Vitamin transport and homeostasis in mammalian brain: Focus on vitamins B and E," *J. Neurochem.*, vol. 103, no. 2, pp. 425–438, 2007.
- [74] S. B. Hladky and M. A. Barrand, *Fluid and ion transfer across the blood-brain and blood-cerebrospinal fluid barriers; a comparative account of mechanisms and roles*, vol. 13, no. 1. BioMed Central, 2016.
- [75] I. Sauer, I. R. Dunay, K. Weisgraber, M. Bienert, and M. Dathe, "An apolipoprotein E-derived peptide mediates uptake of sterically stabilized liposomes into brain capillary endothelial cells," *Biochemistry*, vol. 44, no. 6, pp. 2021–2029, 2005.
- [76] W. M. Pardridge, "CSF, blood-brain barrier, and brain drug delivery.," *Expert Opin. Drug Deliv.*, vol. 5247, no. May, pp. 1–13, 2016.
- [77] M. D. Sweeney, A. P. Sagare, and B. V. Zlokovic, "Blood–brain barrier breakdown in Alzheimer disease and other neurodegenerative disorders," *Nat. Rev. Neurol.*, 2018.
- [78] M. D. Sweeney, K. Kisler, A. Montagne, A. W. Toga, and B. V. Zlokovic, "The role of brain vasculature in neurodegenerative disorders," *Nat. Neurosci.*, vol. 21, no. 10, pp. 1318–1331, 2018.
- [79] and M. V. S. Joshua E. Burda, Alexander M. Bernstein, "Astrocyte roles in traumatic brain injury," vol. 150, no. 2, pp. 137–143, 2016.
- [80] B. V. Zlokovic, "Neurovascular mechanisms of Alzheimer’s neurodegeneration," *Trends Neurosci.*, vol. 28, no. 4, pp. 202–208, 2005.
- [81] R. Kortekaas *et al.*, "Blood-brain barrier dysfunction in Parkinsonian midbrain in vivo," *Ann. Neurol.*, vol. 57, no. 2, pp. 176–179, 2005.
- [82] D. Shlosberg, M. Benifla, D. Kaufer, and A. Friedman, "Blood-brain barrier breakdown as a therapeutic target in traumatic brain injury," *Nat. Rev. Neurol.*, vol. 6, no. 7, pp. 393–403, 2010.
- [83] R. K. Jain, E. Di Tomaso, D. G. Duda, J. S. Loeffler, A. G. Sorensen, and T. T. Batchelor, "Angiogenesis in brain tumours," *Nat. Rev. Neurosci.*, vol. 8, no. 8, pp. 610–622, 2007.
- [84] J. H. Suh, R. Kotecha, S. T. Chao, M. S. Ahluwalia, A. Sahgal, and E. L. Chang, "Current approaches to the management of brain metastases," *Nat. Rev. Clin. Oncol.*, vol. 17, no. May, 2020.
- [85] J. F. Deeken and W. Löscher, "The blood-brain barrier and cancer: Transporters, treatment, and trojan horses," *Clin. Cancer Res.*, vol. 13, no. 6, pp. 1663–1674, 2007.
- [86] A. S. Achrol *et al.*, "Brain metastases," *Nat. Rev. Dis. Prim.*, vol. 5, no. 1, 2019.
- [87] J. L. Mikitsh and A. M. Chacko, "Pathways for small molecule delivery to the central nervous system across the blood-brain barrier," *Perspect. Medicin. Chem.*, no. 6, pp. 11–24, 2014.
- [88] W. M. Pardridge, "Treatment of alzheimer’s disease and blood–brain barrier drug delivery," *Pharmaceuticals*, vol. 13, no. 11, pp. 1–25, 2020.
- [89] D. Wang, C. Wang, L. Wang, and Y. Chen, "A comprehensive review in improving delivery of small-molecule chemotherapeutic agents overcoming the blood-brain/brain tumor barriers for glioblastoma treatment," *Drug Deliv.*, vol. 26, no. 1, pp. 551–565, 2019.
- [90] G. Tosi, J. T. Duskey, and J. Kreuter, "Nanoparticles as carriers for drug delivery of macromolecules across the blood-brain barrier," *Expert Opin. Drug Deliv.*, vol. 0, no. 0, p. 1, 2019.
- [91] Y. Chen and L. Liu, "Modern methods for delivery of drugs across the blood-brain barrier," *Adv. Drug Deliv. Rev.*, vol. 64, no. 7, pp. 640–665, 2012.
- [92] J. Li *et al.*, "A multifunctional polymeric nanotheranostic system delivers doxorubicin and imaging agents across the blood-brain barrier targeting brain metastases of breast cancer," *ACS Nano*, vol. 8, no. 10, pp. 9925–9940, 2014.

- [93] K. Gao and X. Jiang, "Influence of particle size on transport of methotrexate across blood brain barrier by polysorbate 80-coated polybutylcyanoacrylate nanoparticles," *Int. J. Pharm.*, vol. 310, no. 1–2, pp. 213–219, 2006.
- [94] H. Gao, "Progress and perspectives on targeting nanoparticles for brain drug delivery," *Acta Pharm. Sin. B*, vol. 6, no. 4, pp. 268–286, 2016.
- [95] M. Shilo, A. Sharon, K. Baranes, M. Motiei, J. P. M. Lellouche, and R. Popovtzer, "The effect of nanoparticle size on the probability to cross the blood-brain barrier: An in-vitro endothelial cell model," *J. Nanobiotechnology*, vol. 13, no. 1, pp. 1–7, 2015.
- [96] I. M. Braverman, "The cutaneous microcirculation," *J. Investig. Dermatology Symp. Proc.*, vol. 5, no. 1, pp. 3–9, 2000.
- [97] Y. Zhou, Z. Peng, E. S. Seven, and R. M. Leblanc, "Crossing the blood-brain barrier with nanoparticles," *J. Control. Release*, vol. 270, no. October 2017, pp. 290–303, 2018.
- [98] J. Kreuter, "Nanoparticulate systems for brain delivery of drugs," *Adv. Drug Deliv. Rev.*, vol. 64, no. SUPPL., pp. 213–222, 2012.
- [99] J. A. Loureiro, B. Gomes, G. Fricker, M. A. N. Coelho, S. Rocha, and M. C. Pereira, "Cellular uptake of PLGA nanoparticles targeted with anti-amyloid and anti-transferrin receptor antibodies for Alzheimer's disease treatment," *Colloids Surfaces B Biointerfaces*, vol. 145, pp. 8–13, 2016.
- [100] S. Wohlfart, S. Gelperina, and J. Kreuter, "Transport of drugs across the blood-brain barrier by nanoparticles," *J. Control. Release*, vol. 161, no. 2, pp. 264–273, 2012.
- [101] H. Peluffo *et al.*, "BBB-targeting, protein-based nanomedicines for drug and nucleic acid delivery to the CNS," *Biotechnol. Adv.*, vol. 33, no. 2, pp. 277–287, 2015.
- [102] R. M. Koffie, C. T. Farrar, L. J. Saidi, C. M. William, B. T. Hyman, and T. L. Spires-Jones, "Nanoparticles enhance brain delivery of blood-brain barrier-impermeable probes for in vivo optical and magnetic resonance imaging," *Proc. Natl. Acad. Sci. U. S. A.*, vol. 108, no. 46, pp. 18837–18842, 2011.
- [103] J. D. Meyers, T. Doane, C. Burda, and J. P. Basilion, "Nanoparticles for imaging and treating brain cancer," *Nanomedicine*, vol. 8, no. 1, pp. 123–143, 2013.
- [104] S. Zhang *et al.*, "Autocatalytic Delivery of Brain Tumor-Targeting, Size-Shrinkable Nanoparticles for Treatment of Breast Cancer Brain Metastases," *Adv. Funct. Mater.*, vol. 30, no. 14, pp. 1–8, 2020.
- [105] C. Spuch and C. Navarro, "Liposomes for Targeted Delivery of Active Agents against Neurodegenerative Diseases (Alzheimer's Disease and Parkinson's Disease)," *J. Drug Deliv.*, vol. 2011, pp. 1–12, 2011.
- [106] Y. Cheng *et al.*, "Blood-brain barrier permeable gold nanoparticles: An efficient delivery platform for enhanced malignant glioma therapy and imaging," *Small*, vol. 10, no. 24, pp. 5137–5150, 2014.
- [107] W. J. Trickler *et al.*, "Silver Nanoparticle Induced Blood-Brain Barrier Inflammation and Increased Permeability in Primary Rat Brain Microvessel Endothelial Cells," *Toxicol. Sci.*, vol. 118, no. 1, pp. 160–170, 2010.
- [108] and C. C. G. Andreas M. Grabrucker, Magali Rowan, "Brain-Delivery of Zinc-Ions as Potential Treatment for Neurological Diseases: Mini Review," *Drug Deliv Lett*, vol. 1, no. 1, pp. 13–23, 2011.
- [109] T. Patel, J. Zhou, J. M. Piepmeier, and W. M. Saltzman, "Polymeric nanoparticles for drug delivery to the central nervous system," *Adv. Drug Deliv. Rev.*, vol. 64, no. 7, pp. 701–705, 2012.
- [110] J. Li and C. Sabliov, "PLA/PLGA nanoparticles for delivery of drugs across the blood-brain barrier," *Nanotechnol. Rev.*, vol. 2, no. 3, pp. 241–257, 2013.
- [111] Y. Zhang, Y. F. Zhang, J. Bryant, A. Charles, R. J. Boado, and W. M. Pardridge, "Intravenous RNA interference gene therapy targeting the human epidermal growth factor receptor prolongs survival in intracranial brain cancer," *Clin. Cancer Res.*, vol. 10, no. 11, pp. 3667–3677, 2004.
- [112] S. W. L. Lee *et al.*, "MicroRNA delivery through nanoparticles," *Journal of Controlled Release*, vol. 313. Elsevier B.V., pp. 80–95, 10-Nov-2019.

- [113] J. Kreuter, R. N. Alyautdin, D. A. Kharkevich, and A. A. Ivanov, "Passage of peptides through the blood-brain barrier with colloidal polymer particles (nanoparticles)," *Brain Res.*, vol. 674, no. 1, pp. 171–174, 1995.
- [114] K. Shao *et al.*, "Angiopep-2 modified PE-PEG based polymeric micelles for amphotericin B delivery targeted to the brain," *J. Control. Release*, vol. 147, no. 1, pp. 118–126, 2010.
- [115] J. Kreuter, "Drug delivery to the central nervous system by polymeric nanoparticles: What do we know?," *Adv. Drug Deliv. Rev.*, vol. 71, pp. 2–14, 2014.
- [116] C. Saraiva, C. Praça, R. Ferreira, T. Santos, L. Ferreira, and L. Bernardino, "Nanoparticle-mediated brain drug delivery: Overcoming blood-brain barrier to treat neurodegenerative diseases," *J. Control. Release*, vol. 235, pp. 34–47, 2016.
- [117] and D. N. M. Kalpana Nagpal, Shailendra Kumar Singh, "Chitosan Nanoparticles: A Promising System in Novel Drug Delivery," *Chem. Pharm. Bull.*, vol. 58, no. November, 2010.
- [118] A. E. Caprifico, P. J. S. Foot, E. Polycarpou, and G. Calabrese, "Overcoming the blood-brain barrier: Functionalised chitosan nanocarriers," *Pharmaceutics*, vol. 12, no. 11, pp. 1–20, 2020.
- [119] A. Trapani *et al.*, "Characterization and evaluation of chitosan nanoparticles for dopamine brain delivery," *Int. J. Pharm.*, vol. 419, no. 1–2, pp. 296–307, 2011.
- [120] P. Kumar *et al.*, "Transvascular delivery of small interfering RNA to the central nervous system," *Nature*, vol. 448, no. 7149, pp. 39–43, 2007.
- [121] D. W. Hwang *et al.*, "A brain-targeted rabies virus glycoprotein-disulfide linked PEI nanocarrier for delivery of neurogenic microRNA," *Biomaterials*, vol. 32, no. 21, pp. 4968–4975, 2011.
- [122] O. S. Fenton, K. N. Olafson, P. S. Pillai, M. J. Mitchell, and R. Langer, "Advances in Biomaterials for Drug Delivery," *Adv. Mater.*, vol. 30, no. 29, pp. 1–29, 2018.
- [123] A. C. Anselmo and S. Mitragotri, "Nanoparticles in the clinic: An update," *Bioeng. Transl. Med.*, vol. 4, no. 3, pp. 1–16, 2019.
- [124] M. J. Mitchell, M. M. Billingsley, R. M. Haley, M. E. Wechsler, N. A. Peppas, and R. Langer, "Engineering precision nanoparticles for drug delivery," *Nat. Rev. Drug Discov.*, 2020.
- [125] A. M. Grabrucker *et al.*, "Nanoparticle transport across the blood brain barrier," *Tissue Barriers*, vol. 4, no. 1, 2016.
- [126] H. Chen *et al.*, "Lactoferrin-modified procationic liposomes as a novel drug carrier for brain delivery," *Eur. J. Pharm. Sci.*, vol. 40, no. 2, pp. 94–102, 2010.
- [127] C. W. Gan and S. S. Feng, "Transferrin-conjugated nanoparticles of Poly(lactide)-d- α -Tocopheryl polyethylene glycol succinate diblock copolymer for targeted drug delivery across the blood-brain barrier," *Biomaterials*, vol. 31, no. 30, pp. 7748–7757, 2010.
- [128] J. Niewoehner *et al.*, "Increased Brain Penetration and Potency of a Therapeutic Antibody Using a Monovalent Molecular Shuttle," *Neuron*, vol. 81, no. 1, pp. 49–60, 2014.
- [129] A. Zensi *et al.*, "Albumin nanoparticles targeted with Apo E enter the CNS by transcytosis and are delivered to neurones," *J. Control. Release*, vol. 137, no. 1, pp. 78–86, 2009.
- [130] P. Wang, Y. Liu, X. Shang, and Y. Xue, "CRM197-induced blood-brain barrier permeability increase is mediated by upregulation of caveolin-1 protein," *J. Mol. Neurosci.*, vol. 43, no. 3, pp. 485–492, 2011.
- [131] Y. Luo, H. Yang, Y. F. Zhou, and B. Hu, "Dual and multi-targeted nanoparticles for site-specific brain drug delivery," *J. Control. Release*, vol. 317, no. September 2019, pp. 195–215, 2020.
- [132] A. Babazadeh, F. Mohammadi Vahed, and S. M. Jafari, "Nanocarrier-mediated brain delivery of bioactives for treatment/prevention of neurodegenerative diseases," *J. Control. Release*, vol. 321, no. February, pp. 211–221, 2020.
- [133] X. Yu *et al.*, "A multimodal Pepstatin A peptide-based nanoagent for the molecular imaging of P-glycoprotein in the brains of epilepsy rats," *Biomaterials*, vol. 76, pp. 173–186, 2016.
- [134] J. Liu *et al.*, "Functionalized nanocarrier combined seizure-specific vector with P-glycoprotein modulation property for antiepileptic drug delivery," *Biomaterials*, vol. 74, pp. 64–76, 2016.
- [135] X. Jiang *et al.*, "Nanoparticles of 2-deoxy-d-glucose functionalized poly(ethylene glycol)-copoly(trimethylene carbonate) for dual-targeted drug delivery in glioma treatment," *Biomaterials*,

- vol. 35, no. 1, pp. 518–529, 2014.
- [136] R. Chiarle, C. Voena, C. Ambrogio, R. Piva, and G. Inghirami, “The anaplastic lymphoma kinase in the pathogenesis of cancer,” *Nat. Rev. Cancer*, vol. 8, no. 1, pp. 11–23, 2008.
- [137] M. Masserini, “Nanoparticles for Brain Drug Delivery,” *ISRN Biochem.*, vol. 2013, pp. 1–18, 2013.
- [138] J. Paterson and C. I. Webster, “Exploiting transferrin receptor for delivering drugs across the blood-brain barrier,” *Drug Discov. Today Technol.*, vol. 20, pp. 49–52, 2016.
- [139] P. Bourassa, W. Alata, C. Tremblay, S. Paris-Robidas, and F. Calon, “Transferrin Receptor-Mediated Uptake at the Blood-Brain Barrier Is Not Impaired by Alzheimer’s Disease Neuropathology,” *Mol. Pharm.*, vol. 16, no. 2, pp. 583–594, 2019.
- [140] D. F. Leitner and J. R. Connor, “Functional roles of transferrin in the brain,” *Biochim. Biophys. Acta - Gen. Subj.*, vol. 1820, no. 3, pp. 393–402, 2012.
- [141] J. M. Scherrmann, “Drug delivery to brain via the blood-brain barrier,” *Vascul. Pharmacol.*, vol. 38, no. 6, pp. 349–354, 2002.
- [142] Y. Uchida *et al.*, “Quantitative targeted absolute proteomics of human blood-brain barrier transporters and receptors,” *J. Neurochem.*, vol. 117, no. 2, pp. 333–345, 2011.
- [143] D. T. Wiley, P. Webster, A. Gale, and M. E. Davis, “Transcytosis and brain uptake of transferrin-containing nanoparticles by tuning avidity to transferrin receptor,” *Proc. Natl. Acad. Sci. U. S. A.*, vol. 110, no. 21, pp. 8662–8667, 2013.
- [144] K. Ulbrich, T. Hekmatara, E. Herbert, and J. Kreuter, “Transferrin- and transferrin-receptor-antibody-modified nanoparticles enable drug delivery across the blood-brain barrier (BBB),” *Eur. J. Pharm. Biopharm.*, vol. 71, no. 2, pp. 251–256, 2009.
- [145] Z. Pang *et al.*, “Enhanced intracellular delivery and chemotherapy for glioma rats by transferrin-conjugated biodegradable polymersomes loaded with doxorubicin,” *Bioconjug. Chem.*, vol. 22, no. 6, pp. 1171–1180, 2011.
- [146] Z. Pang *et al.*, “Brain delivery and cellular internalization mechanisms for transferrin conjugated biodegradable polymersomes,” *Int. J. Pharm.*, vol. 415, no. 1–2, pp. 284–292, 2011.
- [147] K. B. Johnsen *et al.*, “Targeting transferrin receptors at the blood-brain barrier improves the uptake of immunoliposomes and subsequent cargo transport into the brain parenchyma,” *Sci. Rep.*, vol. 7, no. 1, pp. 1–13, 2017.
- [148] I. Cabezón, G. Manich, R. Martín-Venegas, A. Camins, C. Pelegrí, and J. Vilaplana, “Trafficking of Gold Nanoparticles Coated with the 8D3 Anti-Transferrin Receptor Antibody at the Mouse Blood-Brain Barrier,” *Mol. Pharm.*, vol. 12, no. 11, pp. 4137–4145, 2015.
- [149] A. J. Clark and M. E. Davis, “Increased brain uptake of targeted nanoparticles by adding an acid-cleavable linkage between transferrin and the nanoparticle core,” *Proc. Natl. Acad. Sci. U. S. A.*, vol. 112, no. 40, pp. 12486–12491, 2015.
- [150] Y. J. Yu and R. J. Watts, “Developing Therapeutic Antibodies for Neurodegenerative Disease,” *Neurotherapeutics*, vol. 10, no. 3, pp. 459–472, 2013.
- [151] C. Dufès, M. Al Robaian, and S. Somani, “Transferrin and the transferrin receptor for the targeted delivery of therapeutic agents to the brain and cancer cells,” *Ther. Deliv.*, vol. 4, no. 5, pp. 629–640, 2013.
- [152] H. Choudhury *et al.*, “Transferrin receptors-targeting nanocarriers for efficient targeted delivery and transcytosis of drugs into the brain tumors: a review of recent advancements and emerging trends,” *Drug Deliv. Transl. Res.*, vol. 8, no. 5, pp. 1545–1563, 2018.
- [153] S. Seo, H. Kim, J. H. Sung, N. Choi, K. Lee, and H. N. Kim, “Microphysiological systems for recapitulating physiology and function of blood-brain barrier,” *Biomaterials*, vol. 232, no. December 2019, p. 119732, 2020.
- [154] M. N. Pangalos, L. E. Schechter, and O. Hurko, “Drug development for CNS disorders: Strategies for balancing risk and reducing attrition,” *Nat. Rev. Drug Discov.*, vol. 6, no. 7, pp. 521–532, 2007.
- [155] D. Pamies, T. Hartung, and H. T. Hogberg, “Biological and medical applications of a brain-on-a-

- chip,” *Exp. Biol. Med.*, vol. 239, no. 9, pp. 1096–1107, 2014.
- [156] P. Garberg *et al.*, “In vitro models for the blood-brain barrier,” *Toxicol. Vitro.*, vol. 19, no. 3, pp. 299–334, 2005.
- [157] M. W. van der Helm, A. D. van der Meer, J. C. T. Eijkel, A. van den Berg, and L. I. Segerink, “Microfluidic organ-on-chip technology for blood-brain barrier research,” *Tissue barriers*, vol. 4, no. 1, p. e1142493, 2016.
- [158] I. Wilhelm and I. A. Krizbai, “In vitro models of the blood-brain barrier for the study of drug delivery to the brain,” *Mol. Pharm.*, vol. 11, no. 7, pp. 1949–1963, 2014.
- [159] K. Hatherell, P. O. Couraud, I. A. Romero, B. Weksler, and G. J. Pilkington, “Development of a three-dimensional, all-human in vitro model of the blood-brain barrier using mono-, co-, and tri-cultivation Transwell models,” *J. Neurosci. Methods*, vol. 199, no. 2, pp. 223–229, 2011.
- [160] E. Markoutsas *et al.*, “Uptake and permeability studies of BBB-targeting immunoliposomes using the hCMEC/D3 cell line,” *Eur. J. Pharm. Biopharm.*, vol. 77, no. 2, pp. 265–274, 2011.
- [161] S. Nakagawa *et al.*, “A new blood-brain barrier model using primary rat brain endothelial cells, pericytes and astrocytes,” *Neurochem. Int.*, vol. 54, no. 3–4, pp. 253–263, 2009.
- [162] K. Hatherell, P. O. Couraud, I. A. Romero, B. Weksler, and G. J. Pilkington, “Development of a three-dimensional, all-human in vitro model of the blood-brain barrier using mono-, co-, and tri-cultivation Transwell models,” *J. Neurosci. Methods*, vol. 199, no. 2, pp. 223–229, 2011.
- [163] A. Appelt-Menzel *et al.*, “Establishment of a Human Blood-Brain Barrier Co-culture Model Mimicking the Neurovascular Unit Using Induced Pluri- and Multipotent Stem Cells,” *Stem Cell Reports*, vol. 8, no. 4, pp. 894–906, 2017.
- [164] D. Pamies, T. Hartung, and H. T. Hogberg, “Biological and medical applications of a brain-on-a-chip,” *Exp. Biol. Med. (Maywood)*, pp. 1096–1107, 2014.
- [165] M. Grskovic, A. Javaherian, B. Strulovici, and G. Q. Daley, “Induced pluripotent stem cells: Opportunities for disease modelling and drug discovery,” *Nat. Rev. Drug Discov.*, vol. 10, no. 12, pp. 915–929, 2011.
- [166] F. Sohet and R. Daneman, “Genetic mouse models to study blood-brain barrier development and function,” *Fluids Barriers CNS*, vol. 10, no. 1, p. 1, 2013.
- [167] S. Aday, R. Cecchelli, D. Hallier-Vanuxeem, M. P. Dehouck, and L. Ferreira, “Stem Cell-Based Human Blood-Brain Barrier Models for Drug Discovery and Delivery,” *Trends Biotechnol.*, vol. 34, no. 5, pp. 382–393, 2016.
- [168] M. W. Van Der Helm, A. D. Van Der Meer, J. C. T. Eijkel, A. Van Den Berg, and L. I. Segerink, “Microfluidic organ-on-chip technology for blood-brain barrier research,” *Tissue Barriers*, no. March, pp. 1–13, 2016.
- [169] H. Ledford, “Ways to fix the clinical trial,” *Macmillan Publ. Ltd. Nat.*, vol. 477, pp. 526–528, 2011.
- [170] T. Hartung, “Food for Thought Look Back in Anger – What Clinical Studies Tell Us About Preclinical Work,” *ALTEX*, vol. 30, no. 1, pp. 275–291, 2013.
- [171] S. Perrin, “Make mouse studies work,” *Nature*, vol. 507, no. 7493, pp. 423–425, 2014.
- [172] S. M. Paul *et al.*, “How to improve RD productivity: The pharmaceutical industry’s grand challenge,” *Nat. Rev. Drug Discov.*, vol. 9, no. 3, pp. 203–214, 2010.
- [173] E. Urich, C. Patsch, S. Aigner, M. Graf, R. Iacone, and P. O. Freskgård, “Multicellular self-assembled spheroidal model of the blood brain barrier,” *Sci. Rep.*, vol. 3, 2013.
- [174] S. Bergmann *et al.*, “Blood-brain-barrier organoids for investigating the permeability of CNS therapeutics,” *Nat. Protoc.*, vol. 13, no. 12, pp. 2827–2843, 2018.
- [175] C. F. Cho *et al.*, “Blood-brain-barrier spheroids as an in vitro screening platform for brain-penetrating agents,” *Nat. Commun.*, vol. 8, pp. 1–14, 2017.
- [176] B. Cakir *et al.*, “Engineering of human brain organoids with a functional vascular-like system,” *Nat. Methods*, vol. 16, no. 11, pp. 1169–1175, 2019.
- [177] M. Tang, J. N. Rich, and S. Chen, “Biomaterials and 3D Bioprinting Strategies to Model Glioblastoma and the Blood-Brain Barrier,” *Adv. Mater.*, vol. 2004776, pp. 1–25, 2020.

- [178] A. Marino *et al.*, “A 3D Real-Scale, Biomimetic, and Biohybrid Model of the Blood-Brain Barrier Fabricated through Two-Photon Lithography,” *Small*, vol. 14, no. 6, pp. 1–9, 2018.
- [179] O. Tricinci, D. De Pasquale, A. Marino, M. Battaglini, C. Pucci, and G. Ciofani, “A 3D Biohybrid Real-Scale Model of the Brain Cancer Microenvironment for Advanced In Vitro Testing,” *Adv. Mater. Technol.*, vol. 5, no. 10, pp. 1–10, 2020.
- [180] J. A. Kim, H. N. Kim, S. K. Im, S. Chung, J. Y. Kang, and N. Choi, “Collagen-based brain microvasculature model in vitro using three-dimensional printed template,” *Biomicrofluidics*, vol. 9, no. 2, 2015.
- [181] H. Yue, K. Xie, X. Ji, B. Xu, C. Wang, and P. Shi, “Vascularized neural constructs for ex-vivo reconstitution of blood-brain barrier function,” *Biomaterials*, vol. 245, no. October 2019, p. 119980, 2020.
- [182] G. M. Whitesides, “The origins and the future of microfluidics,” *Nature*, vol. 442, no. 7101, pp. 368–73, 2006.
- [183] G. M. Whitesides, E. Ostuni, X. Jiang, and D. E. Ingber, “Soft Lithography in Biology,” *Annu. Rev. Biomed. Eng.*, vol. 3, pp. 335–73, 2001.
- [184] E. W. Esch, A. Bahinski, and D. Huh, “Organs-on-chips at the frontiers of drug discovery,” *Nat. Rev. Drug Discov.*, vol. 14, no. 4, pp. 248–260, 2015.
- [185] F. Zheng, F. Fu, Y. Cheng, C. Wang, Y. Zhao, and Z. Gu, “Organ-on-a-Chip Systems: Microengineering to Biomimic Living Systems,” *Small*, vol. 12, no. 17, pp. 2253–2282, 2016.
- [186] A. D. Roses, “Pharmacogenetics in drug discovery and development: A translational perspective,” *Nat. Rev. Drug Discov.*, vol. 7, no. 10, pp. 807–817, 2008.
- [187] R. Booth and H. Kim, “Characterization of a microfluidic in vitro model of the blood-brain barrier (μ BBB),” *Lab Chip*, vol. 12, no. 10, pp. 1784–1792, 2012.
- [188] A. Herland, A. D. Van Der Meer, E. A. FitzGerald, T. E. Park, J. J. F. Sleeboom, and D. E. Ingber, “Distinct contributions of astrocytes and pericytes to neuroinflammation identified in a 3D human blood-brain barrier on a chip,” *PLoS One*, vol. 11, no. 3, pp. 1–21, 2016.
- [189] L. L. Bischel, S. H. Lee, and D. J. Beebe, “A Practical method for patterning lumens through ECM hydrogels via viscous finger patterning,” *J. Lab. Autom.*, vol. 17, no. 2, pp. 96–103, 2012.
- [190] B. M. Maoz *et al.*, “A linked organ-on-chip model of the human neurovascular unit reveals the metabolic coupling of endothelial and neuronal cells,” *Nat. Biotechnol.*, vol. 36, no. 9, pp. 865–877, 2018.
- [191] S. Bang *et al.*, “A Low Permeability Microfluidic Blood-Brain Barrier Platform with Direct Contact between Perfusable Vascular Network and Astrocytes,” *Sci. Rep.*, vol. 7, no. 1, pp. 1–10, 2017.
- [192] G. Adriani, D. Ma, A. Pavesi, and R. D. Kamm, “A 3D neurovascular microfluidic model consisting of neurons, astrocytes and cerebral endothelial cells as a blood–brain barrier,” *Lab Chip*, vol. 12, pp. 169–182, 2017.
- [193] Y. Shin *et al.*, “Blood–Brain Barrier Dysfunction in a 3D In Vitro Model of Alzheimer’s Disease,” *Adv. Sci.*, vol. 6, no. 20, 2019.
- [194] S. I. Ahn *et al.*, “Microengineered human blood–brain barrier platform for understanding nanoparticle transport mechanisms,” *Nat. Commun.*, vol. 11, no. 1, pp. 1–12, 2020.
- [195] G. D. Vatine *et al.*, “Human iPSC-Derived Blood-Brain Barrier Chips Enable Disease Modeling and Personalized Medicine Applications,” *Cell Stem Cell*, vol. 24, no. 6, pp. 995-1005.e6, 2019.
- [196] S. Lee, M. Chung, S. R. Lee, and N. L. Jeon, “3D brain angiogenesis model to reconstitute functional human blood–brain barrier in vitro,” *Biotechnol. Bioeng.*, vol. 117, no. 3, pp. 748–762, 2020.
- [197] B. Chung *et al.*, “Evaluation of Cell-Penetrating Peptides Using Microfluidic In Vitro 3D Brain Endothelial Barrier,” *Macromol. Biosci.*, vol. 20, no. 6, pp. 1–10, 2020.
- [198] Y. I. Wang, H. E. Abaci, and M. L. Shuler, “Microfluidic blood-brain barrier model provides in vivo-like barrier properties for drug permeability screening,” *Biotechnol. Bioeng.*, vol. 114, no. 1, pp. 184–194, 2017.

- [199] H. Cho *et al.*, “Three-dimensional blood-brain barrier model for in vitro studies of neurovascular pathology,” *Sci. Rep.*, vol. 5, pp. 1–9, 2015.
- [200] S. P. Deosarkar, B. Prabhakarapandian, B. Wang, J. B. Sheffield, B. Krynska, and M. F. Kiani, “A novel dynamic neonatal blood-brain barrier on a chip,” *PLoS One*, vol. 10, no. 11, pp. 1–21, 2015.
- [201] J. D. Wang, E. S. Khafagy, K. Khanafer, S. Takayama, and M. E. H. Elsayed, “Organization of Endothelial Cells, Pericytes, and Astrocytes into a 3D Microfluidic in Vitro Model of the Blood-Brain Barrier,” *Mol. Pharm.*, vol. 13, no. 3, pp. 895–906, 2016.
- [202] J. A. Brown *et al.*, “Recreating blood-brain barrier physiology and structure on chip: A novel neurovascular microfluidic bioreactor,” *Biomicrofluidics*, vol. 9, no. 5, 2015.
- [203] K. L. Sellgren, B. T. Hawkins, and S. Grego, “An optically transparent membrane supports shear stress studies in a three-dimensional microfluidic neurovascular unit model,” *Biomicrofluidics*, vol. 9, no. 6, 2015.
- [204] S. F. Merkel *et al.*, “Trafficking of adeno-associated virus vectors across a model of the blood–brain barrier; a comparative study of transcytosis and transduction using primary human brain endothelial cells,” *J. Neurochem.*, vol. 140, no. 2, pp. 216–230, 2017.
- [205] T. E. Park *et al.*, “Hypoxia-enhanced Blood-Brain Barrier Chip recapitulates human barrier function and shuttling of drugs and antibodies,” *Nat. Commun.*, vol. 10, no. 1, pp. 1–12, 2019.
- [206] C. S. Lee and K. W. Leong, “Advances in microphysiological blood-brain barrier (BBB) models towards drug delivery,” *Curr. Opin. Biotechnol.*, vol. 66, pp. 78–87, 2020.
- [207] S. Jackson, C. Meeks, A. Vézina, R. W. Robey, K. Tanner, and M. M. Gottesman, “Model systems for studying the blood-brain barrier: Applications and challenges,” *Biomaterials*, vol. 214, no. December 2018, p. 119217, 2019.
- [208] L. Jiang, S. Li, J. Zheng, Y. Li, and H. Huang, “Recent progress in microfluidic models of the blood-brain barrier,” *Micromachines*, vol. 10, no. 6, pp. 1–20, 2019.
- [209] A. K. Miri, A. Khalilpour, B. Cecen, S. Maharjan, S. R. Shin, and A. Khademhosseini, “Multiscale bioprinting of vascularized models,” *Biomaterials*, vol. 198, no. August 2018, pp. 204–216, 2019.
- [210] J. A. Brassard, M. Nikolaev, T. Hübscher, M. Hofer, and M. P. Lutolf, “Recapitulating macro-scale tissue self-organization through organoid bioprinting,” *Nat. Mater.*, vol. 20, no. January, 2020.
- [211] A. Oddo *et al.*, “Advances in Microfluidic Blood–Brain Barrier (BBB) Models,” *Trends Biotechnol.*, vol. 37, no. 12, pp. 1295–1314, 2019.
- [212] X. W. and J. A. K. G.J. del Zoppo, R. Milner, T. Mabuchi, S. Hung, “Vascular matrix adhesion and the blood–brain barrier,” *Biochem. Soc. Trans.*, pp. 1261–1266, 2006.
- [213] V. Muoio, P. B. Persson, and M. M. Sendeski, “The neurovascular unit - concept review,” *Acta Physiol.*, vol. 210, no. 4, pp. 790–798, 2014.
- [214] L. Cucullo, M. Hossain, V. Puvenna, N. Marchi, and D. Janigro, “The role of shear stress in Blood-Brain Barrier endothelial physiology,” *BMC Neurosci.*, vol. 12, no. 1, p. 40, 2011.
- [215] R. Deane and B. Zlokovic, “Role of the Blood-Brain Barrier in the Pathogenesis of Alzheimers Disease,” *Curr. Alzheimer Res.*, vol. 4, no. 2, pp. 191–197, 2007.
- [216] P. F. Benson and M. C. Joseph, “The Blood-Brain Barrier,” *Dev. Med. Child Neurol.*, vol. 3, no. 5, pp. 510–514, 1961.
- [217] H. Brain and A. Resource, “News and Views,” *Altern. Lab. Anim.*, vol. 48, no. 3, pp. 97–100, 2020.
- [218] Anon, “Report from the Commission to the European Parliament and the Council 2019: report on the statistics on the use of animals for scientific purposes in the Member States of the European Union in 2015–2017,” *Brussel Eur. Comm.*, vol. 20, p. pp, 2020.
- [219] D. Qin, Y. Xia, and G. M. Whitesides, “Soft lithography for micro- and nanoscale patterning,” *Nat. Protoc.*, vol. 5, no. 3, pp. 491–502, 2010.
- [220] Y. Shin *et al.*, “Microfluidic assay for simultaneous culture of multiple cell types on surfaces or within hydrogels,” *Nat. Protoc.*, vol. 7, no. 7, pp. 1247–59, 2012.
- [221] M. Campisi, Y. Shin, T. Osaki, C. Hajal, V. Chiono, and R. D. Kamm, “3D self-organized

- microvascular model of the human blood-brain barrier with endothelial cells, pericytes and astrocytes,” *Biomaterials*, vol. 180, pp. 117–129, 2018.
- [222] A. S. Pitek, D. O’Connell, E. Mahon, M. P. Monopoli, F. Francesca Baldelli, and K. A. Dawson, “Transferrin coated nanoparticles: Study of the bionano interface in human plasma,” *PLoS One*, vol. 7, no. 7, 2012.
- [223] C. Mattu *et al.*, “Alternating block copolymer-based nanoparticles as tools to modulate the loading of multiple chemotherapeutics and imaging probes,” *Acta Biomater.*, vol. 80, pp. 341–351, Oct. 2018.
- [224] F. E. Curry, V. H. Huxley, and R. H. Adamson, “Permeability of single capillaries to intermediate-sized colored solutes,” *Am. J. Physiol. - Hear. Circ. Physiol.*, vol. 14, no. 3, 1983.
- [225] G. S. Offeddu *et al.*, “An on-chip model of protein paracellular and transcellular permeability in the microcirculation,” *Biomaterials*, vol. 212, pp. 115–125, Aug. 2019.
- [226] S. W. L. Lee *et al.*, “Modeling Nanocarrier Transport across a 3D In Vitro Human Blood-Brain-Barrier Microvasculature,” *Adv. Healthc. Mater.*, vol. 9, no. 7, Apr. 2020.
- [227] S. R. Popielarski, S. H. Pun, and M. E. Davis, “A nanoparticle-based model delivery system to guide the rational design of gene delivery to the liver. 1. Synthesis and characterization,” *Bioconjug. Chem.*, vol. 16, no. 5, pp. 1063–1070, 2005.
- [228] T. Osaki, Y. Shin, V. Sivathanu, M. Campisi, and R. D. Kamm, “In Vitro Microfluidic Models for Neurodegenerative Disorders,” *Adv. Healthc. Mater.*, vol. 7, no. 2, pp. 1–29, 2018.
- [229] R. D. B. B. V. Zlokovic, “Neurovascular mechanisms and blood–brain barrier disorder in Alzheimer’s disease,” *Acta Neuropathol.*, vol. 36, no. 3, pp. 490–499, 2010.
- [230] W. Yuan, Y. Lv, M. Zeng, and B. M. Fu, “Non-invasive measurement of solute permeability in cerebral microvessels of the rat,” *Microvasc. Res.*, vol. 77, no. 2, pp. 166–173, Mar. 2009.

Section III –

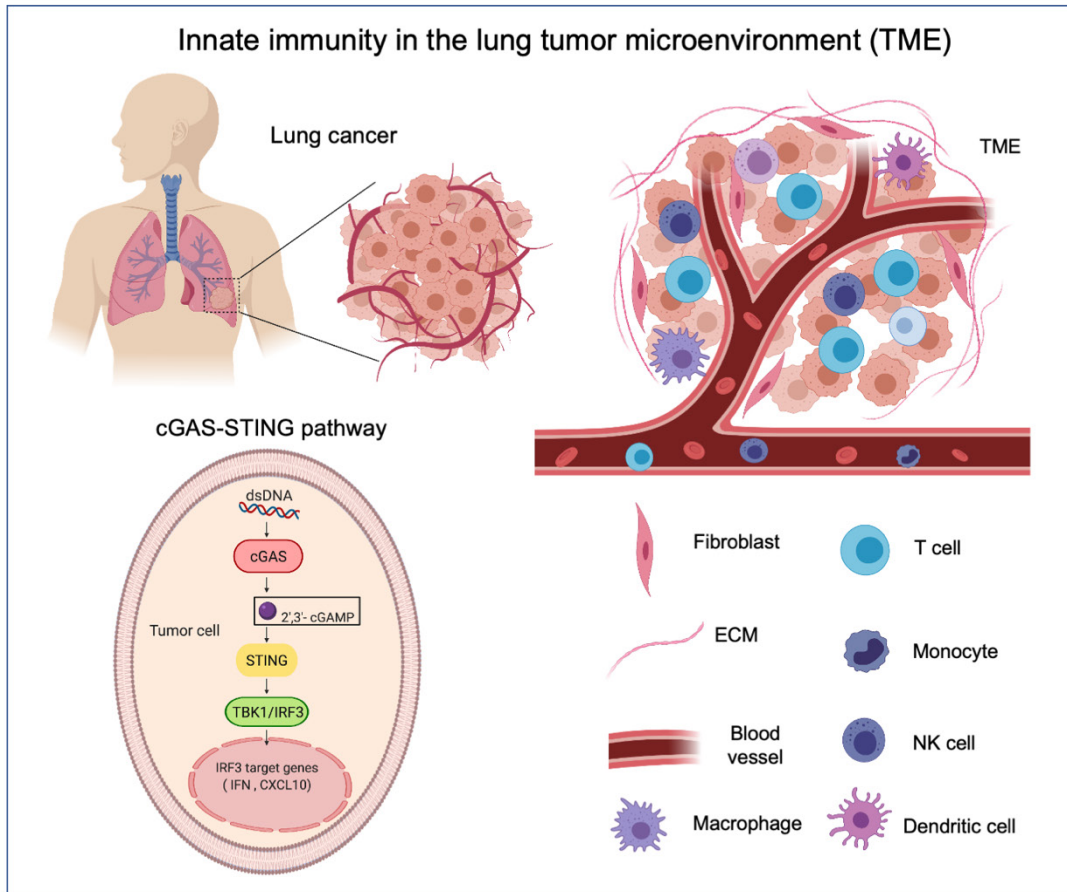
3D Microphysiological models of tumor-vascular interactions in KRAS/LKB1 Non-Small Cell Lung Cancer and ALK⁺ Anaplastic Large Cell Lymphoma

Chapter 5 – Modelling cGAS-STING driven innate immunity and T-cell infiltration/exclusion in the non-small cell lung tumor microenvironment

Abstract

Lung cancer is one of the leading causes of cancer-related deaths worldwide with an estimated 1.6 million deaths each year. Even though important advances in treatments have been achieved, survival rates remain low. Treatments that activate the immune system to recognize and reject tumors have shown promises but fail to benefit the majority of patients. The field suffers from a lack of preclinical models to predict molecular mechanisms of drug resistance. Insights into the multi-cellular interactions in the tumor microenvironment will identify novel therapeutic strategies to help patients whose tumors are refractory or resistant to current immunotherapies.

In this chapter 5, fundamentals of lung cancer biology and mechanisms of tumor progression and driver oncogene mutations are introduced, focusing on *KRAS/LKB1* mutant non-small cell lung cancer. Activation of innate immune signaling via the cGAS-STING pathway is described, which shows early promise in combination with cancer immunotherapies such as inhibition the of PD-1/PD-L1 immune checkpoint. Next, the cellular and non-cellular components of the lung and its tumor microenvironment are described. Finally, we discuss designs for *in vitro* preclinical models including utilizing transwells and cellular organoids, before proposing microphysiological cancer models using microfluidic devices. Potential opportunities, current challenges and future perspectives on modelling lung cancer through *in vitro* and *ex vivo* models are discussed.



Graphical abstract 6: *cGAS-STING* driven innate immunity in the non-small cell lung tumor microenvironment comprising tumor cells, fibroblasts, ECM, microvasculature and immune cells.

Schematic created with biorender.com

Introduction

Lung cancer biology

Lung cancer is one of the most frequently diagnosed cancers and is the leading cause of cancer-related mortality worldwide[1]. Lung cancers are highly heterogeneous, invasive, and rapidly metastasize to several tissues, most commonly the brain, bone and liver[2]. Lung carcinomas are histologically divided into non-small cell lung cancer (NSCLC), which includes adenocarcinoma, squamous cell carcinoma and large-cell carcinoma subtypes, representing approximately 85% of all cases of lung cancer patients[1][3], and small cell lung cancer (SCLC), accounting for the remaining 15% [4][5][6][7]. Lung cancer is a molecularly heterogeneous disease and understanding its biology, in particular its genomic alterations including driver mutations in proto-oncogenes and loss of tumor-suppressor genes has proven crucial for the development of new effective treatments [8][3]. Effective treatment must also address intra-tumoral genomic heterogeneity (recurrently mutated oncogenic pathways), tumor evolution during metastasis, and the development of resistance to molecularly targeted therapies [9], [10].

Comprehensive studies have profiled the genomic landscape of lung cancers[11][12]. The identification of driver oncogene mutations was pivotal in stratifying mechanisms of lung carcinoma-genesis and potential therapeutic targets. Acquired genetic mutations in kinases result in constitutive signaling and, in susceptible cells, this leads to oncogenic transformation. Oncogenes implicated in NSCLC include activating mutations in the epidermal growth factor receptor (EGFR) gene[13], and translocations of the anaplastic lymphoma kinase (ALK) gene[14][15]. EGFR and ALK driver abnormalities occur primarily in adenocarcinomas (10–60%). Less common abnormalities have also been established as targets, including translocations of RET, ROS1 and receptor tyrosine kinases, mutations in BRAF, MET (encoding the hepatocyte growth factor (HGF) receptor) and HER2 [1], and amplifications of MET and fibroblast growth factor receptor 1 (FGFR1). The tumor suppressor genes, TP53 and RB1, are universally lost in all SCLCs and the former is frequently altered in NSCLCs. Activating mutations in the KRAS oncogene are common in lung adenocarcinomas, uncommon in squamous tumors and absent in SCLCs[15],[16]; also, recurring inactivating mutations in the tumor suppressor serine/threonine kinase 11 (STK11; also known as LKB1) are very common, although the therapeutic implications of mutations in this gene are unclear [12][11]. Dozens of other mutations have been identified in

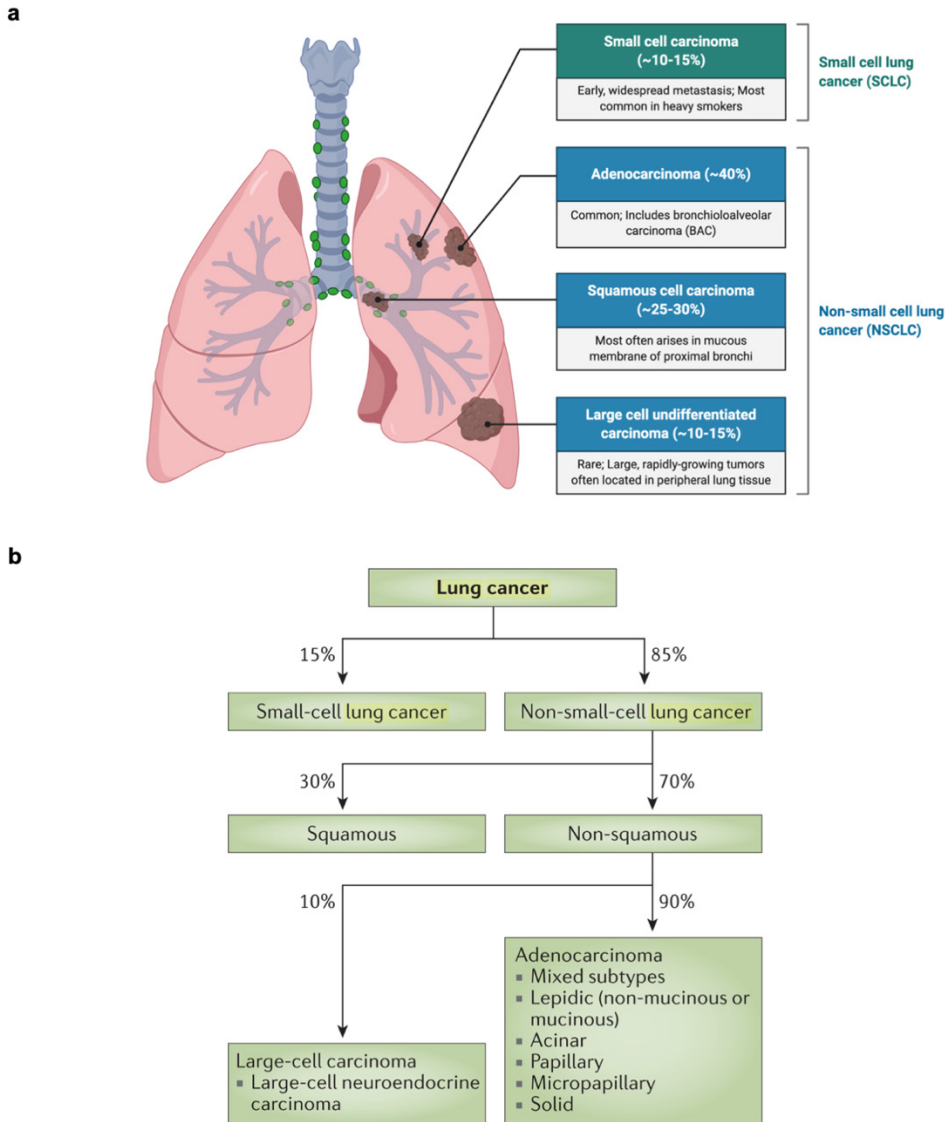


Figure 3.1: The biology of lung cancer.

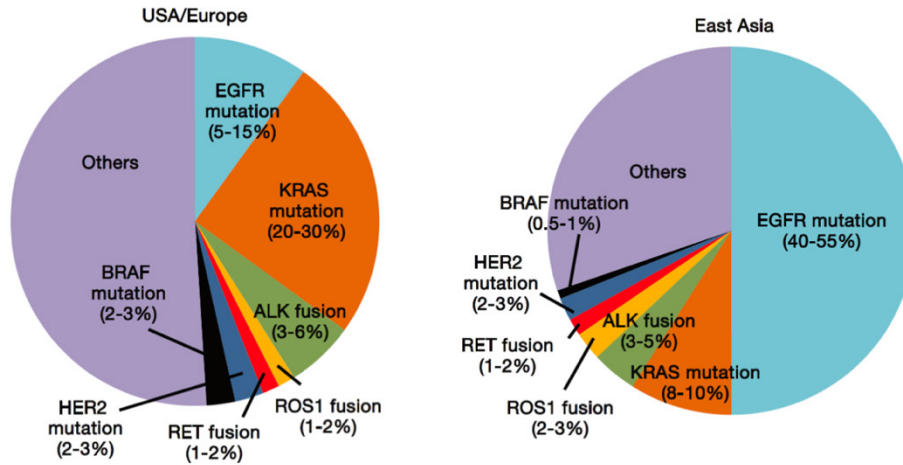
a) and **b)** lung cancer classification in small cell and non-small cell lung cancer classification and frequency among all lung cancers. **a)** Schematic created with biorender.com **b)** Reproduced with permission from[1].

genetic analyses, and include mutations in the AKT pathway, MAPK (MEK) pathway, cyclins and many others, and studies are underway to determine how to take therapeutic advantage of such mutations[18], [19]. In contrast with NSCLC, beside RB1 and TP53, SCLC is not associated with predominant somatic mutations in oncogenes[7][20]. SCLC have a relatively high tumor

mutational burden[21], with recurrent aberrations among the MYC family of genes (MYC, MYCL and MYCN) as proto-oncogene drivers[22], [23].

Although mutations in the tumor suppressor genes TP53 and RB1, as well as the KRAS oncogene frequently occur in several lung cancer subtypes, they are not yet therapeutically targetable, however studies are underway to determine how to take therapeutic advantage of such mutations[24].

a



b

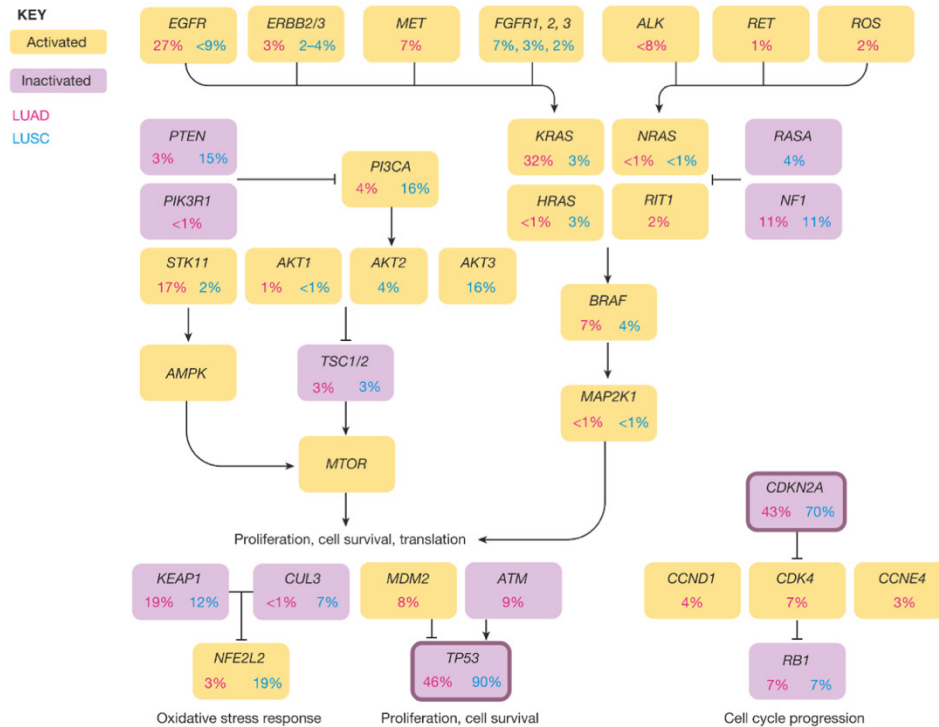


Figure 3.2: The biology of lung cancer.

a) lung cancer mutation distribution in Europe/US and Asia **b)** Oncogenic pathways in lung adenocarcinoma and downstream signaling. Reproduced with permission from **a)**[25] and **b)** [3].

KRAS/LKB1 mutant Non-Small Cell Lung Cancer

Kirsten Rat Sarcoma virus (*KRAS*)- mutant is a proto-oncogene that was discovered by Werner H. Kirsten, a German-American cancer researcher[16], [18]. The RAS family of oncogenes was one of the first to be identified as mutated in human cancer. Somatic *KRAS* mutations are found at a high frequency in colorectal, pancreatic and lung cancers. In lung cancer, oncogenic *KRAS* and *EGFR* mutations are generally mutually exclusive. *KRAS* converts GTP into GDP, acting as on/off switch for signaling downstream of various growth factors, and also upregulates the glucose transporter GLUT1[13],[17][18]. Oncogenic mutations in *KRAS* are observed in approximately 30% of lung adenocarcinoma, are strongly associated with smoking[16], [18], and confer poor prognosis and high risk of tumor recurrence. Among all the *KRAS* mutations[26], the development of therapies targeting one of the most common mutation, the *KRAS*-G12C, has advanced rapidly and several agents have shown promising results in clinical trials[27], [28]. In addition, about half of NSCLCs with activating *KRAS* lesions also have deletions or inactivating mutations in the serine/threonine kinase 11 (*STK11*), also known as liver kinase B1 (*LKB1*) gene. *LKB1* is a tumor suppressor kinase, and the loss of *LKB1* in a *KRAS*-mutant background contributes to poor response to treatment, with an aggressive phenotype distinct from that of *KRAS* mutations alone[29]–[31]. Two distinct *KRAS* co-mutation patterns have been described: *STK11/LKB1*(KL) or *TP53* (KP). *KRAS* mutant non-small cell lung cancers with concurrent inactivation of the *STK11/LKB1* tumor suppressor (KL) have been one of the clearest genotypic categories associated with anti-PD-L1 treatment resistance and exhibit T cell exclusion. Patients with KL NSCLC show significantly shorter progression free and overall survival compared to patients with intact *LKB1* after PD-1 blockade. Indeed, as is recently demonstrated, mutations in *STK11* (*LKB1*) are a major cause of primary resistance to immunotherapy in NSCLC [32].

Innate immunity and cGAS-STING pathway

The Stimulator of Interferon Genes (STING), an ER-resident protein encoded by *TMEM173*, is a central mediator of innate immunity via the recognition of nucleic acids from microbial agents and is an essential mechanism by which the immune system initiates host defense against

infections[33]. Cyclic GMP-AMP (cGAMP) synthase (cGAS) is a cytosolic DNA sensor that recognizes double-stranded DNA in the cytosol and binds it to produce 2'3'-cGAMP, a cyclic dinucleotide and soluble second messenger which binds to STING protein in the endoplasmic reticulum (ER) causing its cascade activation, which triggers TBK1 activation via phosphorylation (pTBK1) and its downstream substrate, the transcription factor IRF3[34]–[37], that controls the transcription of numerous genes, including type I interferons (IFNs) and pro-inflammatory cytokines, such as CXCL10, The cGAS-STING pathway plays an important role in tumor cells, antigen presenting cells, and potentially other cell types [38], establishing a link between the innate and adaptive immune responses[39], [40].

Furthermore, it is important to note that the STING sensor is present in virtually all types of cells, including cancer cells. As cancer cells are known to bypass cellular checkpoints to proliferate, they accumulate cytosolic DNA. Literature has shown that this accumulation of cytosolic DNA in cancer cells is capable of producing a STING-driven immune response as important mediator of the innate immune response in cancer. Indeed, the cGAS–STING pathway not only mediates protective immune defense against infection by a large variety of DNA-containing pathogens but also detects tumor-derived DNA and is capable of generating intrinsic antitumor immunity[41][42]. STING signaling is important in immunotherapy because of its ability to activate the immune cells recruitment[40]. Indeed, it has been demonstrated that multiple tumors silence STING to evade the immune response. On the other hand, STING agonists show promise in immunotherapy, where both the initiation of the adaptive immune response and T cell recruitment are critical for a robust response to immunotherapy. It is also known that mutations in STK11 (LKB1) are a major cause of primary resistance to immunotherapy in NSCLC[43]. The mechanism of this immune-resistant phenotype was dissected, demonstrating that LKB1 loss leads directly to suppression of stimulator of interferon genes (STING) and insensitivity to cytoplasmic double-strand DNA detection, and downstream anti-tumor immunity. Indeed, it has been shown that the expression of STING via IHC correlates with T-cell infiltration in patient tumor biopsies: LKB1-intact STING-high tumors are associated with higher T cell infiltration. When LKB1 is lost, STING-low tumors are associated with lower T cell infiltration[32][44]. Therapies that reactivate LKB1 or the STING pathway may boost anticancer immune response in cancers with resistance to immune-checkpoint blockade. Facilitating immune recognition of tumor cells in the tumor microenvironment (TME) requires that key effector T cells and other immune cell types adhere

and extravasate from the vasculature and migrate through the extracellular matrix (ECM) to recognize tumor antigens [45], [46]. Indeed, resistance to PD-1 immune checkpoint blockade (ICB) in a number of different tumor contexts has been linked to an “immune cell excluded” phenotype [47]. For example, KRAS mutant non-small cell lung cancers that inactivate the STK11/LKB1 tumor suppressor are strongly resistant to anti-PD-(L)1 therapy and exhibit T cell exclusion[44] [32]. Accordingly, many pharmaceutical companies are now developing STING agonists, and some of them are in clinical trials to treat lung carcinomas in combination with immunotherapies.

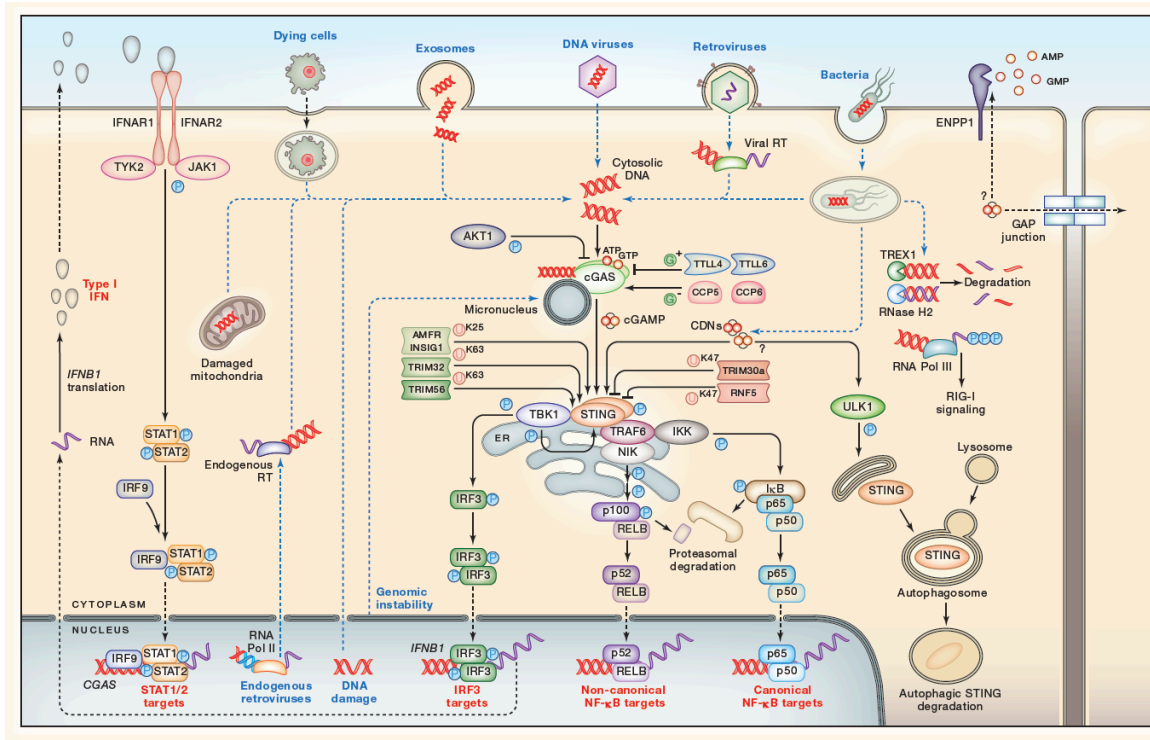


Figure 3.3: The cGAS-STING pathway.

a) The accumulation of cytosolic DNA is recognized by the endogenous enzyme cGAS, which binds the DNA and converts it into the canonical ligand for STING, a cyclic dinucleotide known as 2',3'-cGAMP. cGAMP then binds STING in the ER, which triggers (TBK1-IRF3)-dependent signaling process leading to the production of pro-inflammatory cytokines. Reproduced with permission from[48].

Lung Tumor microenvironment

The lung is a complex organ composed of many types of epithelial cells, immune cells, and stromal cells. It can be divided into the conducting zone (nasal passage, trachea, main bronchi) and the respiratory zone, which participate in gas exchange, namely, intra-pulmonary bronchi and

bronchioles. The respiratory zone consists of respiratory bronchioles, alveolar ducts and alveolar sacs, and is the site of gas exchange between the air within the lung and the blood within pulmonary capillaries. The human airway, from the nasal passage to the alveolar sacs, is covered with a continuous epithelial sheet that differs in morphology and cellular composition between the conducting and respiratory zones. The major cell types of the large airway epithelium are goblet cells that secrete mucus, ciliated cells that promote mucus motility. Alveolar epithelium contains type I and II alveolar epithelial cells (AECs).

In this microenvironment, lung cancers typically start in the cells lining the airways of the bronchus, bronchioles or alveoli[49]. Lung cancers comprise more than cancer cells alone; they are complex ‘ecosystems’ comprising many different cell types and noncellular factors[50]. The tumor microenvironment (TME) usually contains stromal cells such as cancer associated fibroblasts (CAF) and endothelial cells, immune cells such as myeloid cells and infiltrating T-lymphocytes[51]. Interplay between tumor cells and non-malignant cells plays a crucial role in shaping anti-tumor immune responses [51][52]. Vascular, and stromal components support tumor growth [52][50]. The tumor vasculature is highly abnormal and dysfunctional, consequently immune cells have impaired trafficking ability into tumors. The stroma, including specialized connective tissue cells such as pericytes and fibroblasts, has multiple functions that produce and shape the extracellular matrix (ECM) in which they reside, as well as generating cytokines. Stromal cells have been demonstrated to have crucial roles in tumorigenesis, cancer progression, metastasis, and therapy resistance[53]. Indeed, angiogenesis, the formation of new blood vessels from preexisting vasculature, is a hallmark of cancer [8] [54].

Another essential constituent of the TME is the ECM, formed by collagens, proteoglycans and glycosaminoglycans. It mediates the interactions between cellular components[55], provides structure and support for cells and contributes to paracrine signaling[56].

The density of the lung ECM has been correlated with less immunoinfiltration into the tumor in NSCLC, functioning as immune cell barrier[57].

Over the past few decades, the importance of the TME in determining disease progression and treatment outcomes has become increasingly evident[58]. It has become possible to identify different subclasses of the immune microenvironment that influence tumor initiation and response to therapy [51][59]. It remains to be understood how tumor-produced cytokines and chemokines, tumor oncogenes and mutation landscapes determine the composition of the TME[51]. In

progressing lung cancers, the tumor and TME are not static, but dynamic reciprocal interactions occur between tumor and TME, which evolve and mutate as the tumor grows, thus allowing for modulation of both tumor cell- intrinsic and -extrinsic processes[56].

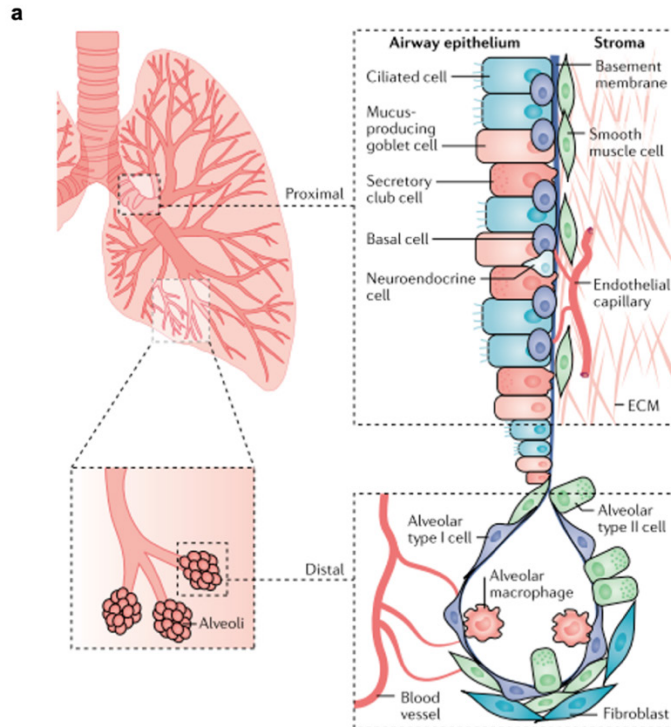


Figure 3.4: The lung microenvironment.

a) A schematic representation of the normal lung showing anatomic regions encompassing the proximal and distal airways. The proximal airways are composed of ciliated cells, secretory club cells, undifferentiated basal cells, and neuroendocrine cells; the distal airways are composed of alveolar type I and type II cells. Other cell types in the lung microenvironment include smooth muscle cells, fibroblasts, endothelial cells and immune cells, including resident alveolar macrophages and dendritic cells. Reproduced with permission from [56].

***In vitro* Preclinical models of lung cancer**

Traditional two-dimensional (2D) cell culture models using cell lines derived from patients have had a profound impact on both basic and clinical research[60]. However, the inherent differences when compared with *in vivo* and clinical observations pose an impediment to answering research questions. Recent progress in microengineering and isolation of lung epithelial progenitor and stromal cells, as well as defining stem cell niche factors that are important for lung development, has led to the establishment of *in vitro* three-dimensional (3D) culture systems. Several specialized models, aimed to recapitulate the morphological and functional complexity of the human lung,

have been developed. 3D lung models fall broadly into three categories: Transwell systems, organoids[61] and microphysiological systems or so-called “Organs on a Chip”[62].

Transwell techniques were initially developed to recapitulate lung airways with air liquid-interface (ALI) culture. Stem and progenitor cells differentiate into a stratified bronchial epithelium containing ciliated, goblet and basal cells, which show mucus secretion, barrier properties, as well as remodeling and restoration properties similar to the native airway epithelium[63]–[65]. Cells are grown in submerged cultures on permeable inserts until they become fully confluent. Medium is removed from the apical surface, which allow full differentiation, with slow but constant turnover. Combination of exposure to air and specialized cell culture medium triggers differentiation of the monolayer culture to a pseudo-stratified epithelium that resembles the native human airway. This model has been utilized for many applications ranging from inhalation toxicology in the airway interface, to drug-screening, to basic research.

Lung organoids are formed by epithelial stem and progenitor cells cultured in ECM-like (Matrigel) structures with a mixture of growth factors. The organoids then self-organize into complex spheroidal structures retaining clusters of multi-lineage epithelial cells. Individual cells are able to grow into clonal spheres called bronchospheres, bronchioalveolar spheres or alveolospheres, depending on the origin of the starting cells. Several groups demonstrated that lung organoids can be generated from human pluripotent stem cells following a stepwise-directed differentiation[66][67]. Recently, NSCLC organoids[68] and patient-derived organoids from human lung cancer biopsies have been established, enabling the analysis of resistance mechanisms for targeted therapies in individual patients[69][70]. Using a similar concept design, *ex vivo* culture called murine and patient-derived organotypic tumor spheroids (MDOTS/PDOTS) have been established. Samples are isolated from mouse and human tumors retain autologous lymphoid and myeloid cell populations and are cultured in 3D microfluidic culture systems.

Lastly, Lung-on-chip microdevices that reconstitute the mechanically active alveolar–capillary barrier in the human lung have been developed [71]. This model is created in a compartmentalized 3D microfluidic system (two PDMS layers separated by a 10 μm -thick PDMS membrane) in which human alveolar epithelial cells are cultured in close apposition with human pulmonary microvascular endothelial cells on a thin porous elastomeric membrane to form a barrier tissue that resembles the *in vivo* alveolar–capillary interface[72]. This microfluidic cell culture system is integrated with a biologically inspired mechanical actuation system that uses computer-controlled

negative pressure to cyclically stretch the alveolar–capillary barrier to mimic physiological breathing motions. The same system was further engineered to recapitulate a NSCLC model of microenvironment-specific cancer growth, tumor dormancy, and response to tyrosine kinase inhibitors (TKIs) [73]. A similar approach utilizes a physiological microfluidic device containing capillary-size vessels and tumor spheroids for studying tumor vascular interactions[74].

Discussion

Here, lung biology and its tumor microenvironment were described including recent cancer immunology principles involving the cGAS-STING pathway. Over the past few decades, to experimentally model lung cancer biology in a preclinical setting, many 2D and 3D *in vitro* platforms were developed. Traditional models, such as 2D culture transwell systems, when compared with *in vivo* and clinical observations, are too simple to answer complex research questions. The advantages of these models over *in vivo* animal studies include the use of human tissue and a relatively low cost of maintenance and ease of handling. The downside is the inability to improve the mimicry of the physiological human structure compared to 2D culture systems, which may finally influence experimental outcomes. On the other hand, organoid culture has the advantages of propagation ability, amenability for high throughput screening, and feasibility of establishing a long-term culture that mimics cellular interactions in the tissue microenvironment using a more physiologically-relevant culture system. The ability to rapidly generate organoids from individual patients also enables testing of chemotherapies for personalized medicine development and targeted therapies. Similarly, *ex vivo* systems using microfluidic technology, incorporate patient-derived samples, become features of the tumor microenvironment and model the dynamic response to immune checkpoint blockade may facilitate efforts in precision immunology and the development of effective combination therapies. Unlike organoids, MDOTS/PDOTS retain the immune components and do not require several days of manipulation. Both *ex vivo* systems (MDOTS/PDOTS) and organoids still lack perfusable vasculature. Organoids instead, are unable to maintain an immune cell compartment, which complicates studying immunological signaling, such as the cGAS-STING pathway and its application in the context of cancer immunotherapies. These drawbacks make lung-on-a-chip culture and microphysiological systems or combination with PDOTS excellent platforms for a wide range of

applications including studying the interaction of tumor cells with the vasculature, and potentially all the components of the tumor microenvironment in both basic and translational contexts.

Conclusion

In this chapter, the fundamentals of lung cancer biology including driver oncogene mutations and mechanisms of tumor progression were introduced, focusing on KRAS/LKB1 mutant non-small cell lung cancer. Then, activation of innate immunity signaling via the cGAS-STING pathway was described, which has achieved potential relevance as a combination treatment with cancer immunotherapies. Subsequently, the cellular and non-cellular components of the lung tumor microenvironment were outlined. Tumor-produced cytokines and chemokines, cell elements, tumor oncogenes and mutation landscapes determine the composition of the TME. Studying the dynamic reciprocal interactions between tumor and TME, which evolves and mutates as the tumor grows, allows better prediction of clinical outcomes. Finally, different designs of *in vitro* preclinical models were outlined, including Transwell, organoids and emerging microphysiological cancer models using microfluidic devices. These advanced cultures allow investigation of the TME, including lung stem cells or patient-derived specimens residing in distinct regions of lung, while also monitoring their behavior in different micro-environments.

Although 3D culture systems are still in their infancy, facing many challenges, their great potential supports their use in biomedical applications modelling many diseases, including cancer, and allows scientists and clinicians to begin to predict treatment efficacy. Recent progress in microengineering and isolation of cells are valid for all models. Generation of lung models from biopsies provides a powerful resource for a wide range of translational and medical approaches, such as drug toxicity and efficacy studies. Remaining challenges for the current lung preclinical models include culture conditions to better maintain genetic stability and physiological function over the long-term, and development of high-throughput screening platforms. Addressing these technical difficulties by combining technologies will rapidly advance their reliability and preclinical significance.

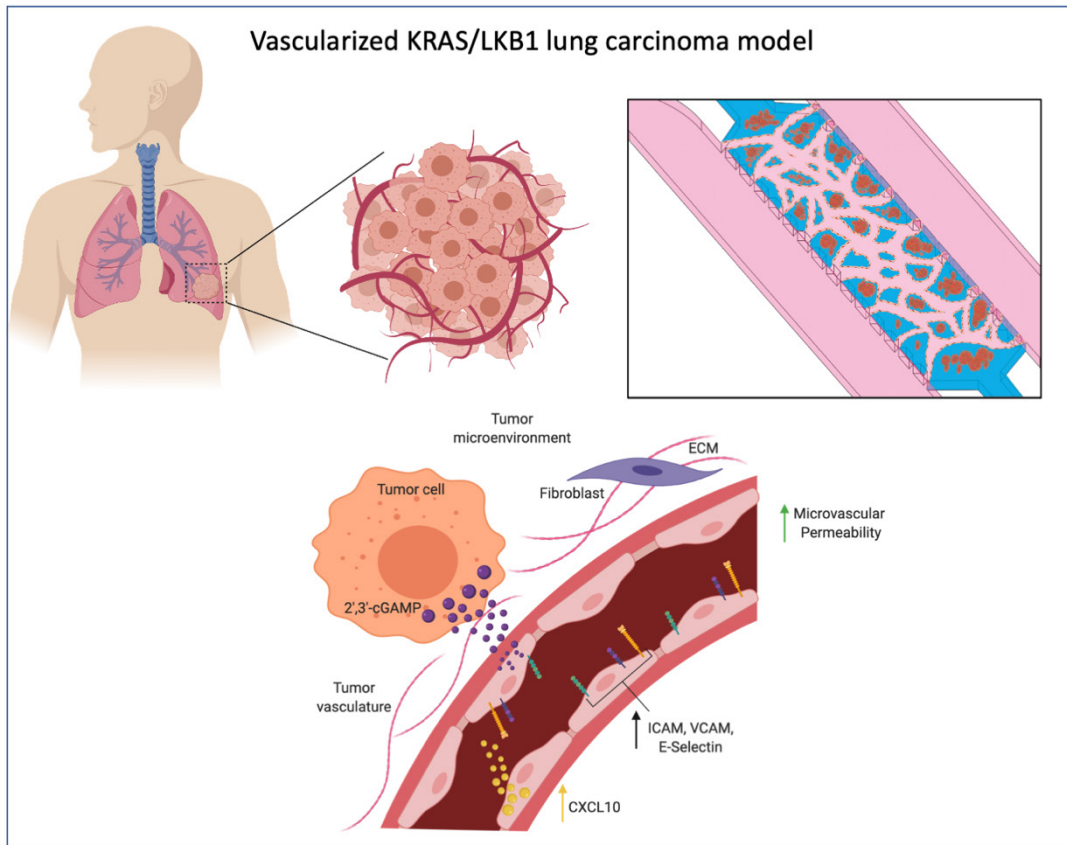
Chapter 6 – *A microphysiological vascular-tumor model uncovers Tumor-derived cGAMP export to promote cGAS-STING driven microvascular inflammation in the tumor microenvironment*

Abstract

The recruitment of immune cells following innate immune activation through the cGAS/STING pathway is critical for anti-tumor immunity in the tumor microenvironment (TME), and this axis has gained great relevance in the context of cancer immunotherapy. Notably, certain tumor types that silence STING and are resistant to PD-1 blockade, such as *KRAS-LKB1* (KL) mutant non-small lung cancer, exhibit T cell exclusion that is partially related to impaired production of chemokines essential for T cell recruitment. T cells and other immune cells must also actively adhere and extravasate from the microvessels to enter in close contact with tumor cells. Since the tumor vasculature is crucial for immune cell infiltration in tumors, novel 3-D microphysiological systems using a microfluidic device which incorporates vascularized KL mutant tumor spheroids was developed to study tumor-vascular interactions.

This more physiologic *in vitro* model revealed particularly strong cooperative production of STING-dependent cytokines, such as CXCL10, in the co-culture system of cancer cells and vasculature, independent of cancer cell-intrinsic STING status, suggesting that tumor-vascular interaction promotes paracrine signaling which triggers STING activation in the vasculature.

Indeed, extracellular export of 2'3' cGAMP by cancer cells was found to activate endothelial cells, which co-operate with type 1 interferon to increase vascular permeability and upregulate specific adhesion molecules such as E selectin, VCAM-1, and ICAM-1 that promote Jurkat T cell adhesion to the endothelium. Thus, developing these more complex 3D microphysiological models that incorporate the vasculature to study tumor-vascular interactions may elucidate important aspects of STING biology and may ultimately aid further development of effective immunotherapies targeting this signaling axis.



Graphical abstract 7: Preclinical models of KRAS/LKB1 tumor spheroids and microvasculature to model the tumor microenvironment.

Schematic created with biorender.com

This work was performed at the David A. Barbie Laboratory at the Dana-Farber Cancer Institute (DFCI), Harvard Medical School, Boston, during an exchange period at DFCI for the doctoral candidate.

Part of the work described in this chapter has been previously published in:

<https://doi.org/10.3389/fimmu.2020.02090>

“Tumor-Derived cGAMP Regulates Activation of the Vasculature”.

Frontiers in Immunology. Sept. 2020

Marco Campisi*, Shriram K. Sundararaman*, Sarah E. Shelton*, Erik H. Knelson, Navin R. Mahadevan, Ryohei Yoshida, Tetsuo Tani, Elena Ivanova, Israel Cañadas, Tatsuya Osaki, Sharon Wei Ling Lee, Tran Thai, Saemi Han, Brandon P. Piel, Sean Gilhooley, Cloud P. Paweletz, Valeria Chiono, Roger D. Kamm, Shunsuke Kitajima and David A. Barbie

* shared first-authorship

An experiment described in this chapter has been previously published in:

<https://cancerdiscovery.aacrjournals.org/content/9/1/34>

“Suppression of STING Associated with LKB1 Loss in KRAS-Driven Lung Cancer”

Cancer discovery, January 2019

Shunsuke Kitajima, Elena Ivanova, Sujuan Guo, Ryohei Yoshida, **Marco Campisi**, Shriram K. Sundararaman, Shoichiro Tange, Yoichiro Mitsuishi, Tran C. Thai, Sayuri Masuda, Brandon P. Piel, Lynette M. Sholl, Paul T. Kirschmeier, Cloud P. Paweletz, Hideo Watanabe, Mamiko Yajima and David A. Barbie

Introduction

The recruitment of T cells following intratumoral administration of **Stimulation of Interferon Genes (STING)** agonists in the tumor microenvironment (TME) is a critical event in the STING-driven antitumor immune response, a pathway with great relevance in the context of cancer immunotherapy. Immune recognition of tumor cells requires migration and trans-endothelial extravasation of effector T cells to recognize tumor antigen. However, resistance to PD-1 immune checkpoint blockade (ICB) has been linked to immune exclusion in many tumors [45][46][47]. Consistent with this, immunohistochemical staining of patient samples showed poor infiltration of T cells into LKB1 negative (lost) versus LKB1 intact cancer epithelium, and instead, retention of T-cells in the stroma. To investigate the role of KRAS-LKB1 co-mutations and the tumor vasculature in influencing immune cell recruitment in a STING-dependent manner, a 3D microphysiological model using a microfluidic device was established to support 3-dimensional culture of perfusable microvascular networks (MVNs), comprised of human umbilical vein endothelial cells (HUVECs) and human lung fibroblasts (hLFBs), which self-organize into vessels after 7 days of co-culture. This microsystem facilitated investigation of interactions between vasculature and tumor spheroids derived from a KRAS/LKB1 mutated (KL) cell line with LKB1 reconstitution +/- STING deletion. The same microfluidic devices also enable 3-D culture of cancer cells in an ECM-like gel (collagen and fibrin) using tumor cell aggregates previously formed in in ultra-low attachment plate for 24 hours (spheroids). Therefore, this microfluidic system enables more detailed study of the biological interactions between KRAS mutant cancer cells and three-dimensional tumor microvasculature. Thus, a microengineered model that could support culture and formation of vascularized cancer spheroids was designed, with the specific goal of studying changes in cGAS-STING mediated immune signaling that may occur in this more physiologically relevant milieu.

Materials and methods

Materials and reagents

H1355 (obtained from the Broad Institute), RPMI-1640 (Thermo Fisher Scientific, Cat.# 11875-119), FBS, 1X penicillin–streptomycin, plasmocin prophylactic (InvivoGen, Cat.# ant-mpp), HUVECs (Lonza, C2519AS), (VascuLife® VEGF Endothelial Medium Complete Kit, #LL-0003), NHLF- human Lung Fibroblasts (Lonza, CC-2512), (FibroLife® S2 Fibroblast Medium Complete Kit, # LL-0011),

Cell culture

Cells were maintained in culture following manufacturer protocols. Briefly, H1355 were cultured in RPMI-1640 (Thermo Fisher Scientific, Cat.# 11875-119) supplemented with 10% FBS, 1X penicillin–streptomycin, and 2.5 µg/mL plasmocin prophylactic (InvivoGen, Cat.# ant-mpp). Human umbilical vein endothelial cells, HUVECs were cultured in vascular medium (VascuLife® VEGF Endothelial Medium Complete Kit, #LL-0003). NHLF- human Lung Fibroblasts (Lonza, CC-2512) were cultured in fibroblast growth supportive medium (FibroLife® S2 Fibroblast Medium Complete Kit, # LL-0011). Culture medium was refreshed every 2 days, and all experiments were performed before reaching 10 passages.

Immunohistochemical (IHC) Staining and analysis

Brain tumor and brain metastasis tissue microarrays (GL2082, GL861) were purchased from US Biomax, Inc and IHC was performed on the Leica Bond III automated staining platform. The antibody for phospho-TBK1 (Cell Signaling Technology #5483, clone D52C2) was run at 1:50 dilution using the Leica Biosystems Refine Detection Kit with EDTA antigen retrieval. The antibody for STING (Cell Signaling Technology #13647, clone D2P2F) was run at 1:50 dilution using the Leica Biosystems Refine Detection Kit with citrate antigen retrieval. Staining was visually scored in a binary manner (presence/absence) in endothelial cells identified using the hematoxylin counterstain marking a circumferential layer of nuclei surrounding red blood cell

fragments. These results were confirmed by a board-certified anatomic pathologist (NRM), who also quantified infiltrating lymphocytes by morphology on hematoxylin-counterstained per high power field (HPF = 40x objective), averaged across confidently identified endothelial lumens in 1–4 HPF per specimen. Average tumor infiltrating lymphocytes per HPF was compared for pTBK1+ and pTBK1- blood vessels in each tumor specimen.

Genetic engineering and CRISPR/Cas9 systems

Target sequences for CRISPR interference were designed using the single-guide RNA (sgRNA) designer (<https://portals.broadinstitute.org/gpp/public/analysis-tools/sgrna-design>). A nontargeting sgRNA from the Gecko library v2 was used as a scramble sgRNA. sgRNA target sequences are listed in Table 6. HEK293T cells (3×10^6) were plated onto a 60-mm dish and transfected using X-tremeGENE HP DNA Transfection Reagent (Roche, Cat.# 06366236001) with 1 μ g of lentivirus-based expression vectors together with 1 μ g of pCMV-dR8.91 and 1 μ g of pCMV-VSV-G. After 48-hour incubation, the media containing lentivirus particles were collected, passed through a 0.45 μ m filter, and concentrated using Lenti-X Concentrator (Clontech, Cat.# 631231). For selection of virally infected cells, 1 μ g/mL of puromycin (pCRISPR-v2 sgRNAs) or 6 μ g/mL of blasticidin (plx304-NanoLuc or plx304-hLKB1) was used 24 hours after infection.

RT-PCR

Total cellular RNA was extracted from 2D culture using the RNeasy Mini Kit (Qiagen, Cat.# 74106) according to manufacturer's instructions. RNA samples (1 μ g) were reverse-transcribed using Super-Script III First-Strand Synthesis SuperMix (Thermo Fisher Scientific, Cat.# 1683483). Quantitative real-time PCR was performed using Power SYBR Green PCR Master Mix (Thermo Fisher Scientific, Cat.# 4367659), and the Applied Biosystems 7300 Fast real-time PCR system and software. The relative expression was normalized with the expression of the housekeeping gene 36B4. The sequences of the primers used for qRT-PCR are listed in Table 6. The profile expression of 84 genes related to endothelial cell biology were performed using the RT² Profiler PCR Array for human endothelial cell biology (Cat. # PAHS-015ZC, Qiagen), reverse

transcribed and quantitative real-time PCR was performed using RT² First Strand Kit (Cat.# 330404, Qiagen), QuantiTect Reverse Transcription Kit (Cat.# 205313, Qiagen), RT² SYBR Green ROX qPCR Mastermix (Cat.# 330523, Qiagen) and Applied Biosystems 7300 Fast real-time PCR system and software. Values represent the average of four technical replicates from at least two independent experiments (biological replicates). The profile expression of 84 genes related to endothelial cell biology were performed using the RT (2). Profiler PCR Array for human endothelial cell biology (Cat. # PAHS-015ZC, Qiagen), reverse transcribed and quantitative realtime PCR was performed using RT (2) First Strand Kit (Cat.# 330404, Qiagen), QuantiTect Reverse Transcription Kit (Cat.# 205313, Qiagen), RT (2) SYBR Green ROX qPCR Mastermix (Cat.# 330523, Qiagen) and Applied Biosystems 7300 Fast realtime PCR system and software.

Immunoblotting

Cells were lysed in RIPA buffer containing 1x protease inhibitors (Roche, Cat.# 11-836-145-001) and phosphatase inhibitors (50 mmol/L NaF and 100 mmol/L Na₃VO₄). Target proteins were isolated from cell lines and measured by BCA (Pierce Biotechnology). Protein extracts were subjected to polyacrylamide gel electrophoresis using the 4%–12% NuPAGE gel system (Invitrogen), transferred to PVDF (Millipore) membranes, and immunoblotted using antibodies that specifically recognize STING (#13647, Cell Signaling Technology), cGAS (#15102, Cell Signaling Technology), LKB1 (#3047, Cell Signaling Technology), phospho-TBK1 (#5483, Cell Signaling Technology), TBK1 (#3013, Cell Signaling Technology), and β -actin (#3700, Cell Signaling Technology). Secondary antibodies were from LI-COR Biosciences: IRDye 680LT Goat anti-Mouse IgG (#926-68020) and IRDye 800CW Goat anti-Rabbit IgG (#926- 32211). LICOR blocking buffer (no. 927-40000) was used to dilute primary and secondary antibodies, with the exception of phospho-specific antibodies, which were diluted in HIKARI Signal Enhancer Solutions 1 and 2 (Nacalai USA, Inc., no. NU00101). Imaging of blots and quantitation of bands were performed using the LI-COR Odyssey system.

Immunohistochemistry

Brain tumor and brain metastasis tissue microarrays (GL2082, GL861) were purchased from US Biomax, Inc and IHC was performed on the Leica Bond III automated staining platform. The antibody for phospho-TBK1 (Cell Signaling Technology #5483, clone D52C2) was run at 1:50 dilution using the Leica Biosystems Refine Detection Kit with EDTA antigen retrieval. The

antibody for STING (Cell Signaling Technology #13647, clone D2P2F) was run at 1:50 dilution using the Leica Biosystems Refine Detection Kit with citrate antigen retrieval. Staining was visually scored in a binary manner (presence/absence) in endothelial cells identified using the hematoxylin counterstain marking a circumferential layer of nuclei surrounding red blood cell fragments. These results were confirmed by a board-certified anatomic pathologist, who also quantified infiltrating lymphocytes by morphology on hematoxylin-counterstained per high power field (HPF = 40X objective), averaged across confidently identified endothelial lumens in 1–4 HPF per specimen. Average tumor infiltrating lymphocytes per HPF was compared for pTBK1+ and pTBK1- blood vessels in each tumor specimen.

dsDNA Stimulation

Cells (2 to 5×10^5) were plated onto a 6-well plate and transfected using X-tremeGENE HP DNA Transfection Reagent (Roche, Cat.# 06366236001) with the indicated amount of poly (dA:dT) (Invivo- Gen, Cat.# tlr1-patn). Cells utilized for 3D culture in microfluidic devices were transfected for 24h, then transferred into ultra-low attachment dish to form spheroids as described below.

3D microfluidic device

Microphysiological systems were developed using a commercial microfluidic chip ‘3-D cell culture chip’ (DAX-1, AIM Biotech). Briefly, the single layer slide format (75 mm × 25 mm) device or ‘chip’ contains 3 microfluidic chambers, each chamber has a central gel channel (width 1.3 mm) flanked by two media channels (width 0.5 mm), and 4 reservoirs. The height of the microfluidic chambers is 0.25 mm. Microfluidic device design and fabrication using cyclic olefin polymer (COP) was conducted at AIM biotech. The height of the microfluidic chambers is 0.25 mm. Media channels were designed including larger reservoirs to prevent over-aspiration (Fig. 3a-c).

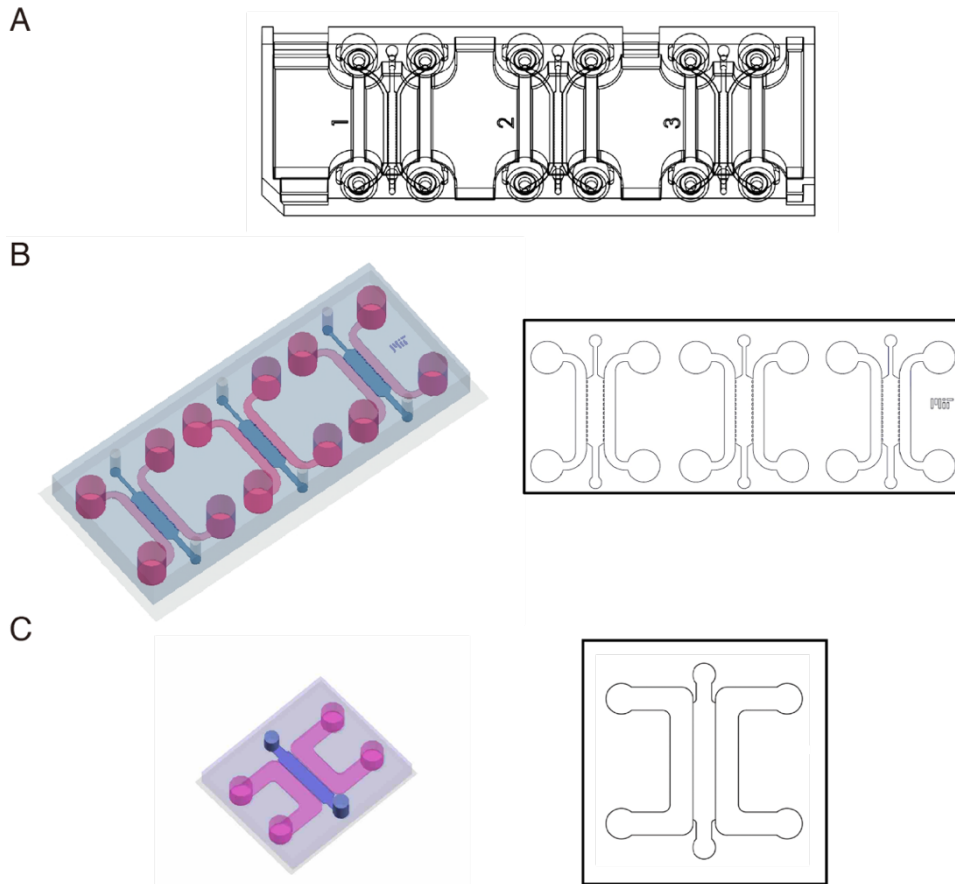


Figure 3.5: Design of microfluidic devices.

a) The 3D cell culture chip (AIM Biotech) is shown with three independent microfluidic chambers (referred to as “device”) per chip, Each device contains a center gel region with posts separating the gel region from the anti-parallel side channels. *b,c)* Custom PDMS-based microfluidic devices were designed using Autocad (Autodesk) and are comprised of a central gel channel, two medium channels and four reservoirs. Devices were bonded to glass coverslips. Reproduced with permission from [76].

3D Microphysiological system: Lung cancer - microvasculature model

Spheroids culture: Cancer cell spheroids were generated by seeding 5×10^5 cells in suspension in an ultra-low attachment dish (Corning, Cat.# 3471) for 24 hours. Samples were pelleted and resuspended in collagen hydrogel formed by a type I rat tail collagen (Corning) at a concentration of 2.5 mg/mL following the addition of $10 \times$ PBS with phenol red with pH adjusted using NaOH. pH of 7.0 to 7.5 was confirmed using PANPEHA Whatman paper (Sigma-Aldrich). All pelleted spheroids were resuspended in 250 μ L of collagen hydrogel. The spheroid-collagen suspension was then injected into the central gel region of the 3D microfluidic device. After

injection, devices containing spheroid-collagen mixture were incubated for 30 minutes at 37 °C in humidity chambers, then hydrated with culture media, and refreshed daily for 7 days.

Microvascular network culture: Microvascular networks (MVN) were created by detaching HUVEC and hLFB cells from cell culture flasks and spun down at 1200 rpm for 5 min, and cell pellet was resuspended in cold vascular medium (Vasculife, Lifeline #LL-0003) with 2 U/ml thrombin from bovine plasma (Millipore Sigma, #T7326). The two cell types were combined with cell densities of 12×10^6 /ml endothelial cells and 2×10^6 /ml hLFB. Cell suspensions were mixed 1:1 volume ratio with 6 mg/ml fibrinogen (Millipore Sigma, #341573) and gently injected into microfluidic devices. After allowing several minutes of fibrin polymerization (15 min) in a 37° C incubator, warm vascular medium was added to the flanking media channels and refreshed each day of culture. MVN self-assembled over several days refreshing media daily for 7 days.

Spheroids with Microvascular network: To generate the MVN + Spheroids samples, MVN were co-cultured with tumor spheroids and protocols were combined, while maintaining the same final cellular densities used in each individual protocol. Briefly, cell densities were doubled to 24×10^6 /ml endothelial cells and 4×10^6 /ml hLFB, were mixed 1:1 volume ratio with 6 mg/ml fibrinogen (Millipore Sigma, #341573), and spheroids were resuspended into 125 μ L of collagen hydrogel. MVN and spheroids suspensions were finally mixed at 1:1 ratio, and gently injected into microfluidic devices. After hydrogel polymerization (15-30 min) in a 37° C incubator, warm vascular medium was added to the flanking media channels and refreshed each day of culture. MVN self-assembled over several days refreshing media daily for 7 days.

To maintain consistency for cytokine analysis, all microfluidic devices conditions were cultured in vascular medium (Vasculife, Lifeline #LL-0003). MVN alone in microfluidic devices were treated with 1 μ g/ml 2'3'-cGAMP, or 100 ng/ml IFN- β , or both in combination after 6 days of culture, after which conditioned medium was collected or device were imaged with confocal microscopy 24 hours later.

3D Migration assay

Cancer cell spheroids were generated as previously described. Samples were pelleted and then resuspended in collagen hydrogel. The spheroids-collagen suspension was then injected into the central gel region of the DAX-1 3-D microfluidic cell culture chip (AIM Biotech, Singapore, Cat.# DAX-1). After injection, collagen hydrogels containing cells were incubated for 40 minutes at

37°C in humidity chambers, then hydrated with RPMI culture media, with or without 2.5×10^4 CXCR3-overexpressing Jurkat cells and in one of the side media channels. CXCR3-overexpressing Jurkat cells were labeled with Cell Tracker Red (Thermo Fisher Scientific, Cat.# C34552) following the manufacturer's instructions. After 72 to 96 hours of incubation, cancer cell spheroids and infiltrated Jurkat cells were rinsed twice in PBS and fixed in 4% paraformaldehyde (Electron Microscopy Sciences, Cat.# 15700) for 15 minutes at room temperature. Cell membranes were permeabilized with 0.1% vol/vol Triton X 100 (Sigma-Aldrich, Cat.# X100-500ML) for 5 minutes at room temperature (RT) and washed twice in PBS. After blocking with 1% BSA (Sigma-Aldrich, Cat.# A4503-100G) in PBS overnight at 4°C, devices were stained by conjugated Alexa Fluor 647 anti-human CD326 (EPCAM) Antibody (BioLegend, Cat.# 324212; 1:100, volume ratio) and placed on a shaker at RT for 3 to 4 hours. After PBS washing, devices were imaged using a confocal laser scanning microscope (FMV-1000, Olympus). For quantification, images were captured on a Nikon Eclipse 80i fluorescence microscope equipped with Z-stack (Prior) and CoolSNAP CCD camera (Roper Scientific). Image capture and analysis was performed using NIS-Elements AR software package. Whole device images were achieved by stitching in multiple captures. Quantification of immune cell infiltration into the 3-D tumor microenvironment was performed by measuring the total cell area of cell tracker dye in the entire gel region.

3D perfusion and adhesion assay

To test adhesion of T cells to the vascular endothelium, Jurkat T cells were perfused through microvascular networks on day 7 after loading the microfluidic devices. Jurkat cells (Clone E6, ATCC TIB-152) were cultured in RPMI-1640 medium with 10% FBS and 1% penicillin–streptomycin and dyed with CellTracker Green CMFDA Dye (ThermoFisher Scientific) before experiments. Half of the networks were treated with 1 µg/ml of 2'3'-cGAMP in vascular medium on day 6, and incubated for 24 hours. On day 7 devices were perfused with fresh medium and then incubated with sterile rhodamine Ulex Europaeus Agglutinin I (Vector Laboratories) for 20 minutes to label the endothelium and washed again with fresh vascular medium before introducing Jurkat T cells. The Jurkat cells were pelleted and suspended in vascular medium at 10^6 cells/ml. Each device received 40 µl of the cell suspension in one channel of the microfluidic device, and cells were allowed to flow through the vascular networks for 30 minutes before perfusing fresh medium to wash away unbound cells. Jurkat cells that remained bound to the vascular networks

were imaged with confocal microscopy (Olympus FV1000) and counted in FIJI. The number of cells retained in untreated networks and those treated with 2'3'-cGAMP were compared using a 2-sided student's T-test.

Permeability measurements

The vascular permeability was evaluated as the flux of solute across the wall of vascular network. Using mass conservation, the quantity of fluorescent dextran crossing the microvascular network equals to the rate at which it accumulates outside the vessels in the 3D tissue gel region. MVN alone in microfluidic device were cultured for 7 days and treated with 1 µg/ml 2'3'-cGAMP or 100 ng/ml IFN-β. Firstly, medium was removed from both media channels of a macro-device. A solution of fluorescein isothiocyanate (FITC)-conjugated dextran (Sigma-Aldrich) (70 kDa, 0.1 mg/ml) was added to each media channel in succession, and the device was transferred to a confocal microscope (Olympus FV1000). Three regions of interest (ROI) were chosen randomly along the gel channel to ensure non-biased sampling of the microvasculature, and z-stacks approximately 50 µm high were acquired immediately after addition of the fluorescent tracer and 15 minutes later (512 × 512 pixels, 20X magnification). Microvascular permeability was quantified by considering the increase in fluorescence intensity of FITC-dextran within the extra-vascular gel region as previously described in Chapter 4. Briefly, Vascular network permeability, P , was quantified by measuring the average fluorescence intensity of the vascular (I_v) and matrix (I_m) compartments at two different time points t_1 and t_2 ($t_2 - t_1 = \Delta t$):

$$P = \frac{V_m}{(SA \Delta I)} \frac{(\Delta I_m)}{\Delta t}$$

$\Delta I_m = I_{m,2} - I_{m,1}$ is the increase in mean fluorescence intensity, in the matrix of volume V_m between time points and $\Delta I = I_{v,1} - I_{m,1}$, is the difference in fluorescence intensity, therefore solute concentration, between the vasculature (with surface area SA) and matrix at the start of the measurement. Reconstruction and segmentation was performed with Imagej (Fiji)[75] using the 3D Trainable Weka Segmentation plugin for quantification of parameters such as surface area (SA) and volume of the vascular network and matrix. The fluorescent intensity values were computed using Imagej (Fiji).

Immunofluorescence and confocal imaging

Mature microvascular networks were rinsed with warm PBS twice followed by the addition of 50 μ l of 4% paraformaldehyde (Electron Microscopy Sciences, # 15700) to each media channel and left at room temperature. After 10 minutes of fixation, cell membranes were permeabilized with 0.1% Triton X-100 (Sigma-Aldrich) for 5 min at RT and devices were rinsed twice with PBS, and blocking solution (4% bovine serum albumin, 0.5% goat serum) (Sigma-Aldrich) was added. Devices were incubated for 1 day at 4° C, washed with PBS, and stained with primary antibodies: ICAM-1 (Biolegend, 4453320), VCAM-1 (Abcam, ab134047), CD31 (Abcam, ab28364), conjugated Alexa Fluor 647 anti-human CD326 (EPCAM) (BioLegend, 324212), Acti-stain 555 phalloidin, F-actin (Cytoskeleton, PHDH1-A) and incubated at 4° C for another day. Devices were again washed with PBS and secondary antibodies (ThermoFisher, A-11070, A-11011, A-21052) DAPI (4',6-Diamidino-2-Phenylindole, Dihydrochloride, Invitrogen) or DyLight 649 labeled Ulex Europaeus Agglutinin I (Vector Laboratories) were added, followed by incubation at 4° C protected from light. Finally, samples were washed again with PBS and 3D images were acquired with a confocal microscope (Olympus FV1000) at 20X. Z-stacks were collapsed with maximum intensity projections for viewing (800 \times 800 pixels) using FIJI 22 .

Multiplexed cytokine/chemokine profiling

Multiplexed assays were performed utilizing the bead-based immunoassay approach Bio-Plex Pro Human Cytokine 40-plex Assay (Cat.# 171AK99MR2) on a Bio-Plex 200 system (Bio-Rad Laboratories, Cat.# 171000201) and the Human Cytokine/Chemokine Magnetic Bead Panel (Cat.# HCYTMAG-60K-PX30) on a Luminex MAGPIX system (Merck Millipore). Conditioned media concentration levels (pg/mL) of each protein were derived from 5-parameter curve fitting models. Fold changes relative to the corresponding control were calculated and plotted as log₂FC. Lower and upper limits of quantitation (LLOQ/ULOQ) were imputed from standard curves for cytokines above or below detection. The degree of cytokine/chemokine modulation (D) in the MVN C Spheroids co-culture samples was calculated from absolute concentration levels (pg/mL) of the values from isolated MVN culture were subtracted to the MVN C Spheroids co-culture and results normalized to spheroid-only results as represented by the following equation:

$$D = \frac{((MVN + Spheroids) - MVN)}{Spheroids}$$

Where the resulted degree cytokine/chemokine modulation is simply additive ($D = 1$) versus supra-additive ($D > 1$) or antagonistic ($D < 1$).

ELISA

Human IFN- β (Thermo Fisher Scientific, Cat.# 414101), CXCL10 (R&D systems, Cat.# DIP100), and 2'3'-cGAMP (Cayman Chemical, Cat.#501700) were detected with ELISAs according to the manufacturer's instructions. Conditioned media from each cell line were collected after 24-, 48- or 168-hours culture. Values from 2-D cell culture represent the average of two replicates from at least two independent experiments. Values from 3-D cell culture devices represent the average of four replicates from at least three independent experiments (biological replicates).

Cell Sorting by CD31

Cells (1×10^6) resuspended in 100 mL PBS containing 3% FBS were stained by APC-conjugated anti-CD31 antibody (R&D Systems, Cat.# FAB3567A-025) for 30 min at room temperature, washed by PBS containing 3% FBS, and then analyzed by FACSCanto II (BD Biosciences). PE/Cy7-conjugated mouse IgG2b (BioLegend, Cat.# 400325) was used as isotype control antibody. Flow sorting for CD31-positive cells was then confirmed with CD31 gene expression by RT-PCR.

Statistical analysis

All data are plotted as mean \pm SD. Sample size (n) is equal to 2 biological replicates or otherwise stated. Unpaired student's t-test was used for significance testing between two conditions. One-way ANOVA with pairwise comparisons by the Tukey post-hoc test was used to determine whether three or more data-sets were statistically significant. Statistical tests were performed using PRISM7 (GraphPad software) and R. P values less than 0.05 were considered significant, ** $P < 0.01$, * $0.01 < P < 0.05$.

Results

3-D spheroids microphysiological system reveals STING-driven cytokine /chemokine production after LKB1 reconstitution

We first explored the potential consequences of STING signaling defects on the tumor immune microenvironment. The H1355 cells stably expressing a luciferase control (H1355-LUC) or reconstituted with LKB1 (H1355-LKB1) were therefore cultured in ultra-low-attachment dishes for 24 hours to allow self-aggregation into 3-D spheroids. Spheroids were cultured in a microfluidic device within a collagen/fibrin hydrogel (Figs. 3.6 a, b). Consistent with the tumor suppressive nature of LKB1, H1355-LKB1 spheroids grown for 7 days and were visualized with confocal microscopy, exhibited decreased proliferation compared to H1355-LUC spheroids, due to LKB1 reconstitution (Fig. 3.6c). The direct role of LKB1 in modulating cancer cell-intrinsic dsDNA sensing was validated using both 2-D and 3-D Microphysiological systems. As expected, introduction of cytoplasmic DNA via transfection with 1 $\mu\text{g/ml}$ of poly(dA:dT), a synthetic double-strand DNA sequence, resulted in significantly more robust TBK1 activation following LKB1 reconstitution, consistent with its ability to restore STING expression [44] (Fig. 3.6a). 3-D culture revealed that LKB1-reconstituted spheroids (previously transfected with Poly(dA:dT) transfection, followed by spheroid formation) uniquely responded to transfection of cytoplasmic DNA, significantly upregulating multiple immune cell chemoattractants including CCL5, CCL2, and CXCL10, after 7 days (Figs. 3.6d, e, f). Notably, IL-6 was suppressed by LKB1 reconstitution as previously described [30] (Figs. 3.6e, f). Considering studies were conducted at the 7-day endpoint, we next sought to understand the kinetics of CXCL10 and IFN- β , a major T cell chemokine, downstream of STING signaling. Notably, IFN- β secretion was induced by poly(dA:dT) and potently restored by LKB1 reconstitution, but fell off by day 3, whereas CXCL10 production was maintained over the 7 day (Fig. 3.7c). Then, we evaluated the functional activation of cGAS-STING regulated cytokine/chemokine production over time, in particular focusing on its major T cells attraction ability mediated by CXCL10. The 3-D Microphysiological spheroid culture of isogenic LKB1 reconstituted STING-low H1355 cells was exploited to unveil immune cells infiltration, which exhibited strong differential immune cell infiltration by poly(dA:dT)-induced CXCL10 (Fig. 3.7b), and uncovered a direct relationship between LKB1 loss and defective recruitment of CXCR3- expressing Jurkat T cells (Fig. 3.7b, d).

tailed student *t*-test; ** $P < 0.01$. Data shown as mean values, error bars \pm SD. Reproduced with permission from [76].

Consistent with these findings, IHC of patient-derived KRAS NSCLCs revealed a preferential decrease in intratumoral T-cell infiltration in STING/LKB1-negative specimens (Fig. 2E, F)[44]. Thus, LKB1 reconstitution in tumor spheroids restores sensitivity to dsDNA sensing, which is maintained in this 3-D Microphysiological system, and the KL non-small-cell lung cancer (NSCLC) cell line NCI-H1355 (H1355), accurately models T cell recruitments following LKB1 reconstitution and STING activation in tumor cells.

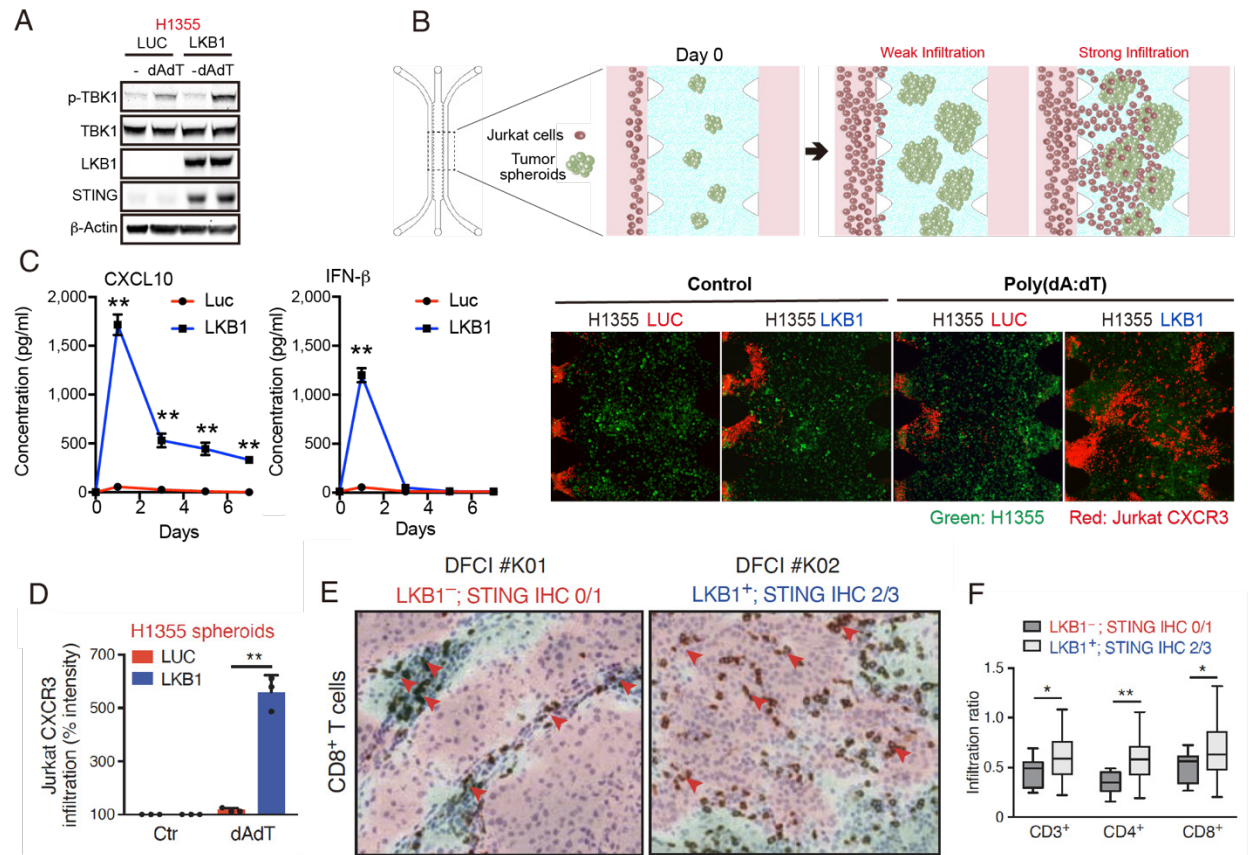


Figure 3.7: Immune infiltration in 3-D KL model and response to dsDNA in microfluidic culture.

a) Immunoblot of the indicated proteins in H1355 cells transduced with LUC and LKB1, **b)** Schematic of the 3D migration assay and Confocal images of H1355 spheroids (green) and migrated Jurkat CXCR3 cells (red) in microfluidic devices. Scale bars: 200 μ m. **c)** ELISA of human CXCL10 and IFN- β over 7 days of 2D culture, treated \pm 1 μ g/mL poly(dA:dT), ($n=3$ biological replicates). CM was collected and refreshed daily. **d)** Quantification of Jurkat CXCR3 infiltration into H1355 tumor spheroids. **e)** IHC images and analysis from primary tumor LKB1-negative; STING IHC 0/1 ($n = 12$) and LKB1-positive; STING IHC 2/3 NSCLC ($n = 22$) samples. Red arrows

highlight stained CD8⁺ T cells in both tumor epithelium (red) and stroma (green; H). f) PathAI was used to quantify CD3⁺/CD4⁺/CD8⁺ T-cell infiltration. Reproduced with permission from [76].

Innate immune signaling changes captured in a 3-D Microphysiological system of lung tumor-vasculature interactions

Since LKB1 modulates STING expression in KRAS-LKB1 tumor cells [44], additional interactions between tumor cell dsDNA sensing and the vasculature were investigated. Our hypothesis considered the possibility that LKB1-mutant status of tumor cells might influence innate immune signaling in the neighboring vasculature, especially following dsDNA stimulation of tumor cells. H1355 spheroids were co-cultured with the self-assembling microvascular network (MVN) within the microfluidic devices for 7 days using our established HUVEC and hLFB vasculogenesis method (Fig. 3.8a). Co-culture of HUVECs/hLFB with H1355 spheroids for 7 days, resulted in effective formation of MVNs and encapsulation of tumor spheroids that are randomly distributed in the perivascular space and/or in contact interaction with the MVNs (Fig. 3.8b). To capture differences in cytokine production that occurred in co-culture with the microvasculature, multiplexed profiling of conditioned media of co-culture of MVN with tumor spheroids (H1355-LKB1 vs LUC) was performed. Tumor spheroids were exposed to poly(dA:dT) prior to loading in the device. To estimate the degree (additive, supra-additive or antagonistic) of which the combination of MVN and spheroids modulated cytokine/chemokine production in a simply, values from isolated MVN culture were subtracted, and results normalized to spheroid-only results (Fig. 3.8c). This calculation revealed supra-additive upregulation of multiple cytokines/chemokines in LKB1-reconstituted tumor spheroids co-cultured with MVNs, including CCL2 and CXCL10, as well as IL-6 (Fig. 3.8d, e, f). Thus, activation of cGAS-STING signaling by dsDNA in tumor cells alone strongly cooperated with MVNs to amplify innate immune production of specific cytokines and chemokines.

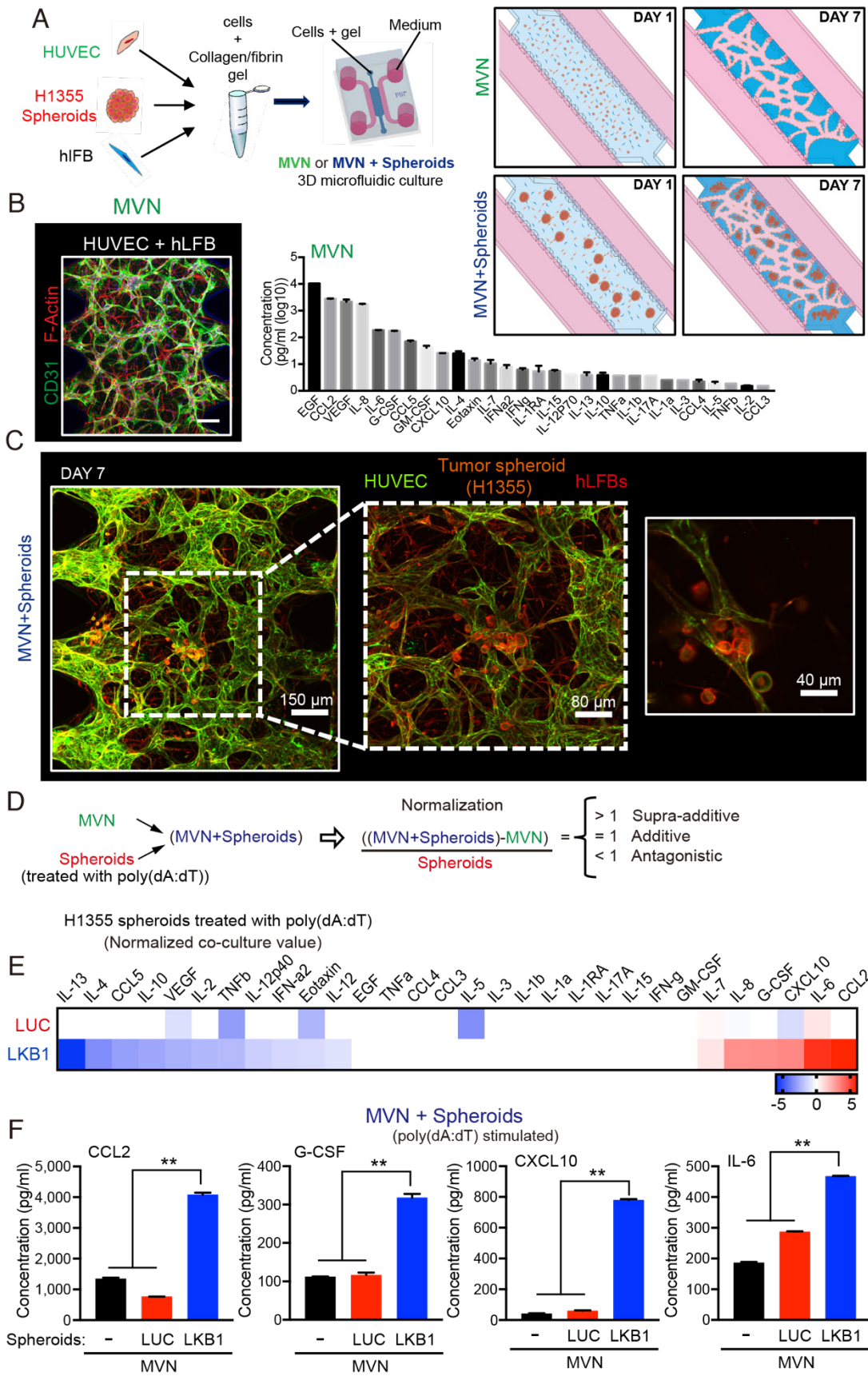


Figure 3.8: Impact of LKB1 reconstitution on dsDNA sensing in co-culture with MVNs.

a) Schematic of H1355 spheroids, human lung fibroblasts (hLFB) and human umbilical vein endothelial cells (HUVECs) and their *in vitro* dynamic 3D Microphysiological culture in a microfluidic device within a collagen/fibrin hydrogel. Schematic of microvasculature (MVN) or combination of H1355 tumor spheroids and microvasculature (MVN + Spheroids) in 3D microfluidic device at day 1 and day 7. **b)** Confocal images of microvasculature (MVN) immunostained for F-actin (red) and CD31 (green). Scale bar, 150 μm (left), \log_{10} of the absolute values of cytokine production corresponding to the heatmap in Fig.2E. from 3D Microphysiological culture of microvascular networks (MVN) alone. **c)** Confocal images at 10x, 20x, and 40x magnification of MVNs formed from HUVECs and hLFBs co-cultured with H1355 tumor spheroids within collagen/fibrin hydrogel after 7 days, immunostained for F-actin (red) and EpCAM (CD326) (orange) and CD31 (green). Scale bars, 150, 80 and 40 μm . **d)** Schematic equation illustrating normalization of cytokine production from combination of MVN and H1355 tumor spheroids. Cytokine production is considered supra-additive (> 1), additive ($= 1$) or antagonistic (< 1). **e)** Heat map of \log_2 fold change cytokine/chemokine profiles in conditioned medium after 7 days of 3D Microphysiological culture of MVN with H1355 LUC and LKB1 spheroids pre-stimulated with 1 $\mu\text{g}/\text{mL}$ poly (dA:dT). **f)** Absolute values of supra-additive cytokine release of human CCL2, G-CSF, CXCL10 and IL-6, from 3D Microphysiological culture of MVN + spheroids of H1355 LKB1 and LUC control spheroids and MVN only after 7 days of culture in 3D microfluidic devices. *P* values were calculated by one-way ANOVA followed by Tukey post-hoc test; ** *P* < 0.01. Data shown as mean values, error bars \pm SD. Reproduced with permission from [76].

The cooperative production of cytokines in the Microphysiological tumor-vasculature interaction is not dependent on cancer cell intrinsic STING

To dissect how dsDNA activated tumor cells and might cooperate with MVNs to enhance cytokine release, STING was deleted by knocked out via CRISPR/CAS9 in H1355 cells with or without LKB1 reconstitution. As expected, STING deletion prevented LKB1 restoration of STING expression and suppressed activation of TBK1, as measured by TBK1 phosphorylation after poly(dA:dT) treatment (Fig 3.9a). In accordance, STING knockout in LKB1-reconstituted H1355 tumor spheroids also inhibited production of CXCL10 (Fig 3.9b). We then conducted tumor spheroid/MVN co-culture experiments with STING knockout cell lines, expecting that the cooperative increase in cytokine production seen in co-culture would be similarly blunted after deleting STING in the LKB1-reconstituted tumor spheroids. Surprisingly, comparable induction of cytokines/chemokines following poly(dA:dT) treatment in LKB1-reconstituted H1355 spheroids and MVNs was observed even in the absence of tumor cell STING (Fig 3.9c).

Specifically, CXCL10 and IL-6 production that was significantly higher in co-culture compared to the vasculature alone, regardless of tumor cell STING (Fig. 3.9d). These data revealed that dsDNA-mediated cooperative induction of cytokines/chemokines in tumor spheroid/MVN co-culture does not rely on tumor cell STING. In contrast to STING knockout in LKB1-reconstituted H1355 spheroids, STING knockout in HUVECs (Fig. 3.9e) consistently resulted in impaired production of CXCL10 and IFN- β in 2D culture and in 3D MVN co-culture, despite only treating tumor cells with poly-(dA:dT) (Fig. 3.9f, g).

Endogenous activation of TBK1 in the tumor vasculature

Expression of STING and activation of its immediate downstream target, phosphorylated TBK1 (pTBK1), was examined across different tumor microenvironments in tissue microarrays (TMA) derived from patient samples. Brain tumors and brain metastases were chosen, given the low baseline neuroinflammation and absent STING activation in normal brain. Interestingly, we found that the most prominent areas of TBK1 activation were in cross-sections of tumor vasculature (Fig. 3.10a, b). STING expression and TBK1 activation were binary scored based on the presence or absence of STING and pTBK1 stain, in endothelial cells lining the lumen of blood vessels. IHC demonstrated endothelial STING staining in nearly every sample from either tumor- or normal brain-associated microvasculature (Fig. 3.10a, c). Notably, pTBK1 IHC revealed specific activation of STING in the tumor endothelium of both primary GBM and metastatic NSCLC (Fig. 3.10a, c), whereas normal brain samples stained uniformly negative for pTBK1 (Fig. 3.10b, c). Taken together with our *in vitro* microphysiological culture findings, these data suggested a potential influence of tumor cells on activation of STING in the microvasculature, potentially in the form of tumor-derived 2'3'-cGAMP. In addition, both HUVEC and fibroblasts exhibited 4-fold higher expression of basal STING level relative to H1355 in 2D culture (Fig. 3.10d). Therefore, we next considered the effect of exogenous 2'3'-cGAMP on tumor cells and established MVNs. Notably, HUVECs were significantly more sensitive to 2'3'-cGAMP treatment compared to H1355 tumor cells and fibroblasts, producing significantly higher levels of IFN- β and especially CXCL10 (Fig. 3.10e, f). Cytokine/chemokine profiling analysis of Microphysiological MVNs in microfluidic device revealed that treatment with 1 μ g/mL of 2'3'-cGAMP led to strong upregulation of several cytokines downstream of STING, such as CXCL10, CCL5, IFN- β , CCL2 and IL-6 (Fig. 3.10g). These data suggested that the enhanced cytokine/chemokine production

observed in co-culture could be predominantly produced by the endothelial cells and could be mediated by the effects of tumor derived 2'3'-cGAMP on endothelial cells.

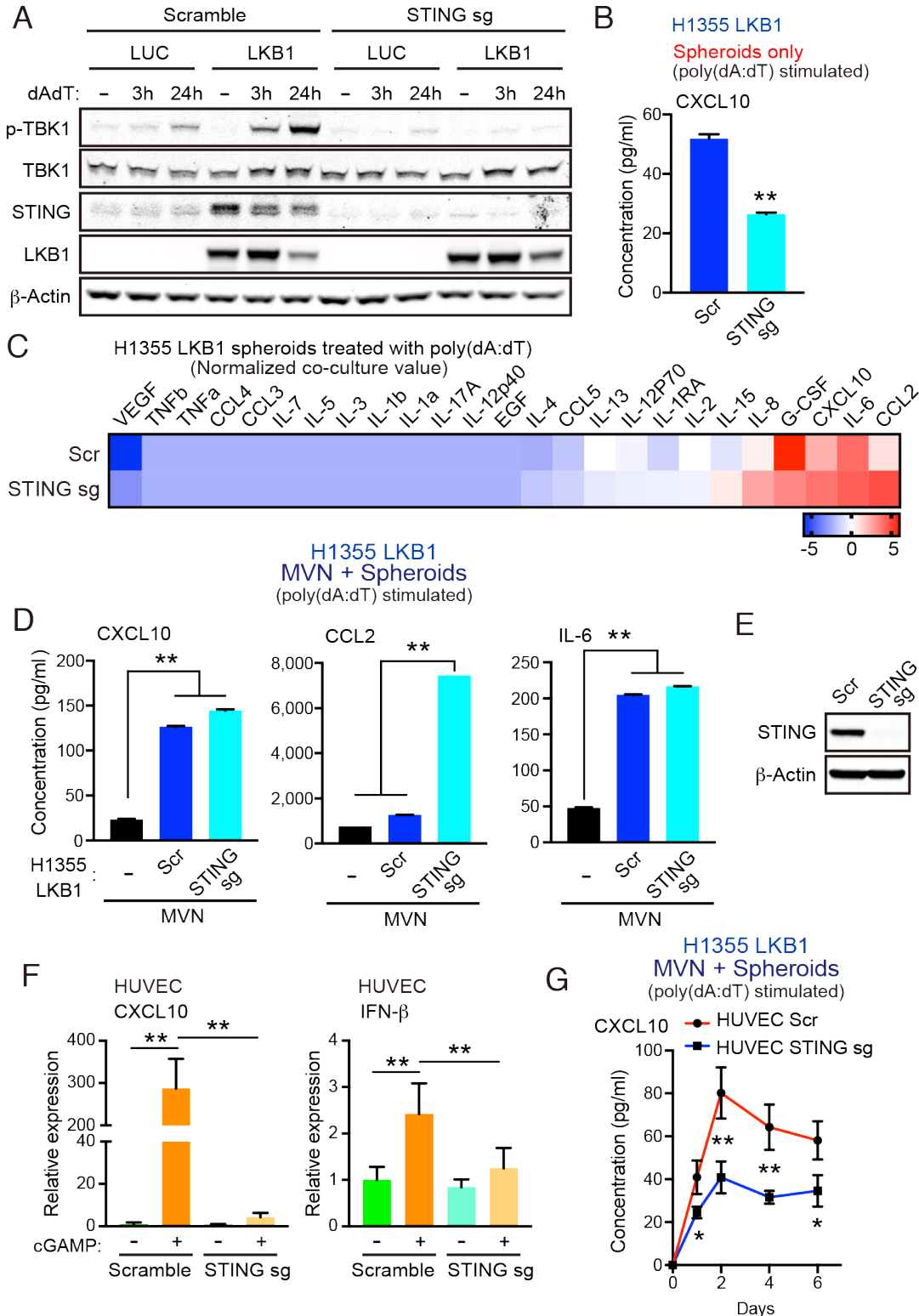
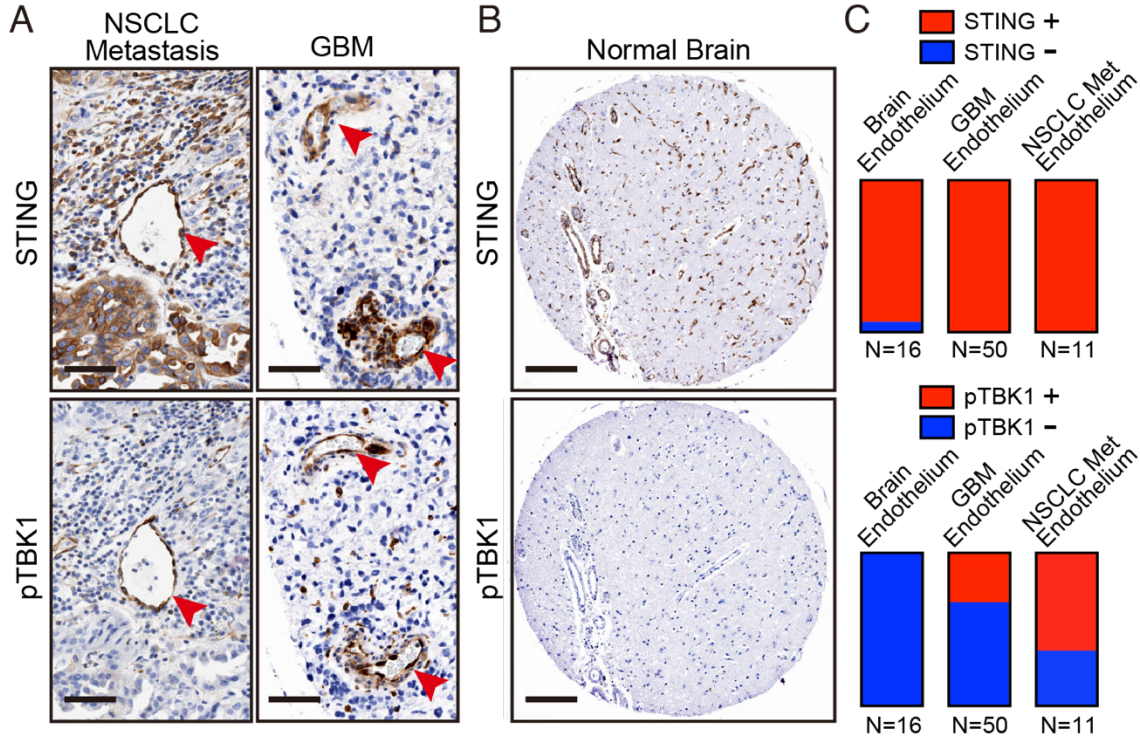


Figure 3.9: MVN co-culture enhances dsDNA-induced cytokines/chemokines even in the absence of tumor cell STING.

a) Immunoblot of the indicated proteins in H1355 cells transduced with LUC and LKB1 +/- scramble (control sgRNA) or STING knockout (STING sgRNA) in 2D culture. **b)** CXCL10 production in H1355-LKB1 spheroids after STING knockout, (n=3 biological replicates). **c)** Heat map of log₂ fold change cytokine/chemokine profiles in conditioned medium (CM) after 7 days of 3D microfluidic culture of MVN with H1355 LUC and LKB1 spheroids with scramble or STING knockout. Spheroids were pre-treated with 1 µg/mL poly (dA:dT). **d)** Absolute values of cytokine/chemokine release of CXCL10, CCL2, and IL-6 production. **E,** Immunoblot of the indicated proteins in HUVEC transduced with scramble (control sgRNA) or STING knockout (STING sgRNA). **f)** qRT-PCR of CXCL10 and IFN-β of HUVECs transduced with scramble (control sgRNA) or STING knockout (STING sgRNA), after exogenous 2'3'-cGAMP treatment (1 µg/mL) for 24 h. **g)** ELISA of human CXCL10 over 6 days of 3D microfluidic culture of HUVEC STING knockout (STING sgRNA) or HUVEC scramble (control sgRNA) with H1355 LKB1 spheroids. Spheroids were pre-treated with 1 µg/mL poly (dA:dT). CM was collected after 1 day and every 2 days of 3D culture. P values were calculated by unpaired two tailed student t-test or one-way ANOVA followed by Tukey post-hoc test; ** P < 0.01, * 0.01 < P < 0.05. Data shown as mean values, error bars ± SD. Reproduced with permission from [76].



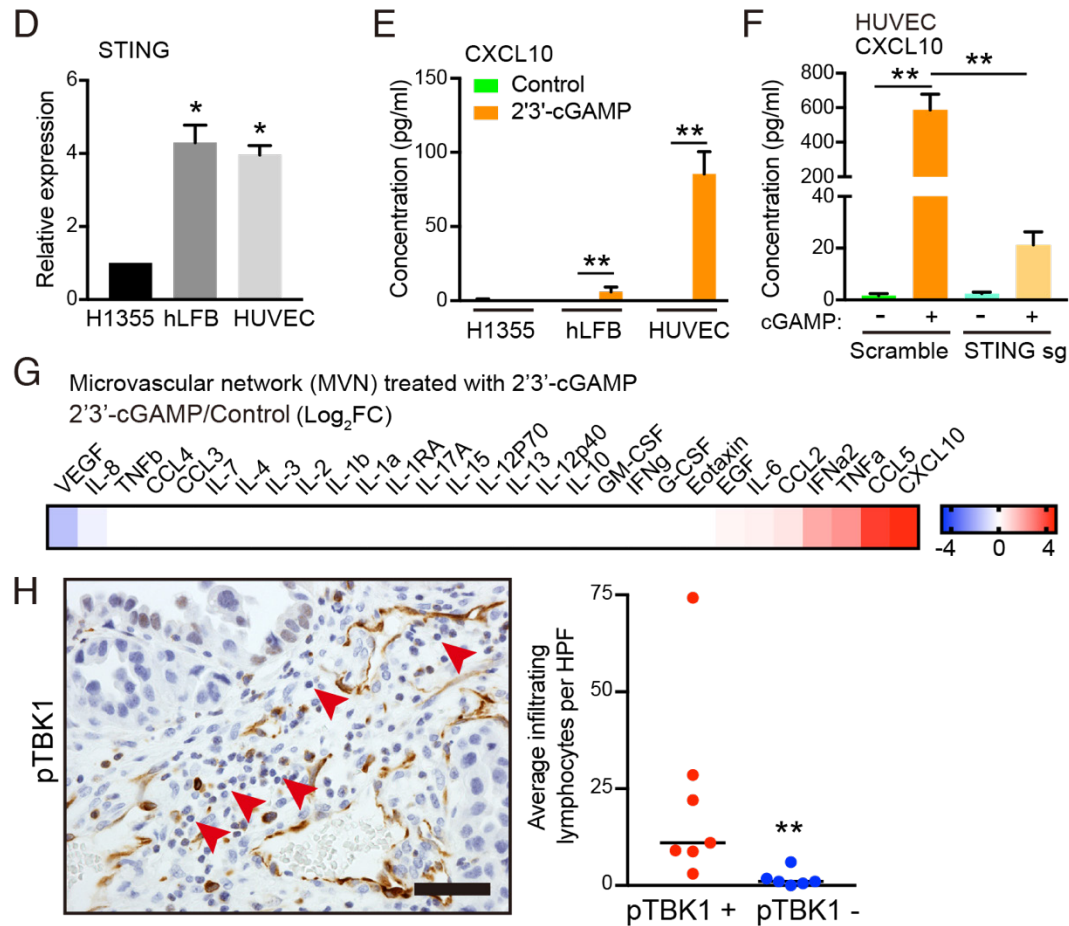


Figure 3.10: Activation of STING-TBK1 signaling in tumor vasculature and lymphocyte infiltration.

a) and b) Representative IHC images from metastatic non-small cell lung cancer (NSCLC) and primary glioblastoma multiforme (GBM) patient brain tissue samples. Red arrows highlight STING (upper) and phospho-TBK1 (pTBK1, lower) staining. Scale bars, 50 μ m. **c)** Representative STING (upper) and pTBK1 (lower) IHC images from control patient brain tissue. Scale bars, 100 μ m **d)** Endothelial STING and pTBK1 IHC was scored in a blinded manner for each sample on a binary scale based on the presence (positive, +) or absence (negative, -) of staining in cells surrounding the presumed endothelial lumen. **e)** qRT-PCR of basal STING in parental H1355, hLFB and HUVEC. **f)** qRT-PCR of IFN- β and CXCL10 in HUVECs after exogenous 2'3'-cGAMP treatment. Cells were treated with 1 μ g/mL 2'3'-cGAMP for 24 h. **g)** ELISA of human CXCL10 levels in conditioned medium derived from parental H1355, hLFB and HUVEC after exogenous 2'3'-cGAMP treatment (1 μ g/mL) for 24 h. **h)** ELISA of human CXCL10 levels in conditioned medium derived from HUVECs transduced with scramble (control sgRNA) or STING knockout (STING sgRNA), after exogenous 2'3'-cGAMP treatment (1 μ g/mL) for 24 h. **i)** Heat map of log₂ fold change cytokine/chemokine profiles in conditioned medium (CM) after 7 days of 3D microphysiological culture of MVN treated with 1 μ g/mL 2'3'-cGAMP treatment over MVN control. MVN were treated for 2 days after MVN formation. **j)** Representative IHC image from

*metastatic non-small cell lung cancer (NSCLC) with pTBK1+ endothelial microvessels. Red arrows highlight infiltrating lymphocytes. Scale bars, 50 μ m (left). Quantification of infiltrating lymphocytes per high power field (HPF) surrounding pTBK1+ or pTBK1- endothelial lumens, (right). P values were calculated by unpaired two tailed student t-test, one-way ANOVA, or two-way ANOVA followed by Tukey post-hoc test; ** $P < 0.01$, * $0.01 < P < 0.05$. Data shown as mean values, error bars \pm SD, (n=3 biological replicates). Reproduced with permission from [76].*

Export of 2',3'-cGAMP by tumor cells activates STING in neighboring endothelial cells

We therefore directly tested the model that 2'3'-cGAMP produced by cancer cells following dsDNA-mediated activation, could activate the STING/TBK1 pathway in neighboring tumor vasculature (Fig. 3.11a). Firstly, intracellular and extracellular 2'3'-cGAMP levels in H1355-LUC and H1355-LKB1 cells were measured using the same concentration of double-stranded DNA used in co-culture experiments. Transfection of poly(dA:dT) not only increased levels of intracellular 2'3'-cGAMP, but also increased extracellular 2'3'-cGAMP levels in the media, which was significantly enhanced by LKB1 reconstitution (Fig. 3.11b). As expected, knockout of STING failed to suppress either 2'3'-cGAMP intracellular and extracellular production, regardless of the LKB1 status (Fig. 3.11b). To determine directly whether 2'3'-cGAMP generated from tumor cells could activate STING in endothelial cells, we next generated cGAS knockout H1355 cells and treated them with poly(dA:dT) in 2D culture. As expected, recognition of dsDNA and subsequent activation of STING was abolished in cGAS null H1355-LUC and H1355-LKB1 cell lines, even with STING induction following LKB1 re-constitution (Fig. 3.11c). Consistently, intracellular 2'3'-cGAMP production was significantly diminished, and there were undetectable levels of 2'3'-cGAMP in the media from the cGAS knockout cell line (Fig. 3.11d). We next investigated the impact of co-culturing poly(dA:dT) transfected H1355-LKB1 cells following STING or cGAS knockout with HUVECs, sorting CD31⁺ cells to measure HUVEC specific cytokines/chemokines (Fig. 3.11e). Similar with the 3D culture results, dsDNA stimulation of H1355-LKB1 cells potently activated CXCL10 as well as IFN- β expression in HUVECs, even following STING knockout (Fig. 3.11f). In contrast, cancer cell cGAS deletion significantly decreased expression of both CXCL10 and IFN- β in co-cultured HUVECs, providing direct evidence that ablation of 2'3'-cGAMP export from tumor cells suppresses STING signaling in endothelial cells (Fig. 3.11g, h). Expression of CXCL10 and IFN- β in HUVECs was not completely abolished following cGAS

knockout, suggesting the potential for additional paracrine mediators of this response downstream of alternate dsDNA sensors. These data confirm that cGAS-driven 2'3'-cGAMP export from cancer cells is directly involved in activation of STING signaling in neighboring endothelial cells, prompting us to examine whether it might play additional roles in priming the vasculature to promote immune cell recruitment.

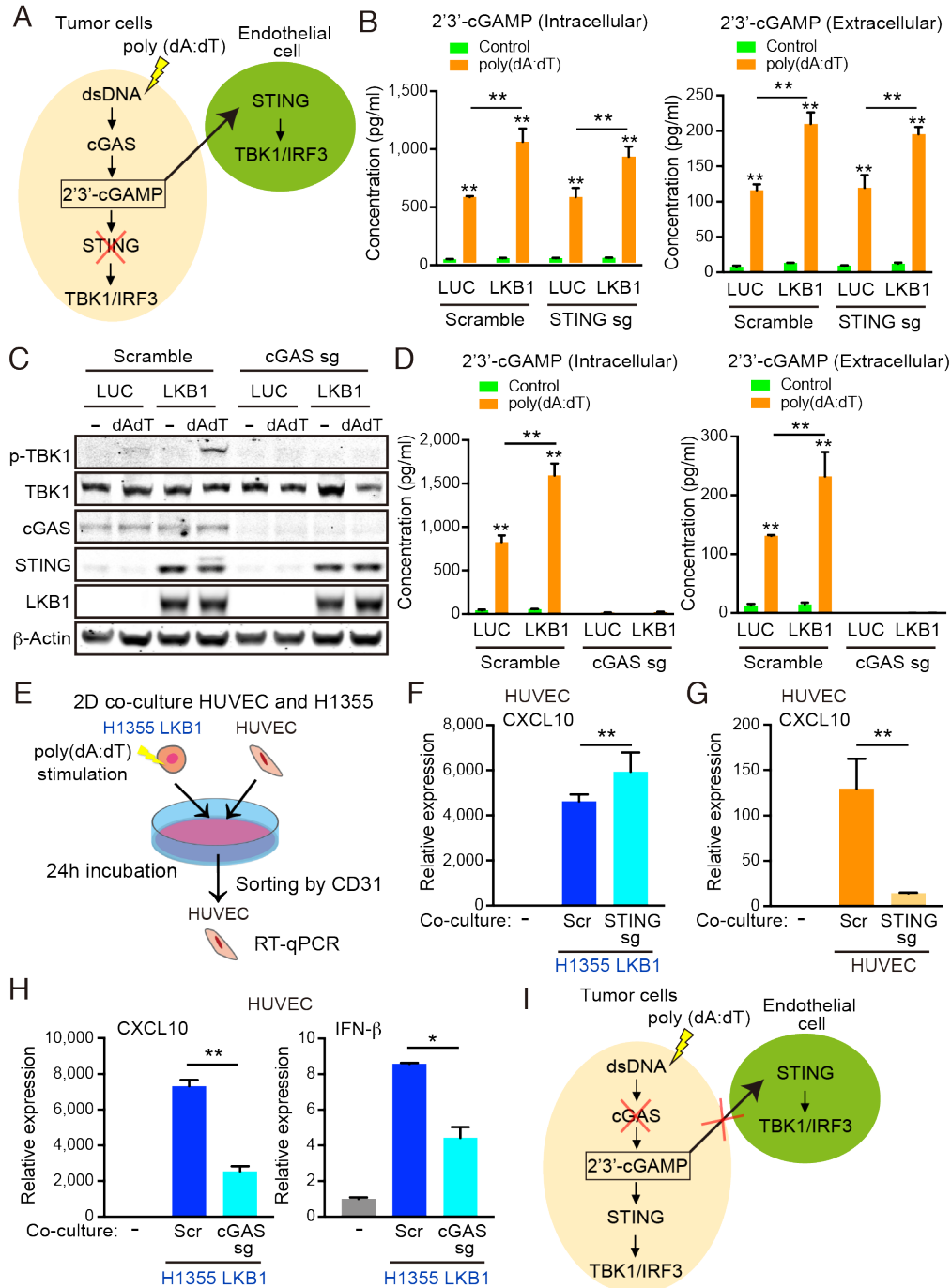


Figure 3.11: 2'3'-cGAMP exported by cancer cells activates STING signaling in endothelial cells.

a) Schematic of cGAS-STING signaling in tumor cells after poly(dA:dT) stimulation and hypothesized export of 2'3'-cGAMP activating STING in the endothelial cells, unaffected by tumor cell STING knockout. **b)** Intracellular and extracellular 2'3'-cGAMP ELISA of transduced LUC and LKB1 H1355 +/- scramble or STING knockout. **c)** Immunoblot of the indicated proteins in H1355 cells transduced with LUC and LKB1 with scramble or cGAS knockout (cGAS sgRNA) in 2-D culture. **d)** Intracellular and extracellular 2'3'-cGAMP ELISA of transduced LUC and LKB1 H1355 with scramble or cGAS knockout. **e)** Schematic of the 2-D co-culture experiment and sorting by CD31+ cells. **f)** qRT-PCR of CXCL10 of HUVECs after 2-D co-culture with H1355 cells for 24 h with scramble or STING knockout. **g)** qRT-PCR of CXCL10 of HUVECs scramble or STING knockout after 2-D co-culture with H1355 cells for 24 h. **h)** qRT-PCR of CXCL10 and IFN- β of HUVECs after 2-D co-culture with H1355 cells for 24 h with scramble or cGAS knockout. **i)** Schematic of cGAS-STING pathway in tumor cells after poly (dA:dT) stimulation demonstrating that silencing of cGAS impairs accumulation of 2'3'-cGAMP and export from the cells, limiting the STING activation in endothelial cells. P values were calculated by one-way ANOVA, or two-way ANOVA followed by Tukey post-hoc test; ** $P < 0.01$, * $0.01 < P < 0.05$. Data shown as mean values, error bars \pm SD, (n=3 biological replicates). Reproduced with permission from [76].

2'3'-cGAMP and IFN- β prime the endothelium for immune cell extravasation

To elucidate the potential consequences of 2'3'-cGAMP in altering the vasculature to promote immune cell recruitment, we first assessed its impact on microvascular permeability. Permeability coefficient of microphysiological MVNs model in microfluidic device was measured by monitoring the flux overtime of a fluorescent tracer from the luminal compartment of the vasculature to the interstitial space. We found that both 2'3'-cGAMP and IFN- β treatment individually enhanced permeability of the microvasculature (Fig. 3.12a, b). We therefore performed a quantitative PCR array of endothelial activation markers to identify whether expression of specific adhesion molecules or other related genes are also upregulated after treatment of endothelial cells with 2'3'-cGAMP or IFN- β . Notably, analysis of this list to identify common targets shared by both 2'3'-cGAMP and IFN- β treatment revealed upregulation of multiple genes involved in T cell trafficking, including E-selectin, ICAM-1, and VCAM-1 (Fig. 3.12c). We therefore examined expression of these specific genes in HUVECs in response to 2'3'-cGAMP, IFN- β , or the combination. Indeed, all three genes were significantly induced by 2'3'-cGAMP or IFN- β , treatment, and further increased by the combination (Fig. 3.12d). We therefore validated by immunostaining the expression of these adhesion molecules in established MVNs in

3D microfluidic devices. Treatment with 2'3'-cGAMP and/or IFN- β increased expression of membrane-bound ICAM-1 and VCAM-1 on MVNs by confocal images of microphysiological systems (Fig. 3.12e). To determine the functional consequences of this adhesion molecule upregulation in the Microphysiological MVN model, Jurkat T cells were perfused through the MVNs and observed significantly increased attachment of Jurkat cells to the endothelial walls of the microvasculature in the presence of 2'3'-cGAMP pre-treatment.

Together, these findings reveal that tumor-derived 2'3'-cGAMP not only activates innate immune cytokine/chemokine production in the adjacent vasculature, but also increases permeability and upregulates adhesion molecules known to facilitate immune cell extravasation (Fig. 3.12h).

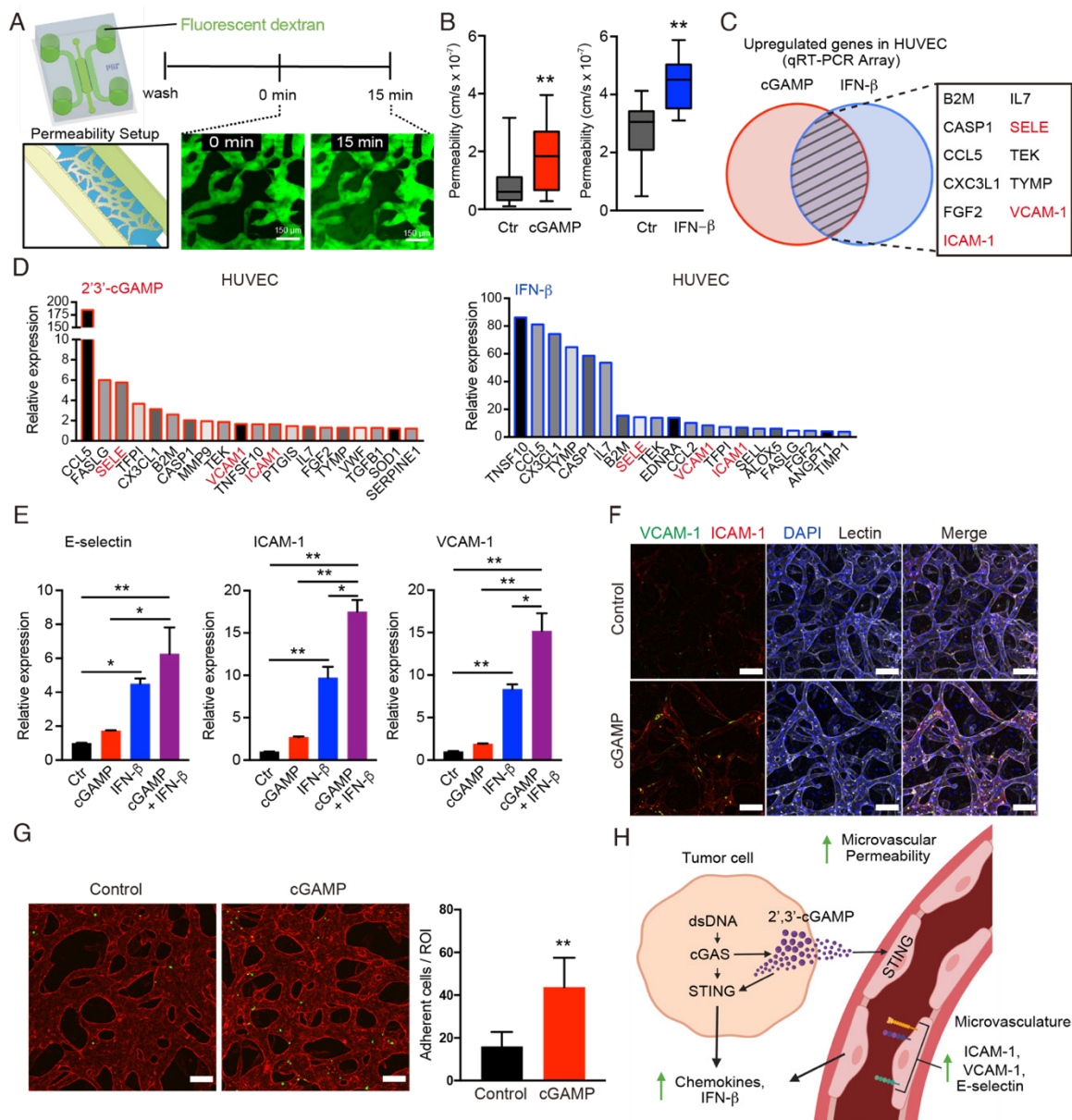


Figure 3.12: 2'3'-cGAMP and IFN- β promote vascular permeability and upregulation of adhesion molecules.

a) Schematic of permeability experiments and analysis. Dextran dye was injected, and image stacks were captured at time 0 and at 15 minutes. **b)** Permeability coefficients for different conditions (control, cGAMP, IFN- β), ($n=9$ biological replicates). **c)** Venn diagram of top genes upregulated in HUVEC after treatment with 2'3'-cGAMP or IFN- β . **d)** Upregulated genes from HUVEC treated with 2'3'-cGAMP or IFN- β . **e)** qRT-PCR of E-selectin, ICAM-1, VCAM-1 in HUVEC treated with 2'3'-cGAMP, IFN- β , or combination of 2'3'-cGAMP+IFN- β ($n=3$ biological replicates). **f)** Confocal images of microvasculature treated +/- 2'3'-cGAMP immunostained for ICAM-1, VCAM-1, and lectin. Scale bars, 100 μ m. **g)** Confocal images of microvasculature (red)

treated +/- 2'3'-cGAMP and Jurkat cells (green) (left). Quantification of the number of Jurkat cells adherent to microvasculature per Region of Interest (ROI) (right). Scale bars, 100 μ m. **h**) Schematic of tumor-derived cGAMP (via cGAS) and IFN- β (via STING) influencing the vascular permeability, adhesion molecules, and chemokines. Schematic was created with BioRender. *P* values were calculated by unpaired two tailed student *t*-test or one-way ANOVA followed by Tukey post-hoc test; ** *P* < 0.01, * 0.01 < *P* < 0.05. Data shown as mean values, error bars \pm SD. Reproduced with permission from [76].

Discussion

In this work, multiple 3-D microphysiological models were designed to probe the impact of LKB1 loss on cancer cell cGAS-STING signaling and their association with the tumor microvasculature, which represents the first barrier for immune cell homing to the tumor microenvironment.

First, a microphysiological model of LKB1 reconstituted STING-low H1355 tumor spheroids embedded in ECM-like hydrogel (collagen) was exploited to analyze immune cell infiltration and uncover the mechanisms of defective recruitment of immune cells in the absence of STING expression. Secondly, a 3-D microphysiological model of microvascular networks (MVNs) unveiled sensitivity to STING agonist treatments (cGAMP) and facilitated advanced quantification of vascular permeability and T-cells adhesion assays. Specifically, it indicated enhanced vascular permeability and increased production of endothelial CXCL10 and CCL5, possibly contributing to defective chemokine gradients that retain T cells near the vasculature.

Lastly, a novel microphysiological model of vascularized lung tumors revealed synergistic production of multiple immune cell chemo-attractants such as CXCL10, CCL2, CCL5, and G-CSF by multiplexed cytokine profiling. Interestingly, this more physiologic *ex vivo* tumor model of LKB1 reconstitution revealed particularly strong cooperative production of STING-dependent cytokines such as CXCL10 in the vasculature. Moreover, STING depletion in LKB1 reconstituted tumor cells did not significantly attenuate production of CXCL10 and other cytokines in co-culture, suggesting that tumor/vessel interaction may promote STING activation in the vasculature regardless of cancer cell-intrinsic STING function.

These findings were supported by *in vivo* quantitative IHC data from patients' biopsies that demonstrated impaired intra-tumoral T-cell infiltration from KL tumors that lacked STING expression, and instead, retention of T cells in the stroma. Furthermore, primary tumor and brain metastases from patients demonstrated STING-TBK1 activation in contrast with healthy vascular

endothelium. Data suggest paracrine signaling from tumor to the vasculature, which was demonstrated to be in the form of tumor 2'3' -cGAMP. Finally, STING activation of the endothelium enhance functional modification in the vasculature that are favorable to immune cell extravasation. Several recent studies have highlighted an emerging role of cancer cell derived 2'3'-cGAMP in the tumor microenvironment (TME). For instance, it has been demonstrated that in brain malignances tumor cells transfer 2'3'-cGAMP to astrocytes to drive adaptation of the TME [35], but also prime NK cells innate immunity[36][77] and macrophages to drive type 1 interferon production in the TME via accumulation of extracellular cancer cell derived 2'3'-cGAMP[78]. However, to date, a role for endogenous 2'3'-cGAMP in promoting vascular activation, a prerequisite for this immune cell influx into tumors, has yet to be described.

Importantly, tumor vascular endothelial cells have been identified as a major source for cytokines production in the TME following intratumoral injection of 2'3' cGAMP-based STING agonists, which can promote T-cell-mediated therapeutic antitumor immunity [79]. Furthermore, communication between cancer cells and vasculature has been shown to modulate the infiltration of immune cells and can induce an immunosuppressive TME lacking T-cells, a critical mechanism of resistance in the context of solid tumor immunotherapy.

Our innovative 3-D microphysiological system demonstrates that tumor-derived 2'3'-cGAMP can activate endothelial STING to enhance vascular permeability and adhesion molecules, offering a compelling explanation for defective T cells chemotaxis. In the context of cancer immunotherapy, such disrupted immune infiltration may promote resistance to anti-PD1 treatments in KL TME and other tumors.

Our findings also highlight a critical need for more studies regarding the contributions of different subcomponents of the TME during the innate immune response, especially as it relates to immune cell exclusion by tumors.

Conclusion

In summary, our data expand upon the increasingly recognized role of endogenous tumor-derived 2'3'-cGAMP in the TME [38], revealing a novel function in vascular activation and immune escape following LKB1 loss. They also suggest that DNA damaging agents or targeted therapeutics that increase endogenous 2'3'-cGAMP production may act to enhance vascular activation and improve immune cell infiltration and subsequent response to PD-1 blockade in these treatment refractory cancers.

More generally, these studies demonstrate that developing more representative physiological preclinical models of TME can elucidate important aspects of innate immune signaling that cannot be examined using traditional *in vitro* systems[62]. Indeed, microfluidic technologies help developing new tools for cancer diagnosis and treatment. Important future directions to enhance the physiologic relevance of the microphysiological systems of vascularized lung tumors include introduction of continuous perfusion to mimic blood microcirculation using a microfluidic pump for medium recirculation. Moreover, these systems will enable modeling of immune cell trafficking using cell lines, patient-derived peripheral blood mononuclear cells or Chimeric Antigen Receptor T cells (CAR T cells) in a long-term culture system. Furthermore, advances in *ex vivo* modeling may allow long-term culture of patient-derived tumor samples as a personalized medicine approach to study drug or immune cell penetration in patient-specific tumor niches [80]. The ability to investigate immune cell killing during immunotherapy treatments would represent a paradigm-shifting basic and translational advance. Thus, developing these more complex microphysiological models to incorporate components of the tumor microenvironment including tumor spheroids, fibroblasts and blood vessels may elucidate important aspects of STING biology and may ultimately aid further development of effective therapies.

Acknowledgments

The doctoral candidate would like to thank all the scientists involved in these experiments.

In particular, the candidate would like to acknowledge the contribution of the following:

- Shriram K. Sundararaman highly contributed to design and perform the experiments
- Shunsuke Kitajima highly contributed to design and perform experiments
- Sarah E. Shelton performed permeability analysis and the 3D perfusion assay
- Erik H. Knelson, Navin R. Mahadevan, Elena Ivanova and Israel Cañadas performed immunohistochemistry analysis from patient samples
- Ryohei Yoshida, Tetsuo Tani highly contributed to perform immunoblotting
- Tatsuya Osaki and Sharon Wei Ling Lee, contributed to the design of the microfluidic device
- Tran Thai, Saemi Han, Brandon P. Piel, Sean Gilhooley highly contributed with the ELISA assays and cytokine profiling
- Cloud P. Paweletz, Valeria Chiono, Roger D. Kamm, Shunsuke Kitajima and David A. Barbie designed and supervised the projects and acquired funding.

Chapter 7 – ALK-positive Anaplastic Large Cell lymphoma - vascular interactions promote resistance to ALK inhibitor via CCL19/21-CCR7 signaling axis

Abstract

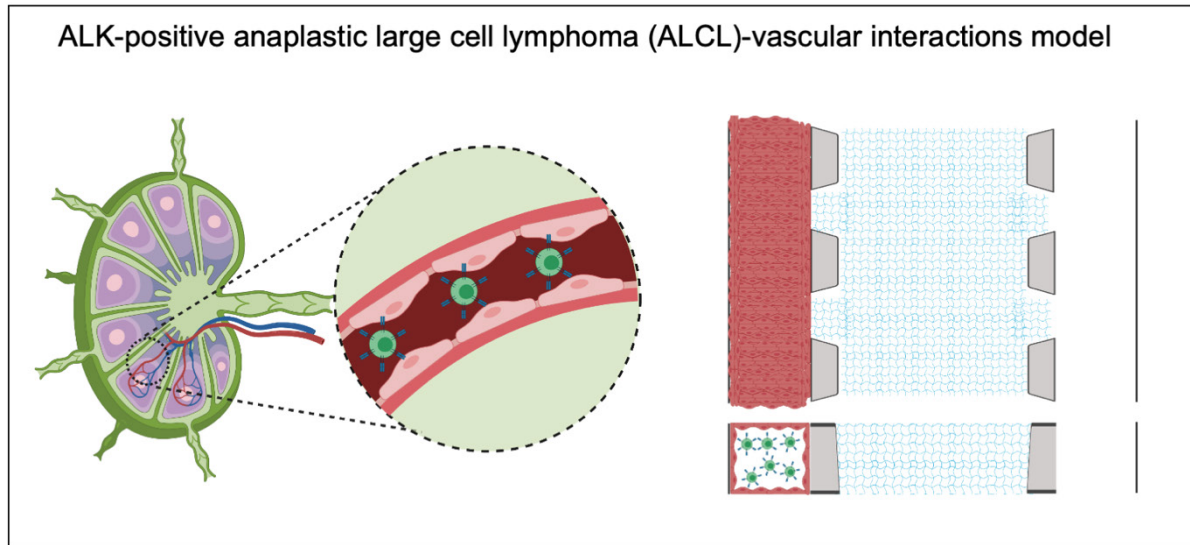
Anaplastic large cell lymphoma (ALCL) is a T cell lymphoma frequently driven by chromosomal rearrangements involving the Anaplastic Lymphoma Kinase (ALK) gene.

Patients with relapsed ALK-positive ALCL initially respond well to Anaplastic Lymphoma Kinase (ALK) tyrosine kinase inhibitor (TKI) therapies (e.g. crizotinib, that has recently been approved by FDA for ALK+ ALCL therapy); however, the emergence of resistance appears once the treatment is withdrawn and persistent lymphoma cells are not fully eradicated. Histologically, recurrent ALCL after ALK TKI discontinuation can be identified in and around the blood and lymphatic vessels in the perivascular region of lymph nodes, suggesting that vascular-tumor cell interactions may be important in mediating tumor cell survival and recrudescence. It has been shown that the CCL19/21-CCR7 signaling pathway regulates memory T cell trafficking, and preliminary data have evidenced that CCL19/21-CCR7 chemokine-receptor signaling axis may be involved in TKI resistance of ALCL cells.

To investigate this mechanism, an advanced microphysiological model of ALK⁺ ALCL -vascular interaction was established using a microfluidic chip with patterned microchannel design to generate a 3D macro-vessel. Confocal imaging revealed that ALCL cells introduced lumenally interacted with the well-formed perfusable macro-vessel generated by endothelial cells. A viability assay demonstrated that the presence of endothelial cells conferred resistance to crizotinib and sustained cell viability of wild type ALCL, whereas the protective effect was lost in CCR7-depleted lymphoma cells.

Given the challenges of more personalized and precise cancer therapies, these results suggest that this physiologically-relevant ALCL-vascular preclinical model has great potential to unveil the molecular mechanisms of drug resistance in a more complex TME and more reliably predict therapeutic vulnerabilities by recapitulating patient-specific cell-cell interactions.

This work was performed in Roberto Chiarle Laboratory at the “Center for Experimental Research and Medical Studies (CERMS), University of Torino”, Turin, as part of the collaboration between University of Turin and the Politecnico di Torino, during a research period at CERMS for the doctoral candidate.



Graphical abstract 8: *Preclinical models of Anaplastic large cell lymphoma and vascular interactions to model the tumor microenvironment and the perivascular niche in the lymph node.*

Schematic created with biorender.com

Introduction

Anaplastic Lymphoma Kinase (ALK) in the pathogenesis of cancer

Aberrant tyrosine kinase signaling is known to be involved in the pathogenesis of cancers. A tyrosine kinase is an enzyme that can transfer a phosphate group from ATP to a protein in a cell and serves as an "on" or "off" switch for many cellular functions. A mutation in these enzymes can cause constitutive signaling, leading to an unregulated growth of cells which is a necessary step for the development of cancer. An example of a tyrosine kinase, in particular a receptor tyrosine kinase (RTK) is the anaplastic lymphoma kinase (ALK) [81].

ALK is an enzyme originally described in anaplastic large cell lymphoma (ALCL), resulting from a translocation event on chromosomes 2 and 5 [t(2;5)(p23;q35)]. This translocation generates a fusion protein, NPM1-ALK, where the ALK kinase domain is fused to a part of the nucleophosmin (NPM) protein, which dimerizes and thus constitutively activates the ALK kinase [82] (Fig. 3.13a). The ALK receptor is comprised of three domains: an extracellular ligand-binding domain, a transmembrane and an intracellular tyrosine kinase domain. In physiological conditions, the ALK receptor is involved in neural cell differentiation/development and the function of the nervous system, synapse development at the neuromuscular junction, and growth of the entire organism [83].

The ALK gene can become oncogenic in multiple ways: rearrangement mutations such as fusion and gene translocation, gain of additional copies, or mutation of the DNA code of the gene itself that finally drives spontaneous transformation (Fig. 3.13b). ALK mutations, including gene rearrangements such as translocations or inversions, gain of function, point mutations in the tyrosine kinase domain and overexpression are associated with many tumor types: ALCL, inflammatory myofibroblastic tumors, breast and renal carcinomas, non-small cell lung cancer (NSCLC), neuroblastomas, colonic adenocarcinoma, anaplastic thyroid cancer and glioblastoma multiforme[84]. The most prevalent genomic aberration of ALK in human cancer are chromosomal rearrangements resulting in fusion genes, such as NPM1-ALK in ALCL and EML4-ALK in NSCLC[15][14].

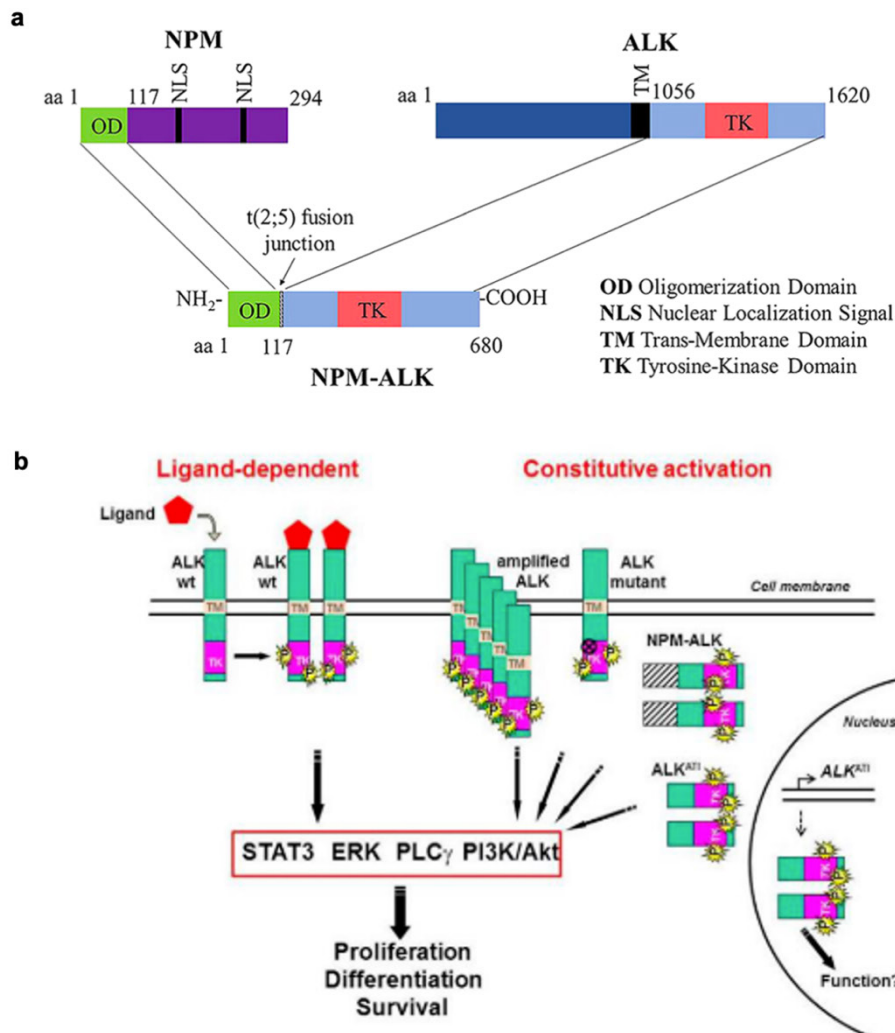


Figure 3.13: Anaplastic lymphoma kinase (ALK) signaling.

a) The chromosomal translocation $t(2;5)(p23;q35)$ results in production of the NPM-ALK fusion gene and protein. The Oligomerization Domain (OD) of NPM provides the biochemical basis for NPM-ALK fusion protein oligomerization, allowing auto phosphorylation and constitutive activation of NPM-ALK that plays a major role in the pathogenesis of ALK+ ALCL. Reproduced with permission from [85] **b)** ALK activation can be achieved in the presence of a ligand (left), or constitutively (right) when ALK is either amplified, mutated, involved in a fusion such as NPM-ALK that cause downstream activation of proliferation pathways. Reproduced with permission from [86].

ALK as therapeutic target in Anaplastic Large Cell Lymphoma

Although ALK translocation was first identified in ALCL (NPM1-ALK), not all anaplastic lymphomas express ALK translocations. Indeed, the World Health Organization classifies ALK-positive (50-60% of all ALCL) and ALK-negative ALCL. ALK-positive ALCL is a type of non-Hodgkin lymphoma involving aberrant T cells or null lymphocytes. ALK-transformed lymphoid cells are completely dependent on ALK tyrosine kinase activity for survival and proliferation.

ALCL encompasses the presence of large pleomorphic cells, or horseshoe-kidney-shaped cells, with large nuclei and abundant grey-blue cytoplasm, that express CD30 and T-cell markers. ALCL usually grows around blood and lymphatic vessels in the lymph node[84].

Several important characteristics make ALK an attractive target for cancer therapy. First, ALK is not widely expressed in adult tissues, being abundant only in a few neuronal cells, therefore, few toxic effects might be expected from treatment aimed at blocking ALK function.

Since ALK-driven tumors are dependent on constitutively activated ALK for their proliferation, a number of tyrosine kinase inhibitors have been developed to block tumor growth, called ALK inhibitors (listed here from the first to last generations: crizotinib, ceritinib, alectinib, brigatinib and lorlatinib)[82]. All of these inhibitors are FDA approved for ALK-rearranged NSCLC while so far only crizotinib has been approved for ALK+ ALCL. Their efficacy is remarkable, though sometimes transient, as tumors initially respond but escape and become resistant, leading to relapse. A frequent event in ALK-driven resistance is the appearance of secondary mutations in the same tyrosine kinase domain. Some of these mechanisms have been elucidated and can be addressed by targeted therapies; other resistance mechanisms are still poorly understood [87][88]. Previously, it has been shown that CCL19/21-CCR7 chemokine-receptor signaling axis is known to regulate T cell trafficking and migration toward the lymph node [81], [82]. Recently, preliminary data have shown that CCR7-positive ALCL cells, which accumulate in the perivascular space of the lymph nodes, and CCL19/21, produced by endothelial cells of blood and lymphatic vessels and fibroblasts [89], [90], may be involved in resistance of ALCL cells to crizotinib.

Preclinical modeling of microphysiological ALK-vascular interactions

Experimental modeling of ALK-driven cancers has mostly relied on 2D culture of suspension cell lines, mouse models such as orthotopic isogenic models and patient-derived xenograft models[83]. Animal models have been an invaluable tool to understand several mechanisms of ALK-driven within a relevant living system, however, have failed to recapitulate complex cell-cell interactions within a human-relevant system. Alternatives to animal models seem quite reasonable but poorly explored. Occasionally, patient-derived samples from peripheral blood and lymph node biopsy sections have been used, but mostly kept as suspension cultures in 2D flasks with the limitations discussed before[91]. In ALK-driven lung cancer, a CTC-derived organoid was useful in forecasting the therapeutic response to specific ALK inhibitors (ceritinib and crizotinib)[92]. Likewise, a B-cell organoid [93][94], was cultured to reproduce a lymphoid tissue structure, called a germinal center, where B-cells rapidly mature into antibody producing cells. Such systems can enable mechanistic understanding of ALK biology and/or the immune system and more importantly, accelerate a deeper understanding of the mechanisms that lead to their malignant transformation into a variety of B and T cell malignancies. There are numerous engineered fluidic systems to understand lymphatic interaction with cancer cells and replicate the mechanisms of cancer trans-endothelial migration in the lymphatic vessels and metastasis[95]; however, none of them have been established to study ALK-positive ALCL.

To the best of our knowledge, advanced preclinical models of ALK-positive ALCL have not been reported. Thus, more complex *in vitro* models are needed to uncover the continuous interactions that exist between ALCL tumor cells and nontumor cellular elements of the tumor microenvironment through direct cell–cell or cell–matrix contact or by the secretion of signaling factors such as cytokines, chemokines and growth factors. Microfluidic technology offers a platform to replicate these microenvironmental interactions and specifically test novel cancer therapeutics, overcoming the limitations of 2D culture and intrinsic caveat of mouse models. To overcome the current limitations, here an advanced 3D microphysiological model of ALCL-vascular interactions was developed, where ALCL cells are contained within the lumen of a 3D engineered macrovessel. After characterization of the model in terms of integrity and formation of the blood vessel, the additional role of microvasculature in the resistance mechanism of ALCL to ALK inhibitor was examined.

Materials and methods

Materials and reagents

COST and Karpas299, HUVECs (Lonza), RPMI, Trypsin-EDTA, Collagen Rat tail, microfluidic chip '3-D cell culture chip' (DAX-1, AIM Biotech).

Cell culture

Two ALK⁺ ALCL cell lines (COST and Karpas299) were culture in RPMI with 10% FBS, as cell suspension at cell density of 1×10^5 up to 3×10^5 cells/ml. Cell population usually has 24-48h doubling rate. Cell culture medium was refreshed every 2 days. Firstly, Medium was added until reaching the limit volume of the culture flask for culture in suspension. After that, cells were pelleted at 1200 rpm for 5 min, and plated in a larger flask with fresh medium to expand the population or used for the study. Human umbilical vein endothelial cells (HUVECs) were cultured in vascular medium were cultured in EGM-2 MV (Lonza). Culture medium was refreshed every 2 days, detached using Trypsin-EDTA 1X 0.05%, blocked with medium and pelleted at 1200 rpm for 5 min. All experiments were performed before reaching 6 passages.

Genetic engineering and CRISPR/Cas9 systems

Two ALK⁺ ALCL cell lines (COST and Karpas299) were knocked out by CRISPR/Cas9 of the CCR7 receptor by single cell cloning, transduced with GFP for microscopic visualization.

ALCL-vascular microphysiological model

Microphysiological systems were developed using a commercial microfluidic chip '3-D cell culture chip' (DAX-1, AIM Biotech) as previously described. To generate the ALCL-vascular Microphysiological model collagen rat tail hydrogel mixture (2.5 mg/ml) was injected into the center gel region of the 3D microfluidic chamber (10-15 μ L per each microfluidic chamber). Before injection collagen hydrogel is kept in ice. After incubation for 30 minutes at 37 °C in sterile humidity chambers, collagen hydrogel channels were hydrated with RPMI. Then, all the side walls of one flanked channel (media channel) were coated with a 150 μ g/ml collagen solution in PBS to allow a better adhesion of ECs to the channel. After 15 mins, channel was washed once with

medium. To create the 3D macrovessel, 50 μL cell suspension of 3×10^6 cells/ml human umbilical vein endothelial cells (HUVECs) were injected in the media channel coated with collagen. twice on the fluidic channel, chip was rotated twice to create a confluent hollow-lumen 3D macrovessel. To allow the cells to attach to the media-gel interface to form a monolayer, the chip was placed to let the cells face down for 15 mins so that the media-gel interface would face down. After that a 50 μL cell suspension were reinjected, and the chip was faced upside down to cover the upper part of the 3D vascular channel. After 90 mins of incubation in the humidity chamber in incubator at 37 °C, cell culture medium was gently added in both media channels. Chips are placed in incubator to form a confluent monolayer. The day after, 2×10^5 cells/ml ALCL cells were added inside of the 3D macrovessel. Medium was refreshed daily, supplemented +/- 300 nM of crizotinib (ALK TKI).

Immunocytochemistry and Imaging

Image capture and analysis were performed using fluorescence confocal microscope and a processing software. The 3D vascular channels were cultured for 7 days followed by rinsing in PBS and fixation in 4% PFA for 15 min at RT. Cell membranes were permeabilized with 0.1% Triton X-100 for 5 min at RT and washed twice with PBS. HUVECs cell were stained for F-ACTIN with red phalloidin (PHDH1, Cytoskeleton, Inc.).

Cell viability assays

Cell viability was evaluated by measuring ATP using a lysing reagent with luminescent readout using CellTiter-Glo (Promega, USA) according to manufacturer's instruction. Briefly, cells were extracted from the device and plated into white walled 96-well plates (3wells/sample), cellTiter-Glo reagent was added to each well and luminescence output data were taken by GloMax-Multi Detection System (Promega, USA).

Results

It has been shown that ALCL grows around blood and lymphatic vessels in the lymph node (Fig. 3.14a). According to our hypothesis, the perivascular niche provides pro-survival signals contributing to ALK-positive ALCL persistence and ALK inhibitor resistance. To prove that, a 3D microphysiological model of ALCL-vasculature was developed (Fig. 3.14b). Model characterization by confocal microscope imaging showed macrovessel formation by patterned channel design. The 3D model consisted of a well-formed and perfusable macro-vessel with endothelial cells that reached an acceptable confluency in all sides (apical, basal and lateral layers), without evident discontinuity, forming a tight 3D monolayer ((Fig. 3.14c-e). Two ALK-positive ALCL cell lines, COST and Karpas299, GFP-transfected, were deleted of the CCR7 receptor by CRISPR/Cas9. At day 2 of culture, ALCL were inserted in the fluidic channel of the device by injecting a solution of cells treated with (+/- crizotinib) in the macro-vessel.

Cells were allowed to circulate inside the macro-vessels and interact with the endothelial cells. ALCL viability was evaluated with a luminescent readout assay after 3 days of interactions with HUVECs (Fig. 3.14g). Strikingly, Karpas299 cultivated within the vasculature showed no marked resistance to treatment with ALK TKI compared to cells cultivated in the absence of vessels. CCR7-depleted Karpas299 lymphoma cells showed slightly decreased viability. In the case of COST cells, cell viability assay of ALCL co-culture with vasculature showed lower percentages of cell death under crizotinib treatment compared to COST without the vasculature. In addition, we noticed that a slight decrease of viable cells is present in the CCR7-depleted cells were compared to the wild type control (presenting the CCR7 receptor).

Moreover, we notice that COST CCR7-depleted cells showed increased diffusion and perivascular localization compared to wild type control cells, which was not remarkable in the Karpas299 model.

In summary, COST cells cultivated within the vasculature showed marked resistance to treatment with ALK inhibitors and CCR7-depleted cells showed decreased viability and decrease perivascular localization compared to wild type control cells compared to Karpas299 cells cultivated in the absence of vessels.

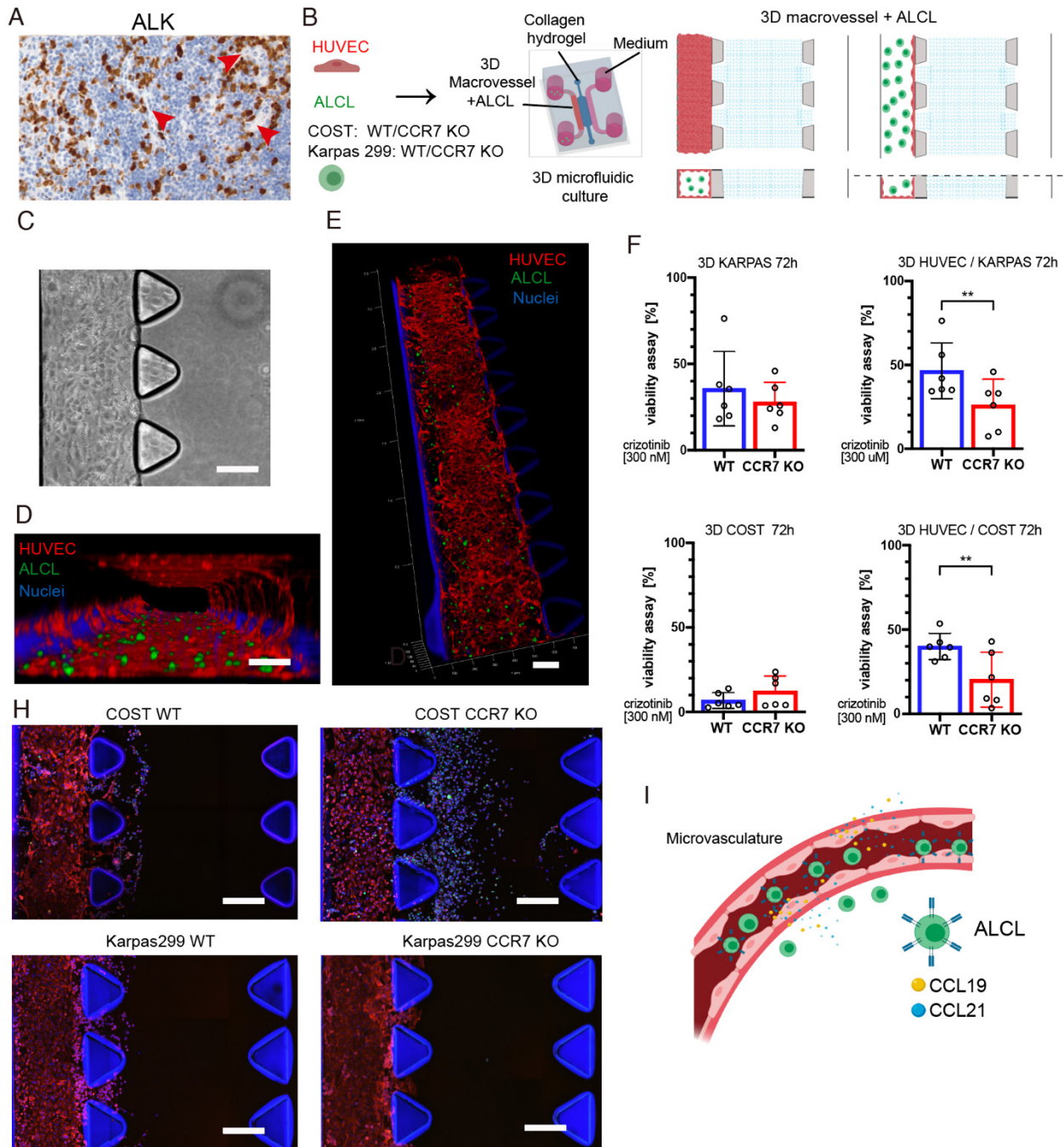


Figure 3.14: Modelling ALK⁺Anaplastic Large Cell Lymphoma (ALC) interaction with blood vessel.

a) Representative IHC image Anaplastic lymphoma Kinase (ALK) staining. Reproduced with permission from [84]. **b)** Schematic of Microphysiological model of ALCL-vascular interaction, and blood vessel formation in a 3D microfluidic model. **c)** Bright field and **d) e)**, confocal microscope imaging of macrovessels (F-actin, red) and ALCL (GFP, green) in the microfluidic model. **h)** Confocal images of ALCL trans-endothelial migration. **G,** Viability assay of wild type (WT) or CCR7-depleted (CCR7 KO) ALCL cells (COST, Karpas299) in co-culture with blood vessels treated with +/- 300 nM crizotinib. **i)** Schematic of ALCL cells interacting with blood-vessels with CCL9/21 cytokines. P values were calculated by one-way ANOVA ** P < 0.01. Data shown as mean values, error bars ± SD, (n=3 biological replicates).

Discussion

ALK-driven cancers, such as ALK-positive Anaplastic large cell lymphoma (ALCL) are highly dependent on the proto-oncoprotein, ALK tyrosine kinase.

Inhibition of ALK activity is an optimal target to shut down proliferation, however, cell-extrinsic survival mechanisms can arise in which interaction of the tumor with close cellular and non-cellular components of the tumor microenvironment leads to drug resistance. Therefore, patients treated with ALK inhibitors experience tumor recurrence, and recent studies have hypothesized that endothelial cells of lymphatic and blood vessels of the TME provide survival signaling[96]. In this work, a 3-D microphysiological model of ALCL cells interacting with a 3D vasculature using a microfluidic chip was designed to unveil the molecular mechanisms of drug resistance to ALK inhibitors in ALK-positive ALCL. The presence of macro-vessels was sufficient to induce resistance to ALK TKIs, which was overcome in CCR7-depleted ALCL cells. These data suggest that CCL19/21-CCR7 signaling driven by ALCL-vascular interactions might contribute to ALCL resistance to the ALK inhibitors. However, Karpas299 showed no significant difference in viability which suggests that there might be other operative resistance mechanisms, e.g., other cytokines produced by macro-vessels, or other cells of the TME generate survival signals in ALCL cells treated with ALK inhibitors.

Our model will benefit from the introduction of lymphatic vessels and fibroblasts which will further improve physiologic relevance by mimicking ALCL-vascular interactions similar to the lymph node on a microfluidic chip. Alternatively, organoid systems could be utilized for drug screening. Similarly, as with previous methods, an ALCL patient-derived organoid model could be developed to further enhance long term culture, but so far, organoids still lack vascular components. In general, these *ex vivo* models or their combinations, are able to uncover the continuous interactions and chemokine signaling that exist between cells of the tumor microenvironment (TME), and evaluate the preclinical efficacy of novel and personalized cancer therapeutics.

Conclusions

Here, we developed a 3D microphysiological model of ALCL-vascular interactions designed by patterned channel, which showed great potential to unveil the molecular mechanisms of drug resistance in a more complex TME compared to 2D culture. Results suggest that the 3D ALCL-vascular model offers a tool to genetically dissect the TME contribution to drug resistance, more reliably predict therapeutic vulnerabilities in a pre-clinical setting, and recapitulate patient-specific cell-cell interactions, towards personalized medicine applications.

In particular, this robust and physiologically relevant ALCL-vascular model potentially offers an innovative platform for testing drug efficacy which must be further validated and compared with traditional models. It may also contribute to the study of targeted therapies and unveil the mechanisms of resistance due to its complex mimicry of the tumor microenvironment.

Furthermore, the flexibility of the model allows for the introduction of additional cell types, such as lymphatic fibroblast that could also contribute to the pro-survival microenvironment for ALCL cells.

Overall, our results suggest that the perivascular lymph node niche could promote survival of ALK⁺ ALCL persister cells and protect them from the effect of ALK TKIs via the CCL19/21-CCR7 axis. The disruption of this survival axis could contribute to the eradication of minimal residual disease in combination with ALK inhibitors.

Acknowledgments

The doctoral candidate would like to thank all the scientists from the Center for Experimental Research and Medical Studies (CERMS), University of Torino involved in these experiments.

In particular, the candidate would like to acknowledge the contribution of the following:

- Enrico Patrucco and Ines Mota, developed the CRISPR/cas9 cells
- Valeria Chiono, Roger Kamm, Claudia Voena and Roberto Chiarle supervised the project

Table 6. Primers for real-time RT-PCR**For qRT-PCR**

	Forward (5'-3')	Reverse (5'-3')
human IFN β	ATGACCAACAAGTGTCTCCTCC	GGAATCCAAGCAAGTTGTAGCTC
human ICAM1	ATGCCCAGACATCTGTGTCC	GGGGTCTCTATGCCCAACAA
human VCAM1	GGGAAGATGGTCGTGATCCTT	TCTGGGGTGGTCTCGATTTTA
human E-selectin	AGAGTGGAGCCTGGTCTTACA	CCTTTGCTGACAATAAGCACTGG
human CXCL10	GTGGCATTCAAGGAGTACCTC	TGATGGCCTTCGATTCTGGATT
human 36B4	CAGATTGGCTACCCAAGTGT	GGAAGGTGTAATCCGTCTCCA
human STING	CCAGAGCACACTCTCCGGTA	CGCATTGTTGGGAGGGAGTAGTA

For sgRNA vector

	Target sequence (5'-3')
scramble sgRNA	ATCGTTTCCGCTTAACGGCG
human LKB1 sgRNA1	GTA CTCCATCACCATATACG
human LKB1 sgRNA2	CTTCAAGGTGGACATCTGGT
human STING sgRNA	GGTACCGGGGCAGCTACTGG
human cGAS sgRNA	AAGTGCGACTCCGCGTTCAG

For Mycoplasma detection

	Forward (5'-3')	Reverse (5'-3')
	ACACCATGGGAGCTGGTAAT	CTTCWATCGACTTYCAGACCCAAGGC

References

- [1] C. Gridelli *et al.*, “Non-small-cell lung cancer,” *Nat. Rev. Dis. Prim.*, vol. 1, pp. 1–16, 2015.
- [2] H. H. Popper, “Progression and metastasis of lung cancer,” *Cancer Metastasis Rev.*, vol. 35, no. 1, pp. 75–91, 2016.
- [3] R. S. Herbst, D. Morgensztern, and C. Boshoff, “The biology and management of non-small cell lung cancer,” *Nature*, vol. 553, no. 7689, pp. 446–454, 2018.
- [4] M. Zheng, “Classification and Pathology of Lung Cancer,” *Surg. Oncol. Clin. N. Am.*, vol. 25, no. 3, pp. 447–468, 2016.
- [5] R. J. Cersosimo, “Lung cancer: A review,” *Am. J. Heal. Pharm.*, vol. 59, no. 7, pp. 611–642, 2002.
- [6] H. Lemjabbar-Alaoui, O. Hassan, Y.-W. Yang, and P. Buchanan, “Lung cancer: Biology and treatment options,” *Biochim. Biophys. Acta*, vol. 1856, 2015.
- [7] R. Rosell and L. Wannesson, “A genetic snapshot of small cell lung cancer,” *Cancer Discov.*, vol. 2, no. 9, pp. 769–771, 2012.
- [8] D. Hanahan and R. A. Weinberg, “Hallmarks of cancer: The next generation,” *Cell*, vol. 144, no. 5, pp. 646–674, 2011.
- [9] J. Zhang *et al.*, “Intratumor heterogeneity in localized lung adenocarcinomas delineated by multiregion sequencing,” *Science (80-.)*, vol. 346, no. 6206, pp. 256–259, 2014.
- [10] E. C. De Bruin *et al.*, “Spatial and temporal diversity in genomic instability processes defines lung cancer evolution,” *Science (80-.)*, vol. 346, no. 6206, pp. 251–256, 2014.
- [11] P. S. Hammerman *et al.*, “Comprehensive genomic characterization of squamous cell lung cancers,” *Nature*, vol. 489, no. 7417, pp. 519–525, 2012.
- [12] E. A. Collisson *et al.*, “Comprehensive molecular profiling of lung adenocarcinoma: The cancer genome atlas research network,” *Nature*, vol. 511, no. 7511, pp. 543–550, 2014.
- [13] D. Irmer, J. O. Funk, and A. Blaukat, “EGFR kinase domain mutations - Functional impact and relevance for lung cancer therapy,” *Oncogene*, vol. 26, no. 39, pp. 5693–5701, 2007.
- [14] W. Pao and N. Girard, “New driver mutations in non-small-cell lung cancer,” *The Lancet Oncology*, vol. 12, no. 2. Elsevier, pp. 175–180, 01-Feb-2011.
- [15] A. Qin and S. Gadgeel, “The Current Landscape of Anaplastic Lymphoma Kinase (ALK) in Non-Small Cell Lung Cancer: Emerging Treatment Paradigms and Future Directions,” *Target. Oncol.*, vol. 12, no. 6, pp. 709–718, 2017.
- [16] N. Karachaliou *et al.*, “KRAS mutations in lung cancer,” *Clin. Lung Cancer*, vol. 14, no. 3, pp. 205–214, 2013.
- [17] J. M. Ostrem, U. Peters, M. L. Sos, J. A. Wells, and K. M. Shokat, “K-Ras(G12C) inhibitors allosterically control GTP affinity and effector interactions,” *Nature*, vol. 503, no. 7477, pp. 548–551, 2013.
- [18] G. J. Riely, J. Marks, and W. Pao, “KRAS mutations in non-small cell lung cancer,” *Proc. Am. Thorac. Soc.*, vol. 6, no. 2, pp. 201–205, 2009.
- [19] S. Kitajima, R. Thummalapalli, and D. A. Barbie, “Inflammation as a driver and vulnerability of KRAS mediated oncogenesis,” *Semin. Cell Dev. Biol.*, vol. 58, pp. 127–135, 2016.
- [20] J. P. Van Meerbeeck, D. A. Fennell, and D. K. M. De Ruyscher, “Small-cell lung cancer,” *Lancet*, vol. 378, no. 9804, pp. 1741–1755, 2011.
- [21] L. B. Alexandrov *et al.*, “Signatures of mutational processes in human cancer,” *Nature*, vol. 500, no. 7463, pp. 415–421, 2013.
- [22] G. Mollaoglu *et al.*, “MYC Drives Progression of Small Cell Lung Cancer to a Variant Neuroendocrine Subtype with Vulnerability to Aurora Kinase Inhibition,” *Cancer Cell*, vol. 31, no. 2, pp. 270–285, 2017.
- [23] J. Brägelmann, S. Böhm, M. R. Guthrie, G. Mollaoglu, T. G. Oliver, and M. L. Sos, “Family matters: How MYC family oncogenes impact small cell lung cancer,” *Cell Cycle*, vol. 16, no. 16, pp. 1489–1498, 2017.

- [24] L. A. Byers *et al.*, “Proteomic profiling identifies dysregulated pathways in small cell lung cancer and novel therapeutic targets including PARP1,” *Cancer Discov.*, vol. 2, no. 9, pp. 798–811, 2012.
- [25] T. Kohno *et al.*, “Beyond ALK-RET, ROS1 and other oncogene fusions in lung cancer,” *Transl. Lung Cancer Res.*, vol. 4, no. 2, pp. 156–164, 2015.
- [26] M. B. Ryan and R. B. Corcoran, “Therapeutic strategies to target RAS-mutant cancers,” *Nat. Rev. Clin. Oncol.*, vol. 15, no. 11, pp. 709–720, 2018.
- [27] J. Hallin *et al.*, “The KRASG12C inhibitor MRTX849 provides insight toward therapeutic susceptibility of KRAS-mutant cancers in mouse models and patients,” *Cancer Discov.*, vol. 10, no. 1, pp. 54–71, 2020.
- [28] J. Canon *et al.*, “The clinical KRAS(G12C) inhibitor AMG 510 drives anti-tumour immunity,” *Nature*, vol. 575, no. 7781, pp. 217–223, 2019.
- [29] F. Facchinetti *et al.*, “LKB1/STK11 mutations in non-small cell lung cancer patients: Descriptive analysis and prognostic value,” *Lung Cancer*, vol. 112, pp. 62–68, 2017.
- [30] S. Koyama *et al.*, “STK11/LKB1 deficiency promotes neutrophil recruitment and proinflammatory cytokine production to suppress T-cell activity in the lung tumor microenvironment,” *Cancer Res.*, vol. 76, no. 5, pp. 999–1008, 2016.
- [31] C. L. Mahoney *et al.*, “LKB1/KRAS mutant lung cancers constitute a genetic subset of NSCLC with increased sensitivity to MAPK and mTOR signalling inhibition,” *Br. J. Cancer*, vol. 100, no. 2, pp. 370–375, 2009.
- [32] F. Skoulidis *et al.*, “STK11/LKB1 mutations and PD-1 inhibitor resistance in KRAS-mutant lung adenocarcinoma,” *Cancer Discov.*, vol. 8, no. 7, pp. 822–835, 2018.
- [33] G. N. Barber, “STING: infection, inflammation and cancer,” *Nat. Rev. Immunol.*, vol. 15, no. 12, pp. 760–770, Dec. 2015.
- [34] A. Ablasser *et al.*, “Cell intrinsic immunity spreads to bystander cells via the intercellular transfer of cGAMP,” *Nature*, vol. 503, no. 7477, pp. 530–534, 2013.
- [35] Q. Chen *et al.*, “Carcinoma-astrocyte gap junctions promote brain metastasis by cGAMP transfer,” *Nature*, vol. 533, no. 7604, pp. 493–498, May 2016.
- [36] A. Marcus, A. J. Mao, M. Lensink-Vasan, L. A. Wang, R. E. Vance, and D. H. Raulet, “Tumor-Derived cGAMP Triggers a STING-Mediated Interferon Response in Non-tumor Cells to Activate the NK Cell Response,” *Immunity*, vol. 49, no. 4, pp. 754–763.e4, 2018.
- [37] J. K. Won and S. F. Bakhoun, “The cytosolic DNA-sensing cGAS–sting pathway in cancer,” *Cancer Discov.*, vol. 10, no. 1, pp. 26–39, 2020.
- [38] S. K. Sundararaman and D. A. Barbie, “Tumor cGAMP Awakens the Natural Killers,” *Immunity*, vol. 49, no. 4, pp. 585–587, 2018.
- [39] Q. Chen, L. Sun, and Z. J. Chen, “Regulation and function of the cGAS-STING pathway of cytosolic DNA sensing,” *Nat. Immunol.*, vol. 17, no. 10, pp. 1142–1149, 2016.
- [40] X. Cai, Y. Chiu, and Z. J. Chen, “The cGAS-cGAMP-STING Pathway of Cytosolic DNA Sensing and Signaling,” *Mol. Cell*, vol. 54, no. 2, pp. 289–296, 2014.
- [41] S. R. Woo *et al.*, “STING-dependent cytosolic DNA sensing mediates innate immune recognition of immunogenic tumors,” *Immunity*, vol. 41, no. 5, pp. 830–842, Nov. 2014.
- [42] L. Corrales *et al.*, “Direct Activation of STING in the Tumor Microenvironment Leads to Potent and Systemic Tumor Regression and Immunity,” *Cell Rep.*, vol. 11, no. 7, pp. 1018–1030, 2015.
- [43] C. M. Della Corte and L. A. Byers, “Evading the STING: LKB1 loss leads to STING silencing and immune escape in KRAS-mutant lung cancers,” *Cancer Discov.*, vol. 9, no. 1, pp. 16–18, 2019.
- [44] S. Kitajima *et al.*, “Suppression of STING Associated with LKB1 Loss in KRAS-Driven Lung Cancer,” *Cancer Discov.*, vol. 9, no. 1, pp. 34–45, Jan. 2019.
- [45] T. E. Keenan, K. P. Burke, and E. M. Van Allen, “Genomic correlates of response to immune checkpoint blockade,” *Nat. Med.*, vol. 25, no. 3, pp. 389–402, 2019.
- [46] and D. T. F. Johanna A. Joyce, “T cell exclusion, immune privilege, and the tumor microenvironment,” *Science (80-)*, vol. 348, no. 6230, pp. 74–80, 2015.

- [47] R. W. Jenkins, R. Thummalapalli, J. Carter, I. Cañadas, and D. A. Barbie, “Molecular and Genomic Determinants of Response to Immune Checkpoint Inhibition in Cancer,” *Annu. Rev. Med.*, vol. 69, no. 1, pp. 333–347, 2018.
- [48] L. Galluzzi, C. Vanpouille-Box, S. F. Bakhoun, and S. Demaria, “SnapShot: CGAS-STING Signaling,” *Cell*, vol. 173, no. 1, pp. 276–276.e1, 2018.
- [49] R. G. Crystal, S. H. Randell, J. F. Engelhardt, J. Voynow, and M. E. Sunday, “Airway epithelial cells: Current concepts and challenges,” *Proc. Am. Thorac. Soc.*, vol. 5, no. 7, pp. 772–777, 2008.
- [50] K. C. Valkenburg, A. E. De Groot, and K. J. Pienta, “Targeting the tumour stroma to improve cancer therapy,” *Nat. Rev. Clin. Oncol.*, vol. 15, no. 6, pp. 366–381, 2018.
- [51] M. Binnewies *et al.*, “Understanding the tumor immune microenvironment (TIME) for effective therapy,” *Nat. Med.*, vol. 24, no. 5, pp. 541–550, 2018.
- [52] M. J. Smyth, S. F. Ngiew, A. Ribas, and M. W. L. Teng, “Combination cancer immunotherapies tailored to the tumour microenvironment,” *Nat. Rev. Clin. Oncol.*, vol. 13, no. 3, pp. 143–158, 2016.
- [53] Y. Huang, B. Y. S. Kim, C. K. Chan, S. M. Hahn, I. L. Weissman, and W. Jiang, “Improving immune–vascular crosstalk for cancer immunotherapy,” *Nat. Rev. Immunol.*, vol. 18, p. 195, Jan. 2018.
- [54] D. Hanahan and R. A. Weinberg, “The hallmarks of cancer.,” *Cell*, vol. 100, no. 1, pp. 57–70, Jan. 2000.
- [55] and Z. W. Pengfei Lu, Valerie M. Weaver, “The extracellular matrix: A dynamic niche in cancer progression,” *J. Cell Biol.*, vol. 196, no. 4, pp. 395–406, 2012.
- [56] N. K. Altorki *et al.*, “The lung microenvironment: an important regulator of tumour growth and metastasis,” *Nat. Rev. Cancer*, vol. 19, no. 1, pp. 9–31, 2019.
- [57] H. Salmon *et al.*, “Matrix architecture defines the preferential localization and migration of T cells into the stroma of human lung tumors,” *J. Clin. Invest.*, vol. 122, no. 3, pp. 899–910, 2012.
- [58] S. Maman and I. P. Witz, “A history of exploring cancer in context,” *Nat. Rev. Cancer*, vol. 18, no. 6, pp. 359–376, 2018.
- [59] W. T. Iams, J. Porter, and L. Horn, “Immunotherapeutic approaches for small-cell lung cancer,” *Nat. Rev. Clin. Oncol.*, vol. 17, no. May, 2020.
- [60] D. Konar, M. Devarasetty, D. V. Yildiz, A. Atala, and S. V. Murphy, “Lung-On-A-Chip Technologies for Disease Modeling and Drug Development,” *Biomed. Eng. Comput. Biol.*, vol. 7s1, p. BECB.S34252, 2016.
- [61] J. Choi, E. Iich, and J. H. Lee, “Organogenesis of adult lung in a dish: Differentiation, disease and therapy,” *Dev. Biol.*, vol. 420, no. 2, pp. 278–286, 2016.
- [62] A. Sontheimer-Phelps, B. A. Hassell, and D. E. Ingber, “Modelling cancer in microfluidic human organs-on-chips,” *Nat. Rev. Cancer*, vol. 19, no. 2, pp. 65–81, 2019.
- [63] A. R. W. Michael J. Whitecutt, Kenneth B. Adler, “A biphasic chamber system for maintaining polarity of differentiation of cultured respiratory tract epithelial cells,” *Vitr. Cell. Dev. Biol.*, vol. 24, no. 5, 1988.
- [64] S. H. Randell, M. L. Fulcher, W. O’Neal, and J. C. Olsen, “Primary epithelial cell models for cystic fibrosis research.,” *Methods Mol. Biol.*, vol. 742, pp. 285–310, 2011.
- [65] A. P. Wong *et al.*, “Directed differentiation of human pluripotent stem cells into mature airway epithelia expressing functional CFTR protein,” *Nat. Biotechnol.*, vol. 30, no. 9, pp. 876–882, 2012.
- [66] S. Konishi *et al.*, “Directed Induction of Functional Multi-ciliated Cells in Proximal Airway Epithelial Spheroids from Human Pluripotent Stem Cells,” *Stem Cell Reports*, vol. 6, no. 1, pp. 18–25, 2016.
- [67] L. D. S. and J. R. S. Alyssa J. Miller, Briana R. Dye, Daysha Ferrer-Torres, David R. Hill, Arend W. Overeem, “Generation of lung organoids from human pluripotent stem cells in vitro,” *Nat. Protoc.*, vol. 14, no. 11, pp. 3082–3100, 2019.
- [68] R. Shi *et al.*, “Organoid cultures as preclinical models of non-small cell lung cancer,” *Clin. Cancer Res.*, vol. 26, no. 5, pp. 1162–1174, 2020.

- [69] M. Kimura *et al.*, “Analysis of ERBB ligand-induced resistance mechanism to crizotinib by primary culture of lung adenocarcinoma with EML4-ALK fusion gene,” *J. Thorac. Oncol.*, vol. 10, no. 3, pp. 527–530, 2015.
- [70] M. Kim *et al.*, “Patient-derived lung cancer organoids as in vitro cancer models for therapeutic screening,” *Nat. Commun.*, vol. 10, no. 1, 2019.
- [71] D. E. I. Dongeun Huh, Benjamin D. Matthews, Akiko Mammoto, Martín Montoya-Zavala, Hong Yuan Hsin, “Reconstituting Organ-Level Lung function on a chip,” *Science (80-.)*, no. June, pp. 1662–1668, 2010.
- [72] D. Huh *et al.*, “Microfabrication of human organs-on-chips,” *Nat. Protoc.*, vol. 8, no. 11, pp. 2135–57, 2013.
- [73] B. A. Hassell *et al.*, “Human Organ Chip Models Recapitulate Orthotopic Lung Cancer Growth, Therapeutic Responses, and Tumor Dormancy In Vitro,” *Cell Rep.*, vol. 21, no. 2, pp. 508–516, 2017.
- [74] A. Sobrino *et al.*, “3D microtumors in vitro supported by perfused vascular networks,” *Sci. Rep.*, vol. 6, no. August, pp. 1–11, 2016.
- [75] J. Schindelin *et al.*, “Fiji: An open-source platform for biological-image analysis,” *Nat. Methods*, vol. 9, no. 7, pp. 676–682, 2012.
- [76] Campisi, Marco Shriram K. Sundararaman, Sarah E. Shelton, Erik H. Knelson, Navin R. Mahadevan, Ryohei Yoshida, Tetsuo Tani, Elena Ivanova, Israel Cañadas, Tatsuya Osaki, Sharon Wei Ling Lee, Tran Thai, Saemi Han, Brandon P. Piel, Sean Gilhooley, Cloud P., S. K. Roger D Kamm, and D. A. Barbie, “Tumor-Derived cGAMP Regulates Activation of the Vasculature,” *Front. Immunol.*, vol. 11, no. September, pp. 1–16, 2020.
- [77] C. J. Nicolai *et al.*, “NK cells mediate clearance of CD8+ T cell-resistant tumors in response to STING agonist,” *Sci. Immunol.*, vol. 5, no. 45, pp. 1–14, 2020.
- [78] Y. Zhou *et al.*, “Blockade of the Phagocytic Receptor MerTK on Tumor-Associated Macrophages Enhances P2X7R-Dependent STING Activation by Tumor-Derived cGAMP,” *Immunity*, vol. 52, no. 2, pp. 357-373.e9, 2020.
- [79] O. Demaria *et al.*, “STING activation of tumor endothelial cells initiates spontaneous and therapeutic antitumor immunity,” *Proc. Natl. Acad. Sci. U. S. A.*, vol. 112, no. 50, pp. 15408–15413, 2015.
- [80] R. W. Jenkins *et al.*, “Ex vivo profiling of PD-1 blockade using organotypic tumor spheroids,” *Cancer Discov.*, vol. 8, no. 2, pp. 196–215, 2018.
- [81] H. M. Amin and R. Lai, “Pathobiology of ALK+ anaplastic large-cell lymphoma,” *Blood*, vol. 110, no. 7, pp. 2259–2267, 2007.
- [82] V. R. Holla *et al.*, “ALK: a tyrosine kinase target for cancer therapy,” *Mol. Case Stud.*, vol. 3, no. 1, p. a001115, 2017.
- [83] R. Chiarle, C. Voena, C. Ambrogio, R. Piva, and G. Inghirami, “The anaplastic lymphoma kinase in the pathogenesis of cancer,” *Nat. Rev. Cancer*, vol. 8, no. 1, pp. 11–23, 2008.
- [84] N. Tsuyama, K. Sakamoto, S. Sakata, A. Dobashi, and K. Takeuchi, “Anaplastic large cell lymphoma: pathology, genetics, and clinical aspects,” *J. Clin. Exp. Hematop.*, vol. 57, no. 3, pp. 120–142, 2017.
- [85] K. Kourentzi *et al.*, “Recombinant expression, characterization, and quantification in human cancer cell lines of the Anaplastic Large-Cell Lymphoma-characteristic NPM-ALK fusion protein,” *Sci. Rep.*, vol. 10, no. 1, pp. 1–7, 2020.
- [86] A. Aubry, S. Galiacy, and M. Allouche, “Targeting ALK in cancer: Therapeutic potential of proapoptotic peptides,” *Cancers (Basel)*, vol. 11, no. 3, 2019.
- [87] D. Fiore, L. V. Cappelli, A. Broccoli, P. L. Zinzani, W. C. Chan, and G. Inghirami, “Peripheral T cell lymphomas: from the bench to the clinic,” *Nat. Rev. Cancer*, vol. 20, no. 6, pp. 323–342, 2020.
- [88] S. S. Rajan *et al.*, “The mechanism of cancer drug addiction in ALK-positive T-Cell lymphoma,” *Oncogene*, vol. 39, no. 10, pp. 2103–2117, 2020.

- [89] S. Jalkanen and M. Salmi, “Lymphatic endothelial cells of the lymph node,” *Nat. Rev. Immunol.*, vol. 20, no. 9, pp. 566–578, 2020.
- [90] R. H. Farnsworth, T. Karnezis, S. J. Maciburko, S. N. Mueller, and S. A. Stacker, “The interplay between lymphatic vessels and chemokines,” *Front. Immunol.*, vol. 10, no. APR, pp. 1–14, 2019.
- [91] J. Settleman, “Cell Culture Modeling of Genotype-Directed Sensitivity to Selective Kinase Inhibitors: Targeting the Anaplastic Lymphoma Kinase (ALK),” *Semin. Oncol.*, vol. 36, no. SUPPL. 1, pp. S36–S41, 2009.
- [92] Z. Zhang, H. Shiratsuchi, N. Palanisamy, S. Nagrath, and N. Ramnath, “Expanded Circulating Tumor Cells from a Patient with ALK-Positive Lung Cancer Present with EML4-ALK Rearrangement Along with Resistance Mutation and Enable Drug Sensitivity Testing: A Case Study,” *J. Thorac. Oncol.*, vol. 12, no. 2, pp. 397–402, 2017.
- [93] A. Purwada *et al.*, “Ex vivo engineered immune organoids for controlled germinal center reactions,” *Biomaterials*, vol. 63, pp. 24–34, 2015.
- [94] A. Purwada and A. Singh, “Immuno-engineered organoids for regulating the kinetics of B-cell development and antibody production,” *Nat. Protoc.*, vol. 12, no. 1, pp. 168–182, 2017.
- [95] J. D. Greenlee and M. R. King, “Engineered fluidic systems to understand lymphatic cancer metastasis,” *Biomicrofluidics*, vol. 14, no. 1, 2020.
- [96] M. Campisi, C. Voena, I. Mota, E. Patrucco, R. D. Kamm, and R. Chiarle, “Abstract PO-17: Microphysiologic model of ALK+ anaplastic large cell lymphoma and vascular interactions predicts drug efficacy in a 3D microfluidic chip,” *Blood Cancer Discov.*, vol. 1, no. 3 Supplement, p. PO-17 LP-PO-17, Nov. 2020.

Section IV

Bioartificial polymer nanoparticles for synthetic oligonucleotide release in the tumor microenvironment

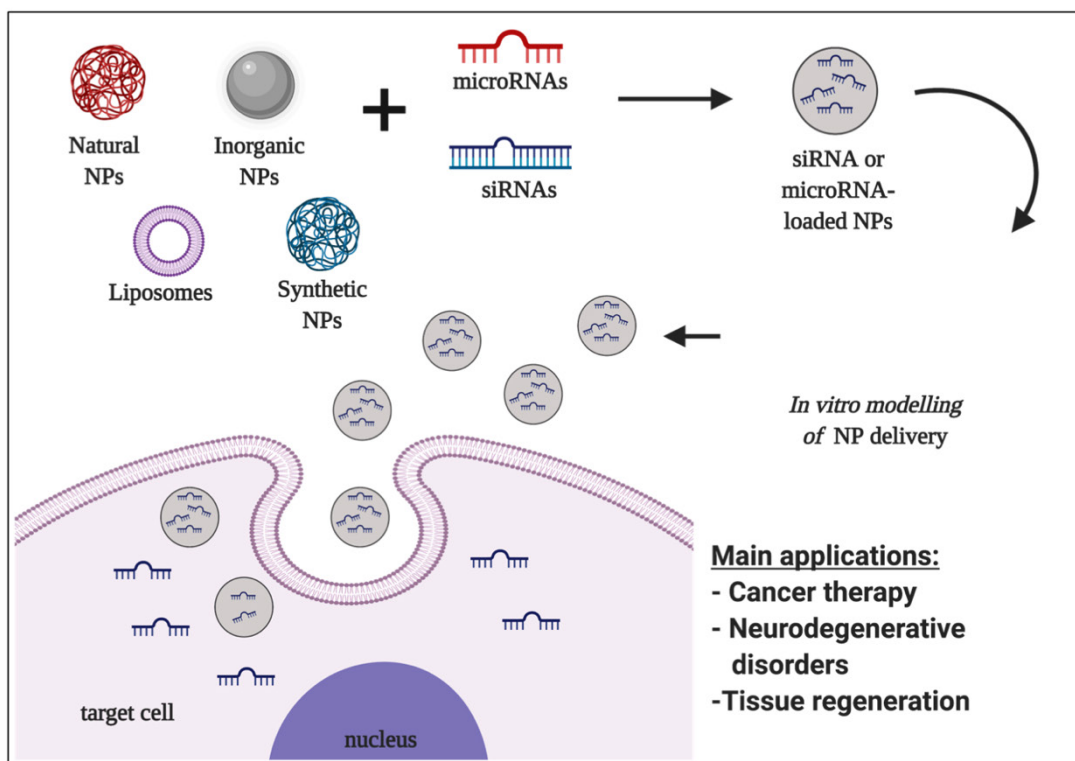
Chapter 8 – *Nanocarriers as delivery systems for oligonucleotide release*

Abstract

Oligonucleotides are becoming of interest in the scientific community due to their central role in the etiology of major diseases and their emerging role in therapeutic applications such as gene silencing, activation and editing. However, their lack of stability in physiological fluids, the existence of a multitude of biological barriers and the poor penetration into cells remain the major limitations for a successful clinical translation of oligonucleotides. On the other hand, engineered delivery systems, such as lipid-based and polymer-based nanoparticles, offer unprecedented opportunities for cell-specific and controlled delivery of oligonucleotides for therapeutic purposes. In chapter 8, different oligonucleotides are introduced, including antisense oligonucleotides, small interfering RNAs (siRNA) and microRNAs (miRNA). Next, the design of viral and non-viral delivery systems is described, focusing on polymer-based (synthetic and natural polymers) and lipid-based nanoparticles, including their production processes.

A perspective on the design and characterization of nanoparticles is presented to accelerate the translation of basic research into clinical application of miRNA- and siRNA-delivery systems.

Potential opportunities, current challenges and future perspectives on the design principles of delivery systems and the engineering of siRNA and miRNA-loaded nanoparticles for oligonucleotide release are discussed, and key application examples are highlighted to underline their therapeutic potential for effective and personalized nanomedicine.



Graphical abstract 9: *Nanoparticles as delivery systems for oligonucleotide release.*

Schematic created with biorender.com

Part of the work described in this chapter has been previously published in:

<https://doi.org/10.1016/j.jconrel.2019.10.007>

“MicroRNA delivery through nanoparticles” Journal of Controlled Release, 2019.

Sharon Wei Ling Lee, Camilla Paoletti, **Marco Campisi**, Tatsuya Osaki Giulia Adriani, Roger D. Kamm, Clara Mattu, Valeria Chiono.

Introduction

Oligonucleotide as therapeutic strategies

Oligonucleotides are polymers of nucleic acid with the potential to treat or manage a wide range of diseases. Focusing on gene silencing, splice modulation and gene activation, oligonucleotides expand the range of possible targets beyond what is generally accessible to conventional drugs[1]. Most oligonucleotide modalities interact with prevent protein translation of certain messenger RNA strands by binding to them, in a process called hybridization[2].

The antisense oligonucleotides can be used to target a specific complementary (coding or non-coding) RNA. If binding occurs, this hybrid can be degraded by an enzyme called RNase H, which hydrolyzes RNA, resulting in 80-95% down-regulation of mRNA expression[3]. The use of oligonucleotides allows for precision and/or personalized medicine approaches, as they can, theoretically, be designed to selectively target any gene [4]. Furthermore, it is possible to target patient-specific sequences or specific alleles that are causative of rare diseases. In addition to their ability to recognize specific target sequences via complementary base pairing, nucleic acids can also interact with proteins through the formation of secondary three-dimensional structures[5].

Although the enormous potential applications are quite intriguing for the treatment of many genetic diseases, the main limitation in preventing the use of oligonucleotide therapeutics is the difficulty in achieving an efficient delivery to target organs and tissues other than the liver. Moreover, off-target interactions[6], [7], sequence and chemical-dependent toxicity and saturation of endogenous RNA processing pathways should also be carefully considered[8].

There are several oligonucleotide-based platforms: antisense oligonucleotides, small interfering RNAs and microRNAs.

Antisense oligonucleotides (ASOs) are small (~18–30 nucleotides), synthetic single-stranded nucleic acid polymers that modulate gene expression through several mechanisms: such as blocking translation and acting with RNase H or steric block [1].

The antisense oligonucleotides bind to their mRNA transcripts and catalyzes the degradation of RNA by the RNase H, causing cleavage at the ASO binding site results in the destruction of the target RNA, thus silencing the target gene expression. Steric block oligonucleotides are ASOs designed to bind target transcripts with high affinity, but do not induce target transcript degradation

by RNase H. Instead, they can mask specific sequences within a target transcript, thereby interfering with transcript RNA–RNA and/or RNA–protein interactions [9].

Small interfering RNAs (siRNAs) are double-stranded RNA consisting of a duplex of two 21-nucleotide RNA molecules with 19 complementary bases (base pairs) and 2 terminal nucleotides [1][10]. As a non-coding RNA, siRNA consists of two strands: 1) the guide or antisense strand that is complementary to a target, and 2) passenger or sense strand. siRNAs are recognized by action of the Argonaute 2 protein that degrades the sense strand as part of the RNA-induced silencing complex. The guide siRNA binds completely to mRNA with perfect complementarity causing the cleavage of the target opposite position, leading to gene silencing[11].

microRNAs (miRNAs) are small single-stranded non-coding endogenous RNAs and their final form consists of triggers that have been implicated in a multitude of physiological and pathophysiological processes[12]. miRNAs are composed of short sequences of nucleotides, 20–24 nucleotides, which act in the post-transcriptional regulation of gene expression [13]. In contrast to siRNAs, miRNAs usually bind with partial complementarity and induce silencing via slicer-independent mechanisms[1].

Design principles of bioartificial nanocarriers

Achieving effective delivery of oligonucleotide therapeutics remains a major translational challenge. Oligonucleotides are typically large hydrophilic polyanions that do not readily pass through the plasma membrane (molecular weight of single-stranded ASOs is ~4–10 kDa, for double-stranded siRNAs and miRNAs is ~14-20 kDa) [1].

There are several key challenges in delivering naked oligonucleotides *in vivo*. When injected systemically, naked oligonucleotides are rapidly degraded by nucleases present in the blood, cleared quickly via renal excretion, leading to a short half-life in the systemic circulation[14]. Oligonucleotides must overcome multiple barriers, such as the vascular endothelium to reach their cellular target. Even there, ‘naked’ oligonucleotides are characterized by poor cellular uptake due to negatively charged groups of oligonucleotides, undesirable off-target or on-target effects[15], [16]. (Fig. 4.1a).

Beside strategies of local delivery and chemical modifications of oligonucleotide, a research area that has gained increasing interest is the design of delivery vehicles, with the ability to maintain the stability and integrity of oligonucleotides in circulation, achieving a long-lasting therapeutic

efficacy[15]. An effective delivery system must successfully overcome the above-mentioned barriers to reach the site of action and access the biological targets. The requirements for effective delivery platforms are low cytotoxicity and high transfection efficiency, biocompatibility, non-immunogenicity, biodegradability and ability to deliver the payload to a specific tissue or organ in a local and sustained manner[17][18]. (Fig. 4.1b).

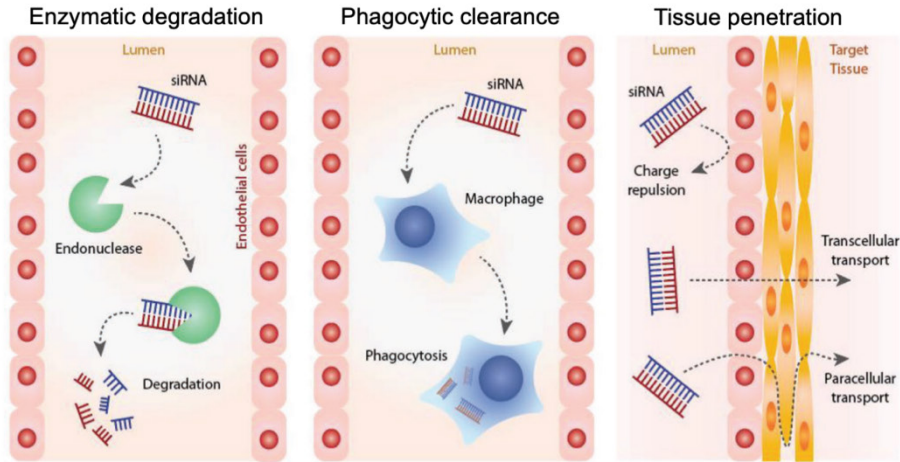
Numerous systems have been engineered, such as viral and non-viral vectors for oligonucleotides delivery [19]. (Fig. 4.2a). Several viral vectors, such as retrovirus, adenoviruses, lentiviruses and adeno-associated viruses have been used to deliver oligonucleotides efficiently into cells[20][21]. The vectors encoding small nuclear RNAs were engineered to shuttle antisense sequences into cells, allowing appropriate subcellular localization. The advantages of using viral vectors are their natural capability to enter the cells and express their own proteins, as well as their high transduction efficiency and sustained transgene expression, making them attractive for the delivery of oligonucleotides *in vitro* and *in vivo* [22]. However, the use of viruses in gene therapy may be limited by some factors. First, they present a low risk of genomic insertions that might lead to tumorigenesis. Second, viruses might cause immune and inflammatory responses. Lastly, viral vectors are difficult to scale up compared with non-viral vectors with low loading capacity and quality control[23].

The limitations of viral vectors in clinical applications have led to the evaluation and development of alternative vectors based on non-viral carriers. Inorganic, polymer and lipid nanoparticles (NPs) as delivery systems of oligonucleotides demonstrated that non-viral carriers can also achieve clinically relevant efficiency with rational design and suitable modifications. These delivery systems reduce the degradation of miRNAs by nucleases and increase their half-life in the blood, can escape endosomal and/or lysosomal degradation, and deliver miRNAs to the cytoplasm or nuclei [19].

NPs encapsulate oligonucleotides, thus i) shielding their charged groups and allowing their uptake by cells, ii) increasing their half-life by protecting the payload from degradation. The functionalization of NPs with cell-specific ligands allows NPs to deliver the payload to specific cells, thereby reducing off-target effects and preventing excessive activation of multiple gene targets [24].

Biological barriers to oligonucleotide therapy

a



b

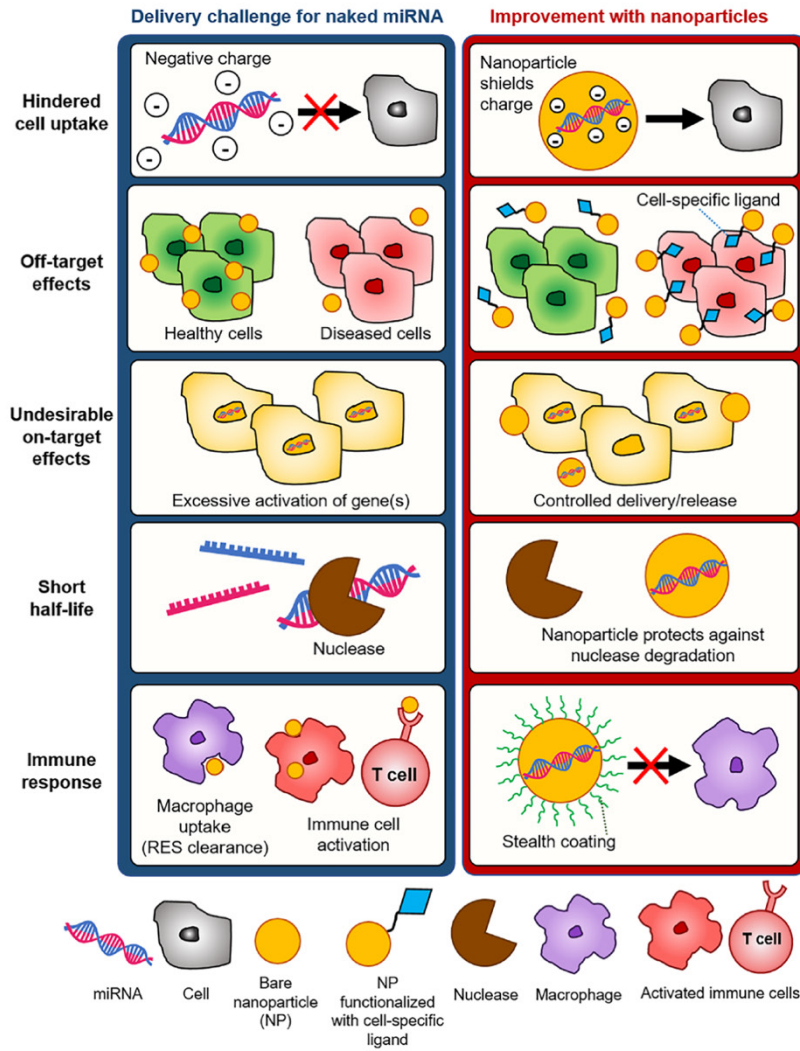


Figure 4.1: Biological barriers and challenges of oligonucleotide (miRNA/siRNA) therapy.

a) Endonucleases degrade siRNA in circulation; clearance by the phagocytic system, in particular the macrophages remove oligonucleotides from circulation. Tissue penetration of siRNA is limited by charge repulsion between the anionic oligonucleotides and vascular barrier that requires specific transcellular and paracellular transport mechanisms. **b)** Key challenges of miRNA delivery in vivo and potential improvements with nanoparticles system delivery. Reproduced with permission from **a)**[25] and **b)** [26].

Lipid-based nanoparticle delivery systems

Phospholipids are the natural components that forms the cellular membrane. Lipid-based nanoparticles, such as liposomes, are able to interact with cells and promote cellular uptake[27], [28]. Due to their relative simplicity, biocompatibility and biodegradability, lipid-based NPs have been widely used as effective carriers of siRNA[29] and miRNA[22] in systemic delivery. LNPs can protect nucleic acids from enzymatic degradation and increase the oligonucleotides circulation half-life [30]. These lipid-NPs are formed with cationic lipids, neutral lipids and PEG-modified lipids, can transport hydrophobic and hydrophilic molecules with low toxicity and prolonged half-life[31]. Spontaneous electrostatic interaction between cationic lipids [32] with negatively charged oligonucleotides results in an efficient packaging, protecting the payload from enzymatic degradation[29]. Also, the positive charge might facilitates the interaction with the opposite-charged cellular membrane[27]. However, the use of cationic lipids might be associated with cell toxicity, as they can disrupt cell membrane integrity, induce cytoplasmic vacuolization, and instability[19], as well as interaction with negatively charged serum proteins which induce aggregation [33], [34]. To overcome these limitations, several strategies to reduce the cationic charge have been attempted. For instance, combination with neutral lipids, such as cholesterol (Chol), dioleoylphosphatidyl ethanolamine (DOPE) and phosphatidylcholine (PC) has been proposed to enhance stability and reduce the toxicity of NPs[28] [35]. Polyethylene glycol (PEG) modifications on the NP surface have also been implemented to increase their half-life. PEGylated cationic/neutral NPs have been used for delivery of miR-122 in hepatocellular carcinoma (HCC), achieving ~ 50% growth suppression after 1 month [35]. Recently, successful tumor inhibitory effects were reported by employing a neutral lipid for the systemic delivery of synthetic miRNA mimics (miR-34a) [36].

A promising system for siRNA delivery consist of a mix of natural and artificially synthesized materials - DLinDMA, DSPC (1,2-distearoyl-sn-glycero-3-phosphocoline), cholesterol and PEG-c-DMA (3-N-[ω -methoxypoly(ethyleneglyol)2000carbamoyl]dimyristyloxy-propylamine). The DLinDMA lipid provides the cationic surface, the DSPC stabilizes the structure and cholesterol stabilizes the function by controlling the slow release, uptake and premature leakage[25].

Polymer-based nanoparticles delivery systems

Polymers represent the most widely used nanomaterial for siRNA and miRNA delivery, after lipids. NPs formed with polymers are colloidal spherical particles of submicron size capable of carrying a therapeutic agent of interest by encapsulation within their material matrix, adsorption or conjugation onto their surface. Moreover, NPs have many advantages, including biocompatibility, the ability to overcome several biological barriers, and the targeting capacity as previously discussed [37], [38]. With the exciting advent of stimuli-responsive biomaterials, multi-functional NPs that change their properties upon modification of external conditions (including temperature or pH) have been developed for an expanding range of therapeutic applications [39][40].

The choice of the nanomaterial that constitutes the NP defines the choice of the preparation technique, as well as the final properties and structure of the NP. The main manufacturing methods for the formation of nanoparticles include solvent evaporation, nanoprecipitation, emulsification and salting out [41], which are briefly described below.

Solvent evaporation: the polymer is dissolved in a volatile organic solvent, such as dichloromethane, chloroform, or ethyl acetate to prepare an emulsion. The emulsion is converted into a NPs suspension on evaporation of the solvent from the polymer, which is allowed to diffuse through the continuous phase of the emulsion[42]. Subsequently, NPs can be ultra-centrifuged and washed with distilled water to remove any additives, such as surfactants, and finally lyophilized. In this most widely used and conventional method, two main strategies are used for the formation of emulsions: the preparation of single-emulsions, e.g., oil-in-water (o/w) by homogenizing or sonicating a polymer solution into an external, surfactant-containing, water phase, or double-emulsions, e.g., (water-in-oil)-in-water, (w/o)/w, typically used to encapsulate hydrophilic payloads[43][44].

Emulsification is a modification of the solvent evaporation method, which is eliminated by evaporation or filtration, according to its boiling point. A water-soluble organic solvent, such as acetone and methanol, is interfaced with an insoluble solvent, such as dichloromethane and chloroform. The spontaneous diffusion of the first in the second creates an interfacial turbulence and the formation of smaller nanocarriers. For instance, emulsion methods have been used to prepare monomethoxy(polyethyleneglycol)-poly(D,L-lactide-co-glycolide)-poly(L-lysine)-lactobionic acid (mPEGPLGA-PLL-LA)[45], PLGA and poly(glycerol adipate-co- ω -pentadecalactone) (PGA-co-PDL) NPs for miRNA delivery[46].

Nanoprecipitation (solvent displacement method) is a widely used method for the preparation of NPs. It consists of the precipitation of a polymer from an organic solution and displacement of the semipolar solvent in an aqueous medium. The rapid diffusion of the solvent in the non-solvent phase results in the decrease of the interfacial tension between the two phases, leading to the formation of small droplets of organic solvent [41][45]. The deposition at the interface between water and organic solvent causes a rapid diffusion of the solvent and formation of a colloidal suspension. A commonly used solvent is acetone, which is miscible with water and easily removed by evaporation[47][20], [48]. For instance, miRNA-loaded PLGA/chitosan (PLGA/CS) NPs with 150–180 nm size have been prepared via the nanoprecipitation method by dropwise addition of PLGA solution into a water solution of CS and miR-34, in the presence of Poloxamer surfactant. This method could achieve miR-34 high entrapment efficiency (EE) between 50% and 95%, depending on the amount of miR-34 in the formulation, and controlled release up to 48 hours [49].

Salting out consists in the separation of a water-miscible solvent from an aqueous solution, by salting out. The polymer and the drug are dissolved in a solvent, such as acetone, then emulsified in an aqueous gel containing a stabilizing colloid and the salting out agent (e.g., magnesium chloride hexahydrate). The fast addition of water to the o/w emulsion under mild stirring reduces the ionic strength and leads to the migration of the water-soluble organic solvent to the aqueous phase inducing nanosphere formation. The salting out agent and the solvent are then eliminated by crossflow filtration or centrifugation [50].

The most frequently used materials in the design of nanosystems for oligonucleotide release are synthetic and natural polymers. Synthetic polymers that are regularly used include poly(lactic co-glycolic acid) (PLGA), poly(ϵ -caprolactone) (PCL) and polyethyleneimine (PEI). While common

natural polymers are chitosan (CS) and hyaluronic acid (HA). These materials are described in the paragraphs below.

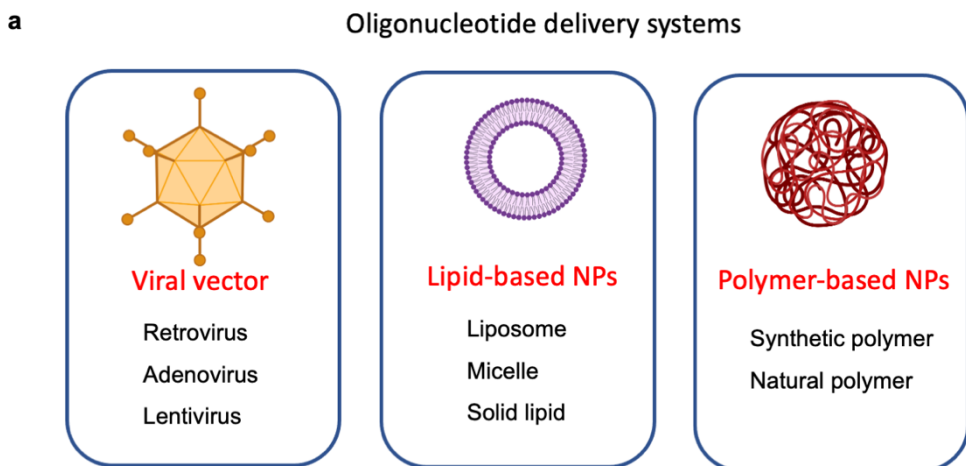


Figure 4.2: Viral and non-viral delivery systems for oligonucleotide release.

a) Viral vectors (retrovirus, adenovirus and lentivirus), lipid-based Nanoparticles (NPs) and polymer-based NPs designed with synthetic and natural polymers. Schematic created with BioRender.com.

Synthetic polymers

Synthetic polymers have been examined as effective carriers for oligonucleotides release due to sustained release of cargo, easy modification and manufacturing.

Polyethylenimine (PEI) is a polycationic polymers with a linear or branched structure, consisting of amine groups and ethylene spacer[51]. PEI chains are positively charged, able to interact electrostatically with the negative charges of the nucleic acids, allowing formation of complexes. The main advantage of the PEI-based delivery system is the rapid uptake and release (so called ‘proton sponge effect’) of the nucleic acid within the cytoplasm through an endocytic mechanism[51]. PEI has been employed to deliver miR-145 and miR-33a allowing the assessment of the *in vivo* anti-tumor activity of these miRNAs in a mouse model of colonic carcinoma[52], miR-145 in metastatic breast cancer[53] and siRNA [54], [55]. However, there are some limitations associated with the PEI delivery system, such as poor biodegradability inside the cell due to its excessive cationic charge, that result in cytotoxicity and prevents clinical application[25]. In this context, several modifications were suggested to reduce the cytotoxicity and enhance the transfection efficiency or targeted delivery of a PEI nanocarrier. Different modifications have been

explored such as polyurethane-short branch polyethylenimine (PU-PEI), the poly(L-lysine)-modified polyethylenimine (PEI-PLL) copolymer, poly(1,8-octanediocitric acid)-co-polyethylene glycol grafted with polyethyleneimine (POCG-PEI) and polylactic-co-glycolic acid (PLGA)/cetylated PEI/hyaluronic acid nanoparticles (PCPH NPs) [19][36]. NPs that are surface-modified or based on blends of PEI and PEG have been proposed to reduce toxicity and improve biodistribution, such as PEI-PEG NPs to deliver miR-145[56].

Poly(lactic-co-glycolic acid) (PLGA) is a biodegradable, biocompatible and FDA approved polyester that has been widely used for drug delivery[57]. PLGA can be hydrolyzed and broken down into non-toxic lactic acid and glycolic acid monomers and subsequently metabolized by the body without any side effect[58]. Because of its ability to sustain therapeutic drug levels for prolonged periods of time and its capability to encapsulate and protect nucleic acids (i.e. miRNA and siRNA) from degradation, PLGA has been used to prepare NPs with high production efficiency and stable mechanical properties [59]. However, one of the few drawbacks associated with PLGA-based drug delivery system of oligonucleotides is the low targeting ability. In fact, the ester groups that compose the repeating units of PLGA have low reactivity. By varying the ratio between the constituent monomers, lactic and glycolic acid, the degradation rate of PLGA NPs can be tuned in the range from several months to years. Moreover, the PLGA-based NPs showed low encapsulation efficiency (<50%) for low molecular weight and hydrophilic molecules [61]. Surface modification of PLGA NPs, such as PEGylation, ligand decoration or functionalization with free carboxyl (COOH) terminals, has been widely adopted to improve the encapsulation efficiency and control pharmacodynamic [57], [62]. PEGylation can reduce the uptake of PLGA NPs by the reticuloendothelial system (RES) improving the circulation time of [63], [64] and enhancing tumor uptake through the enhanced permeability and retention (EPR) effect[65].

Poly(lactic acid) (PLA) is a biocompatible synthetic polyester produced from lactic acid. PEG-conjugated PLA is a promising carrier for drug delivery, including oligonucleotide [66]. In PEG-PLA polymeric micelles, the hydrophilic PEG functions as the shell and hydrophobic PLA works as the core, as shown with mPEG-PLA/PEI and mPEG-PLA/chitosan NPs used for siRNA delivery[67]. Another strategy is fabricating PEG-PLA/siRNA stealth NP systems with the assistance of cationic lipids. By adding the cationic lipid N,N-bis(2-hydroxyethyl)-N-methyl-N-(2-cholesteryloxycarbonyl aminoethyl) ammonium bromide (BHEM-Chol), the siRNA encapsulation efficiency in PEG-PLA NPs was above 90% and the particle diameter was from 170

to 200 nm. In addition, this delivery system presented the ability to down-regulate gene expression in an orthotopic liver tumor model and to inhibit the tumor growth in a MDA-MB-435s xenograft tumor model following systemic administration, suggesting its potential for siRNA delivery in cancer therapy[68].

PCL (poly- ϵ -caprolactone) is a hydrophobic semicrystalline polymer, typically synthesized from the ring-opening polymerization of ϵ -caprolactone[69]. PCL is soluble in a large variety of organic solvents, and capable of forming miscible blends with a wide range of polymer. PCL nanoparticles can be prepared with nanoprecipitation, solvent displacement or solvent evaporation techniques. PCL has attracted high attention for the preparation of biocompatible NPs for nucleic acid delivery[26]. NPs composed of PCL are promising for their high colloidal stability, rapid cellular uptake, low *in vitro* and *in vivo* toxicity, and controlled release of their drug cargo. The degradation product of PCL is 6-hydroxyhexanoic acid, which is a natural metabolite in the human body[70]. An example is the PEG-peptide-PCL NPs obtained by the double emulsion method to codeliver miR-200c and docetaxel[71].

Natural Polymers

Natural polymeric NPs have proven to be effective in stabilizing and protecting oligonucleotides from degradation. Natural polymer-based NPs enhanced the therapeutic efficacy as a result of prolonged systemic circulation, cellular uptake, and targeted drug delivery[72].

Chitosan (CS) is obtained by alkaline deacetylation of chitin and is one of the most promising natural polymers for nucleic acids release[72] [73]. It is a linear, biodegradable, biocompatible, non-cytotoxic, non-immunogenic cationic polysaccharide consisting of D-glucosamine and N-acetyl-D-glucosamine units linked via (1–4) glycosidic bonds[74], [75]. At acidic pH (below pH 6), the protonated amino groups of CS rapidly interact with opposite charged molecules, resulting in the formation of polyelectrolyte complexes with negatively charged nucleotides. This property led to the extensive use of chitosan for nucleic acid delivery, such as siRNA or miRNA with high loading efficiency[72]. For example, self-assembled CS-miRNA complexes were prepared using CS with a different degree of acetylation and molecular weight. The average particle diameter of the complexes was <200 nm, which is suitable for uptake by endocytosis to release miRNA-145 to MCF-7 breast cancer cells [76] [77]. However, at physiological pH the charge of CS is reduced,

leading to reduced efficacy of complexation and interaction with serum proteins; this stability issue can represent a major problem for gene silencing *in vivo* upon systemic delivery[77], [78][72]. Moreover, CS NPs offer limited control over the delivery of nucleic acids because of their strong interaction with the loaded agent [74], which results in inefficient unpacking of the complex in the cytoplasm [79]. To overcome these drawbacks, hydrophobic moieties have been conjugated to CS to weaken the polymer/nucleic acid interaction and enhance cytoplasmic drug delivery. Lipid chains or negatively charged polymers, such as PLGA, have also been combined with CS to facilitate miRNA release[80], [81]. PEG grafting is another strategy that has been widely used to improve the physicochemical characteristics of chitosan-based NPs in a medium containing serum [82]–[84], resulting in prevented aggregation of chitosan–siRNA complexes, increased steric stabilization, and reduced nonspecific interactions with serum proteins [72] [84]–[86].

Furthermore, chitosan has often been used in combination with PLGA NPs to modify the charge of PLGA surface, improve targeting effects and facilitate miRNA and siRNA release[72]–[77], [79]. Other strategies to improve CS interaction with nucleic acids include thiolation, aminomethylation, cholesterol conjugation, ligand targeting and acylation[87].

Hyaluronic acid (HA) is a hydrophilic anionic water-soluble natural polysaccharide, which can be recognized and internalized by cells through the CD44 receptors on their surface [88][89]. HA is approved by the FDA for the treatment of osteoarthritis [72]. It is a non-immunogenic, biodegradable and biocompatible polymer, with multiple functional groups for different possible conjugations. Due to its chemical versatility, HA has been extensively used to prepare NPs for the delivery of several drugs, including oligonucleotides[72]. Covalent grafting of HA to cationic polymers or lipids has been proposed to release oligonucleotides. Several researchers have proposed surface modification with HA to mask the positive charge of cationic NPs, to reduce the elimination rate and toxicity [90]. For this purpose, HA has been electrostatically attached to the surface of positively charged liposomes[90], [91] and calcium phosphate NPs, as well as chemically bound to lipids or synthetic polymers. For example, HA chemically linked to PEI and PEG has been used to release miRNA and DOX [92], [93] as well as siRNA[94], [95], [96]. Moreover, HA-decorated NPs were designed to deliver anti-KRAS siRNA to colorectal cancer cell models, via CD44-HA interactions, leading to suppression of unregulated tumor growth. Likewise, HA-NPs were used to deliver miR-145 to colon cancer cells by targeting the CD44 receptors, suggesting the potential therapeutic success of utilizing such NPs in the clinic [26]. As

mentioned before, siRNA/HA complexes are harder to construct because of the electrostatic repulsion between negatively charged macromolecules, leading to low siRNA loading efficiency and stability issues. HA has been used to overcome the limitation of CS complexes that are prone to aggregation in the presence of serum proteins[97]. The association of siRNA with both CS polycation and HA polyanion is an effective strategy to overcome these problems, where CS ensures a strengthened siRNA binding and promotes endosomal escape, while the HA provides stability and lower protein adsorption [72].

Discussion

The development of therapeutic oligonucleotides for the treatment of genetic diseases holds an immense potential in clinical applications. ASOs and siRNAs share important similarities as drug candidates. Both oligonucleotides are nucleic acids designed to modulate gene expression containing an antisense strand that recognizes a target mRNA. In contrast, the main difference between siRNAs and miRNAs is related to their potential of affecting gene expression: siRNAs inhibit the expression of one specific target mRNA, while miRNAs regulate the expression of multiple mRNAs [1] [99]. Unlike miRNAs, siRNAs bind sequences with perfect or nearly perfect complementarity. Beside their slightly different structures, all oligonucleotide strategies have some limitations that have affected their translation in terms of efficacy, stability, and specificity in body circulation[25]. To maximize the benefits of siRNA and miRNA therapeutics in humans, several challenges still need to be overcome, mainly linked to efficient delivery. One possibility is the use of viral vectors, which have demonstrated promising results[21][100]. In spite of this, several limitations are associated with viral vectors, including carcinogenesis[101] and immunogenicity[102]. To address the issues, new delivery systems have been developed to enhance targeting efficacy and reduce off-target effects of the encapsulated payload[100].

Lipid-based systems are widely used for oligonucleotide release due to their similarity with the cell membrane. However, one common limitation is cell toxicity, since lipids can disrupt integrity of the cell membrane, induce cytoplasmic vacuolization and interact with negatively charged serum proteins, resulting in aggregation [31]. To avoid such issues, conjugation with neutral lipids or polymer can increase their stability and reduce non-specific targeting effects[30].

In addition, nanostructured delivery systems provide unique advantages, such as protection against premature degradation and improved interaction with the biological environment. They also offer the possibility of increasing tissue uptake, extending therapeutic half-life, improving cellular internalization, and facilitating transport to the cytoplasm of target cells[25].

Polyester-based NPs, such as PLGA, PCL and PLA have also been extensively studied for siRNA delivery for their excellent biocompatibility and biodegradability, hydrolysis and enzymatic activity[103]. Polyesters are usually conjugated with positively-charged polymers to promote miRNAs and siRNAs encapsulation and reduce particle aggregation due to electrostatic repulsion. On the other hand, a cationic NP surface can induce non-specific interactions with negatively charged groups of plasma proteins, vessel endothelium and blood cells. These undesirable interactions can make the NPs unstable, alter biodistribution and/or promote clearance *in vivo*. Shielding agents such as PEG are used to prevent non-specific interactions[86]. Moreover, synthetic polymers, in comparison with natural polymers, have the advantage of sustaining the release of the encapsulated therapeutic agent for a period ranging from days to several weeks, but are generally limited by the use of organic solvents and relatively harsher formulation conditions[50][58]. Natural polymers, such as CS and HA have also been used to deliver oligonucleotides due to their properties such as biocompatibility, biodegradability and non-immunogenicity. First, positively charged CS can interact with siRNA and miRNA to form stable complexes. These strong electrostatic interactions help protecting oligonucleotides from degradation, but may also limit their release. Combination between CS or HA with synthetic polymers, such as PLGA or PLA can enhance the release of miRNA and siRNA, by reducing the surface charge.

The establishment of therapeutic delivery systems for the release of oligonucleotide in specific organs or tissues will likely involve more chemical modification, combined with conjugation/complexation strategies that confer predictable pharmacokinetic and pharmacodynamic properties and well-understood mechanisms of action [15]. In this manner, therapeutic applications of oligonucleotide will rapidly evolve to extend the range of possible pharmaceutical targets and provide solutions for unmet clinical needs [2], [32], [104].

Conclusion

Despite its potential in genetic therapies, many challenges are still associated with the clinical use of oligonucleotides such as: low stability and lack of specificity, rapid degradation, low cell uptake and off-target effects[14]. To overcome these limitations, several delivery systems have been engineered. In this chapter, the design of bioartificial systems for oligonucleotide delivery was described, focusing on carriers made of lipids, synthetic and natural polymers.

Furthermore, some of the recent applications of NPs as miRNAs and siRNAs carriers were reviewed and the potential applications that may benefit from miRNA-based therapies were highlighted. The most promising carriers appeared to be those based on lipids and polymers, by virtue of their efficacy and reduced toxicity. Future work should focus on optimizing the design of the nanocarrier, exploring chemical modifications that have not yet been tested and combining the advantages of different polymeric materials to obtain highly efficient and biocompatible hybrid nanosystems. Although many challenges remain, such as safe selection of oligonucleotide sequences and massive production [98][105], [106], further development of oligonucleotide delivery carriers that are simultaneously safe and effective will be decisive for the success of the application of oligonucleotide-based therapies[45].

Chapter 9 - Bioartificial PLGA-Chitosan nanoparticles for miRNA and siRNA release

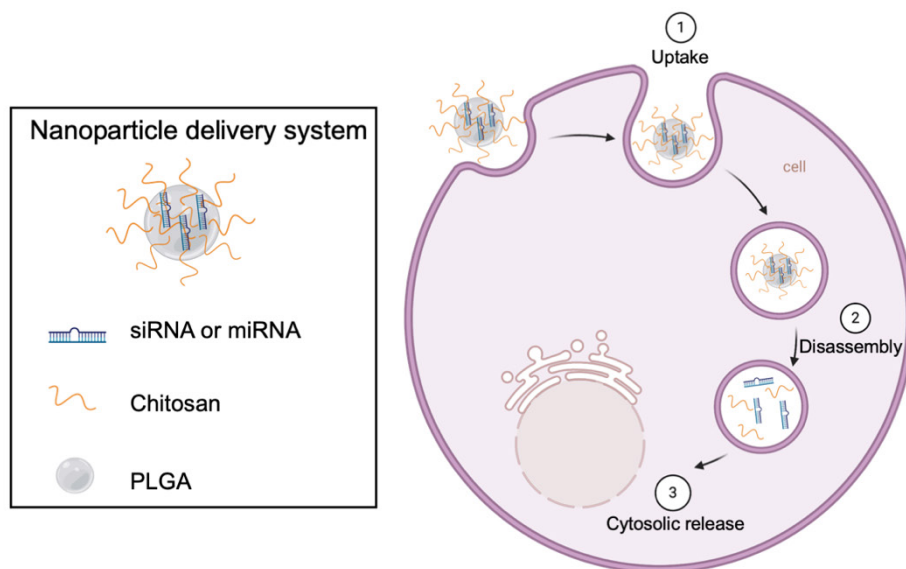
Abstract

Oligonucleotides, including siRNA and miRNA, have enormous potential for the treatment of a number of diseases, including cancer, neurodegenerative diseases and tissue regeneration. However, lack of stability in physiological fluids and poor cell penetration represent two main limitations for their clinical translation.

In this chapter, bioartificial polymeric nanoparticles (NPs) based on chitosan (CS) and poly(lactic-co-glycolic acid) (PLGA) were prepared by nanoprecipitation for oligonucleotide release. As model oligonucleotides, siRNA and miRNA negative controls were encapsulated. CS/miRNA complexes and PLGA/CS/miRNA formulations were prepared with different N:P ratio (ratio between amino groups (N) of CS and phosphate groups (P) of oligonucleotides), by varying the CS amount in each formulation and maintaining miRNA constant. They were characterized for their hydrodynamic size and zeta potential by dynamic light scattering, production yield by gravimetric analysis, entrapment efficiency and oligonucleotide release by fluorometric analysis. Such characterizations allowed to select CS/miRNA complexes formulation with N:P ratio of 8 allowing sufficiently strong interactions for the formation of CS/miRNA complexes without hindering miRNA release. To obtain more stable NPs formulation, PLGA/CS/miRNA NPs were prepared having a hydrodynamic size of around 150 nm (0.1 PDI) and a surface charge increasing from -20 mV to +30 mV as a function of CS amount, efficiently encapsulating ~90% of their cargo. In a second phase of the work, PLGA/CS/miRNA NPs were stabilized by the use of Tween 80 (T) emulsifier, which can help reducing the formation of protein corona, increasing NP stability over time. With the addition of Tween 80, PLGA/CS/miRNA/T formulations were stable with size ranging between 150-250 nm in water and serum-containing media.

Cell viability assay was performed on human umbilical vein endothelial cells (HUVECs) after 24 and 48 h, demonstrating cytocompatibility of PLGA/CS/miRNA NPs, in the range 0.25 - 0.5 mg/ml concentration. Flow cytometry analysis of cells (HEK 293T, HUVEC, COST, Karpas299) treated with NPs encapsulating Fluorescein amidites (FAM)-labelled miRNA or CY3-labelled

siRNA controls revealed high level of transfection efficiency, comparable with lipofectamine-based NPs (LIPO), after 24 h. PLGA/CS/siRNA NPs containing siRNA targeting the anaplastic lymphoma kinase (ALK) showed higher cytotoxicity in COST and Karpas299 compared to LIPO systems. Immunofluorescence analysis also confirmed NPs internalization by HUVECs and HEK 293 T cells. This work showed preliminary evidence that PLGA/CS NPs represent promising candidates for the encapsulation and release of miRNAs and siRNAs needing further investigation with therapeutic payloads in microphysiological systems and preclinical *in vivo* models.



Graphical abstract 10: *Uptake and cytosolic release of bioartificial PLGA-Chitosan nanoparticles for miRNA and siRNA release.*

Schematic created with biorender.com

This work was mainly performed at the Valeria Chiono Laboratory, “the Bioengineering and Biolab laboratories of the Department of Mechanical and Aerospace Engineering (DIMEAS) at Politecnico di Torino”. Some experiments were also performed in Roberto Chiarle Laboratory at the “Center for Experimental Research and Medical Studies (CERMS), University of Torino”, Turin, as part of the collaboration between University of Turin and the Politecnico di Torino, during a research period at CERMS for the doctoral candidate.

The last experiments were performed in David A. Barbie Laboratory at the Dana-Farber Cancer Institute (DFCI), Harvard Medical School, Boston, during an exchange period at DFCI for the doctoral candidate.

Introduction

Oligonucleotides, including siRNA, miRNA and synthetic cyclic dinucleotides, have enormous potential for the treatment of a variety of diseases, including cancer, and neurodegenerative disorders, as well as applications in tissue regeneration [26].

However, several impairments have yet to be overcome, including their lack of stability in physiological fluids, and poor cell penetration, before their effective clinical translation, as discussed [1] [5][107]. In addition, the delivery of oligonucleotides is impaired by many barriers present at different level. One possible strategy is to design nanocarriers, such as polymer nanoparticles (NP), that not only have great potential to improve cellular uptake but also may reduce miRNA- and siRNA-related toxicities, preventing off-target effects and improving pharmacokinetic profiles of miRNA- and siRNA-based therapeutics [108].

Here we designed bioartificial polymeric nanoparticles (NPs) for oligonucleotide encapsulation, based on chitosan (CS) and poly(lactic-co-glycolic acid) (PLGA), prepared by nanoprecipitation. CS is derived from deacetylation of chitin and is one of the most promising natural polymer for nucleic acids release[72], [75]. The positively charged amino groups of CS are able to interact electrostatically with the negatively charged phosphate groups of oligonucleotides (e.g. miRNA, siRNA), forming complexes[77], [78]. PLGA, a biocompatible and biodegradable polymer (FDA-approved) was selected to confer stability to NPs, shielding the payload from degradation, increasing intracellular delivery and reducing cytotoxicity [103][57].

In Chapter 9, evaluation of different ratios between the amino groups (N) in chitosan and the phosphate groups (P) in the oligonucleotides were studied. Moreover, one aim of this study was to determine an optimal N:P ratio that allows sufficiently strong interactions for the formation of CS/miRNA complexes without hindering miRNA release. The physicochemical properties (size, zeta potential) of CS/miRNA complexes were characterized. Then, PLGA was included in the formulation to produce a more stable nanocarrier system.

PLGA/CS/miRNA NPs systems encapsulating miRNA and siRNA were characterized, including morphological studies with scanning electron microscopy (SEM). NPs were further stabilized by the use of Tween 80 (T) emulsifier, which can help reduce the formation of protein corona. Cytotoxicity and transfection efficiency were evaluated using different cellular models: HEK

293T, human umbilical vein endothelial cells (HUVEC) and anaplastic large cell lymphoma cells (ALCL), in particular COST and Karpas299 lines.

Material and methods

Materials and reagents

Poly (D,L-lactide-co-glycolide) acid terminated (PLGA-COOH) 75:25 (MW = 4000-15000 g/mol) was purchased from Sigma Aldrich-USA and Sigma Aldrich-Germany respectively. Chitosan was purchased from Hepe Medical Chitosan (Halle, Germany). NegmiR (miRVana™ miRNA Mimic) and fluorescently labelled miRNA (Ambion mirVana miRNA mimic, FAM-labelled, 4464073), siRNA (Silencer™ Cy™3-labeled Negative Control No. 1, AM4621) siRNA-ALK (Silencer® Pre-designed siRNA, ALK, siRNA ID 147308, Human, 5nmol, AM16708) were purchased from Thermo Fisher and Life Technologies. Milli-Q and deionized water were produced by a Millipore water purification system (Millipore Corporation).

Fabrication process of bioartificial nanoparticles

PLGA/CS nanoparticles formulations were fabricated by nanoprecipitation process [41]. CS was purchased from Hepe Medical Chitosan (Halle, Germany) with a deacetylation degree higher than 92.6% and Mw from 100 kDa to 250 kDa determined by gel permeation chromatography, as previously demonstrated [109]. The CS solution in water (final concentration, 60 µg/mL) was prepared starting from a 3.6% (w/V) CS solution in 0.2 M HCl (Sigma Aldrich, Milan, Italy), by stirring the CS powder in 0.2 M HCl for 24 hours and stored at 4 °C to reach pH ~6.

MiRNAs or siRNAs were stored at -80 °C and thawed on ice, then, 10 µL of miRNAs or siRNAs (100 µM, 1 nmol) were added in the 2.5 mL of CS solution. By keeping the same miRNA amount, the amount of chitosan was varied consequently (CS µg/ml: 5.5, 13.6, 23.5, 38.9, 62.3, 116.8) in order to have the different N:P ratios (0.7; 1.75; 3; 5; 8; 15). The solution was stirred for 15 min to allow CS/miRNA or CS/siRNA complexes formation. 1 mL of 1.5 mg/ml PLGA-COOH (previously reconstituted in acetone) was added dropwise into chitosan solution contained either miRNA or siRNA. PLGA-COOH was included in the blend formulation with a composition rate of PLGA/CS ratios of 99% w/w. After stirring for additional 15 min, NPs solutions were

centrifuged at 4000 rpm for 10-12 min using centrifugal filters (Millipore Sigma Amicon® Ultra-15 Centrifugal Filter Unit, 10 KDa cut-off, #UFC901024). Centrifugation was repeated 3 times adding water to wash NPs. NPs solution was stored at 4 °C until use (Fig. 4.3), obtaining PLGA/CS/miRNA or PLGA/CS/siRNA with a final volume of 1000 μ L.

As control condition, NPs were generated using lipofectamine (Lipofectamine™ 2000 Transfection Reagent, 11668019) (LIPO). Briefly, 1 μ L of miRNA or siRNA (100 μ M, 100 pmol) is diluted in 50 μ L opti-MEM (Opti-MEM™ I Reduced Serum Medium, 11058021), while 1 μ L of lipofectamine (Lipo) is diluted in 50 μ L opti-MEM to 1:1 ratio (oligonucleotide, lipo). After 5 min incubation at room temperature, 100 μ L of LIPO containing miRNA or siRNA are added to cells plated in 6 well plate containing 600 μ L of opti-MEM with a final concentration of 142 nM. Similarly, 100 μ L of PLGA/CS/miRNA or PLGA/CS/siRNA are added to cells plated in 6 well plate containing 600 μ L of opti-MEM with a final concentration of 142 nM.

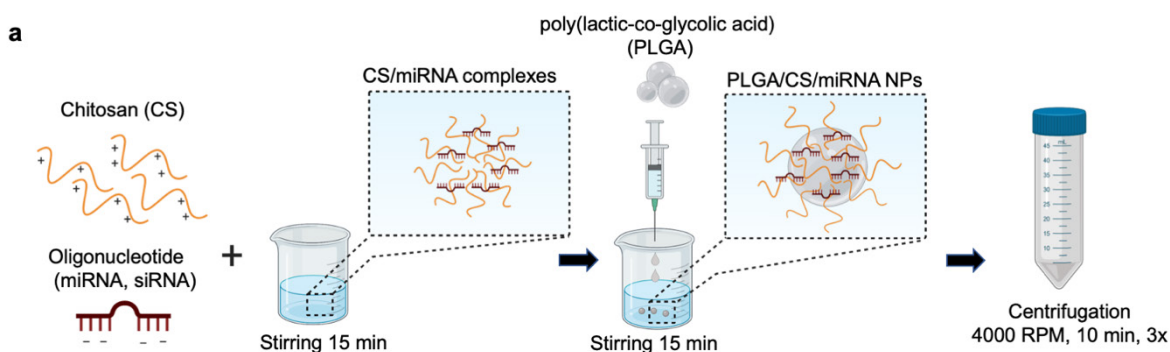


Figure 4.3: Fabrication process of complexes and nanoparticle (NPs) delivery systems.

a) Schematic representation of PLGA/CS complexes and PLGA/CS/miRNA Nanoparticle preparation by nanoprecipitation process Schematic created with Biorender.com.

Size and zeta potential by dynamic light scattering (DLS)

Dynamic Light Scattering (DLS, Litesizer™ 500, Anton Paar, USA) was used to measure NPs dimensions (size), polydispersity index (PDI) and zeta potential. Complexes and NPs stability have been studied in water and DMEM (with FBS). Several different time points were considered for measuring size and zeta potential (day: 0, 1, 3, 5, 7, 9, 14). Complexes and NPs were incubated at 37°C to reproduce the physiological temperature. NPs were analyzed by 3 technical replicate measurements repeated on 3 different batches of NPs.

Morphological characterization: scanning electron microscopy (SEM)

The morphological characterization of the nanoparticles was performed using a Scanning Electron Microscopy (SEM). Before analysis, samples were placed on aluminum stabs and sputter-coated with gold, using an Agar Auto Sputter Coater. The following parameters were fixed: execution time of 50 s with a 30 mA deposition current. The coated samples were then imaged with a scanning electron microscope (LEO 435VP). Samples were analyzed with 1000x, 2000x and 5000x magnification at a working distance of 15 mm and a voltage of 20 kV.

Entrapment efficiency and payload release

Entrapment efficiency (EE) of miRNA in NPs was studied using an Invitrogen Qubit 4 Fluorometer (Thermo Fisher Scientific, US) and its dedicated analysis kit, the Qubit microRNA buffer (Thermo Fisher Scientific, US), used according to manufacturer's protocol. Briefly, 20 μ L of the supernatant from NPs solution were mixed with 180 μ L of the buffer reagent, allowed to react for 5 min, and analyzed. Qubit returns miRNA concentration (ng/mL) in the supernatant (i.e. the non-encapsulated miRNA). The entrapment efficiency was calculated using the following formula:

$$EE (\%) = \frac{(\mu g \text{ miRNA}_{initial} - \mu g \text{ miRNA}_{final})}{\mu g \text{ miRNA}_{initial}} * 100$$

The payload release was evaluated for 14 days. Samples were incubated at 37°C in incubator. For each time point, NPs solutions were centrifuged at 15000 rpm in order to create a pellet and 500 μ L of supernatant was withdrawn and analyzed with Qubit 4 Fluorometer (Thermo Fisher Scientific, US) to study the miRNA released. 500 μ L of deionized water were added to the NPs solution.

Production yield

The production yield was quantified by gravimetric analysis. Briefly, yield is the ratio between the final weight amount of material obtained after freeze-drying process of the NPs over the total

weight amount of starting materials (polymers) employed in the protocol. The Yield (Y) in percentages has been obtained using the following formula:

$$Y(\%) = \frac{\text{Weight NPs}}{\text{Weight materials}} * 100$$

Cell culture

Human umbilical vein endothelial cells, HUVECs (Lonza, C2519AS) were cultured in vascular medium (VascuLife, VEGF Endothelial Medium Complete Kit, #LL-0003) HUVECs were chosen as microvascular barrier model and were previously used 3D Microphysiological models of tumor-vascular interactions in KRAS/LKB1 Non-Small Cell Lung Cancer and ALK+ ALCL (section III, Chapter 6). HEK 293T were cultured in DMEM. HEK 293 T cells were chosen as model for transfections, as previously reported, this cell line is used for lentivirus production after transfection (section III, Chapter 6 and 7, Genetic engineering and CRISPR/Cas9 systems). Anaplastic large cell lymphoma (ALCL) cells COST was kindly provided by Dr. Lamant (Toulouse, France), and Karpas 299 were obtained from DSMZ (German collection of Microorganisms and Cell Cultures), were cultured in RPMI (RPMI-1640 Media, Thermo Fisher 11875093). ALCL were chosen as tumor target cells and were previously used 3D Microphysiological models of ALCL-vascular interactions model (section III, Chapter 7).

Human umbilical vein endothelial cells, HUVECs (Lonza, C2519AS) were cultured in vascular medium (VascuLife, VEGF Endothelial Medium Complete Kit, #LL-0003). HEK 293T were cultured in DMEM. Anaplastic large cell lymphoma (ALCL) cells COST was kindly provided by Dr. Lamant (Toulouse, France), and Karpas 299 were obtained from DSMZ (German collection of Microorganisms and Cell Cultures), were cultured in RPMI (RPMI-1640 Media, Thermo Fisher 11875093).

Cell viability assay

Cell viability assays were performed using the CellTiter-Glo (Promega) according to manufacturer's instructions. Briefly, HUVECs were seeded into white walled 96-well plates (3 wells/sample at a density of 2000 cells/well). After 24h, cells were treated with increasing

concentrations of NPs (0.25, 0.50 mg/mL) and incubated for 24 h and 48 h. CellTiter-Glo reagent was added to each well and luminescence output data were taken at 24 and 48 h from GloMax-Multi Detection System (Promega).

Flow cytometry

293T cells, HUVEC and ALCL cells (COST and Karpas299) were treated with 50 µg/mL of solutions containing PLGA/CS/miRNA and PLGA/CS/siRNA NPs for 24h. siRNA controls were Cyanine-3 (CY3)-labelled (Silencer™ Cy™3-labeled Negative Control No. 1, AM4621) visualized in the R-phycoerythrin (PE) channel, (Excitation-Max 496 nm, Emission-Max 578 nm), and carboxyl fluorescein (FAM)-labelled miRNA (Ambion mirVana miRNA mimic, FAM-labelled, 4464073), visualized in the FITC channel (Excitation-Max 494 nm, Emission-Max 520 nm). After washing with PBS, cells were resuspended in PBS containing 2% FBS and analyzed on a LSRFortessa flow cytometer (Becton Dickinson, Franklin Lakes, NJ). Levels were compared with untreated cells. 20000 events were collected for each sample. Mean fluorescence intensity (MFI) was normalized to untreated controls and quantified. The data analyses were performed with FlowJo software (TreeStar).

Statistical analysis

All data are plotted as mean ± SD. Sample size (n) is equal to 3 technical or biological replicates or otherwise stated. Unpaired student's t-test was used for significance testing between two conditions. One-way ANOVA with pairwise comparisons by the Tukey post-hoc test was used to determine whether three or more data-sets were statistically significant. Statistical analysis was performed using PRISM8 (GraphPad software). P values less than 0.05 were considered significant, **** $P < 0.001$, *** $P < 0.001$, ** $P < 0.01$, * $0.01 < P < 0.05$.

Results

As model oligonucleotides, miRNA (NegmiR, negative control) and siRNA (Cy3-labeled negative Control) were considered for NP design. In this Chapter, initially different CS/miRNA complexes were studied in order to select a range of optimal N:P ratios of amino groups (N) in chitosan to phosphate groups (P) in the oligonucleotides, based on physicochemical characterization (hydrodynamic size, zeta potential) (N:P ratio from 0.7 to 15). Then, stability studies were performed for CS/miRNA complexes with preselected N:P ratios (from 3 to 8) by their incubation in deionized water (unless specified) for different time points (from day 0 to day 14, specified in each experiment). In parallel, PLGA-COOH (referred as PLGA) was included in the blend formulation with a composition rate of PLGA/CS ratios of 99% w/w. PLGA/CS/miRNA NPs with preselected N:P ratios (from 3 to 8) were prepared by simple nanoprecipitation and again physicochemical characterization (hydrodynamic size, zeta potential) was performed, allowing further refinement in the optimal range of N:P ratio (5 and 8). The stability of PLGA/CS/miRNA NPs with such N:P ratios were further characterized for their stability (by their incubation in deionized water and DMEM), encapsulation efficiency, miRNA release kinetics, production yield. Such tests allowed the selection of one optimal PLGA/CS/miRNA formulation.

Finally, dose-dependent biocompatibility and transfection ability were characterized by loading non-conjugated or fluorescently labelled oligonucleotides (FAM-NegmiR and Silencer™ Cy™3-labeled Negative Control). Finally, the problem of NP aggregation in serum containing media was addressed.

Physicochemical characterization of complexes and miRNA-loaded NPs

CS/miRNA and PLGA/CS/miRNA were prepared to encapsulate oligonucleotides (miRNA and siRNA). PLGA/CS NPs were prepared as control (Fig. 4.4a). First, physicochemical properties of CS/miRNA complexes with different N:P ratio (0.7, 1.75, 3, 5, 8, 15, i.e. positive to negative charge ratio) were analyzed. Different N:P ratio were obtained by keeping constant the miRNA amount, by varying the amount of CS. In all these preliminary experiments, CS/miRNA complexes were in deionized water solutions. By progressively adding positively charged CS to the formulation, the size of CS/miRNA complexes increased from 170 ± 11 nm to $450 \pm$ nm and $600 \pm$ nm with increasing N:P ratio from 0.7 to 5. For CS/miRNA complexes with N:P ratio of 8 and 15,

the hydrodynamic size decreased to 270 ± 71 nm and 290 ± 63 nm, respectively. As expected, the zeta potential of CS/miRNA complexes increased as a function of N:P ratio. All zeta potential values ranged between 3 mV for N:P ratio of 0.7 to 35 ± 3 mV for N:P ratio of 15 (Fig. 4.4b, c). Then, the PLGA/CS/miRNA NPs were formed by dropping the same amount of PLGA-COOH solution into the solution containing CS/miRNA complexes. Similarly, the zeta potentials of hydrodynamic size of PLGA/CS/miRNA with different N:P ratio were evaluated. The addition of PLGA-COOH into the solution containing CS/miRNA complexes of several N:P ratio resulted in the formation of NPs with a size between 170 to 270 nm ($PDI < 0.25$), slightly lower than CS/miRNA complexes (Fig. 4.4d). The zeta potential was negative with values of -20 and -2 mV for NPs with 0.7 and 3 N:P ratios, respectively, while it shows positive values for NPs with 5 to 15 N:P ratios (5 to 25 mV). This behavior might be attributed to the progressively higher amount of CS with increasing N:P ratio. Particularly, at low N:P ratio (0.7 to 3), CS amount was probably not enough to cover the entire NP surface or it was encapsulated within PLGA nanoparticles (Fig. 4.4e). At higher N:P ratio, CS coated the NP surface, with a consequent increase in zeta potential, without significantly modifying the final NP size, suggesting that CS/miRNA was present on the surface of the PLGA NPs.

Then, the yield of PLGA/CS/miRNA NPs preparation process was evaluated, calculating the ratio between the final NPs weight over the weight of materials used for NP production (Fig. 4.4f). The yield reached $62 \pm 15\%$ for NPs with N:P ratio of 8, while it was around 38-45% for the other formulations.

NPs with N:P ratio of 0.7 and 1.75 and 15, were not further considered for additional analyses, due to their low zeta potential (N:P ratio of 0.7 and 1.75) or reduced yield (N:P ratio of 15). On the other hand, subsequent analyses were performed on NPs with N:P ratio of 3, 5 and 8, having increasing yield and zeta potential.

Stability studies (in terms of size and zeta potential) of CS/miRNA complexes with N:P ratio of 3, 5 and 8 were then performed up to 9 days (Fig. 4.4g). The samples were incubated at 37°C to reproduce the physiological condition. The aim was to select a formulation with proper N:P ratio, allowing interactions between CS and miRNA to form stable complexes, without affecting miRNA release. CS/miRNA size were unchanged on day 1 for all three complexes. On day 3, CS/miRNA size increased for complexes with N:P ratio of 3 (728 ± 252 nm), exceeding $1 \mu\text{m}$ on day 5-9. Therefore, complexes with N:P ratio of 3 were only stable up to 2 days incubation at 37°C ,

probably due to weak interactions between CS and miRNA. In contrast, complexes with N/P ratio of 5 were stable, showing a size range of 250-430 nm. Complexes with N/P ratio of 8 were also stable up to day 5 (250 nm-470 nm), but their size reached 1.2 μm on day 7-9.

Likewise, complexes with N:P ratio of 3 showed a stable zeta potential for the first three days (16 ± 6 mV), followed by a progressive decrease over time, reaching -6 ± 4 and -10 ± 4 mV after 7 and 9 days, respectively (Fig. 4.4h). Complexes with N:P ratio of 5 and 8 showed a stable zeta potential of around 24 mV which slightly decreased to 12 ± 2 mV after 9 days, remaining positive. In summary, complexes with N:P ratio of 3 were only stable for 2 days. On the other hand, complexes with N:P ratio of 5 and 8 were stable for 9 days and 5 days, respectively. Based on this, complexes with N:P of 5 and 8 were selected for further characterization.

Then, the stability of bioartificial PLGA/CS/miRNA NPs (N:P ratio of 5 and 8) was studied for 14 days, at 37°C. In this case, NP size was ~ 200 nm and appeared stable for up to 3 days. After 5 days, the nanoparticles with N:P ratio of 5 increased in size, reaching a size value of 1.2 ± 0.6 μm , while NPs with N:P ratio of 8 remained stable for up to 5 days (170 ± 28 nm), then their size increased to 1.8 μm at 7 and 14 days (Fig. 4.4i).

For NPs with N:P of 5, zeta potential was positive (20-30 mV) and stable up to 3 days, then it decreased and became negative after 5 days incubation (-4 ± 1.5 mV), and kept constant up to 14 days incubation.

NPs with N:P ratio of 8 showed a positive Zeta potential of 25-38 mV up to 5 days, then decreased and reached a negative zeta potential value of -9 ± 4 mV after 7 days (Fig. 4.4l).

These results suggested that PLGA/CS/miRNA NPs with N:P 5 and 8 probably released CS and miRNA from day 3-7 and day 5-7, respectively, further suggested by the inversion of zeta potential while the size of NPs increases, as data reported in Fig. 4.4i and Fig. 4.4l. Changes in hydrodynamic size and zeta potential in these two-time intervals suggested CS and miRNA release and aggregation phenomena.

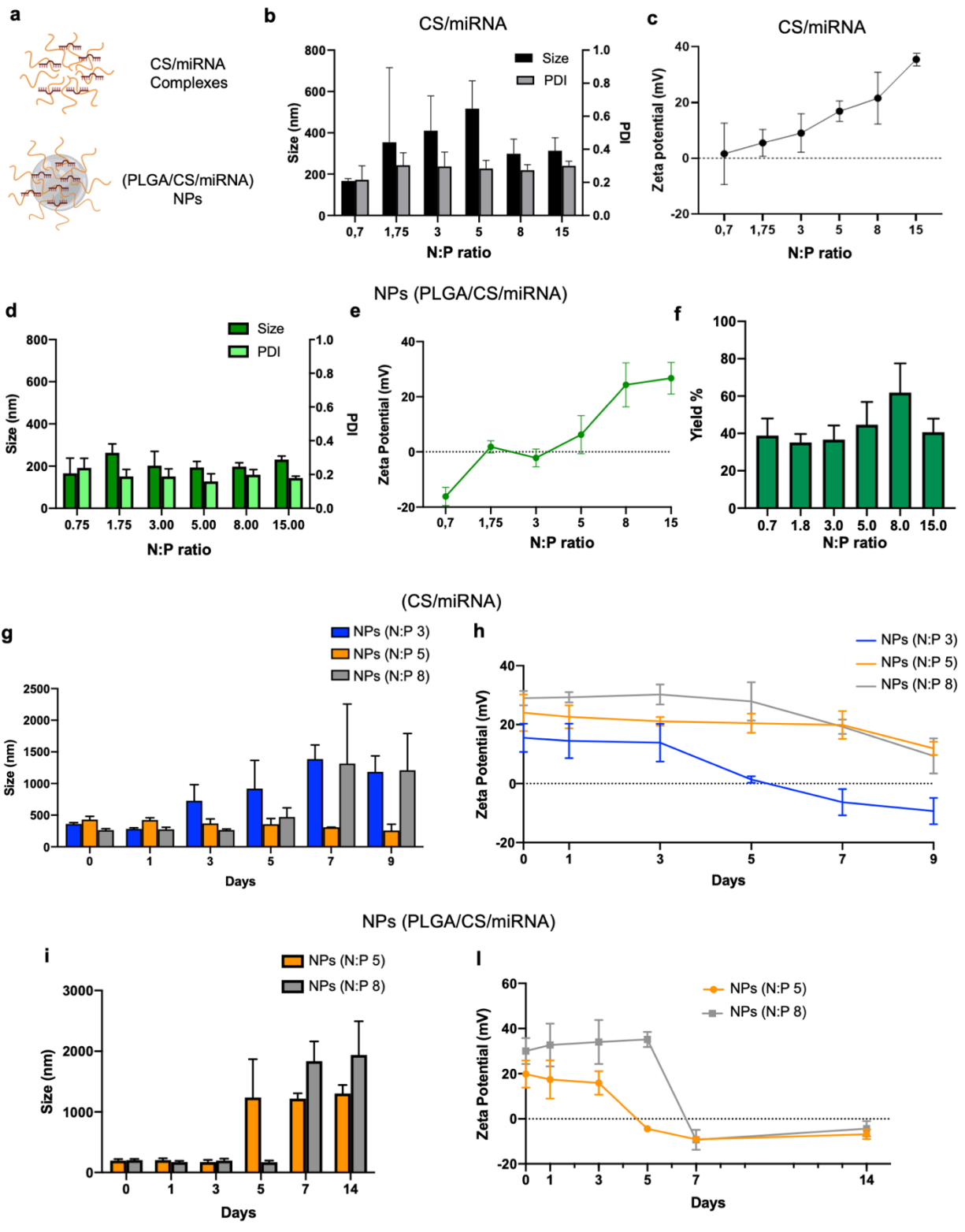


Figure 4.4: Physicochemical characterization of complexes and nanoparticles (NPs).

a) Schematic of chitosan-miRNA (CS/miRNA) complexes and PLGA/CS/miRNA nanoparticles (NPs). **b)** Hydrodynamic size, Polydispersity index (PDI) and **c)** zeta potential of chitosan-miRNA (CS/miRNA) complexes at different ratios of amino groups (N) in chitosan over the phosphate groups (P) in the oligonucleotides (N/P ratio: 0.7, 1.75, 3, 5, 8, 15), N/P ratios at day 0, after preparation. **d)** Hydrodynamic size and PDI, **e)** zeta potential and **f)** yield of the production process of PLGA/CS/miRNA NPs at different N/P ratios: 0.7, 1.75, 3, 5, 8, 15) at day 0. **g)** Hydrodynamic size and **h)** zeta potential of CS/miRNA complexes with different N/P ratios (3, 5, 8) after incubation in deionized water for different days (0, 1, 3, 5, 7, 9) and at 37 °C to study stability. **i)** Hydrodynamic size and **l)** zeta potential of PLGA/CS/miRNA with different N/P ratios (5 and 8) incubated in deionized water for different days (0, 1, 3, 5, 7, 14) at 37 °C, to study their stability.

Entrapment efficiency, payload release and morphological characterization

Entrapment efficiency (EE) of PLGA/CS/miRNA NPs with 5 and 8 N:P ratio efficiently encapsulated ~90% of their cargo. Effective entrapment efficiency can positively influence *in vitro* cell transfection and *in vivo* therapeutic response (Fig. 4.5a).

The release kinetics of miRNA from NPs was studied by incubating them at 37°C in deionized water for different time intervals up to 14 days. At each time step, the supernatant containing the released miRNA was separated from NPs by centrifugation and miRNA was quantified by Qubit fluorometer using miRNA assay kit. Then, the NPs were supplemented with fresh water/medium, resuspended and incubated at 37 °C. The advantage of this method is the low amount of NP samples requested and the simple analytical equipment. NP release study showed that NPs with N:P 8 have a very low release after 2 h and 5 h (< 7%) and no significant release (<10%) after 5 days. The payload release only started to be significant after 7 days, reaching 33±8% at 7 days, 68±5% at 9 days and 70±4 % after 14 days (Fig. 4.5b).

On the contrary, NPs with N:P ratio of 5 did not significant release any amount of entrapped miRNA, showing 11±1% release after 14 days. These results are in agreement with the previous data obtained during the stability study for CS/miRNA complexes and NPs. In fact, although the NPs with N:P ratio of 5 showed instability after 5 days incubation (Fig. 4.4i), their respective complexes remained stable for 9 days (Fig. 4.4g). Therefore, the interaction between CS and miRNA was probably strong and hindered significant miRNA release. On the contrary, NPs with N:P ratio of 8 and their complexes were instable after 7 days incubation (Fig. 4.4i), allowing

miRNA release (Fig. 4.5b). Overall, the performed analyses allowed the selection of PLGA/CS/miRNA with N:P ratio of 8. Morphology of such NPs (N:P ratio of 8) was characterized by SEM, showing their spherical shape, and uniform nanometric size (Fig. 4.4c).

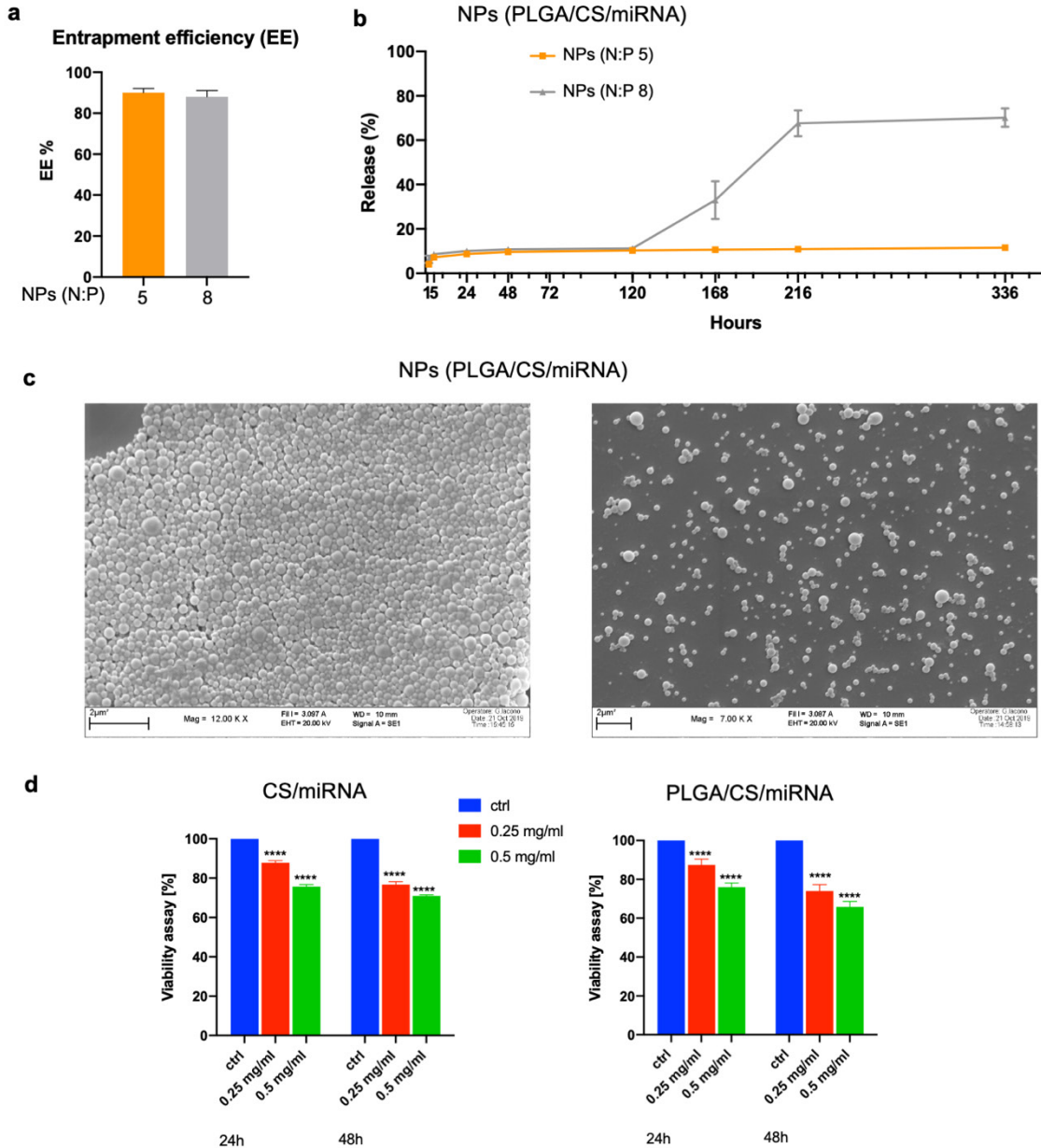


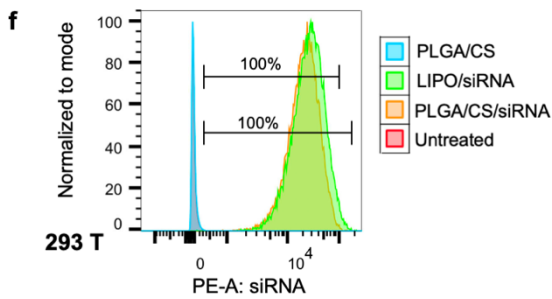
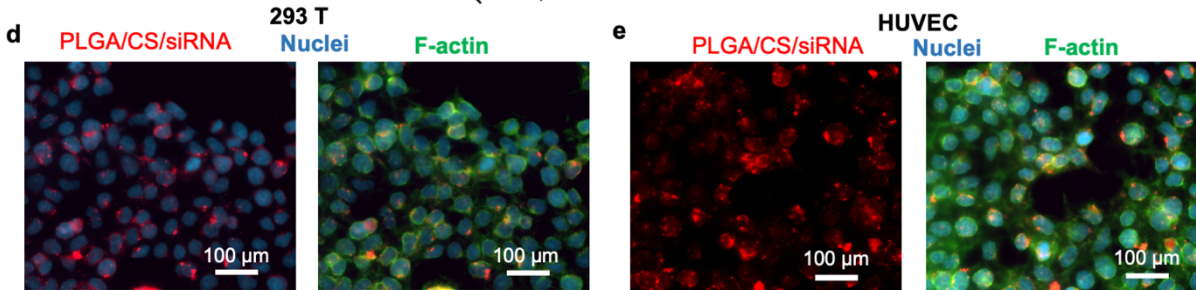
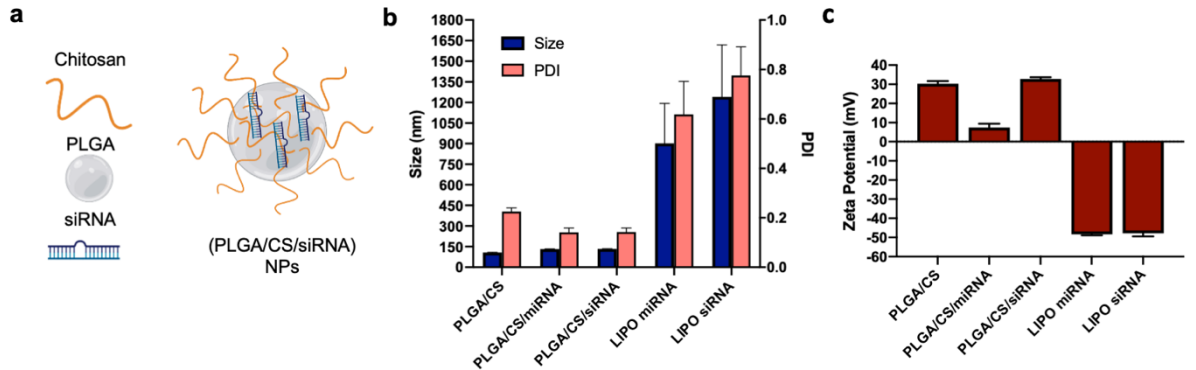
Figure 4.5: Physicochemical and morphological characterization of nanoparticles (NPs) and viability assay.

a) Entrapment efficiency (EE) of miRNA within NPs with different N:P ratios and **b)** percentages of miRNA release over 336 hours (14 days) from NPs with different N:P ratios. **c)** Morphological analysis by scanning electron microscopy (SEM) of PLGA/CS/miRNA NPs at 1000 and 10 µg/mL **d)** Viability assay in 2D culture of HUVECs with 0.0, 0.25 and 0.5 mg/mL of PLGA/CS and PLGA/CS/miRNA NPs after 24 and 48h.

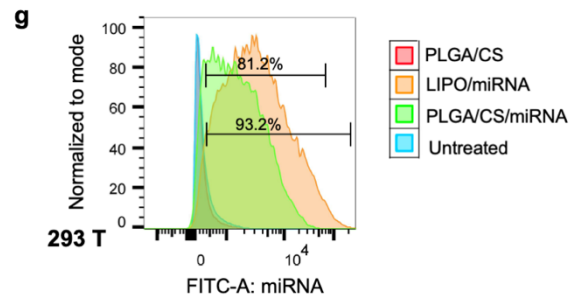
Biological characterization and transfection efficacy of miRNA and siRNA-loaded NPs

To evaluate cellular cytotoxicity and biocompatibility of this delivery system, 2D *in vitro* cell culture tests were performed. The viability assays with HUVECs showed the biocompatibility of PLGA/CS NPs after 24 and 48 h (Fig. 9b). Cell viability slightly decreased in a dose-dependent manner (from 0 to 0.5 mg/mL), but always above 70% viable even at the highest doses (0.5 mg/mL) after 48 h (Fig. 4.5d).

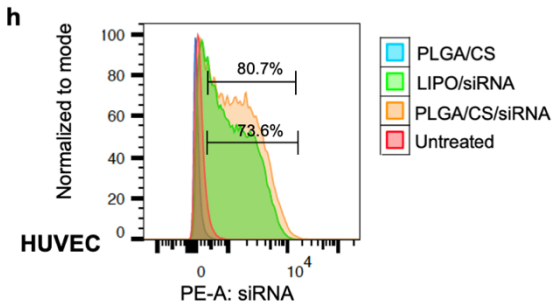
In order to widen the application of designed PLGA/CS NPs to siRNA delivery, their biological outcomes were compared to those of commercially available lipofectamine (LIPO) based lipoplexes. Hence PLGA/CS/siRNA, PLGA/CS/miRNA, LIPO/miRNA and LIPO/siRNA NPs were prepared and characterized (Fig. 4.6a). PLGA/CS NPs were prepared with the selected N:P ratio of 8. Initial miRNA and siRNA concentrations utilized in the following experiments were identical. Assuming that the NPs and LIPO EE% is equal to 90%, The final concentration of NPs and LIPO is also comparable (for 6 well plates, 50 μ L of NPs or LIPO solution were used, 142 nM siRNA final concentration). Results showed that PLGA/CS, PLGA/CS/miRNA and PLGA/CS/siRNA were monodisperse (< 0.2 PDI) with 150 nm hydrodynamic size, evaluated in deionized water. On the contrary, LIPO/miRNA and LIPO/siRNA NPs were polydisperse with higher hydrodynamic size in the micrometer range (1-1.2 μ m), measured in deionized water (Fig. 4.6b). Zeta potential was positive for PLGA/CS based NPs, including PLGA/CS/miRNA and PLGA/CS/siRNA NPs (10-30 mV), while LIPO based NPs showed a negative zeta potential (-47 mV) (Fig. 4.6c). Moreover, immunofluorescence images of cells (293 T cells and HUVECs) treated with 50 μ g/mL NPs encapsulating Cyanine-3 (CY3)-labelled siRNAs (PLGA/CS/siRNA), showed in red, were acquired using a fluorescence microscope. F-Actin was stained with Phalloidin (green) while nuclei were stained with DAPI (blue). Interestingly, the images showed that the NPs were internalized by the cells after 24h (Fig. 4.6d, e).



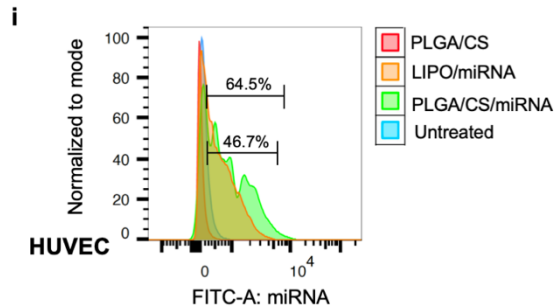
	% of PE-A ⁺ cells	MFI: PE-A
Untreated	0.33%	65.5
PLGA/CS	0.25%	66.8
LIPO siRNA	100%	20715
PLGA/CS siRNA	100%	25458



	% of FITC-A ⁺ cells	MFI: FITC-A
Untreated	6.33%	227
PLGA/CS	7.40%	206
LIPO miRNA	93.2%	2799
PLGA/CS miRNA	81.2%	1376



	% of PE-A ⁺ cells	MFI: PE-A
Untreated	0.49%	120
PLGA/CS	1.69%	187
LIPO siRNA	73.6%	1935
PLGA/CS siRNA	80.7%	2156



	% of FITC-A ⁺ cells	MFI: FITC-A
Untreated	1.52%	102
PLGA/CS	1.69%	125
LIPO miRNA	46.7%	644
PLGA/CS miRNA	64.5%	702

Figure 4.6: Transfection efficiency of siRNA- and miRNA-loaded nanoparticle (NPs).

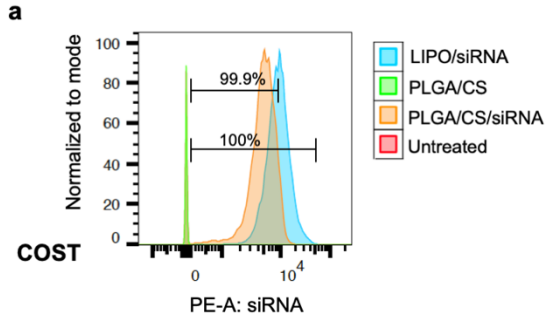
a) Schematic representation of PLGA/CS/siRNA NPs. **b)** Hydrodynamic size, PDI and **c)** zeta potential of PLGA/CS, PLGA/CS/miRNA and PLGA/CS/miRNA compared to LIPO/miRNA and LIPO/siRNA lipoplexes. **d)** Immunofluorescence images of NPs (50 $\mu\text{g/mL}$) containing Cyanine-3 (CY3)-labelled siRNAs (PLGA/CS/siRNA, red) uptake by 293 T cells and **e)** HUVEC. Scale bars indicate 100 μm . Nuclei are stained with DAPI and visualized in blue, F-actin is stained with green phalloidin. **f)** Transfection efficiency of PLGA/CS (NPs ctrl), PLGA/CS/siRNA and LIPO/siRNA (PE channel) and **g)** PLGA/CS, PLGA/CS/miRNA and LIPO/miRNA (FITC channel), measured by flow cytometry on 293 T cells, after 24h incubation. **h)** Transfection efficiency of PLGA/CS (NPs ctrl), PLGA/CS/siRNA and LIPO/siRNA (PE channel) and **i)** PLGA/CS, PLGA/CS/miRNA and LIPO/miRNA (FITC channel) measured by flow cytometry on HUVECS after 24h incubation. Tables indicate percentages (%) of PE-A (siRNA) or FITC-A (miRNA) positive cells. Median fluorescent intensity (MFI) of PE-A (siRNA) or FITC-A (miRNA) are indicated.

To confirm NPs internalization, flow cytometry of cells (293T cells, HUVECs) treated with NPs encapsulating FAM-labelled miRNA or CY3-labelled siRNA revealed high transfection efficiency. 293T cells are commonly used for lentivirus generation and represent a positive control for transfection efficiency. Indeed, PLGA/CS/siRNA NPs showed similar transfection efficiency compared to commercial LIPO/siRNA lipoplexes in 293 cells (Fig. 4.6f, g). Instead, the transfection efficiency was slightly lower for PLGA/CS/miRNA NPs compared to LIPO/miRNA lipoplexes. Moreover, immunofluorescence images of cells (293 T cells and HUVECs) treated with 50 $\mu\text{g/mL}$ NPs encapsulating Cyanine-3 (CY3)-labelled siRNAs (PLGA/CS/siRNA), showed in red, were acquired using a fluorescence microscope. F-Actin was stained with Phalloidin (green) while nuclei were stained with DAPI (blue). Interestingly, the images showed that the NPs were internalized by the cells after 24h (Fig. 4.6d, e).

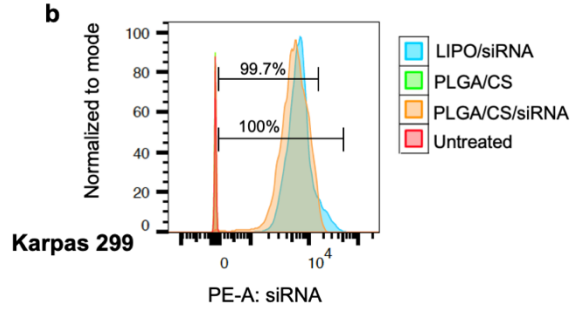
To confirm NPs internalization, flow cytometry of cells (293T cells, HUVECs) treated with NPs encapsulating FAM-labelled miRNA or CY3-labelled siRNA revealed high transfection efficiency. 293T cells are commonly used for lentivirus generation and represent a positive control for transfection efficiency. Indeed, PLGA/CS/siRNA NPs showed similar transfection efficiency compared to commercial LIPO/siRNA lipoplexes in 293 cells (Fig. 4.6f, g). Instead, the transfection efficiency was slightly lower for PLGA/CS/miRNA NPs compared to LIPO/miRNA lipoplexes. In the case of HUVECs, the overall transfection efficiency was lower than for 293T cells. Similarly, to the trials with 293 T cells, PLGA/CS/siRNA NPs showed superior transfection efficiency than PLGA/CS/miRNA NPs. No differences in transfection efficiency were observed between PLGA/CS based NPs and LIPO based lipoplexes containing either miRNA or siRNA

(Fig. 4.6h, i). PLGA/CS/siRNA-based NPs and LIPO/siRNA lipoplexes showed comparable transfection efficiency in anaplastic lymphoma kinase (ALK)-positive anaplastic large cell lymphoma cells (ALCL) COST and Karpas 299 (Fig. 4.7a, b). This could potentially expand the application of designed NPs to release specific siRNA to ALCL, able to downregulate ALK expression. Indeed, to preliminarily compare cell viability of LIPO and PLGA/CS based NPs in ALCL models (COST and Karpas299), a siRNA targeting ALK was encapsulated into CS/PLGA NPs and LIPO lipoplexes. Firstly, the viability assays of ALCL confirmed the biocompatibility of unloaded CS/PLGA NPs and LIPO lipoplexes at two different time points (24 h and 48 h). As expected, cell viability slightly decreased for both PLGA/CS NPs and LIPO lipoplexes encapsulating siRNA targeting ALK (Fig. 4.7c, d). Interestingly, CS/PLGA/siRNA(ALK) NPs showed higher cytotoxicity with a drop in viability as a function of culture time from 70% to 30% for COST and from 75% to 35% for Karpas299 model, while LIPO/siRNA showed a slightly more robust effect after 24 h (60% viability in COST and Karpas299) but limited additional effect at 48 h (50% COST and Karpas299). These results suggested that the PLGA/CS/siRNA(ALK) NPs achieved a sustained cytotoxic effect over 48h compared to the LIPO/siRNA(ALK) lipoplexes (Fig. 4.7c, d).

In order to reduce the protein corona formation and aggregation phenomena, observed during the cell tests, Tween 80 (T) emulsifier was used. In this case, the NPs sizes measured in water ranged from 150 nm for control PLGA/CS/T NPs to 200 nm for PLGA/CS/miRNA/T NPs, which were similar to the sizes of PLGA/CS NPs and PLGA/CS/miRNA NPs in water. These values were compared with measures performed with NPs in DMEM medium (containing 10% fetal bovine serum (FBS)): PLGA/CS/T and PLGA/CS/miRNA/T sizes were of around 250 nm with 0.2 PDI, while PLGA/CS size increased to 0.5 μm (Fig. 4.7e, f). Results suggested that the addition of T may hinder protein adsorption on NP surface, avoiding consequent NP aggregation.



	% of PE-A ⁺ cells	MFI: PE-A
Untreated	0.039%	11.8
PLGA/CS	0.020%	12.8
LIPO siRNA	100%	5347
PLGA/CS siRNA	99.9%	9427



	% of PE-A ⁺ cells	MFI: PE-A
Untreated	0.35%	12.8
PLGA/CS	0.02%	15.8
LIPO siRNA	99.7%	6896
PLGA/CS siRNA	100%	6015

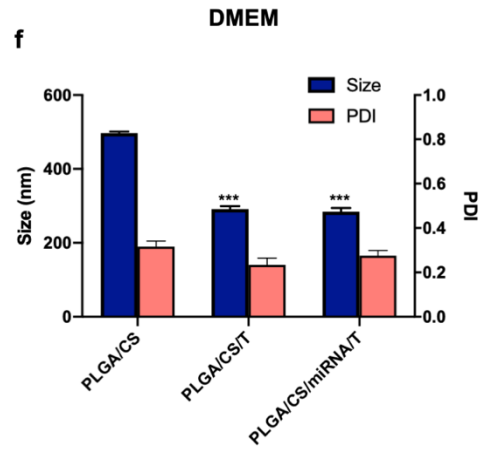
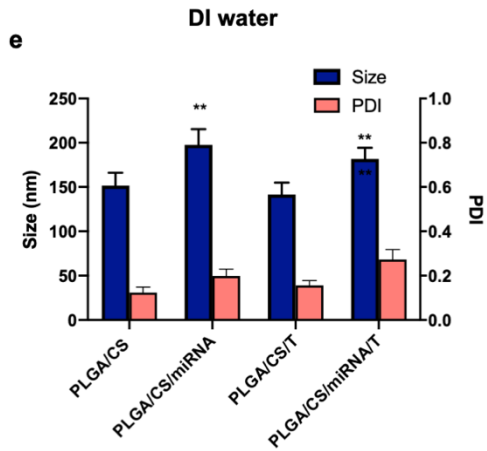
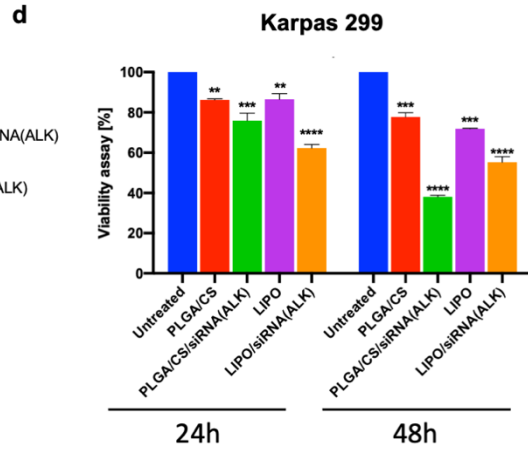
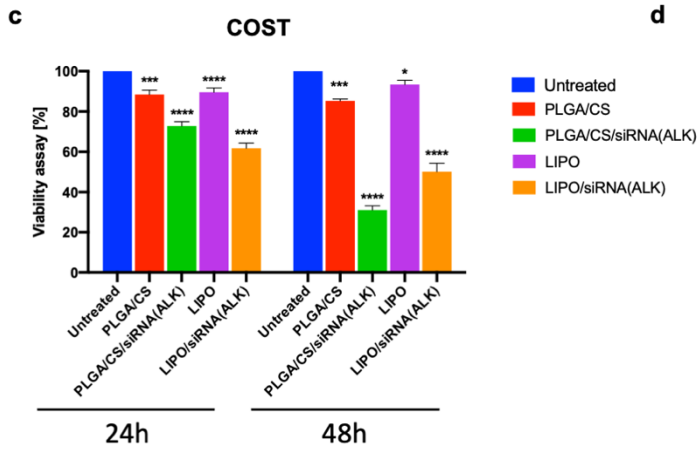


Figure 4.7: Transfection efficiency of nanoparticles (NPs) in anaplastic large cell lymphoma (ALCL) cell models and NPs stability.

a) Transfection efficiency of PLGA/CS (NPs ctrl), PLGA/CS/siRNA and LIPO/siRNA (PE channel) and **b)** PLGA/CS, PLGA/CS/miRNA and LIPO/miRNA (FITC channel) measured by flow cytometry on ALCL cells (COST, Karpas299) after 24h incubation. Tables indicate percentages (%) of PE-A (siRNA) or FITC-A (miRNA) positive cells. Median fluorescent intensity (MFI) of PE-A (siRNA) or FITC-A (miRNA) are indicated. **c) d)** Viability assay in 2D culture of ALCLs with PLGA/CS and PLGA/CS/siRNA(ALK) NPs, LIPO, LIPO/siRNA(ALK) and untreated after 24 and 48h. **e)** Hydrodynamic size and PDI of PLGA/CS, PLGA/CS/miRNA +/- Tween 80 (PLGA/CS/T and PLGA/CS/miRNA /T) in deionized water or **f)** DMEM containing fetal bovine serum (FBS) at day 0.

Discussion

In this chapter, CS and PLGA were used to form PLGA/CS NPs by nanoprecipitation. CS was chosen for its known biocompatibility and positively charged amino groups, able to interact with the negatively charged phosphate groups of oligonucleotides (e.g. miRNAs or siRNAs), forming complexes [77] [78]. Strong electrostatic interactions may help protecting oligonucleotides from degradation, but may also limit their release. Hence a careful selection of N:P ratio during complexation has to be performed. The main hurdles associated with the clinical use of chitosan-based delivery systems are their low stability in physiological pH, weak buffering capacity and lack of cell specificity. However, understanding these limitations has encouraged the use of polymer combination as innovative delivery systems. PLGA, a biocompatible and biodegradable polymer (FDA-approved) was selected to confer stability to the resulting NPs [57]. A carboxylic acid terminated PLGA-COOH, more hydrophilic than non-carboxylic acid terminated PLGA counterpart, was used to facilitate interaction with CS.

In this work, the N:P ratio of CS/miRNA and PLGA/CS/miRNA NPs were characterized in terms of their effects on hydrodynamic size and zeta potential, in order to select the optimal ratio of amino to phosphate groups ratio, to have a balance between efficient miRNA entrapment and miRNA release ability by the NPs.

Initial characterization of CS/miRNA complexes allowed the pre-selection of three N:P ratios (3, 5, 8) which allowed to prepare NPs with positive zeta potential as indicative of efficient miRNA complexation. CS/miRNA complexes with N:P ratio of 15 showed similar properties to the ones with N:P ratio of 8 in terms of size and zeta potential, suggesting that complete miRNA complexation was probably already achieved with CS/miRNA complexes with N:P of 8 (Fig. 4.4a-e). Ideally, CS/miRNA complexes should efficiently encapsulate miRNA without blocking miRNA release. NPs ability to reach their target with therapeutic efficacy is largely determined by their capability to maintain their size, encapsulate the drug and properly release it into the cells. NPs should remain stable until they reach the target sites. Instability of NPs causes altered biodistribution and premature drug release, compromising the efficacy of the delivery system [40]. To select the optimal N:P ratio among the preselected ones (3, 5 and 8) in CS/miRNA complexes, their stability was characterized.

In parallel, PLGA-COOH was included in the formulation with PLGA/CS composition of 99/1 w/w. The stability of PLGA/CS/miRNA prepared at the same N:P ratios was also tested (Fig. 4.4g-h). In such tests, any significant variations in the average NPs size range can be interpreted as a signal of NP instability. From these experiments, CS/miRNA complexes with N:P ratio of 3 showed low stability after 5 days incubation in deionized water (Fig. 4.4 g-h). On the contrary, CS/miRNA complexes with N:P ratio of 5 and 8 showed superior stability thanks to their higher CS amount and more efficient complexation (Fig. 4.4 g-h). PLGA/CS/miRNA NPs with the same N:P ratios (5 and 8) evidenced that hydrodynamic size and zeta potential changes occurred between 3 and 5 days for those with N:P 5 and between 5 and 7 days for those with N:P 8. For this reason, PLGA/CS/miRNA NPs with N:P ratio of 8 were selected.

Similarly to other NPs [49],[98], PLGA/CS/miRNA NPs with N:P 8 also showed high production yield ($62\pm 15\%$) (Fig. 4.4f) and increased entrapment efficiency (above 90%), suggesting their promising properties for oligonucleotide release (Fig. 4.5a).

Then, PLGA/CS/miRNA NPs were further characterized in terms of viability and transfection efficacy, and the system was compared with lipofectamine-based lipoplexes (LIPO), which represent a standard for miRNA and siRNA transfection *in vitro*.

Cells were always treated with the same amount of miRNA or siRNA with a final concentration of 142 nM. PLGA/CS/miRNA and PLGA/CS/siRNA displayed 3 to 5 times reduced size compared to LIPO which exhibited decreased stability (Fig. 4.6b, c).

In contrast, PLGA/CS/miRNA or PLGA/CS/siRNA NPs evidenced a slightly positive charge on the surface that might facilitate the interaction with the opposite-charged cellular membrane.

Viability tests evidenced the biocompatibility of PLGA/CS systems even with high dose of NPs (0.5 mg/mL) after 24 and 48 h. Flow cytometry also showed enhanced transfection efficacy, slightly higher for siRNA loaded PLGA/CS NPs compared to miRNA-loaded NPs.

Differences of transfection efficacy between siRNA and miRNA-loaded NPs are mainly related to the differential endogenous ability of the cells to be transfected, which is generally higher in 293 T and lower for HUVECs. Usually, ALCL are not easily transfected, but in these experiments ALCL transfection efficiency was high. Nevertheless, the quantification by flow cytometry of the transfection efficacy relies on fluorescently labelled miRNAs and siRNA, which might have different fluorescent stability and might be degraded overtime. Indeed, it might be optimal to compare miRNAs and siRNAs conjugated with the same fluorophore.

Preliminary functional assays using NPs releasing a siRNA targeting ALK (fig. 4.7c, d) further proved the cell uptake of NPs. Fluorescence imaging confirmed cell internalization of NPs.

In summary, the association of siRNA with both CS and PLGA in PLGA/CS/siRNA NPs is an effective strategy in which CS ensures efficient siRNA binding while PLGA provides stability.

Finally, the combination with Tween 80 emulsifier for low protein adsorption would potentially prevent the aggregation and formation of protein corona for longer half-life in bloodstream. However, physicochemical and biological characterization of NPs should be repeated in the case of Tween 80 addition.

Further studies are needed to determine long and short-term bloodstream stability, which is an essential requirement for a successful drug delivery system to target tissues.

Conclusion

In this chapter, biocompatible PLGA/CS/miRNA NPs were designed to combine the properties of both polymers having the following characteristics (Table 7).

Table 7. PLGA/CS/NPs characteristics for miRNA release.

PLGA/CS NPs							
N:P	PLGA/CS (w/w)	Hydrodynamic size (nm)	Zeta potential (mV)	EE (%)	Production Yield (%)	Biocompatible dose ensuring cell viability > 70% (mg/mL)	Transfection efficiency
8	99/1	170 ± 21	62 ± 15	90 ± 2	62 ± 15	Up To 0.5	293T: 81.2% HUVEC: 64.5%

The same NPs were also exploited for siRNA release being highly efficient in siRNA delivery to large cell lymphoma (ALCL). Hence, such NPs hold promises for the release of siRNA targeting ALK in ALCL.

In the future, chemical surface modification of such NPs for targeted therapy, not studied in this PhD thesis, will allow obtaining highly efficient nano-systems for oligonucleotide release to specific cells. Future work should also focus on *in vivo* testing characterization.

Acknowledgments

The PhD student would like to thank the scientists from Politecnico di Torino helping in the development of the presented experiments.

Particularly, the candidate would like to acknowledge contribution from:

- 1 Marcello Aramu, master thesis student in Biomedical Engineering, who helped performing the physicochemical characterization of NPs.
- 2 Chiara Tonda-Turo, professor, who kindly provided the chitosan solution protocol.
- 3 Clara Mattu, researcher and tutor, who supervised the project and contributed in the design of NPs.
- 4 Valeria Chiono, professor and tutor, who supervised and design the project and acquired funding.

References

- [1] T. C. Roberts, R. Langer, and M. J. A. Wood, "Advances in oligonucleotide drug delivery," *Nat. Rev. Drug Discov.*, vol. 19, no. 10, pp. 673–694, 2020.
- [2] R. L. Juliano, "The delivery of therapeutic oligonucleotides," *Nucleic Acids Res.*, vol. 44, no. 14, pp. 6518–6548, 2016.
- [3] X. H. Liang, H. Sun, J. G. Nichols, and S. T. Crooke, "RNase H1-Dependent Antisense Oligonucleotides Are Robustly Active in Directing RNA Cleavage in Both the Cytoplasm and the Nucleus," *Mol. Ther.*, vol. 25, no. 9, pp. 2075–2092, 2017.
- [4] S. T. Crooke, "Molecular Mechanisms of Antisense Oligonucleotides," *Nucleic Acid Ther.*, vol. 27, no. 2, pp. 70–77, 2017.
- [5] S. Y. Wu, G. Lopez-Berestein, G. A. Calin, and A. K. Sood, "RNAi therapies: Drugging the undruggable," *Sci. Transl. Med.*, vol. 6, no. 240, pp. 1–8, 2014.
- [6] A. L. Jackson *et al.*, "Expression profiling reveals off-target gene regulation by RNAi," *Nat. Biotechnol.*, vol. 21, no. 6, pp. 635–637, 2003.
- [7] P. C. Scacheri *et al.*, "Short interfering RNAs can induce unexpected and divergent changes in the levels of untargeted proteins in mammalian cells," *Proc. Natl. Acad. Sci. U. S. A.*, vol. 101, no. 7, pp. 1892–1897, 2004.
- [8] D. Grimm *et al.*, "Fatality in mice due to oversaturation of cellular microRNA/short hairpin RNA pathways," *Nature*, vol. 441, no. 7092, pp. 537–541, 2006.
- [9] J. K. Watts and D. R. Corey, "Silencing disease genes in the laboratory and the clinic," *J. Pathol.*, vol. 226, no. 2, pp. 365–379, 2012.
- [10] J. K. W. Lam, M. Y. T. Chow, Y. Zhang, and S. W. S. Leung, "siRNA versus miRNA as therapeutics for gene silencing," *Mol. Ther. - Nucleic Acids*, vol. 4, no. 9, p. e252, 2015.
- [11] H. Siomi and M. C. Siomi, "On the road to reading the RNA-interference code," *Nature*, vol. 457, no. 7228, pp. 396–404, 2009.
- [12] M. Wery, M. Kwapisz, and A. Morillon, "Noncoding RNAs in gene regulation," *Wiley Interdiscip. Rev. Syst. Biol. Med.*, vol. 3, no. 6, pp. 728–738, 2011.
- [13] D. P. Bartel, "MicroRNAs: Genomics, Biogenesis, Mechanism, and Function Review," *Cell*, vol. 116, pp. 281–297, 2004.
- [14] G. Ozcan, B. Ozpolat, R. L. Coleman, A. K. Sood, and G. Lopez-Berestein, "Preclinical and clinical development of siRNA-based therapeutics," *Adv. Drug Deliv. Rev.*, vol. 87, pp. 108–119, 2015.
- [15] R. S. Geary, D. Norris, R. Yu, and C. F. Bennett, "Pharmacokinetics, biodistribution and cell uptake of antisense oligonucleotides," *Adv. Drug Deliv. Rev.*, vol. 87, pp. 46–51, 2015.
- [16] N. B. Y. Tsui, E. K. O. Ng, and Y. M. D. Lo, "Stability of endogenous and added RNA in blood specimens, serum, and plasma," *Clin. Chem.*, vol. 48, no. 10, pp. 1647–1653, Oct. 2002.
- [17] W. Brad Wan and P. P. Seth, "The Medicinal Chemistry of Therapeutic Oligonucleotides," *J. Med. Chem.*, vol. 59, no. 21, pp. 9645–9667, 2016.
- [18] R. S. Tomar, H. Matta, and P. M. Chaudhary, "Use of adeno-associated viral vector for delivery of small interfering RNA," *Oncogene*, vol. 22, no. 36, pp. 5712–5715, 2003.
- [19] Z. Bai *et al.*, "Non-viral nanocarriers for intracellular delivery of microRNA therapeutics," *J. Mater. Chem. B*, vol. 7, no. 8, pp. 1209–1225, 2019.
- [20] J. Yang, H. Liu, and X. Zhang, "Design, preparation and application of nucleic acid delivery carriers," *Biotechnol. Adv.*, vol. 32, no. 4, pp. 804–817, 2014.
- [21] M. Imbert, G. Dias-Florencio, and A. Goyenvalle, "Viral vector-mediated antisense therapy for genetic diseases," *Genes (Basel)*, vol. 8, no. 2, 2017.
- [22] Y. Chen, D. Y. Gao, and L. Huang, "In vivo delivery of miRNAs for cancer therapy: Challenges and strategies," *Adv. Drug Deliv. Rev.*, vol. 81, pp. 128–141, 2015.
- [23] A. C. Anselmo, Y. Gokarn, and S. Mitragotri, "Non-invasive delivery strategies for biologics," *Nat. Rev. Drug Discov.*, vol. 18, no. 1, pp. 19–40, 2018.

- [24] M. Muthiah, I. K. Park, and C. S. Cho, “Nanoparticle-mediated delivery of therapeutic genes: Focus on miRNA therapeutics,” *Expert Opin. Drug Deliv.*, vol. 10, no. 9, pp. 1259–1273, 2013.
- [25] B. Kim, J. H. Park, and M. J. Sailor, “Rekindling RNAi Therapy: Materials Design Requirements for In Vivo siRNA Delivery,” *Adv. Mater.*, vol. 31, no. 49, pp. 1–23, 2019.
- [26] S. W. L. Lee *et al.*, “MicroRNA delivery through nanoparticles,” *Journal of Controlled Release*, vol. 313. Elsevier B.V., pp. 80–95, 10-Nov-2019.
- [27] Y. Zhao and L. Huang, “Lipid Nanoparticles for Gene Delivery,” in *Nonviral Vectors for Gene Therapy*, vol. 88, L. Huang, D. Liu, and E. Wagner, Eds. Academic Press, 2014, pp. 13–36.
- [28] X. Cheng and R. J. Lee, “The role of helper lipids in lipid nanoparticles (LNPs) designed for oligonucleotide delivery,” *Adv. Drug Deliv. Rev.*, vol. 99, pp. 129–137, 2016.
- [29] A. Schroeder, C. G. Levins, C. Cortez, R. Langer, and D. G. Anderson, “Lipid-based nanotherapeutics for siRNA delivery,” *J. Intern. Med.*, vol. 267, no. 1, pp. 9–21, 2010.
- [30] L. H. Yuhua Wang*, Lei Miao, Andrew Satterlee, “Delivery of Oligonucleotides with Lipid Nanoparticles,” *Adv. Drug Deliv. Rev.*, vol. 29, no. 87, pp. 68–80, 2015.
- [31] R. Petrilli *et al.*, “Lipid nanoparticles as non-viral vectors for siRNA delivery: Concepts and applications,” in *Nanobiomaterials in Drug Delivery*, A. M. Grumezescu, Ed. William Andrew Publishing, 2016, pp. 75–109.
- [32] Y. Dong, D. J. Siegwart, and D. G. Anderson, “Strategies, design, and chemistry in siRNA delivery systems,” *Adv. Drug Deliv. Rev.*, vol. 144, pp. 133–147, 2019.
- [33] H. Lv, S. Zhang, B. Wang, S. Cui, and J. Yan, “Toxicity of cationic lipids and cationic polymers in gene delivery,” *J. Control. Release*, vol. 114, no. 1, pp. 100–109, 2006.
- [34] J. Heyes, L. Palmer, K. Bremner, and I. MacLachlan, “Cationic lipid saturation influences intracellular delivery of encapsulated nucleic acids,” *J. Control. Release*, vol. 107, no. 2, pp. 276–287, 2005.
- [35] S. hao Hsu *et al.*, “Cationic lipid nanoparticles for therapeutic delivery of siRNA and miRNA to murine liver tumor,” *Nanomedicine Nanotechnology, Biol. Med.*, vol. 9, no. 8, pp. 1169–1180, 2013.
- [36] A. Ganju *et al.*, “miRNA nanotherapeutics for cancer,” *Drug Discov. Today*, vol. 22, no. 2, pp. 424–432, 2017.
- [37] D. F. Emerich and C. G. Thanos, “The pinpoint promise of nanoparticle-based drug delivery and molecular diagnosis,” *Biomol. Eng.*, vol. 23, no. 4, pp. 171–184, 2006.
- [38] N. Desai, “Challenges in development of nanoparticle-based therapeutics,” *AAPS J.*, vol. 14, no. 2, pp. 282–295, 2012.
- [39] O. S. Fenton, K. N. Olafson, P. S. Pillai, M. J. Mitchell, and R. Langer, “Advances in Biomaterials for Drug Delivery,” *Adv. Mater.*, vol. 30, no. 29, pp. 1–29, 2018.
- [40] M. J. Mitchell, M. M. Billingsley, R. M. Haley, M. E. Wechsler, N. A. Peppas, and R. Langer, “Engineering precision nanoparticles for drug delivery,” *Nat. Rev. Drug Discov.*, 2020.
- [41] J. P. Rao and K. E. Geckeler, “Polymer nanoparticles: Preparation techniques and size-control parameters,” *Prog. Polym. Sci.*, vol. 36, no. 7, pp. 887–913, 2011.
- [42] N. Anton, J. P. Benoit, and P. Saulnier, “Design and production of nanoparticles formulated from nano-emulsion templates-A review,” *J. Control. Release*, vol. 128, no. 3, pp. 185–199, 2008.
- [43] A. Lamprecht, N. Ubrich, M. Hombreiro Pérez, C.-M. Lehr, M. Hoffman, and P. Maincent, “Influences of process parameters on nanoparticle preparation performed by a double emulsion pressure homogenization technique,” *Int. J. Pharm.*, vol. 196, no. 2, pp. 177–182, 2000.
- [44] Y. S. Lee, P. J. Johnson, P. T. Robbins, and R. H. Bridson, “Production of nanoparticles-in-microparticles by a double emulsion method: A comprehensive study,” *Eur. J. Pharm. Biopharm.*, vol. 83, no. 2, pp. 168–173, 2013.
- [45] W. Poon, B. R. Kingston, B. Ouyang, W. Ngo, and W. C. W. Chan, “A framework for designing delivery systems,” *Nat. Nanotechnol.*, vol. 15, no. 10, pp. 819–829, 2020.
- [46] A. Mohamed, N. K. Kunda, K. Ross, G. A. Hutcheon, and I. Y. Saleem, “Polymeric nanoparticles for the delivery of miRNA to treat Chronic Obstructive Pulmonary Disease (COPD),” *Eur. J.*

- Pharm. Biopharm.*, vol. 136, pp. 1–8, 2019.
- [47] B. Mishra, B. B. Patel, and S. Tiwari, “Colloidal nanocarriers: a review on formulation technology, types and applications toward targeted drug delivery,” *Nanomedicine Nanotechnology, Biol. Med.*, vol. 6, no. 1, pp. 9–24, 2010.
- [48] A. Bhargava-Shah, K. Foygel, R. Devulapally, and R. Paulmurugan, “Orlistat and antisense-miRNA-loaded PLGA-PEG nanoparticles for enhanced triple negative breast cancer therapy,” *Nanomedicine*, vol. 11, no. 3, pp. 235–247, 2016.
- [49] D. Cosco *et al.*, “Delivery of miR-34a by chitosan/PLGA nanoplexes for the anticancer treatment of multiple myeloma,” *Sci. Rep.*, vol. 5, no. December, pp. 1–11, 2015.
- [50] A. Mahapatro and D. K. Singh, “Biodegradable nanoparticles are excellent vehicle for site directed in-vivo delivery of drugs and vaccines,” *J. Nanobiotechnology*, vol. 9, p. 55, 2011.
- [51] S. Höbel and A. Aigner, “Polyethylenimines for siRNA and miRNA delivery in vivo,” *Wiley Interdiscip. Rev. Nanomedicine Nanobiotechnology*, vol. 5, no. 5, pp. 484–501, 2013.
- [52] A. F. Ibrahim, U. Weirauch, M. Thomas, A. Gruiweller, R. K. Hartmann, and A. Aigner, “MicroRNA replacement therapy for miR-145 and miR-33a is efficacious in a model of colon carcinoma,” *Cancer Res.*, vol. 71, no. 15, pp. 5214–5224, 2011.
- [53] H. J. Lee, R. Namgung, W. J. Kim, J. Il Kim, and I.-K. Park, “Targeted delivery of microRNA-145 to metastatic breast cancer by peptide conjugated branched PEI gene carrier,” *Macromol. Res.*, vol. 21, no. 11, pp. 1201–1209, 2013.
- [54] S. Venkiteswaran, T. Thomas, and T. J. Thomas, “Selectivity of polyethyleneimines on DNA nanoparticle preparation and gene transport,” *ChemistrySelect*, vol. 1, no. 6, pp. 1144–1150, 2016.
- [55] J. M. Lee, T. J. Yoon, and Y. S. Cho, “Recent developments in nanoparticle-based siRNA delivery for cancer therapy,” *Biomed Res. Int.*, vol. 2013, 2013.
- [56] T. Zhang, X. Xue, D. He, and J. T. Hsieh, “A prostate cancer-targeted polyarginine-disulfide linked PEI nanocarrier for delivery of microRNA,” *Cancer Lett.*, vol. 365, no. 2, pp. 156–165, 2015.
- [57] F. Danhier, E. Ansorena, J. M. Silva, R. Coco, A. Le Breton, and V. Préat, “PLGA-based nanoparticles: An overview of biomedical applications,” *J. Control. Release*, vol. 161, no. 2, pp. 505–522, 2012.
- [58] J. K. Vasir and V. Labhasetwar, “Biodegradable nanoparticles for cytosolic delivery of therapeutics,” *Adv. Drug Deliv. Rev.*, vol. 59, no. 8, pp. 718–728, 2007.
- [59] Y. Chen, D. Y. Gao, and L. Huang, “In vivo delivery of miRNAs for cancer therapy: Challenges and strategies,” *Adv. Drug Deliv. Rev.*, vol. 81, pp. 128–141, 2015.
- [60] I. Grizzi, H. Garreau, S. Li, and M. Vert, “Hydrolytic degradation of devices based on poly(DL-lactide) size-dependence,” *Biomaterials*, vol. 16, no. 4, pp. 305–311, 1995.
- [61] S. Arora *et al.*, “Synthesis, characterization, and evaluation of poly (D,L-lactide-co-glycolide)-based nanoformulation of miRNA-150: Potential implications for pancreatic cancer therapy,” *Int. J. Nanomedicine*, vol. 9, no. 1, pp. 2933–2942, 2014.
- [62] S. Y. Wong, J. M. Pelet, and D. Putnam, “Polymer systems for gene delivery—Past, present, and future,” *Prog. Polym. Sci.*, vol. 32, no. 8–9, pp. 799–837, 2007.
- [63] J. Milton Harris and R. B. Chess, “Effect of pegylation on pharmaceuticals,” *Nat. Rev. Drug Discov.*, vol. 2, no. 3, pp. 214–221, 2003.
- [64] G. Aldrian *et al.*, “PEGylation rate influences peptide-based nanoparticles mediated siRNA delivery in vitro and in vivo,” *J. Control. Release*, vol. 256, no. February, pp. 79–91, 2017.
- [65] E. Blanco, H. Shen, and M. Ferrari, “Principles of nanoparticle design for overcoming biological barriers to drug delivery,” *Nat. Biotechnol.*, vol. 33, no. 9, pp. 941–951, 2015.
- [66] B. K. Lee, Y. Yun, and K. Park, “PLA micro- and nano-particles,” *Adv. Drug Deliv. Rev.*, vol. 107, pp. 176–191, 2016.
- [67] J. Wang, S.-S. Feng, S. Wang, and Z. Chen, “Evaluation of cationic nanoparticles of biodegradable copolymers as siRNA delivery system for hepatitis B treatment,” *Int. J. Pharm.*, vol. 400, no. 1, pp. 194–200, 2010.

- [68] X. Z. Yang, S. Dou, T. M. Sun, C. Q. Mao, H. X. Wang, and J. Wang, "Systemic delivery of siRNA with cationic lipid assisted PEG-PLA nanoparticles for cancer therapy," *J. Control. Release*, vol. 156, no. 2, pp. 203–211, 2011.
- [69] W. J. Jia *et al.*, "Preparation of biodegradable polycaprolactone/poly (ethylene glycol)/polycaprolactone (PCEC) nanoparticles," *Drug Deliv.*, vol. 15, no. 7, pp. 409–416, 2008.
- [70] P. Grossen, D. Witzigmann, S. Sieber, and J. Huwyler, "PEG-PCL-based nanomedicines: A biodegradable drug delivery system and its application," *J. Control. Release*, vol. 260, no. April, pp. 46–60, 2017.
- [71] Q. Liu *et al.*, "Targeted delivery of miR-200c/DOC to inhibit cancer stem cells and cancer cells by the gelatinases-stimuli nanoparticles," *Biomaterials*, vol. 34, no. 29, pp. 7191–7203, 2013.
- [72] I. Serrano-Sevilla, Á. Artiga, S. G. Mitchell, L. De Matteis, and J. M. de la Fuente, "Natural polysaccharides for siRNA delivery: Nanocarriers based on chitosan, hyaluronic acid, and their derivatives," *Molecules*, vol. 24, no. 14, 2019.
- [73] M. Prabakaran and J. F. Mano, "Chitosan-based particles as controlled drug delivery systems," *Drug Deliv. J. Deliv. Target. Ther. Agents*, vol. 12, no. 1, pp. 41–57, 2005.
- [74] T. A. Sonia and C. P. Sharma, "Chitosan and its derivatives for drug delivery perspective," *Adv. Polym. Sci.*, vol. 243, no. 1, pp. 23–54, 2011.
- [75] A. Bernkop-Schnürch and S. Dünnhaupt, "Chitosan-based drug delivery systems," *Eur. J. Pharm. Biopharm.*, vol. 81, no. 3, pp. 463–469, 2012.
- [76] B. Santos-Carballal *et al.*, "Physicochemical and biological characterization of chitosan-microRNA nanocomplexes for gene delivery to MCF-7 breast cancer cells," *Sci. Rep.*, vol. 5, no. September, pp. 1–15, 2015.
- [77] M. Denizli *et al.*, "Chitosan nanoparticles for miRNA delivery," *Methods Mol. Biol.*, vol. 1632, pp. 219–230, 2017.
- [78] H. Ragelle, G. Vandermeulen, and V. Préat, "Chitosan-based siRNA delivery systems," *J. Control. Release*, vol. 172, no. 1, pp. 207–218, 2013.
- [79] D. Cosco *et al.*, "Physicochemical features and transfection properties of chitosan/poloxamer 188/poly(D,L-lactide-co-glycolide) nanoplexes," *Int. J. Nanomedicine*, vol. 9, no. 1, pp. 2359–2372, 2014.
- [80] S. Y. Chae, S. Son, M. Lee, M. K. Jang, and J. W. Nah, "Deoxycholic acid-conjugated chitosan oligosaccharide nanoparticles for efficient gene carrier," *J. Control. Release*, vol. 109, no. 1–3, pp. 330–344, 2005.
- [81] B. Layek and J. Singh, "N-hexanoyl, N-octanoyl and N-decanoyl chitosans: Binding affinity, cell uptake, and transfection," *Carbohydr. Polym.*, vol. 89, no. 2, pp. 403–410, 2012.
- [82] P. Sun *et al.*, "Chitosan-based nanoparticles for survivin targeted siRNA delivery in breast tumor therapy and preventing its metastasis," *Int. J. Nanomedicine*, vol. 11, pp. 4931–4945, 2016.
- [83] L. Casettari, D. Villasaliu, G. Mantovani, S. M. Howdle, S. Stolnik, and L. Illum, "Effect of PEGylation on the toxicity and permeability enhancement of chitosan," *Biomacromolecules*, vol. 11, no. 11, pp. 2854–2865, 2010.
- [84] M. Nag, V. Gajbhiye, P. Kesharwani, and N. K. Jain, "Transferrin functionalized chitosan-PEG nanoparticles for targeted delivery of paclitaxel to cancer cells," *Colloids Surfaces B Biointerfaces*, vol. 148, pp. 363–370, 2016.
- [85] A. V. Nascimento, F. Gattacceca, Amit, H. B. D. F. Singh, B. S. & M. M., and Amiji, "Biodistribution and pharmacokinetics chitosan nanoparticles in cisplatin sensitive and resistant lung cancer models," *Nanomedicine*, vol. 11, pp. 767–781, 2016.
- [86] A. Guțoaia *et al.*, "Fine-tuned PEGylation of chitosan to maintain optimal siRNA-nanoplex bioactivity," *Carbohydr. Polym.*, vol. 143, pp. 25–34, 2016.
- [87] M. Muthiah, I.-K. Park, and C.-S. Cho, "Nanoparticle-mediated delivery of therapeutic genes: focus on miRNA therapeutics," *Expert Opin. Drug Deliv.*, vol. 10, no. 9, pp. 1259–1273, 2013.
- [88] K. T. Dicker, L. A. Gurski, S. Pradhan-Bhatt, R. L. Witt, M. C. Farach-Carson, and X. Jia, "Hyaluronan: A simple polysaccharide with diverse biological functions," *Acta Biomater.*, vol. 10,

- no. 4, pp. 1558–1570, 2014.
- [89] A. Cadete and M. J. Alonso, “Targeting cancer with hyaluronic acid-based nanocarriers: Recent advances and translational perspectives,” *Nanomedicine*, vol. 11, no. 17, pp. 2341–2357, 2016.
- [90] Z. R. Cohen *et al.*, “Localized RNAi therapeutics of chemoresistant grade IV glioma using hyaluronan-grafted lipid-based nanoparticles,” *ACS Nano*, vol. 9, no. 2, pp. 1581–1591, 2015.
- [91] D. Haussecker, “Current issues of RNAi therapeutics delivery and development,” *J. Control. Release*, vol. 195, pp. 49–54, 2014.
- [92] S. Wang, J. Zhang, Y. Wang, and M. Chen, “Hyaluronic acid-coated PEI-PLGA nanoparticles mediated co-delivery of doxorubicin and miR-542-3p for triple negative breast cancer therapy,” *Nanomedicine Nanotechnology, Biol. Med.*, vol. 12, no. 2, pp. 411–420, 2016.
- [93] S. Ganesh, A. K. Iyer, D. V. Morrissey, and M. M. Amiji, “Hyaluronic acid based self-assembling nanosystems for CD44 target mediated siRNA delivery to solid tumors,” *Biomaterials*, vol. 34, no. 13, pp. 3489–3502, 2013.
- [94] Z. Zhou *et al.*, “Reversible Covalent Cross-Linked Polycations with Enhanced Stability and ATP-Responsive Behavior for Improved siRNA Delivery,” *Biomacromolecules*, vol. 19, no. 9, pp. 3776–3787, 2018.
- [95] A. Tirella *et al.*, “CD44 targeted delivery of siRNA by using HA-decorated nanotechnologies for KRAS silencing in cancer treatment,” *Int. J. Pharm.*, vol. 561, no. February, pp. 114–123, 2019.
- [96] D. Landesman-Milo *et al.*, “Hyaluronan grafted lipid-based nanoparticles as RNAi carriers for cancer cells,” *Cancer Lett.*, vol. 334, no. 2, pp. 221–227, 2013.
- [97] T. Yin *et al.*, “Smart nanoparticles with a detachable outer shell for maximized synergistic antitumor efficacy of therapeutics with varying physicochemical properties,” *J. Control. Release*, vol. 243, pp. 54–68, 2016.
- [98] G. K. Jain *et al.*, “Microscopic and spectroscopic evaluation of novel PLGA-chitosan Nanoplexes as an ocular delivery system,” *Colloids Surfaces B Biointerfaces*, vol. 82, no. 2, pp. 397–403, 2011.
- [99] C. Rinaldi and M. J. A. Wood, “Antisense oligonucleotides: The next frontier for treatment of neurological disorders,” *Nat. Rev. Neurol.*, vol. 14, no. 1, pp. 9–22, 2018.
- [100] H. Yin, R. L. Kanasty, A. A. Eltoukhy, A. J. Vegas, J. R. Dorkin, and D. G. Anderson, “Non-viral vectors for gene-based therapy,” *Nat. Rev. Genet.*, vol. 15, no. 8, pp. 541–555, 2014.
- [101] C. Baum, O. Kustikova, U. Modlich, Z. Li, and B. Fehse, “Mutagenesis and oncogenesis by chromosomal insertion of gene transfer vectors.,” *Hum. Gene Ther.*, vol. 17, no. 3, pp. 253–263, Mar. 2006.
- [102] N. Bessis, F. J. GarciaCozar, and M.-C. Boissier, “Immune responses to gene therapy vectors: influence on vector function and effector mechanisms.,” *Gene Ther.*, vol. 11 Suppl 1, pp. S10-7, Oct. 2004.
- [103] Z. Xu, D. Wang, Y. Cheng, M. Yang, and L. P. Wu, “Polyester based nanovehicles for siRNA delivery,” *Mater. Sci. Eng. C*, vol. 92, no. May, pp. 1006–1015, 2018.
- [104] R. Kanasty, J. R. Dorkin, A. Vegas, and D. Anderson, “Delivery materials for siRNA therapeutics,” *Nat. Mater.*, vol. 12, no. 11, pp. 967–977, 2013.
- [105] P. Zhang, J. Xia, and S. Luo, “Generation of well-defined micro/nanoparticles via advanced manufacturing techniques for therapeutic delivery,” *Materials (Basel)*, vol. 11, no. 4, 2018.
- [106] P. Angart, D. Vocelle, C. Chan, and S. Patrick Walton, “Design of siRNA therapeutics from the molecular scale,” *Pharmaceuticals*, vol. 6, no. 4, pp. 440–468, 2013.
- [107] R. A. Petros and J. M. Desimone, “Strategies in the design of nanoparticles for therapeutic applications,” *Nat. Rev. Drug Discov.*, vol. 9, no. 8, pp. 615–627, 2010.
- [108] A. L. Jackson and P. S. Linsley, “Recognizing and avoiding siRNA off-target effects for target identification and therapeutic application,” *Nat. Rev. Drug Discov.*, vol. 9, no. 1, pp. 57–67, 2010.
- [109] M. Boido, M. Ghibaudi, P. Gentile, E. Favaro, R. Fusaro, and C. Tonda-Turo, “Chitosan-based hydrogel to support the paracrine activity of mesenchymal stem cells in spinal cord injury treatment,” *Sci. Rep.*, vol. 9, no. 1, pp. 1–16, 2019.

Section V

Final discussion, main achievements and future perspectives

Chapter 10 - *General discussion*

Advanced preclinical models such as microphysiological systems have the potential to transform the drug development pipeline by better predicting the outcome of clinical trials than current animal models and traditional 2-Dimensional (2D) culture [1].

Preclinical models of human disease are essential for the basic understanding of disease pathology and their application for the development of efficient treatments for patients [2]. Nevertheless, most preclinical models have limitations in faithfully recapitulating the local tissue and organ microenvironment and, in certain circumstances, induce misleading outcomes [3]. For instance, static and simple 2D cell culture models often lack the complex multicellular interactions typical of *in vivo* tissues [4]. Some of these caveats are widely known and intrinsically present in experimental modelling. Moreover, the gap between human 2D cell culture and animal models can dramatically affect clinical outcome [5]. There are few existing models that can uncover the continuous interactions and chemokine signaling existing between cells in the tumor microenvironment (TME), and also evaluate the preclinical efficacy of novel and personalized cancer therapeutics. For instance, there is a lack of *in vitro* models describing the immune cell trafficking across a human-relevant model of the tumor microvasculature in the TME.

For these reasons, more effective prediction of clinical outcomes is needed during preclinical testing of drug candidates to reduce high attrition rates in drug development [6], [7].

In this context, engineered living systems using microfluidic technology represent one of the future platforms for *in vitro* experimentation and translational research, such as drug testing of innovative compounds and nanocarriers, improving the reliability of models that mimic a broad spectrum of pathologies, including neurodegenerative diseases and cancer [8].

Similarly, nanomedicine initiates a new era for many cancer and neurodegenerative diseases treatments [9], [10]. Due to their unique physicochemical properties, engineered nanocarriers have shown the ability to overcome the major limitations of conventional free-drug circulation, such as lack of selectivity and low availability to overcome many biological barriers present in the human body [11], [12]. Among nanomedicine tools, polymer nanoparticles emerged as promising candidates, due to their suitable biocompatibility, versatile design and high stability in body fluids [13][14][15][16].

Starting from these two perspectives, three different bio-inspired 3D microphysiological models were designed in this thesis to study multicellular-vascular interactions using the microfluidic technology. The three separate models include a model of the human blood-brain barrier (BBB) and nanoparticle testing using the vasculature model (Section II), as well as two clinically relevant cancer models: KRAS/LKB1 lung carcinoma and ALK-positive anaplastic large cell lymphoma (ALCL) models (Section III).

These three models have in common an advanced perfusable microvasculature, developed by different strategies: self-assembled vasculogenesis with capillary-size microvascular networks, or patterned microchannels, an endothelial cells-based 3D macro-vessel to recreate large blood vessels. Then, initial characterizations of PLGA/Chitosan nanoparticles were performed. These nanosystems encapsulate miRNAs and siRNAs for the final application of gene silencing and the potential treatment of a range of diseases, including cancer (Section IV).

Design of in vitro preclinical models and 3D microphysiological systems

The key to success in developing any advanced preclinical model is to focus on mimicking organ-level physiology or pathophysiology observed *in vivo*. Their validation depends on the demonstration that they can effectively recapitulate behaviors observed *in vivo* [5]. Over the past decade, in addition to microfluidic technology, a wide variety of bioengineering approaches and strategies have been developed as alternatives to traditional cultures, including organoids technology and tissue engineering techniques, such as 3D bioprinting [1],[17],[18]. Tissue engineering and 3D printing represent advanced technologies where living cells are printed embedded in gel inks within precise format that can be derived from images of patients' tissues/organs [19],[20], [21]. The great potential is to reproduce tissue-specific architecture; however, printing speed and resolutions are main limitations. Similarly, it is possible to print 3D blood vessels, but still limited to vasculature with large diameters, and only few printing technologies, such as light-assisted bioprinting techniques, can achieve cell scale resolution and capillary sizes [22]. In addition, organoid cultures present a novel improvement of preclinical disease modeling [23], [24]. Patient-derived samples from surgical resections cultured as organoids are ideal for recapitulating the pathophysiology of the original tissue, such as tumors, however, they require long time to propagate enough material and lack of the native immune and stromal systems [25].

Additional possibilities for preclinical models are microphysiological systems using microfluidic technology. These microengineered systems have in common some of the characteristics of other advanced models (3D bioprinting and organoids), such as dynamic 3D culture with complex microenvironment to mimic cell-cell interactions [1], [6], [26], [27]. Microphysiological systems have shown the ability to recapitulate key microenvironmental characteristics of human organs and mimic their primary functions [27]. Results obtained from microfluidic devices are highly reproducible, relevant and directly translatable to humans. One of the main advantages of these platforms is the ability to control the specific cell and tissue architecture to emulate chemical gradients and biomechanical forces [3]. This allows for precise control over the biochemical and cellular milieu to model *in vivo*-like environments and responses [28]. Compared to other advanced 3D models, microfluidic culture allows the precise formation of microvascular networks and large blood vessels to mimic multicellular vascular interactions.

Microphysiological systems for modeling multicellular-vascular interactions using microfluidic technology

In this thesis, the ability to generate blood vessels from iPSC-ECs in culture with primary pericytes and astrocytes was demonstrated, towards the BBB-like phenotype for BBB transport modelling [29]. We also show a vascularized lung cancer model, comprising a non-small cell lung cancer (NSCLC) cell line spheroids (H1355), with inclusion of self-assembled microvasculature by combining endothelial cells (HUVEC) and lung fibroblasts within the same hydrogel that form perfusable lumens [30]. Similarly, ALK⁺ ALCL-vascular interactions were studied and suggested a mechanism of resistance to crizotinib (ALK inhibitor) mediated by endothelial cells.

The generation of micro-vascularized tumor systems using microfluidic technology is the major advantage over organoid culture [31], [32]. The lack of functional vasculature has contributed to its limited size and rapid advancement. One limitation of the organoids is the formation of an extremely large core that quickly becomes necrotic during development due to increased metabolic demands that cannot be met by diffusion alone [33]. Thus, incorporating functional vasculature in organoid models is indispensable for its growth above several hundred microns. The combination of organoid and microfluidic technology will enhance organoid expansion and applications [34]. Multiple researchers suggest their combination to further improve reliability, long-term stability and functional replication of their *in vivo* counterparts [33]. Recent advances in 3D bioprinting

also open up possibilities for printing larger tissue specimens and complex perfused vasculature to combine other preclinical designs[17].

Also, immune cells usually do not survive more than 10 to 15 days, and this is the time necessary for an organoid to grow and become useful for our scopes, since it allows culture with fewer amount of cells, microfluidic culture can conserve immune cells, as seen in applications with patient-derived organotypic tumor spheroids (PDOTS) and murine MDOTS [35]. These platforms have been used for viability assays to evaluate drug toxicity and metabolism for current immunotherapy as well as resistance and drug or immunotherapy tolerant persister cells[36]. However, one of the limitations of microfluidic culture of tumor spheroids alone is that the gel collapses due to the growth of the cells inside the matrix, which makes culturing in microfluidic devices impossible the in long-term. Instead, in combination with the microvasculature, both the collagen-fibrin combination and the extra-cellular matrix (ECM) production from fibroblasts help to sustain longer culture [32].

Microphysiological systems for blood-brain barrier modeling

The future perspectives for microphysiological models presented in this thesis will also include the combination of more cell lines to effectively recapitulate behaviors and anatomical structures observed *in vivo*. For the BBB microphysiological model, the inclusion of human embryonic stem (ES)-derived neuron spheroid or neurons generated from iPS cells will advance the reliability towards an engineered brain on a chip model [37] [38]. For instance, the BBB model can be modified by culturing cells with inflammatory cytokines, to recapitulate the transport properties of therapeutic agents across a diseased BBB [39]. A leakier BBB has been often associated with brain pathologies, such as Alzheimer's and Parkinson's Diseases, and cancer metastasis to the brain [40]. Studies have associated the disruption of the homeostasis of BBB-associated cell types, called BBB breakdown, with the pathogenesis of neurological disorders and complex multifactorial cognitive diseases [41]. However, the increase in BBB permeability may represent an opportunity for the design of effective NPs that are able to target damaged areas of the brain. In this scenario, our methodology contributes toward a better understanding of transport processes and signaling molecular pathways, potentially leading to the discovery of new targets and membrane transporters, which are highly upregulated in a pathological BBB, and improving drug delivery. The current BBB model would benefit from the inclusion of neurons and microglia,

generating a fully engineered brain on a chip model, and these might have further effects on barrier's functionality. Moreover, alternatives to fibrin gel must be considered, as it might cause neuronal damage [42]. Possible alternatives are combinations of natural polymers (hyaluronic acid, chitosan, or collagen), which have been successfully utilized as ECM for brain models [37].

Microphysiological models of the tumor – vascular interactions in KRAS/LKB1 Non-Small Cell Lung Cancer and ALK⁺ Anaplastic Large Cell Lymphoma

For lung cancer models, the inclusion of additional cells, such as lung epithelial cells for the lung models and lymphatic vessels and fibroblasts to generate a lymph node models, will create a more similar reproduction of the TME [43]. However, this is still limited to the use of cell lines or stem cells. One of the main hurdles to the development of patient-specific microphysiological cancer models that enable the sophisticated level of analysis described above, is the need to separate and isolate all cell types (cancer cells, endothelial cells, stromal cells and immune cells) from the same patient. Then, to build organ chips with the appropriate cell types in the correct relative proportions and location to accurately mimic *in vivo* behaviors and responses is also an obstacle [44]. Each of these cell types requires specific isolation protocols and culture conditions to guarantee that the cell-specific functionality is maintained. Furthermore, the meaningful integration of multiple different cell types in microfluidic devices can be time-consuming and requires continuous optimization [7], [34]. Only when this can be done correctly and rapidly and has been validated against known responses from patient, will it be possible for cancer models to be used to robustly evaluate anticancer therapies for individual patients.

Nevertheless, a main issue of histocompatibility arises when combining PDOTS with endothelial cell lines to generate vascularized tumor models. To avoid alloreaactions, it will be necessary to obtain primary endothelial cells or generate iPSC-ECs from the same patient toward personalized medicine application [45]. Another possibility would be to generate an endothelial cell line with depletion of beta-2 microglobulin (B2M), the main component of the major histocompatibility complex (MHC) class I molecules, generating an “universal” cell line compatible with all patients. This technology can be applied for migration and infiltration of immune cells.

Alternative applications of the microphysiological systems described in this thesis, could be leverage the current vascular systems for studying immune cells trafficking that do not require MHC compatibility, such as natural killer (NK) cells and chimeric antigen receptor (CAR) T cells.

These NK cells are critical components of the innate immune system which recognize and kill cells independently of MHC presentation, but frequently inhibited by ligands on the tumor cell surface[46]. Similarly, CAR T cells are genetically engineered T cells with the ability to target a specific protein on the target cell surface without MHC recognition. CAR T cell therapies have been approved by the FDA to target hematological malignancies[47]. However, infiltration into solid tumors has been challenging due to the suppressive TME. In both cases, further investigations using microphysiological systems of tumor-vascular interaction may uncover fundamental mechanisms of immune cells homing in the TME[47].

In section III of this thesis, ALK inhibitor (crizotinib, approved in January 2021 by the FDA for ALCL) was tested in the microphysiological system of ALCL-vascular interactions. Interestingly, ALCL were more resistant to crizotinib, suggesting that the inclusion of the vasculature produced a different milieu of cytokines and signaling between cells. This further proves that a better mimic of the TME and perivascular niche is fundamental to test drugs that will reach the clinic.

In the section IV of this thesis, the design and fabrication of bioartificial siRNA and miRNA-loaded NPs was explored. In addition, further developments of these nanocarrier systems will be the decoration of the NPs surface with active targeting ligands, characterized by high specificity toward selected receptor overexpressed by the membrane of the cancer cells or targeting other cells of the TME or brain-specific ligands.

Nanomedicine and Nanoparticle transport using microphysiological systems

In the section II, the functionalization of the NP surface with holo-transferrin was investigated for brain-specific targeting. Similarly, an important improvement of the bioartificial NPs system characterized in section IV will be the surface functionalization with molecules for specific and targeted release. For instance, several types of bioactive molecules have been explored for surface decoration, including folic acid, enzymes, natural and synthetic antibodies, proteins, peptides and carbohydrates that could be appropriate in these applications [48].

For instance, suitable functionalization that can be applied in ALCL and NSCLC are: anti-CD30 antibody targeting ALCL [49], anti-DLL3 in SCLC [50], and anti-EGFR [51] antibody targeting specific receptor overexpressed in several subtype of lung carcinoma.

To prevent protein corona formation and increase NP stability, Tween 80 (a PEG-based emulsifier) was incorporated into our NP system. Further characterization *in vivo* and *in vitro* in a vascularized model will help to understand the half-life circulation and biodistribution of NPs system. The payloads used in the NPs used in section IV were fluorescently labelled negative controls, without any biological function. A possible future application will be to load NPs with siRNAs targeting specific genes, such as ALK-targeting siRNA, to study their functionality *in vitro* in microphysiological systems of ALCL-vascular interactions, similarly to the system showed in Section III, Chapter 7.

In this thesis we have also demonstrated that microfluidic systems can be employed to test drug efficacy and NPs transport permeability across biological barriers *in vitro* [52]. The data provided here (section II) present the design and development of a 3D *in vitro* human BBB microvasculature model and its new application as effective and convenient methodology for quantifying the transport and distribution properties of NPs across the BBB. Notably, the functionality and vascular permeabilities of the model are defined by various parameters, including its precise geometry and dimensions and NPs physicochemical properties (including material composition, surface coating, surface functional groups and charge). The inclusion of a perfused endothelium-lined vasculature also offers greater clinical relevance for studying drug delivery [53], [54], as well as modelling pharmacokinetics and pharmacodynamics (PK–PD) which are greatly influenced by drug transport into and across the vascular barrier [55].

Permeability measurements, however, are limited to quantifying concentrations of drugs or NPs conjugated to a fluorescent tracer. Similar measurements can be made by tagging the molecule of interest with a fluorescent marker using this same experimental protocol. Alternatively, samples of interstitial fluid could be directly collected from the gel filling ports in the device and used to quantify transport into the matrix, but this could be problematic due to the low drug concentrations in the gel region, as previously suggested [29].

Translational application of microphysiological systems for personalized medicine

Microphysiological systems also offer the possibility of elevating personalized medicine to a higher level by more faithfully recapitulating patient-specific, organ-level pathophysiology and responses to therapy [11]. Indeed, an additional advantage gained by an even more comprehensive

human patient-derived *in vitro* model, to generate patient-specific microphysiological systems at an integrative system level is critical for personalized medicine [56]. For example, in the BBB model combining iPSCs and/or neural stem cells with the vascular networks, PCs, and ACs described here. Moreover, using iPSC cells derived from patients affected by neurological disorders, such as Alzheimer's disease, a BBB pathological model could be obtained. Similarly, at this point, only cell lines were used to design all the cancer models designed in this thesis. Advances in *ex vivo* modeling may allow long-term culture of patient-derived tumor samples to enable a personalized medicine approach to study drug resistance, innate and adaptive immunity and immune cell penetration in patient-specific tumor niches [45].

In this thesis, to analyze gene expression in co-culture experiments, cells were either sorted by flow cytometry (Section III) or bulk RNA was collected (section II) from the microfluidic device. Sorting cell populations from the device has been challenging, but scaling up the size and consequently the cell density will facilitate sorting out cell population by flow cytometry. To reach a better resolution and improve learning about post-transcriptional modifications, the combination of single cell RNA sequencing and cellular barcoding (or cell tagging) will allow the recognition of the cell population.

Moreover, adult healthy primary cell-derived organoids combined with CRISPR/Cas9-mediated genetic engineering technology may allow the conversion of normal cells into their respective malignancies *in vitro* by adding a combination of cancerous mutations in a sequential manner [57]. Altogether, the combination of genome-wide CRISPR screening, cytokine profiling, single cell-RNA sequences, performed in these advanced preclinical models, including xenografts of primary tumors including neurodegenerative diseases, lung adenocarcinoma and anaplastic large cell lymphoma, should help in the evaluation of new therapeutic agents or new combination therapies. For instance, the development and testing of novel nanocarrier such as polymer nanoparticles containing silencing siRNA targeting ALK to predict both therapeutic efficacies. The study of ALCL-vascular interactions would benefit of a broader CRISPR screening and chemokine profiling to identify additional molecular targets of drug resistance.

Advanced bioengineering tools for microphysiological systems

Despite all the relevant innovations in terms of complexity, *in vitro* devices are still unable to fully recapitulate the biological *in vivo* interactions within an entire organism.

Finally, given recent advances in fluidically-coupled multiple microfluidic systems, to connect microphysiological systems and recreate a human body-on-chip, we can begin to consider the possibility of creating multi-microphysiological models to mimic the systemic interactions between organs [55]. One possibility would be modelling systemic metastasis using a multi organ on chip or body on chip system. The metastatic spread might be modelled from a vascularized lung model to the brain, passing through a lymph node [7]. These systems will still be simplistic representations of organs interactions, far behind from the *in vivo* models obtained with mice or humanized mice models [58], [59], but with the great advantage of using human cells. In view of the biochemical and structural complexity of organs, it is unlikely that only one engineering approach for building artificial *ex vivo* tissues will on their own solve the challenges of manufacturing and modelling artificial equivalents of human biology for pre-clinical systems. The association of engineered 3D environments, stem-cell growth, associated with the cellular self-organization processes to spatial boundary conditions, stem cells are more capable of organizing themselves into high-order and large-scale structures, some external guidance seems to be required to ensure the normalization and direction of cell behavior, offers a promising insight for more advanced *in vitro* preclinical models of tissues [60][61].

Taken together, the advances and combinations of 3D bioengineering approaches [62], including 3D bioprinting and organoids with microphysiological systems seen in this thesis, will provide new opportunities for successful translation of tissue regeneration technologies and also achieve a better understanding of the mechanisms involved in disease pathogenesis and progression.

One of the disadvantages of microfluidic platforms is that they are difficult to maintain for long-term culture (months). Experimental protocols involving microfluidic devices are quite critical, require experienced operators and several training, and have a higher risk of contamination compared to 2-D culture due to the high frequency of media exchange. Microfluidic devices, compared to multiwells, could be considered as low-throughput screening tools (but potentially medium to high throughput screening). One possibility will be to design greater platforms

containing an increased number of devices. Also, automatization will help to speed up the process and exponentially increase the number of experiments [63].

A possible improvement to the current models is the introduction of continuous perfusion by integrating micropumps for fluid-flow stimuli. Indeed, flow perfusion culture could advance the model in several important aspects: transport of nutrients and oxygen into the vessels in favor of more efficient aerobic respiration, useful for maintaining a long-term culture. Secondly, flow-mediated shear stress improves microvascular formation and reduce vascular permeability in a long-term culture system [29]. Specifically, flow stimuli have been demonstrated to promote the differentiation of vascular endothelial cells into a phenotype more similar to the BBB with the highest expression of TJ proteins and membrane transporters, producing further reductions in permeability [64]. This will definitively enhance the physiological relevance of the BBB model. Lastly, fluid stimuli will also be interesting to perturb with fluid flow the microvascular systems containing immune cells to study how the adhesion molecules transform overtime.

Microphysiological systems: a pharma perspective

The field of advanced microphysiological systems has shown promising results and several obvious areas where such models could bring value, but still in its infancy in terms of preclinical application and standard inclusion in drug discovery pipelines. The level of the microphysiological systems is not robust enough to support routine, and high-level testing of characterization is required for microphysiological models for widespread adoption. Thus, allow replacement of existing screens, traditional workflows, platforms assays and animal models. Also, these systems will gain confidence through testing of more than 100 compounds for which clinical data were available, under harmonized data sets must be compared between regulators [65]. For example, it would be necessary to systematically compare these models with traditional platforms and animal models, and define standardized methods and protocols to compare our systems. There are a certain number of ‘minimum’ criteria to be fulfilled, which include the ability to reproduce the desired physiology and functionality and elicit the expected responses to standard or reference compounds and assays, but also, reproducibility and compliance to further adaptation with the industrial settings are fundamental factors [66].

To realize the full potential of microphysiological systems, more collaboration will be needed between stakeholders: regulators, pharmaceutical companies and academic investigators.

A recent survey forecast that within 5 years, microphysiological systems would save between 10% and 26% of R&D cost, with the greatest impact being realized during the lead optimization process [67]. However, before this can happen, pharma companies need to make an upfront investment in the technology, as most of the approaches are still exploratory and require substantial refinement before use in a drug development setting.

To this end, several consortia, such as the Innovation and Quality (IQ) consortium [68] have worked on a series of organ-system manuscripts addressing the context of use, or the European society for alternatives for animal testing (EUSAAT) [69] and the European Organ on chip society (EUROoCS) [70], which organize working groups and international meetings society to promote advanced preclinical models according to the 3Rs Principles (refinement, reduction, replacement). In summary, bridging the gap between proof of concept and ‘industry-grade’ of microphysiological systems for testing drugs and nanocarriers will requires investments, collaboration and communication across all stakeholders. This innovative field, at the intersection between biology and engineering, has an unprecedented opportunity to revolutionize the artificial living creations for preclinical models, and it requires a strong commitment to an ethically responsible research [71]. It involves strategies for systematic validations, precise regulations from government entities and regulators, together with reframing of the challenge and adapting to traditional biomedical research practices to new approaches for drug discovery and development.

Conclusions

In this thesis work, several preclinical models were designed using microfluidic technology to generate microphysiological systems that contained combinations of cells and biomaterials.

Here the design of three different bio-inspired 3D microphysiological models to study multicellular-vascular interactions in a microfluidic device were described. This includes a human blood-brain barrier (BBB) model, as well as two clinically relevant cancer models: KRAS/LKB1 lung carcinoma and ALK-positive anaplastic large cell lymphoma (ALCL) models. In the BBB model, the permeability of polymer NPs across across the model of biological barrier was measured. In the last section, systems for oligonucleotide release were also prepared, including miRNA and siRNA-loaded NPs with “bioartificial” structure composed of PLGA and chitosan (CS).

Nanoparticle-based delivery systems were characterized in terms of complexes formation, viability and transfection efficacy. This approach is a promising strategy to combine high loading performances with optimal *in vivo* pharmacokinetics upon systemic administration. Moreover, the results of section IV evidence enhanced transfection efficiency of siRNA and miRNA NPs.

All the models of this thesis led to new insights that could not have been discovered using traditional *in vitro* 2D cultures. The integration of human microphysiological systems in drug development pipelines holds great potential if we can overcome the challenges related to simplifying their fabrication and use and increasing their robustness. Taken together, our results are highly relevant from the perspective of preclinical screening platforms according to the principle of the 3Rs (reduction, refinement, replacement), warranting further investigations. Future studies will systematically assess the reliability of these models compared with traditional assays and animal models and improve their cultures to a better mimic of the physiological condition.

Overall, these microengineered microphysiological systems have the capability to more reliably predict therapeutic vulnerabilities and study drug transport and innovative nanocarriers across biological barriers, thereby expediting drug discovery and providing important new insights into fundamental biological processes to expand our understanding of several currently incurable diseases.

References

- [1] K. Wang *et al.*, “Microphysiological Systems: Design, Fabrication, and Applications,” *ACS Biomater. Sci. Eng.*, vol. 6, no. 6, pp. 3231–3257, 2020.
- [2] J. P. A. Ioannidis, B. Y. S. Kim, and A. Trounson, “How to design preclinical studies in nanomedicine and cell therapy to maximize the prospects of clinical translation,” *Nat. Biomed. Eng.*, vol. 2, no. 11, pp. 797–809, 2018.
- [3] L. A. Low, C. Mummery, B. R. Berridge, C. P. Austin, and D. A. Tagle, “Organs-on-chips: into the next decade,” *Nat. Rev. Drug Discov.*, 2020.
- [4] S. N. Bhatia and D. E. Ingber, “Microfluidic organs-on-chips,” *Nat. Biotechnol.*, vol. 32, no. 8, pp. 760–772, 2014.
- [5] E. W. Esch, A. Bahinski, and D. Huh, “Organs-on-chips at the frontiers of drug discovery,” *Nat. Rev. Drug Discov.*, vol. 14, no. 4, pp. 248–260, 2015.
- [6] J. J. Hickman, D. Huh, and R. D. Kamm, “Microphysiological systems,” *APL Bioeng.*, vol. 3, no. 4, p. 040401, 2019.
- [7] A. Sontheimer-Phelps, B. A. Hassell, and D. E. Ingber, “Modelling cancer in microfluidic human organs-on-chips,” *Nat. Rev. Cancer*, vol. 19, no. 2, pp. 65–81, 2019.
- [8] B. Zhang, A. Korolj, B. F. L. Lai, and M. Radisic, “Advances in organ-on-a-chip engineering,” *Nat. Rev. Mater.*, vol. 3, no. 8, pp. 257–278, 2018.
- [9] J. Wolfram and M. Ferrari, “Clinical cancer nanomedicine,” *Nano Today*, vol. 25, pp. 85–98, 2019.
- [10] D. J. Irvine and E. L. Dane, “Enhancing cancer immunotherapy with nanomedicine,” *Nat. Rev. Immunol.*, vol. 20, no. 5, pp. 321–334, 2020.
- [11] M. J. Mitchell, M. M. Billingsley, R. M. Haley, M. E. Wechsler, N. A. Peppas, and R. Langer, “Engineering precision nanoparticles for drug delivery,” *Nat. Rev. Drug Discov.*, 2020.
- [12] O. S. Fenton, K. N. Olafson, P. S. Pillai, M. J. Mitchell, and R. Langer, “Advances in Biomaterials for Drug Delivery,” *Adv. Mater.*, vol. 30, no. 29, pp. 1–29, 2018.
- [13] J. P. Rao and K. E. Geckeler, “Polymer nanoparticles: Preparation techniques and size-control parameters,” *Prog. Polym. Sci.*, vol. 36, no. 7, pp. 887–913, 2011.
- [14] Y. Chen, D. Y. Gao, and L. Huang, “In vivo delivery of miRNAs for cancer therapy: Challenges and strategies,” *Adv. Drug Deliv. Rev.*, vol. 81, pp. 128–141, 2015.
- [15] J. M. Caster, C. Callaghan, S. N. Seyedin, K. Henderson, B. Sun, and A. Z. Wang, “Optimizing Advances in Nanoparticle Delivery for Cancer Immunotherapy,” *Adv. Drug Deliv. Rev.*, vol. 144, pp. 3–15, 2019.
- [16] D. Furtado, M. Björnalm, S. Ayton, A. I. Bush, K. Kempe, and F. Caruso, “Overcoming the Blood–Brain Barrier: The Role of Nanomaterials in Treating Neurological Diseases,” *Adv. Mater.*, vol. 30, no. 46, 2018.
- [17] S. Mehrotra, J. C. Moses, A. Bandyopadhyay, and B. B. Mandal, “3D Printing/Bioprinting Based Tailoring of in Vitro Tissue Models: Recent Advances and Challenges,” *ACS Appl. Bio Mater.*, vol. 2, no. 4, pp. 1385–1405, 2019.
- [18] H. Clevers, “Modeling Development and Disease with Organoids,” *Cell*, vol. 165, no. 7, pp. 1586–1597, 2016.
- [19] A. C. Fonseca *et al.*, “Emulating Human Tissues and Organs: A Bioprinting Perspective Toward Personalized Medicine,” *Chem. Rev.*, 2020.
- [20] Y. S. Zhang *et al.*, “3D Bioprinting for Tissue and Organ Fabrication,” *Ann. Biomed. Eng.*, vol. 45, no. 1, pp. 148–163, 2017.
- [21] S. V. Murphy, P. De Coppi, and A. Atala, “Opportunities and challenges of translational 3D bioprinting,” *Nat. Biomed. Eng.*, vol. 4, no. 4, pp. 370–380, 2020.
- [22] A. K. Miri, A. Khalilpour, B. Cecen, S. Maharjan, S. R. Shin, and A. Khademhosseini, “Multiscale bioprinting of vascularized models,” *Biomaterials*, vol. 198, no. August 2018, pp. 204–216, 2019.

- [23] J. Drost and H. Clevers, “Organoids in cancer research,” *Nat. Rev. Cancer*, vol. 18, no. 7, pp. 407–418, 2018.
- [24] J. Drost and H. Clevers, “Organoids in cancer research,” *Nat. Rev. Cancer*, vol. 18, no. 7, pp. 407–418, 2018.
- [25] Y.-H. Lo, K. Karlsson, and C. J. Kuo, “Applications of organoids for cancer biology and precision medicine,” *Nat. Cancer*, vol. 1, no. 8, pp. 761–773, 2020.
- [26] L. Ewart and A. Roth, “Opportunities and challenges with microphysiological systems: a pharma end-user perspective,” *Nat. Rev. Drug Discov.*, no. February, 2020.
- [27] S. Seo, H. Kim, J. H. Sung, N. Choi, K. Lee, and H. N. Kim, “Microphysiological systems for recapitulating physiology and function of blood-brain barrier,” *Biomaterials*, vol. 232, no. December 2019, p. 119732, 2020.
- [28] H. Kimura, Y. Sakai, and T. Fujii, “Organ/body-on-a-chip based on microfluidic technology for drug discovery,” *Drug Metab. Pharmacokinet.*, vol. 33, no. 1, pp. 43–48, 2018.
- [29] M. Campisi, Y. Shin, T. Osaki, C. Hajal, V. Chiono, and R. D. Kamm, “3D self-organized microvascular model of the human blood-brain barrier with endothelial cells, pericytes and astrocytes,” *Biomaterials*, vol. 180, pp. 117–129, 2018.
- [30] M. Campisi *et al.*, “Tumor-Derived cGAMP Regulates Activation of the Vasculature,” *Front. Immunol.*, vol. 11, no. September, pp. 1–16, 2020.
- [31] T. Osaki, V. Sivathanu, and R. D. Kamm, “Vascularized microfluidic organ-chips for drug screening, disease models and tissue engineering,” *Curr. Opin. Biotechnol.*, vol. 52, pp. 116–123, 2018.
- [32] K. Haase and D. Roger, “Advances in on-chip vascularization,” *Regen. Med.*, vol. 12, pp. 285–302, 2017.
- [33] S. Zhang, Z. Wan, and R. D. Kamm, “Vascularized organoids on a chip: Strategies for engineering organoids with functional vasculature,” *Lab Chip*, 2021.
- [34] E. Garreta *et al.*, “Rethinking organoid technology through bioengineering,” *Nat. Mater.*, 2020.
- [35] A. R. Aref *et al.*, “3D microfluidic *ex vivo* culture of organotypic tumor spheroids to model immune checkpoint blockade,” *Lab Chip*, 2018.
- [36] R. W. Jenkins *et al.*, “Ex vivo profiling of PD-1 blockade using organotypic tumor spheroids,” *Cancer Discov.*, vol. 8, no. 2, pp. 196–215, 2018.
- [37] T. Osaki, V. Sivathanu, and R. D. Kamm, “Engineered 3D vascular and neuronal networks in a microfluidic platform,” *Sci. Rep.*, vol. 8, no. 1, pp. 1–13, 2018.
- [38] H. Y. Tan, H. Cho, and L. P. Lee, “Human mini-brain models,” *Nat. Biomed. Eng.*, vol. 5, no. 1, pp. 11–25, 2021.
- [39] Y. Shin *et al.*, “Blood–Brain Barrier Dysfunction in a 3D In Vitro Model of Alzheimer’s Disease,” *Adv. Sci.*, vol. 6, no. 20, 2019.
- [40] D. Shlosberg, M. Benifla, D. Kaufer, and A. Friedman, “Blood-brain barrier breakdown as a therapeutic target in traumatic brain injury,” *Nat. Rev. Neurol.*, vol. 6, no. 7, pp. 393–403, 2010.
- [41] E. a Winkler, R. D. Bell, and B. V Zlokovic, “Central nervous system pericytes in health and disease,” *Nat. Neurosci.*, vol. 14, no. 11, pp. 1398–1405, 2011.
- [42] M. Cortes-Canteli, L. Mattei, A. T. Richards, E. H. Norris, and S. Strickland, “Fibrin deposited in the Alzheimer’s disease brain promotes neuronal degeneration,” *Neurobiol. Aging*, vol. 36, no. 2, pp. 608–617, 2015.
- [43] Y. S. Zhang, Y. N. Zhang, and W. Zhang, “Cancer-on-a-chip systems at the frontier of nanomedicine,” *Drug Discov. Today*, vol. 22, no. 9, pp. 1392–1399, 2017.
- [44] M. Binnewies *et al.*, “Understanding the tumor immune microenvironment (TIME) for effective therapy,” *Nat. Med.*, vol. 24, no. 5, pp. 541–550, 2018.
- [45] C. Pauli *et al.*, “Personalized in vitro and in vivo cancer models to guide precision medicine,” *Cancer Discov.*, vol. 7, no. 5, pp. 462–477, 2017.
- [46] B. Cózar, M. Greppi, S. Carpentier, E. Narni-Mancinelli, L. Chiossone, and E. Vivier, “Tumor-infiltrating natural killer cells,” *Cancer Discov.*, vol. 11, no. 1, pp. 34–44, 2021.

- [47] R. C. Larson and M. V. Maus, “Recent advances and discoveries in the mechanisms and functions of CAR T cells,” *Nat. Rev. Cancer*, vol. 21, no. March, 2021.
- [48] S. K. Golombek *et al.*, “Tumor targeting via EPR: Strategies to enhance patient responses,” *Adv. Drug Deliv. Rev.*, vol. 130, pp. 17–38, 2018.
- [49] R. Chiarle, C. Voena, C. Ambrogio, R. Piva, and G. Inghirami, “The anaplastic lymphoma kinase in the pathogenesis of cancer,” *Nat. Rev. Cancer*, vol. 8, no. 1, pp. 11–23, 2008.
- [50] S. K. Wong and W. T. Iams, “Front line applications and future directions of immunotherapy in small-cell lung cancer,” *Cancers (Basel)*, vol. 13, no. 3, pp. 1–15, 2021.
- [51] D. Irmer, J. O. Funk, and A. Blaukat, “EGFR kinase domain mutations - Functional impact and relevance for lung cancer therapy,” *Oncogene*, vol. 26, no. 39, pp. 5693–5701, 2007.
- [52] S. W. L. Lee *et al.*, “Modeling Nanocarrier Transport across a 3D In Vitro Human Blood-Brain-Barrier Microvasculature,” *Adv. Healthc. Mater.*, vol. 9, no. 7, Apr. 2020.
- [53] G. S. Offeddu *et al.*, “An on-chip model of protein paracellular and transcellular permeability in the microcirculation,” *Biomaterials*, vol. 212, pp. 115–125, Aug. 2019.
- [54] K. Haase, G. S. Offeddu, M. R. Gillrie, and R. D. Kamm, “Endothelial Regulation of Drug Transport in a 3D Vascularized Tumor Model,” *Adv. Funct. Mater.*, 2020.
- [55] A. Herland *et al.*, “Quantitative prediction of human pharmacokinetic responses to drugs via fluidically coupled vascularized organ chips,” *Nat. Biomed. Eng.*, vol. 4, no. 4, pp. 421–436, 2020.
- [56] S. A. Dugger, A. Platt, and D. B. Goldstein, “Drug development in the era of precision medicine,” *Nat. Rev. Drug Discov.*, vol. 17, no. 3, pp. 183–196, 2018.
- [57] F. J. Sánchez-Rivera and T. Jacks, “Applications of the CRISPR-Cas9 system in cancer biology,” *Nat. Rev. Cancer*, vol. 15, no. 7, pp. 387–395, 2015.
- [58] T. M. Allen *et al.*, “Humanized immune system mouse models: progress, challenges and opportunities,” *Nat. Immunol.*, vol. 20, no. 7, pp. 770–774, 2019.
- [59] L. D. Shultz, F. Ishikawa, and D. L. Greiner, “Humanized mice in translational biomedical research,” *Nat. Rev. Immunol.*, vol. 7, no. 2, pp. 118–130, 2007.
- [60] J. A. Brassard, M. Nikolaev, T. Hübscher, M. Hofer, and M. P. Lutolf, “Recapitulating macro-scale tissue self-organization through organoid bioprinting,” *Nat. Mater.*, vol. 20, no. January, 2020.
- [61] J. Laurent *et al.*, “Convergence of microengineering and cellular self-organization towards functional tissue manufacturing,” *Nat. Biomed. Eng.*, vol. 1, no. 12, pp. 939–956, 2017.
- [62] M. M. Alvarez *et al.*, “Emerging Trends in Micro- and Nanoscale Technologies in Medicine: From Basic Discoveries to Translation,” *ACS Nano*, vol. 11, no. 6, pp. 5195–5214, 2017.
- [63] R. Novak *et al.*, “Robotic fluidic coupling and interrogation of multiple vascularized organ chips,” *Nat. Biomed. Eng.*, vol. 4, no. 4, pp. 407–420, 2020.
- [64] A. Appelt-Menzel *et al.*, “Establishment of a Human Blood-Brain Barrier Co-culture Model Mimicking the Neurovascular Unit Using Induced Pluri- and Multipotent Stem Cells,” *Stem Cell Reports*, vol. 8, no. 4, pp. 894–906, 2017.
- [65] K. J. Jang *et al.*, “Liver-Chip: Reproducing Human and Cross-Species Toxicities,” *Sci. Immunol.*, 2019.
- [66] L. Ewart *et al.*, “Navigating tissue chips from development to dissemination: A pharmaceutical industry perspective,” *Exp. Biol. Med.*, vol. 242, no. 16, pp. 1579–1585, 2017.
- [67] N. Franzen, W. H. van Harten, V. P. Retèl, P. Loskill, J. van den Eijnden-van Raaij, and M. IJzerman, “Impact of organ-on-a-chip technology on pharmaceutical R&D costs,” *Drug Discov. Today*, vol. 24, no. 9, pp. 1720–1724, 2019.
- [68] “International consortium for innovation an quality,” <https://iqconsortium.org>
- [69] “European society for alternatives for animal testing (EUSAAT),” <http://www.eusaat-congress.eu>
- [70] “European Organ on chip society,” <https://euroocs.eu/annual-meeting/>
- [71] M. Sample *et al.*, “Multi-cellular engineered living systems: Building a community around responsible research on emergence,” *Biofabrication*, vol. 11, no. 4, 2019.

